

**Density currents driven by differential cooling in lakes:
occurrence, dynamics and implications for littoral-
pelagic exchange**

Présentée le 22 septembre 2022

Faculté de l'environnement naturel, architectural et construit
Laboratoire d'hydraulique environnementale
Programme doctoral en génie civil et environnement

pour l'obtention du grade de Docteur ès Sciences

par

Tomy DODA

Acceptée sur proposition du jury

Prof. M. Lehning, président du jury
Prof. C. Ancey, Dr D. Bouffard, directeurs de thèse
Prof. M. Wells, rapporteur
Prof. D. McGinnis, rapporteur
Dr M. Schmid, rapporteur

Learn how to see.

Realize that everything connects to everything else.

— Leonardo da Vinci

To my parents, for their continuous support...

To my grandfather, who often challenged me to explain
him my PhD topic...



Acknowledgements

Many people contributed, directly or indirectly, to the work presented in this thesis.

In a chronological order, I want to thank Alfred Johnny Wüest, my first thesis director, for having introduced me to the field of limnology, back in 2016, and having continuously supported my work since then. This thesis would not have happened without his Limnology course that remained one of the highlights of the Master studies at EPFL. Thank you Johnny for your support along these years and your availability each time I needed your experience, even after your retirement! And thank you for having connected me with Eawag and Damien Bouffard, my main thesis supervisor.

Summarizing Damien's supervision in a few lines is hard because there is a lot to say... I feel very lucky to have such a unique relationship with my supervisor. Thanks Damien for your personality in general, your constant motivation and optimism, and all the effort you put in this thesis, from the initial brainstorming sessions to the final manuscripts, without forgetting the intense field campaigns! You really contributed to make these four years of PhD enjoyable and unforgettable.

I would like to also thank Christophe Ancely, my third supervisor, for having accepted to replace Johnny after his retirement and for his quick and efficient support in all the administrative duties.

I am grateful to the other committee members for having accepted to evaluate this thesis: Mathew Wells, Daniel McGinnis, Martin Schmid and Michael Lehning. Thank you for your inspiring work.

The work presented in this thesis is part of a larger project that involved two Postdocs: Hugo Ulloa and Cintia Ramón. I definitely believe that having such a close support from Postdocs while doing a PhD is a unique opportunity to learn a lot about science. Thanks to both of you for your amazing work, your constant feedback, your great mood and all what you taught me.

This thesis involved a lot of fieldwork, which would not have been possible without the help of many people. I sincerely thank Michael Plüss, our technician, for his support in planning and performing the measurements, and for dealing with unexpected (but common!) complications. I

Acknowledgements

am also grateful to the other technicians, Sébastien Lavanchy and Guillaume Cunillera from EPFL, and Christian Dinkel from Eawag, who joined us in the field and shared their experience. A special thanks to Hugo Cruz who made the 2021 Lake Tour possible and successful. I am indebted to all the people who helped in the field, who are acknowledged in the corresponding chapters.

Several colleagues from the “biogeochemical side” provided their expertise for this thesis: Marie-Elodie Perga from UNIL, Matthias Brennwald and Rolf Kipfer from Eawag-DD and Carsten Schubert from Eawag-KB. Thank you all for having extended my work beyond the aquatic physics boundaries!

I thank all my former and current colleagues from the EPFL and Eawag Aphys groups for the great time we spent together and for their feedback about my work: Oscar, Love, Fabian, James, Fazel, Bieito, Camille, Hannah, Shubham, Sebastiano, Michele, Josquin, Angelo and Lucas. I also thank Edgar Hédouin, a Master student who helped to create a lake database from our field measurements. Special thanks to Oscar, Fazel, Kathrin, Typhaine and James for their comments on the thesis.

My parents shared a strong interest in my thesis, gave me regular advice and encouragement, and helped me to cope with the challenging aspects of a PhD journey. I would not be here without their continuous support along all these years. Thank you from all my heart. I am also grateful to the other members of my small family who are always present in case I need them.

Last but not least, I would like to thank my other family: all the members of Eawag- Kastanienbaum or KB. I do not think there could be a better place to do a PhD. The unique location, friendly atmosphere, social activities and great facilities made this PhD an enjoyable experience. Thank you all!

Kastanienbaum, May 2022



Abstract

Cross-shore flows exchange water laterally in lakes, with ecological implications for the ecosystem. One example is the convective circulation induced by differential cooling, also known as the thermal siphon. This lateral flow forms when the sloping sides of lakes experience surface cooling. Shallow areas cool faster, which generates lateral density gradients and drives a cold downslope gravity current and an onshore surface flow. The role of this two-layer-circulation in lateral exchange in lakes is poorly understood, due to the lack of long-term and high-resolution measurements of thermal siphons. This thesis aims at filling this gap by investigating the occurrence and dynamics of thermal siphons from extensive in situ observations in a wind-sheltered Swiss lake (Rotsee).

We first quantified the seasonality of thermal siphons from one-year-long observations in Rotsee. Thermal siphons occurred on a daily basis from late summer to winter and flushed the littoral region in ~ 10 h. Their duration increased but their intensity decreased over the same period. We linked this seasonality to the change in forcing conditions by testing scaling relationships from theoretical and laboratory-based studies.

We then focused on the short-term temporal variability of the transport by quantifying the dynamics of thermal siphons over a diurnal cycle and their interaction with convective plumes. Our results reveal that convective plumes penetrated into the gravity current at night and eroded its upper interface. This vertical mixing generated vertical interface fluctuations and reduced the lateral transport at night. The maximal transport was delayed to daylight conditions when radiative heating weakened penetrative convection.

After having quantified the physical water transport, we assessed the role of thermal siphons in the lateral exchange of dissolved gases. We found that both branches of the circulation were capable of transporting gases laterally. The downslope current brought littoral gases to the base of the mixed

Abstract

layer in the stratified region whereas the surface flow transported gases towards the shore. We quantified this exchange for oxygen and methane.

Finally, we generalized our observations to other lakes with different bathymetry and forcing conditions. The frequent occurrence of thermal siphons observed in six lakes confirmed that this lateral transport process is ubiquitous in lakes with shallow littoral regions. We showed that our results from Rotsee were applicable to other systems, where the same scaling relationships predicted the formation and intensity of thermal siphons. Based on these results, we proposed a procedure to predict the contribution of thermal siphons for lateral transport in any lake.

This thesis provides a comprehensive understanding of the formation and dynamics of thermal siphons and paves the route for integrating this lateral transport process in lake ecosystem research.

Keywords

Thermal siphon, gravity current, cross-shore circulation, differential cooling, lateral transport, penetrative convection, lake.



Résumé

Les courants transversaux créent des échanges d'eau latéraux dans les lacs, avec des implications écologiques pour l'écosystème. Un exemple est la circulation convective induite par refroidissement différentiel, aussi connue sous le nom de siphon thermique. Ce courant latéral se forme quand les pentes des lacs sont soumis à un refroidissement de surface. Les régions peu profondes se refroidissent plus vite, ce qui crée des gradients latéraux de densité et produit un courant de gravité froid descendant la pente et un courant de surface dirigé vers la côte. Le rôle de cette circulation à deux couches pour les échanges latéraux dans les lacs est peu compris, dû au manque de mesures à haute résolution sur des longues durées. Cette thèse vise à combler cette lacune en investigant la présence et la dynamique des siphons thermiques à partir d'observations in situ dans un lac suisse protégé du vent (Rotsee).

Nous avons d'abord quantifié la saisonnalité des siphons thermiques à partir d'observations à Rotsee sur une année. Les siphons thermiques se formèrent sur une base journalière de la fin de l'été à l'hiver et vidangèrent la région littorale en ~ 10 h. Leur durée augmenta mais leur intensité diminua sur la même période. Nous avons relié cette saisonnalité aux changements de forçage en testant des relations de mise à l'échelle provenant d'études théoriques et de laboratoire.

Nous nous sommes ensuite focalisés sur la variabilité temporelle à petite échelle du transport en quantifiant la dynamique des siphons thermiques sur un cycle journalier et leur interaction avec les cellules convectives. Nos résultats révèlent que les cellules convectives pénétrèrent dans le courant de gravité pendant la nuit et érodèrent son interface supérieure. Ce mélange vertical généra des fluctuations verticales de l'interface et réduisit le transport latéral durant la nuit. Le transport maximal fut retardé à la journée, quand le réchauffement radiatif affaiblit la convection.

Après avoir quantifié le transport physique d'eau, nous avons évalué le rôle des siphons thermiques pour les échanges latéraux de gaz dissous. Nous avons trouvé que les deux branches de la

Résumé

circulation étaient capables de transporter des gaz latéralement. Le courant de gravité apporta les gaz littoraux jusqu'à la base de la couche mélangée dans la région stratifiée, alors que le courant de surface transporta des gaz vers la côte. Nous avons quantifié ces échanges pour l'oxygène et le méthane.

Enfin, nous avons généralisé nos observations à d'autres lacs avec des bathymétries et des forçages différents. La présence fréquente des siphons thermiques observée dans six lacs confirma que ce processus de transport latéral est omniprésent dans les lacs avec des zones littorales peu profondes. Nous avons montré que nos résultats de Rotsee étaient applicables à d'autres systèmes, où les mêmes relations de mise à l'échelle prédisent la formation et l'intensité des siphons thermiques. En se basant sur ces résultats, nous avons proposé une procédure pour prédire le rôle des siphons thermiques pour le transport latéral dans n'importe quel lac.

Cette thèse fournit une compréhension approfondie de la formation et de la dynamique des siphons thermiques et ouvre la voie à l'intégration de ce processus de transport latéral dans les recherches sur l'écosystème lacustre.

Mots-clés

Siphon thermique, courant de gravité, circulation transversale, refroidissement différentiel, transport latéral, convection pénétrative, lac.

Table of Contents

Acknowledgements	i
Abstract (English/Français)	iii
List of Tables	xi
List of Figures	xiii
Chapter 1 – Introduction	1
1.1 Lake’s lateral boundaries matter	1
1.2 Littoral-pelagic view of lakes	2
1.2.1 Lateral gradients	2
1.2.2 Lateral exchange	3
1.3 Thermal siphon: a daily lateral exchange process	4
1.3.1 From atmospheric heat exchange to differential heating-cooling	4
1.3.2 Two opposite types of thermal siphons	5
1.3.3 Cooling-driven thermal siphon: a gravity current in a convective environment	6
1.3.4 Theoretical, laboratory, and numerical work on thermal siphons	7
1.3.5 Field observations of thermal siphons	9
1.4 Dissertation objectives and structure	10
1.4.1 Objective 1: Seasonality	10
1.4.2 Objective 2: Dynamics	12
1.4.3 Objective 3: Transport	12
1.4.4 Objective 4: Parametrization	13
1.4.5 Conclusions and reproducibility	13
Chapter 2 – Seasonality of density currents induced by differential cooling	14
Abstract	15
2.1 Introduction	15
2.2 Methods	19

Table of Contents

2.2.1	Study site and field measurements	19
2.2.2	Heat and buoyancy fluxes	21
2.2.3	Mixed-layer depth	22
2.2.4	Occurrence of thermal siphons	23
2.2.5	Cross-shore transport by thermal siphons	24
2.2.6	Scaling formulae	24
2.3	Results	27
2.3.1	Diurnal cycle	27
2.3.2	Seasonal variability in the forcing parameters	29
2.3.3	Seasonal occurrence of thermal siphons	30
2.3.4	Scaling the cross-shore transport	32
2.3.5	Flushing period	33
2.4	Discussion	36
2.4.1	Seasonality of thermal siphons	36
2.4.2	Effects of the forcing parameters on the occurrence of thermal siphons . . .	36
2.4.3	Effects of the forcing parameters on cross-shore transport	39
2.4.4	Effects of the forcing parameters on the flushing period	40
2.4.5	Practical recommendations to predict and measure thermal siphons in other lakes	41
2.5	Conclusions	42
	Code and data availability	43
	Acknowledgements	43
	Financial support	44
	References	44
	Supplementary Information for Chapter 2	49
S2.1	Instrumentation	49
S2.2	Diurnal variability in the occurrence and duration of thermal siphons	51
S2.3	Seasonality of the flushing of the littoral region	51
S2.4	Identification of thermal siphons by the algorithm	52
	References	56
	Chapter 3 – Penetrative convection modifies the dynamics of downslope gravity currents	57
	Abstract	58
	Plain Language Summary	58
3.1	Introduction	58
3.2	Methods	60

3.2.1	Field experiments and measurements	60
3.2.2	Data analysis	60
3.2.3	Scaling and dimensionless numbers	61
3.3	Results	63
3.3.1	Diurnal cycle	63
3.3.2	Interface dynamics of the gravity current	64
3.3.3	Structure and propagation of the gravity current	68
3.4	Discussion	68
3.4.1	Role of convection in the small-scale interface dynamics	69
3.4.2	Role of convection in the basin-scale lateral transport	70
3.5	Conclusion	72
	Code and data availability	72
	Acknowledgements	72
	Financial support	73
	References	73
Supplementary Information for Chapter 3		79
Chapter 4 – Lake surface cooling drives littoral-pelagic exchanges of dissolved gases		82
	Abstract	83
4.1	Introduction	83
4.2	Methods	85
4.2.1	Study site	85
4.2.2	Physical measurements	85
4.2.3	Dissolved gases measurements during the two-days-long campaign	87
4.2.4	Gas tracer experiment	88
4.2.5	Velocity data analysis	88
4.3	Cross-shore convective circulation driven by differential cooling	88
4.4	Lateral transport of a littoral gas tracer	89
4.5	Littoral-pelagic downslope transport of oxygen	90
4.6	Pelagic-littoral surface transport of methane	92
4.7	Implications for lateral transport in lakes	94
	Code and data availability	96
	Acknowledgements	96
	Financial support	97
	References	97

Table of Contents

Supplementary Information for Chapter 4	102
Chapter 5 – Towards a parametrization of cooling-driven lateral transport in lakes	107
Abstract	108
5.1 Introduction	108
5.2 Methods	110
5.2.1 Study sites and field measurements	110
5.2.2 Forcing parameters	112
5.2.3 Thermal siphon events and transport estimates	113
5.2.4 Transport scaling	114
5.3 Results and discussion	115
5.3.1 Forcing conditions	115
5.3.2 Thermal siphon events	115
5.3.3 Transport scaling	117
5.3.4 Predictive procedure	119
5.3.5 Sensitivity analysis	121
5.4 Conclusions	123
Code and data availability	124
Acknowledgements	125
Financial support	125
References	125
Supplementary Information for Chapter 5	129
Chapter 6 – Conclusions and outlook	137
6.1 Summary of the thesis	137
6.2 Perspectives for future studies	140
6.2.1 Duration of the flushing period	140
6.2.2 Entrainment into the downslope gravity current	140
6.2.3 Intrusion of TSs	141
6.2.4 Effects of TSs on turbulence	142
6.2.5 Contribution of TSs to the methane paradox	142
6.2.6 Global prediction of TSs	142
Bibliography	144
Curriculum Vitae	163

List of Tables

Table 2.1	Key parameters related to the forcing parameters, bathymetry, and TS dynamics	26
Table 2.2	Comparison of the transport scaling formula $q = c_q h (B_0 L)^{1/3}$ between different studies on sloping basins	40
Table S2.1	Specifications and setup of the sensors from the two moorings and the meteorological station.	50
Table S3.1	Potential mechanisms generating interface fluctuations	81
Table S4.1	Characteristics of the measurement stations	103
Table S5.1	Geometrical characteristics of the lakes and measurement information	130

List of Figures

Figure 1.1	1D and 2D representations of lakes	2
Figure 1.2	Two types of thermal siphons	6
Figure 1.3	Schematic of the cooling-driven thermal siphon, including the research questions and methodology of the thesis	11
Figure 2.1	Data-based schematic of the cooling-driven thermal siphon	17
Figure 2.2	Study site	20
Figure 2.3	Diurnal cycle of a TS	28
Figure 2.4	Seasonal variability in the forcing parameters over 1 year	30
Figure 2.5	Monthly occurrence of TSs and other cross-shore flows at MT	31
Figure 2.6	Comparison between transport estimates and scaling formulae	33
Figure 2.7	Seasonal variability in the diurnal cycle	34
Figure 2.8	Timescales determining the occurrence of TSs	38
Figure S2.1	Box plots of the 2 d averaged net surface buoyancy flux for each month, depending on the occurrence of TS events	51
Figure S2.2	Three examples of TS events	52
Figure S2.3	Fraction of the littoral region flushed by TSs in 1 d for each month	53
Figure S2.4	Sensitivity analysis for the criteria used to define cross-shore flows	54
Figure S2.5	Filtering of the 227 d analyzed	55
Figure 3.1	Diurnal phases for two different thermal siphon events in 2019	64
Figure 3.2	Subsets of the convective and relaxation phases captured in the sloping region (MT) on 6-7 November	66
Figure 3.3	Probability density plots comparing the convective and relaxation phases, for the cooling-heating and continuous-cooling scenarios	67
Figure 3.4	Cross-shore propagation of the gravity current during the convective and relaxation phases on 6-7 November	69
Figure S3.1	Bathymetric map of Rotsee including the weather station, moorings and CTD profiles	79

Figure S3.2 Probability density plots comparing the convective and relaxation phases, for the cooling-heating and continuous-cooling scenarios, for the reduced gravity of the gravity current, the convective Richardson number normalized by $Ri_c^{(crit)} = 10$, and the vertical fluctuations of the interface $ h'_d $ normalized by the penetration depth δ_c	80
Figure S3.3 Burst-averaged vertical fluctuations of the interface normalized by the mean current thickness $ h'_d /\overline{h_d}$ as a function of the convective Richardson number Ri_c during the C-phase for the cooling-heating case and the continuous-cooling case	80
Figure 4.1 Differential cooling drives a diurnal cross-shore convective circulation . . .	86
Figure 4.2 The lower branch of the circulation transports injected krypton offshore. . .	90
Figure 4.3 The lower branch of the circulation transports oxygen offshore	91
Figure 4.4 The upper branch of the circulation transports methane onshore	93
Figure S4.1 Bathymetric map of Rotsee.	102
Figure S4.2 Forcing conditions and convective circulation	104
Figure S4.3 Cross-shore variability of temperature and oxygen saturation	105
Figure S4.4 Surface transport of methane across the sloping region	106
Figure S4.5 Littoral-pelagic surface methane concentrations in summer (July 2019) . . .	106
Figure 5.1 Bathymetric maps and forcing conditions characterizing the nine study sites.	111
Figure 5.2 Examples thermal siphon events in Soppensee, Lioson and Lake Hallwil . .	116
Figure 5.3 Comparison between transport observations and scaling relationships . . .	118
Figure 5.4 Diagram schematizing the TS predictive procedure	120
Figure 5.5 Sensitivity analysis of the parameters controlling the TS occurrence and intensity	122
Figure S5.1 Examples of thermal siphon events in Lioson on 18-20 September	131
Figure S5.2 Examples of thermal siphon events in Soppensee on 29 September-01 October	132
Figure S5.3 Examples of thermal siphon events in Oeschinensee on 5-7 October	133
Figure S5.4 Examples of thermal siphon events in Lake Lungern on 15-17 October . . .	134
Figure S5.5 Examples of thermal siphon events in Lake Hallwil on 8-10 November . . .	135
Figure S5.6 Examples of thermal siphon events in Luzern Bay on 13-15 February	136
Figure 6.1 Schematic of the cooling-driven thermal siphon, including the main quantities and findings of each chapter	138

Chapter 1

Introduction

1.1 Lake's lateral boundaries matter

How to define a lake in one sentence?

The pioneer Swiss limnologist François-Alphonse Forel answered this question in his first monograph about Lake Geneva: “a lake is a mass of stagnant water contained in a land depression and disconnected from the sea” (Forel, 1892, p. 11). In other words, lakes are water bodies surrounded by land (Vincent, 2018). These simple definitions may seem evident, but they highlight a crucial characteristic of lakes: lakes are embedded into the terrestrial environment. Their lateral boundaries mark the transition between aquatic and terrestrial ecosystems. By exchanging energy and matter across these boundaries, lakes are directly affected by human activities and natural processes from the surrounding watershed. They receive nutrients (Carpenter et al., 1998), organic matter (Solomon et al., 2015), inorganic carbon (Weyhenmeyer et al., 2015), sediment (Donohue & Garcia Molinos, 2009) and contaminants (Bonvin et al., 2011) from river inflows, surface water runoff, and wastewater discharges. The shoreline attracts people, as it provides a direct access to fresh water for drinking, irrigation, industrial applications and fishing, and contributes to aesthetic aspects and recreational activities (Schmieder, 2004). These numerous anthropogenic pressures have deteriorated lake shores and modified watersheds, generating major threats to lake ecosystems (Jenny et al., 2020; Strayer & Dudgeon, 2010). A better understanding of the interaction of lakes with the surrounding environment is crucial, not only for the comprehension of lake ecosystems, but also for better management and conservation of these vital freshwater resources (Vander Zanden & Vadeboncoeur, 2020). This thesis investigates how the lake interacts with its surroundings via cross-shore dynamics.

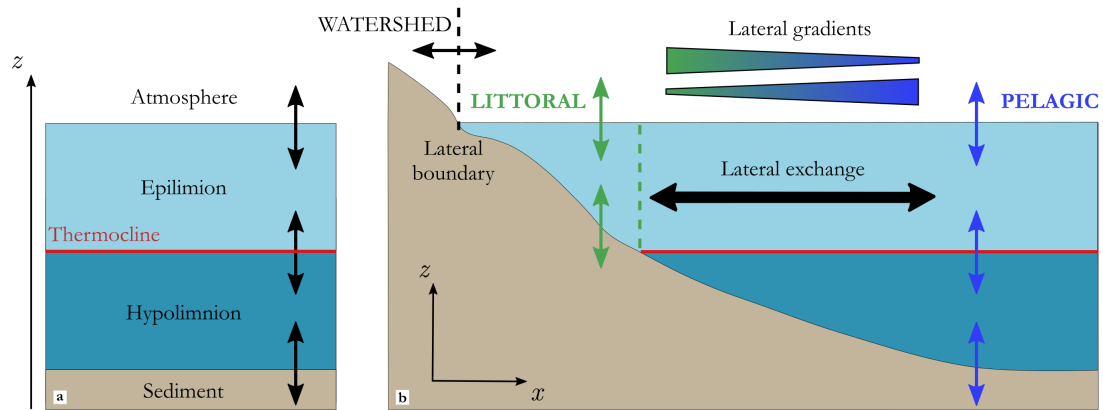


Figure 1.1 – 1D and 2D representations of lakes. (a) One-dimensional vertical representation, dividing the lake into horizontally-homogeneous layers and including vertical fluxes only. (b) Two-dimensional representation adding the cross-shore dimension, with littoral and pelagic regions. Both vertical and lateral fluxes are considered.

Lateral boundaries are absent from the open-water-centric view of lakes, traditionally used in limnology and directly derived from oceanography (Reynolds, 2008; Vander Zanden & Vadeboncoeur, 2020). This vertical one-dimensional representation divides stratified lakes into horizontally homogeneous layers of different densities (epilimnion and hypolimnion), bounded by the air-water interface above and the sediment-water interface below (Fig. 1.1a). Such a framework has been applied to study physical and biogeochemical processes offshore by quantifying fluxes of energy and matter along the vertical direction. Although this approach is suitable to analyze long-term trends over several years, the effects of lateral boundaries at the daily to seasonal scale limits the use of this framework for the study of short-term processes. This calls for a different perception of lakes that includes their lateral boundaries (Reynolds, 2008; Schindler & Scheuerell, 2002; Vander Zanden & Vadeboncoeur, 2020). This thesis aims at quantifying the lateral connectivity between the shore and the deep waters. To address this question, we must extend the one-dimensional framework into a littoral-pelagic representation of lakes (Fig. 1.1b).

1.2 Littoral-pelagic view of lakes

1.2.1 Lateral gradients

The two-dimensional representation of a lake includes both the vertical and cross-shore dimensions. The coordinate system consists of a vertical z -axis directed upward and a horizontal x -axis directed

towards the lake center (Fig. 1.1b). The cross-shore direction is divided into a shallow littoral region near the shore and a deep pelagic region near the center. The boundary between these two regions is defined differently depending on the processes considered. It is related to either the depth of sunlight penetration (Vander Zanden & Vadeboncoeur, 2020) or the thermocline depth (Rao & Schwab, 2007). In this thesis, we will use the terms *sloping region* and *stratified region* to refer to the regions shallower and more profound than the thermocline depth, respectively.

Littoral and pelagic regions differ in their physical and biogeochemical properties. For example, the littoral zone is characterized by more intense sediment resuspension from breaking waves and near-bed currents, larger diurnal temperature fluctuations, higher biodiversity, and specific chemical signature from the catchment (Hofmann et al., 2011; Rao & Schwab, 2007; Vadeboncoeur et al., 2011; Wetzel, 2001; Winfield, 2004). These unique properties fuel biogeochemical reactions (Brothers & Vadeboncoeur, 2021; Hofmann et al., 2011; Juutinen et al., 2003; Wetzel, 2001) and lead to lateral gradients of dissolved gases (Hofmann et al., 2010), nutrients (James & Barko, 1991a) and particles (Hofmann et al., 2011; Warren et al., 2018).

Despite these differences, littoral and pelagic regions are not separated but connected via lateral exchange processes. The coupling of gradients and exchange along the cross-shore direction leads to lateral fluxes of heat, dissolved and particulate matter, with ecological implications for littoral and pelagic habitats (MacIntyre & Melack, 1995; Rao & Schwab, 2007). Recent studies have reported concentration anomalies in the pelagic zone (Donis et al., 2017; Günthel et al., 2019; Murase et al., 2003), errors in the estimates of metabolic rates (Brothers et al., 2017; Hanson et al., 2008), missing sources in mass balances (Czikowsky et al., 2018) and deviations from theoretical parametrizations (Tedford et al., 2014) that could all be explained by lateral transport. The lack of a systematic quantification of this lateral exchange limits our understanding of the lake ecosystem as a whole.

1.2.2 Lateral exchange

A variety of physical processes contribute to the lateral water exchange in lakes. Besides molecular diffusion and horizontal dispersion that act in all directions (Peeters & Hofmann, 2015; Stocker & Imberger, 2003), advection by cross-shore flows is particularly efficient in transporting water laterally. The two main drivers of cross-shore flows are wind forcing and lateral density gradients. Wind induces lateral flows via cross-shore wind-driven circulation, surface and internal gravity waves, cross-shore Ekman transport in rotating systems, and differential deepening (Brink, 2016; Imberger & Patterson, 1989; Rao & Schwab, 2007). Lateral density gradients result from horizontal

differences in temperature, salinity, and/or turbidity. Such gradients generate buoyancy-driven cross-shore flows, or gravity currents, with denser waters flowing below lighter waters (Simpson, 1982). A typical example is the downslope gravity current induced by a cold and turbid river inflow (Alavian et al., 1992; Cortés et al., 2014; Imberger & Patterson, 1989). Lateral temperature gradients from differential heating or cooling are another source of buoyancy-driven cross-shore flows. These temperature gradients occur when heat fluxes are spatially variable because of horizontal differences in either meteorological forcing (Verburg et al., 2011), geothermal heating (Roget et al., 1993), shading by macrophytes (Lövestedt & Bengtsson, 2008) or heat absorption by suspended particles (MacIntyre & Melack, 1995). Spatial differences in lake depth cause a second type of differential heating-cooling. For the same surface heat flux, shallower regions heat up and cool down faster than deeper regions, generating horizontal temperature gradients (Horsch & Stefan, 1988; Monismith et al., 1990). Unlike the site-specific lateral density gradients, topographically controlled differential heating/cooling is a ubiquitous driver of cross-shore flows because all lakes have sloping sides. This thesis focuses on this type of cross-shore flow, known as the *convective circulation* (Horsch & Stefan, 1988) or the *thermal siphon* (Monismith et al., 1990).

1.3 Thermal siphon: a daily lateral exchange process

1.3.1 From atmospheric heat exchange to differential heating-cooling

Lakes exchange heat with the atmosphere across the air-water interface. This surface heat exchange must be quantified to characterize the diurnal cycle of differential cooling/heating. The net surface heat flux is defined as (Schmid & Read, 2021)

$$H_{0,\text{net}} = H_{Q_0} + H_{\text{SW},0} \quad [\text{W m}^{-2}], \quad (1.1)$$

where H_{Q_0} is the non-penetrative surface heat flux and $H_{\text{SW},0}$ is the shortwave radiative surface heat flux. Hereafter, we use the convention of positive heat fluxes directed upward. Net surface cooling and heating occur when $H_{0,\text{net}} > 0$ and $H_{0,\text{net}} < 0$, respectively.

Atmospheric heat exchange modifies the potential energy of the water column, which is expressed by a net surface buoyancy flux (Soloviev & Lukas, 2014)

$$B_{0,\text{net}} = B_0 + B_{\text{SW},0} \quad [\text{W kg}^{-1}], \quad (1.2)$$

where B_0 is the non-penetrative surface buoyancy flux and $B_{SW,0}$ is the radiative surface buoyancy flux. Each buoyancy flux B_i in Eq. (1.2) is related to the corresponding heat flux H_i in Eq. (1.1) as

$$B_i = \frac{\alpha g H_i}{\rho C_{p,w}} \quad [\text{W kg}^{-1}], \quad (1.3)$$

where $\alpha = -(1/\rho) \partial \rho / \partial T$ is the thermal expansivity of water [$^{\circ}\text{C}^{-1}$] which increases with T and is $\alpha = 0$ at the temperature of maximum density $T = T_{\text{MD}} \approx 4^{\circ}\text{C}$, g is the gravitational acceleration [m s^{-2}], ρ is the temperature-dependent water density [kg m^{-3}], and $C_{p,w}$ is the specific heat of water [$\text{J }^{\circ}\text{C}^{-1} \text{kg}^{-1}$]. Surface heat exchange has a net stabilization effect (stratification) when $B_{0,\text{net}} < 0$ and a net destabilization effect (convection) when $B_{0,\text{net}} > 0$. For $T > T_{\text{MD}}$ ($\alpha > 0$), the net surface heating stabilizes the water column, whereas the net surface cooling destabilizes it. The process reverses for $T < T_{\text{MD}}$ ($\alpha < 0$).

During the summer stratified period in temperate lakes, surface heat exchange typically leads to a diurnal cycle of daytime net heating ($H_{0,\text{net}} < 0$) and nighttime net cooling ($H_{0,\text{net}} = H_{Q_0} > 0$) (Imberger & Patterson, 1989). For a spatially uniform $H_{0,\text{net}}$, the shallower littoral region warms faster than the pelagic region during the day (differential heating, $\partial T / \partial x < 0$) and cools faster at night (differential cooling, $\partial T / \partial x > 0$) (James et al., 1994; Monismith et al., 1990). During colder periods in autumn or winter, net surface cooling can be maintained over several days, inducing continuous differential cooling (Fer et al., 2002b).

Lateral temperature gradients are directly related to lateral density gradients $\partial \rho / \partial x = -\alpha \rho \partial T / \partial x$. During the stratified season when $T > T_{\text{MD}}$ ($\alpha > 0$), differential heating (cooling) generates positive (negative) $\partial \rho / \partial x$. When the temperature decreases and approaches T_{MD} in autumn ($\alpha \rightarrow 0$), the density gradients from a given $\partial T / \partial x$ are smaller than at higher temperatures. For dimictic lakes in winter, $T < T_{\text{MD}}$ ($\alpha < 0$), which reverses the temperature-density relationship. In this case, differential heating (cooling) generates negative (positive) $\partial \rho / \partial x$. These density gradients are the drivers of thermal siphons (TSs).

1.3.2 Two opposite types of thermal siphons

Two categories of TSs exist, depending on the sign of $\partial \rho / \partial x$ (Fig. 1.2). When $\partial \rho / \partial x < 0$, littoral waters are more buoyant than pelagic waters, causing an offshore surface flow and a deep onshore flow. This cross-shore circulation occurs when surface heat exchange stratifies the water column ($B_{0,\text{net}} < 0$), as in the case of summer differential heating (Monismith et al., 1990). We can refer to this first category as *stratification-induced* TSs. When $\partial \rho / \partial x > 0$, littoral waters are denser than

pelagic waters, causing a downslope gravity current and an onshore surface flow. This reverse circulation occurs when surface heat exchange destabilizes the stratification ($B_{0,\text{net}} > 0$), as in the case of summer differential cooling (Horsch & Stefan, 1988; Monismith et al., 1990) or under-ice differential heating (Cortés & MacIntyre, 2020; Kirillin et al., 2015; Ramón et al., 2021; Ulloa et al., 2019). This category corresponds to *convectively* induced TSs.

The two types of TSs have different properties. The surface flow of stratification-induced TSs is confined to a shallow stratified layer, which makes this type of TS more sensitive to wind mixing than convectively induced TSs (James et al., 1994; Monismith et al., 1990). In summer, the diurnal cycle of daytime differential heating and nighttime differential cooling alternately generates each type of TSs (Monismith et al., 1990). However, the longer cooling periods in autumn and winter suggest a predominance of convectively driven TSs (Fer et al., 2002b). This thesis focuses on convectively driven TSs formed by differential cooling when $T > T_{\text{MD}}$, which we will hereafter simply call “TSs”.

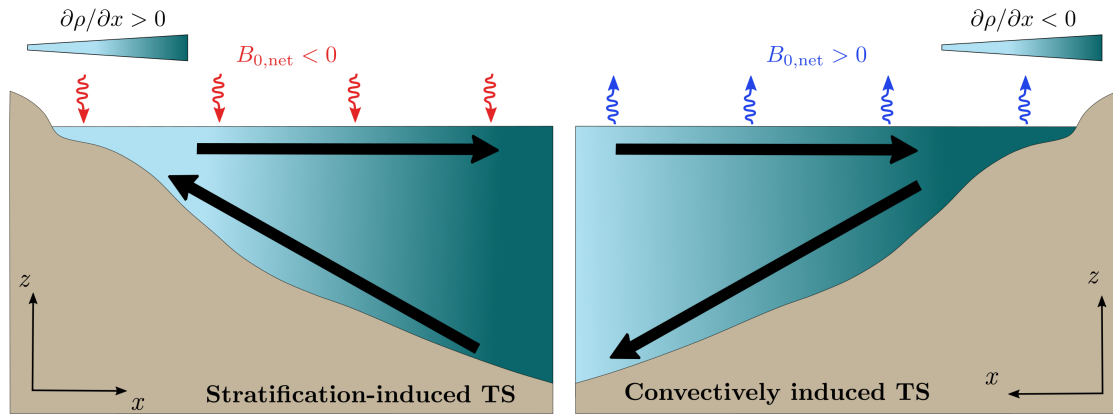


Figure 1.2 – Two types of thermal siphons. A stabilizing surface buoyancy flux (differential heating when $T > T_{\text{MD}}$) generates positive lateral density gradients and drives the stratification-induced TS (left). A destabilizing surface buoyancy flux (differential cooling when $T > T_{\text{MD}}$) causes negative lateral density gradients and drives the convectively induced TS (right). This schematic is inspired by Monismith et al. (1990).

1.3.3 Cooling-driven thermal siphon: a gravity current in a convective environment

When a lake experiences surface cooling ($H_{Q_0} > 0$) at $T > T_{\text{MD}}$, the surface boundary layer becomes colder and denser than the water below ($B_0 > 0$), leading to an unstable density profile. After a certain time, this mass increase overcomes viscous effects, forming thermal instabilities,

or convective plumes (Bouffard & Wüest, 2019). The denser convective plumes sink and, by continuity, generate rising plumes. These convective rolls mix the surface layer vertically and form a diurnal mixed layer (Imberger, 1985). The vertical velocity of convective plumes scales as (Deardorff, 1970)

$$w_* = (B_0 h_{ML})^{1/3} \quad [\text{m s}^{-1}], \quad (1.4)$$

where h_{ML} [m] is the depth of the mixed layer. When convective plumes reach the base of the mixed layer, they overshoot the density interface and penetrate into the stratified layer. This *penetrative convection* deepens the mixed layer by entrainment (Deardorff et al., 1969; Veronis, 1963).

Once h_{ML} reaches the bottom of the shallow littoral region, further surface cooling decreases the temperature of this zone faster than offshore, where the mixed layer keeps deepening. This differential cooling leads to the development of a TS (Fig. 1.3). The denser littoral waters plunge as a downslope gravity current, while surface waters flow in the opposite direction as a return flow. For stratified conditions, the gravity current intrudes at the base of the mixed layer and propagates horizontally towards the pelagic zone. The circulation persists as long as surface cooling occurs, similar to steady gravity currents driven by a continuous supply of dense water (Ellison & Turner, 1959). However, a particularity of TS is the presence of convective plumes in the ambient fluid which can modify the behavior of the gravity current (Fer et al., 2002a; Horsch & Stefan, 1988).

1.3.4 Theoretical, laboratory, and numerical work on thermal siphons

The formation of TSs has been investigated via laboratory and numerical experiments. A delay was observed between the onset of cooling and the TS formation (Bednarz et al., 2008; Horsch & Stefan, 1988; Horsch et al., 1994; Sturman & Ivey, 1998). This transition period is analogous to the development of hydraulically-controlled exchange flows driven by a destabilizing B_0 , for which a transition timescale τ_t has been formulated (Finnigan & Ivey, 1999):

$$\tau_t \sim L^{2/3} B_0^{-1/3} \quad [\text{s}], \quad (1.5)$$

where L [m] is the length scale along which B_0 is applied. Wells and Sherman (2001) used a similar scaling as Eq. (1.5) to characterize the transition period required for the TS formation. In a lake subject to uniform surface cooling, L is the length of the mixed region where differential cooling takes place. Once the convective circulation is established, three subregions have been reported along the cross-shore direction: a vertically-mixed conductive region nearshore, a transitional region where the downslope flow starts, and a convective region offshore, where TS and convective

plumes coexist. The occurrence of the three regimes depends on the Rayleigh number expressing the ratio between buoyancy forces and viscosity forces (Lei & Patterson, 2005; Mao et al., 2010). Laboratory experiments have shown that convective plumes interact with the gravity current (Bednarz et al., 2008; Horsch & Stefan, 1988), although the effects of penetrative convection on the dynamics of the downslope flow have not been investigated.

Scaling formulae that relate the TS characteristics to the forcing conditions have been derived theoretically and verified by laboratory and numerical experiments. Implementing similarity theory, Phillips (1966) provided a velocity scale for the lateral circulation driven by a uniform B_0 in a semi-enclosed sea. He found that the horizontal surface flow velocity scales as $U \sim (B_0 x)^{1/3}$, with x the distance from the shore. Numerous laboratory experiments showed that this velocity scale could be applied to the horizontal velocity of TS, with x replaced by the characteristic length scale L (Harashima & Watanabe, 1986; Sturman & Ivey, 1998; Sturman et al., 1996; Sturman et al., 1999; Wells & Sherman, 2001):

$$U \sim (B_0 L)^{1/3} \quad [\text{m s}^{-1}], \quad (1.6)$$

where L characterizes the length of the littoral region as in Eq. (1.5). From a buoyancy-friction balance, Sturman et al. (1999) also provided a scaling for the velocity parallel to the slope $U \sim (B_0 L \sin \theta / C_D)^{1/3}$, where θ is the slope angle and C_D is a drag coefficient.

The unit-width discharge q of the downslope flow is scaled by

$$q \sim (B_0 L)^{1/3} H \quad [\text{m}^2 \text{s}^{-1}], \quad (1.7)$$

with H a vertical length scale representing the depth of the littoral region (Harashima & Watanabe, 1986; Sturman & Ivey, 1998; Wells & Sherman, 2001). A slope-dependent scaling $q \sim B_0^{1/3} L^{4/3} S^{4/3} \sim B_0^{1/3} H^{4/3}$, where $S \ll 1$ is the slope along the cross-shore direction, was successfully tested by Sturman et al. (1999) on field and laboratory data. For both scaling formulae, the proportional coefficient is $\approx 0.1 - 0.4$ (Harashima & Watanabe, 1986; Sturman & Ivey, 1998; Sturman et al., 1999), although it might vary with the forcing conditions, as suggested by Harashima and Watanabe (1986). Sturman's scaling implies that TS discharge is more sensitive to a bathymetry (H) change than a change of forcing (B_0). By neglecting the variability in B_0 , Chubarenko (2010) found that the simple relationship $q \sim H^{4/3}$ predicts well the discharge from laboratory and field observations. A flushing timescale τ_F , representing the time required for TS to flush the littoral region of unit-width volume V_{lit} , is derived from q as (Sturman et al., 1999)

$$\tau_F \sim \frac{V_{\text{lit}}}{q} \quad [\text{s}]. \quad (1.8)$$

Other studies have investigated more complex forcing than steady cooling. Periodic cooling-heating forcing has been reproduced via laboratory experiments (Bednarz et al., 2009b) and numerical simulations (Bednarz et al., 2009b; Chubarenko et al., 2013; Farrow & Patterson, 1993; Farrow, 2004; Mao et al., 2019). These studies reported inertia effects, with a lag time between the change in forcing and the circulation reversal that increases with distance from the shore. The presence of wind stress (Farrow, 2013; 2016; Woodward et al., 2017) and along-shore flows (Ulloa et al., 2018; Wu et al., 2018) have been shown to either enhance or decrease TS-induced lateral transport.

1.3.5 Field observations of thermal siphons

Oceanic analogs of TSs have been extensively studied in the field, including dense shelf water cascades (Canals et al., 2006; Ivanov et al., 2004; Pattiaratchi et al., 2011; Shapiro, 2003; Shapiro & Hill, 1997; Symonds & Gardiner-Garden, 1994) and thermally driven exchanges in reef systems (Molina et al., 2014; Monismith et al., 2006). In lakes, TSs have been suggested to renew deep waters (Ambrosetti et al., 2010; Biemond et al., 2021; Lemmin, 2020; Peeters et al., 2003) and to explain the numerous observations of cold bottom layers above the sediment (Eccles, 1974; MacIntyre & Melack, 1995; Rueda et al., 2007; Talling, 1963; Wells & Sherman, 2001; Woodward et al., 2017) and cold intrusions (Forrest et al., 2008). Yet, detailed investigations of the occurrence and dynamics of TSs remain scarce.

The in-situ quantification of convective circulation has been documented initially for “cooling lakes”. Warm water from power plants is discharged into these reservoirs, cools in sidearms, and generates TSs (Adams & Wells, 1984). The pioneering work of Monismith et al. (1990) described the diurnal cycle of differential heating-cooling, the resulting TSs, and their interaction with wind. This study was followed by other observations of TSs in lakes of diverse shapes, including elongated regions of reservoirs (James & Barko, 1991a; 1991b; James et al., 1994; Rogowski et al., 2019), small rounded lakes (Sturman et al., 1999), wide bays (Cannaby et al., 2007; Pálmarrsson & Schladow, 2008; Razlutskiy et al., 2021), sloping sides of a large lake (Fer et al., 2002a; Fer et al., 2002b; Fer et al., 2001; Thorpe et al., 1999) and different lake basins (Roget et al., 1993). These studies reported similar TS characteristics, including a TS-induced bottom stratification following the slope, inertia between changes in forcing and changes in flow dynamics, and a flushing timescale of a few hours. Cross-shore velocity estimates of $0.1\text{--}10\text{ cm s}^{-1}$ have been derived from drogue measurements (Monismith et al., 1990), dye tracers (James & Barko, 1991a; 1991b; Razlutskiy et al., 2021), or velocity time series at specific depths (Fer et al., 2002b; Fer et al., 2001; Pálmarrsson & Schladow,

2008; Roget et al., 1993; Sturman et al., 1999). However, few studies have resolved the TS velocity field at a high vertical and temporal resolution (Fer et al., 2002a; Rogowski et al., 2019).

Implications of TSs for the lateral transport of nutrients, pollutants, dissolved gases, plankton, and suspended sediment have frequently been mentioned (Brothers et al., 2017; Fer et al., 2001; MacIntyre & Melack, 1995; Monismith et al., 1990; Pálmarrsson & Schladow, 2008; Stefan et al., 1989). James and Barko (1991a, 1991b) estimated phosphorus lateral exchange rates from simultaneous measurements of lateral phosphorus concentration gradients and TS velocity. Fer et al. (2002b) attributed an increase in acoustic scattering during TS events to the downslope transport of suspended sediment. Razlutskiy et al. (2021) hypothesized an effect of TS advection on the diurnal cross-shore movement of zooplankton. Although these results suggest a role of TS for lateral biogeochemical transport, direct observations of such a transport are lacking.

1.4 Dissertation objectives and structure

The central objective of this thesis is to quantify the occurrence and dynamics of TSs in the field, with the ultimate goal of better predicting TS-induced lateral transport in lakes. This work is part of the HYPOTHESIS project (Hypolimnetic Thermal Siphons, SNSF project 175919), including numerical simulations of TSs (Ramón et al., 2022; Ulloa et al., 2022). Our approach consists of high-frequency in-situ measurements in an elongated wind-sheltered lake (Rotsee, Switzerland, details in Sect. 2.2.1), which can be seen as an ideal field-scale laboratory to study TSs. The four thesis objectives, each corresponding to a different chapter, are described below and summarized in Fig. 1.3.

1.4.1 Objective 1: Seasonality

Most of available field TS observations are limited to specific events during a single season. Scaling relationships (Sect. 1.3.4) have shown that meteorological forcing (B_0) and stratification (defining L and H via the bathymetry) affect the formation and intensity of TSs. These forcing parameters are season-dependent, suggesting that the occurrence and intensity of TSs vary temporally. In temperate lakes, we expect stronger flows in late summer when B_0 is maximal, but longer and more frequent TSs in autumn when the cooling periods are longer. This seasonality, however, needs to be verified in the field. Understanding it is a first step towards the prediction of TS-induced lateral transport.

This objective is addressed in **Chapter 2 – Seasonality of density currents induced by differential cooling**. From one-year-long measurements of TSs and forcing conditions in Rotsee, we determined the seasonality of the occurrence and intensity of the convective circulation. We found that TSs frequently occur from late summer to winter, and we explained this seasonality with relevant timescales. We successfully tested the available transport scaling and confirmed the transport weakening from summer to winter.

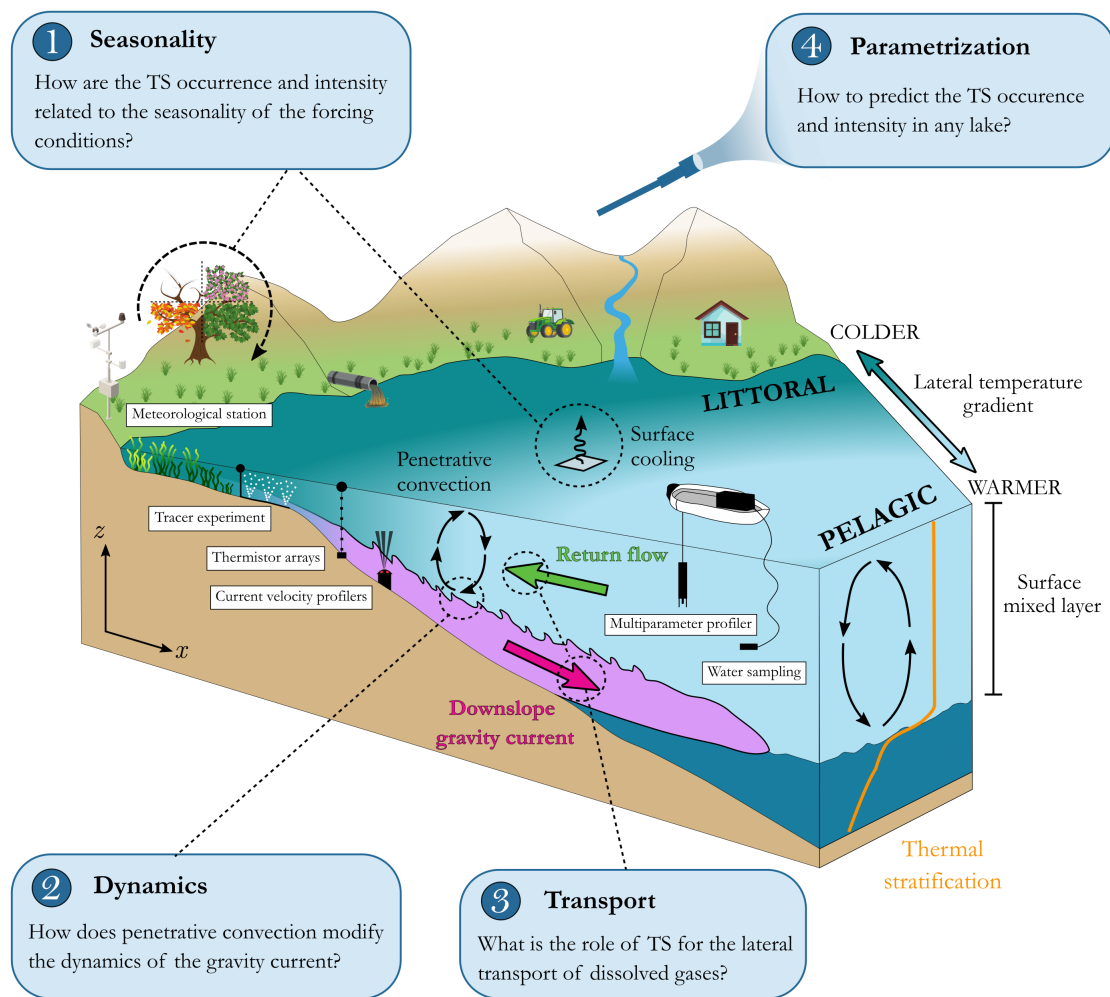


Figure 1.3 – Schematic of the cooling-driven thermal siphon, including the research questions and methodology of the thesis. The schematic represents the cooling-driven thermal siphon, divided into a downslope gravity current (purple) and a surface return flow (green). It connects the littoral region, directly affected by the surrounding watershed, to the stratified pelagic region. The four blue boxes include the research questions of the thesis chapters. The main in-situ measurements performed to answer these questions are shown on the schematic.

1.4.2 Objective 2: Dynamics

The main difference between cooling-driven TSs and classic gravity currents is their propagation into a convective environment. While laboratory experiments have shown that convective plumes interact with the downslope current (Bednarz et al., 2008; Horsch & Stefan, 1988), the effects of this interaction on the dynamics of the current are unknown. Fer et al. (2002a) suggested that convective plumes could increase the entrainment into the gravity current but did not directly observe their effects. The interaction between convective plumes and TS must be characterized to understand the diurnal variability of the lateral transport.

In **Chapter 3 – Penetrative convection modifies the dynamics of downslope gravity currents**, we investigated the effects of convective plumes on the small-scale dynamics and basin-scale propagation of TSs. From high-resolution velocity measurements in Rotsee, we identified two phases with different dynamics. During the nighttime convective phase, convective plumes penetrated into the gravity current, eroded its interface, and reduced the lateral transport. As a result, the maximal transport was delayed to the daytime relaxation phase, when penetrative convection weakened.

1.4.3 Objective 3: Transport

Recent studies have suggested that TSs transport dissolved gases laterally and affect the pelagic ecosystem (Brothers et al., 2017; Czikowsky et al., 2018; Hanson et al., 2008; Sadro et al., 2011). While lateral concentration gradients of dissolved gases are common, there is no direct evidence of such a transport. Our objective is to demonstrate that both branches – the downslope flow and the surface return flow – can transport gases laterally, in the presence of a lateral concentration gradient. This objective is addressed in **Chapter 4 – Lake surface cooling drives littoral-pelagic exchanges of dissolved gases**. We first performed a gas tracer experiment in Rotsee to confirm the capacity of the downslope flow to transport dissolved gases. We tracked this transport along the sloping zone and the intrusion into the stratified region. Next, we quantified the lateral transport of naturally present gases (oxygen and methane) by both branches of the convective circulation.

1.4.4 Objective 4: Parametrization

Based on our comprehension of the formation and dynamics of TSs in Rotsee, we want to test the reproducibility of our findings by attempting a generalization of our results to other lakes. The objectives are (i) to complement our TS dataset with observations from other systems and (ii) to provide a simple approach to parametrize the occurrence and intensity of TSs in any lake.

In **Chapter 5 – Towards a parametrization of cooling-driven lateral transport in lakes**, we tested the transport scaling formulae on TS observations from eight lakes. We proposed a procedure to estimate the occurrence and intensity of TS based on bathymetry, meteorological forcing, and vertical thermal structure. This procedure provided a simple, a priori assessment of the TS-induced transport in a given lake.

1.4.5 Conclusions and reproducibility

Chapter 6 – Conclusions and outlook summarizes the results of the previous chapters and provides a perspective for future studies on TSs. To facilitate further work on this topic, we ensured that our analyses are reproducible by making all the data, metadata and scripts publicly available. We refer the reader to the **Data availability** sections of each chapter.

Chapter 2

Seasonality of density currents induced by differential cooling

Tomy Doda^{1,2}, Cintia L. Ramón^{1,4}, Hugo N. Ulloa^{2,3}, Alfred Wüest, Damien Bouffard¹

¹Eawag, Swiss Federal Institute of Aquatic Science and Technology, Department of Surface Waters – Research and Management, Kastanienbaum, Switzerland

²Limnology Center, École Polytechnique Fédérale de Lausanne, Lausanne, Switzerland

³Department of Earth and Environmental Science, University of Pennsylvania, Philadelphia, USA

⁴Department of Civil Engineering, University of Granada, Granada, Spain

Published in *Hydrology and Earth System Sciences*.

Cited as Doda, T., Ramón, C. L., Ulloa, H. N., Wüest, A., & Bouffard, D. (2022). Seasonality of density currents induced by differential cooling. *Hydrology and Earth System Sciences*, 26(2), 331–353. <https://doi.org/10.5194/hess-26-331-2022>.

Author contributions: TD and DB designed the field experiments. TD led the data collection and analysis with help from DB, HNU, and CLR. TD wrote the initial draft of the manuscript, and all coauthors commented on and edited the text.

Abstract

When lakes experience surface cooling, the shallow littoral region cools faster than the deep pelagic waters. The lateral density gradient resulting from this differential cooling can trigger a cold downslope density current that intrudes at the base of the mixed layer during stratified conditions. This process is known as a thermal siphon (TS). TSs flush the littoral region and increase water exchange between nearshore and pelagic zones; thus, they may potentially impact the lake ecosystem. Past observations of TSs in lakes are limited to specific cooling events. Here, we focus on the seasonality of TS-induced lateral transport and investigate how seasonally varying forcing conditions control the occurrence and intensity of TSs. This research interprets 1-year-long TS observations from Rotsee (Switzerland), a small wind-sheltered temperate lake with an elongated shallow region. We demonstrate that TSs occur for more than 50 % of the days from late summer to winter and efficiently flush the littoral region within ~10 h. We further quantify the occurrence, intensity, and timing of TSs over seasonal timescales. The conditions for TS formation become optimal in autumn when the duration of the cooling phase is longer than the time necessary to initiate a TS. The decrease in surface cooling by 1 order of magnitude from summer to winter reduces the lateral transport by a factor of 2. We interpret this transport seasonality with scaling relationships relating the daily averaged cross-shore velocity, unit-width discharge, and flushing timescale to the surface buoyancy flux, mixed-layer depth, and lake bathymetry. The timing and duration of diurnal flushing by TSs relate to daily heating and cooling phases. The longer cooling phase in autumn increases the flushing duration and delays the time of maximal flushing relative to the summer diurnal cycle. Given their scalability, the results reported here can be used to assess the relevance of TSs in other lakes and reservoirs.

2.1 Introduction

As lateral boundaries in lakes, littoral regions exchange matter and energy with the surrounding watershed. The littoral region receives both sediment and chemicals from the terrestrial environment, including anthropogenic contaminants (Rao & Schwab, 2007). Particulate matter accumulates in the littoral zone (Cyr, 2017), and this biologically active region can host unique and intensified biogeochemical reactions (Wetzel, 2001). Cross-shore flows, which transport water laterally, connect a lake's littoral region to its pelagic region, thereby facilitating critical ecosystem processes (MacIntyre & Melack, 1995). They control the residence time of nearshore waters and redistribute heat as well as dissolved and particulate compounds throughout the lake. Representing

lakes as isolated vertical water columns fails to account for the effects of cross-shore flows on lake biogeochemistry (Effler et al., 2010; Hofmann, 2013).

Various mechanisms drive horizontal exchange flows. The pioneer limnologists have already elucidated the effect of large-scale surface and internal gravity waves on horizontal transport (Forel, 1895; Mortimer, 1952; Wedderburn, 1907). In addition to serving as the primary energy source for gravity waves, wind is also responsible for fueling lateral flows via wind-driven cross-shore circulation, cross-shore Ekman transport in rotating environments, and differential deepening (Brink, 2016; Imberger & Patterson, 1989). Buoyancy-driven lateral flows can be induced by horizontal temperature gradients due to differential heating or cooling. Such gradients could form when heat fluxes are spatially heterogeneous, due to large-scale differences in meteorological forcing (Verburg et al., 2011), variable geothermal heating (Roget et al., 1993), shading from vegetation (Lövstedt & Bengtsson, 2008), wind sheltering (Schlatter et al., 1997), or variation in turbidity (MacIntyre et al., 2002). Horizontal temperature gradients also occur when waters with variable depth experience a spatially uniform heat flux (Horsch & Stefan, 1988; Monismith et al., 1990). For a given surface area, the volume of water in the shallow littoral region is less than its offshore counterpart. Thus, littoral waters will cool or warm faster than pelagic waters. Monismith et al. (1990) designated cross-shore circulation resulting from a bathymetrically induced temperature gradient as a thermal siphon. The fact that all lakes have sloping boundaries makes thermal siphons potentially ubiquitous.

This study focuses on thermal siphons driven by differential cooling, wherein the lake temperature exceeds the temperature of maximum density (Fig. 2.1). The study does not consider heating-driven thermal siphons because induced lateral exchange remains weaker and more sensitive to wind disturbance than cooling-driven thermal siphons (James et al., 1994; Monismith et al., 1990). Atmospheric forcing affects lakes at diurnal, seasonal, or synoptic scales. This includes periods of net cooling when the net surface heat flux is directed towards the atmosphere (Bouffard & Wüest, 2019). This diel or seasonal surface cooling mixes and deepens the surface layer by penetrative convection. Once the shallow littoral region becomes fully mixed, it cools down faster than the deep pelagic region. Littoral waters become denser and plunge as a downslope density current, which intrudes at the base of the mixed layer during stratified conditions. At the surface, a reverse flow brings water from the pelagic to the littoral region (Horsch & Stefan, 1988; Monismith et al., 1990). We will hereafter refer to the density current induced by differential cooling simply as a thermal siphon (TS).

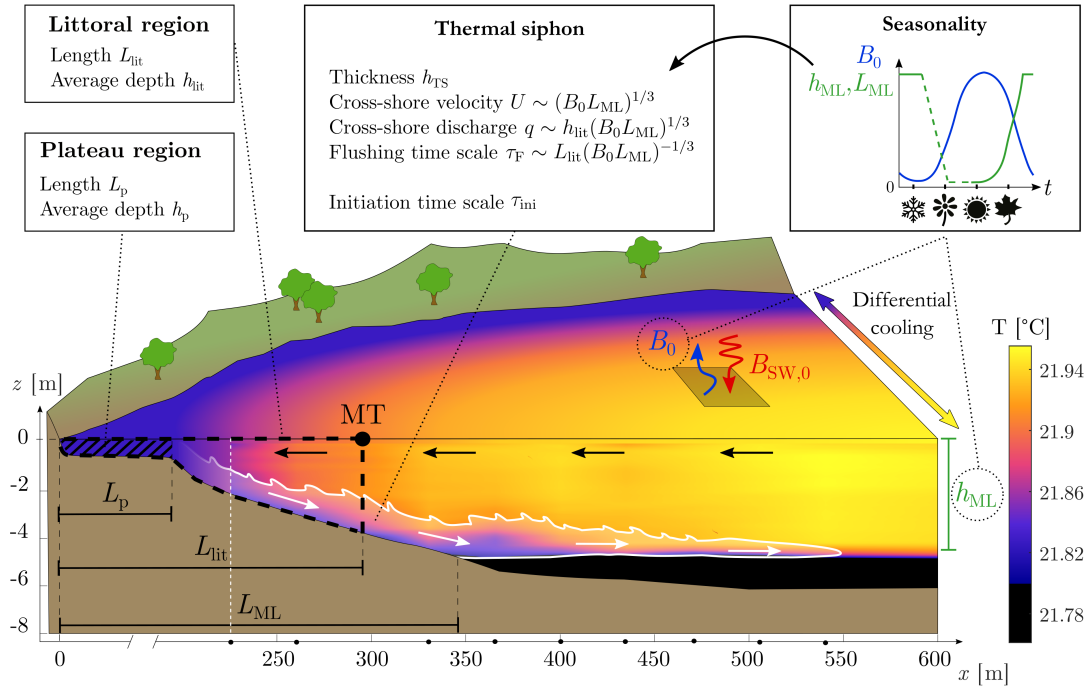


Figure 2.1 – Data-based schematic of the cooling-driven thermal siphon. The schematic shows the plateau, littoral, and mixed regions; the seasonality of the forcing; and the variables used for the transport scaling. Here, the littoral zone is the region upslope of the MT mooring, where the current velocity is measured and transport variables are calculated. The cross-shore temperature field is linearly interpolated from a transect of conductivity–temperature–depth (CTD) profiles collected on the morning of 22 August 2019 (08:20–08:50 UTC), from $x = 225$ m (white dashed line) to $x = 714$ m. Black dots on the x axis show the location of the profiles. The green dashed line in the seasonality diagram corresponds to the transition period between the mixing period (winter) and the stratified period (summer), when the mixed layer is not well defined.

TSs have often been evoked to explain cold anomalies observed in lakes; these include tilted isotherms above the sloping sides (Eccles, 1974; MacIntyre & Melack, 1995; Talling, 1963; Woodward et al., 2017) or cold water intrusions (Ambrosetti et al., 2010; Forrest et al., 2008; Peeters et al., 2003; Rueda et al., 2007; Wells & Sherman, 2001). However, only a few studies have provided detailed in situ descriptions of the process. The first extensive studies of TSs assessed power plant heat disposal within cooling lakes (Adams & Wells, 1984). Warm water discharged into these reservoirs flows onshore at the surface, cools, and induces a TS in sidearms. However, these observations are not representative of naturally formed TSs. Cooling lakes constantly receive heat from power plants, which increases the intensity and duration of surface cooling compared with that experienced in other lakes and reservoirs (Horsch & Stefan, 1988). An extensive review of the literature suggests that Monismith et al. (1990) provided the first in situ observations of a diurnal cycle associated with a naturally formed TS. The authors studied a sidearm of Wellington Reservoir (Australia) in summer and described the complete diurnal cycle of daytime differential

heating and nighttime differential cooling. In both cases, they observed cross-shore flows at velocities of $\sim 2 \text{ cm s}^{-1}$. Cross-shore circulation was characterized by inertia with a delay of several hours between the shift in forcing conditions and the flow reversal. Other studies have reported the presence of TSs along the thalweg of narrow reservoir embayments (James & Barko, 1991a; 1991b; James et al., 1994; Rogowski et al., 2019) but also along the sloping sides of lakes (Fer et al., 2002a; Fer et al., 2002b; Pálmarrsson & Schladow, 2008; Sturman et al., 1999; Thorpe et al., 1999) and between different basins (Roget et al., 1993). In most of these examples, TS characteristics comported with the description given in Monismith et al. (1990). These included thermal stratification above the sloping bottom, inertial effects, and a cross-shore velocity on the order of 1 cm s^{-1} . The work by Fer et al. (2002b) on the sloping sides of Lake Geneva (Switzerland) represents one of the most extensive TS studies. The authors collected continuous measurements over two winters and identified density currents initiated in the middle of the night and lasting until the late morning. The research detected increasing discharge with distance downslope and found that one TS event could flush the littoral region almost twice.

The lake stratification and the intensity and duration of the daily cooling period vary seasonally (Bouffard & Wüest, 2019). These changes in forcing conditions may affect the occurrence and magnitude of TSs over time. Previous studies have focused on specific TS events and did not monitor the process over different seasons. A 3-year-long dataset on Lake Anna (VA, USA; Adams and Wells, 1984) addressed a cooling lake and, thus, did not reflect the seasonality of naturally formed TSs. Although the time series collected by Roget et al. (1993) between two lobes of Lake Banyoles (Spain) spans 8 months (October–May), these authors do not address seasonal variability in the observed TS. Geothermal fluxes between the lobes enhance differential cooling in Lake Banyoles, which may modify TS seasonality. James and Barko (1991b) performed six tracer experiments between June and September. These authors obtained estimates of TS velocity that varied between the experiments and were higher for days with stronger lateral temperature gradients. While the experiments did not identify a clear seasonal trend, thermistor arrays detected an increase in the occurrence of differential cooling from May to August, suggesting a higher frequency of TS events in late summer. This hypothesis was not verified due to the lack of long-term velocity measurements. Thus, the seasonality of TS occurrence and intensity has not been systematically investigated in lakes.

Dimensional analysis and laboratory experiments have provided relationships linking forcing and background conditions (surface cooling, stratification) to cross-shore transport by TSs (Harashima & Watanabe, 1986), but these lack validation in the field. The comprehension of the TS seasonality would improve the prediction of TS events in lakes and their contribution to exchanges between

littoral and pelagic regions. The present research monitored TSs in a small temperate lake over a 1-year period. The study establishes three characteristics of TS seasonality including its occurrence (Sect. 2.3.3), intensity (Sect. 2.3.4), and diurnal dynamics (Sect. 2.3.5). The observed TS seasonality clearly relates to forcing parameters and, thus, pinpoints key parameters for predicting TS events in lakes (Sect. 2.4). The observation and interpretation of TS events across seasonal timescales provides a comprehensive understanding of the conditions required to form TSs in lakes.

2.2 Methods

2.2.1 Study site and field measurements

Rotsee is a small peri-alpine monomictic lake near Lucerne, Switzerland (Fig. 2.2a). It is located at 419 m a.s.l. (above sea level) and has a surface area of 0.5 km^2 with a mean and maximum depth of 9 and 16 m, respectively. The main in- and outflows are located at the southwestern and northeastern ends of the lake, respectively, and have a low discharge of $\sim 0.1 \text{ m}^3 \text{ s}^{-1}$. Rotsee is an elongated lake (2.5 km long, 0.2 km wide), with steep sides (slope of 15°) across its longitudinal axis and more gradual slopes (1.5°) at its two ends. The northeastern end of the lake finishes with a 200 m long plateau region of approximately 1 m depth that can trigger TSs. Moreover, Rotsee is located in a depression and sheltered from wind; hence, it is famous for international rowing championships and an ideal field-scale laboratory where convective processes are distinctively observable.

This study focuses on quantifying TSs originating from the northeastern plateau region (Fig. 2.2a). Because of the elongated shape of Rotsee, we use the 2D (x, z) framework shown in Fig. 2.1 by orienting the x axis along the thalweg. We assume that TSs flow preferentially along the x axis, and we neglect the influence of perpendicular flows. We will now refer to the northeastern end of the lake as the “shore” and call the direction of the x axis the “offshore direction”.

We monitored the background stratification at the deepest location (“background mooring” MB, approx. 16 m deep) as well as the dynamics of TSs off the plateau region (“TS mooring” MT, approx. 4 m deep) from March 2019 to March 2020 (Fig. 2.2a). Mooring MT was located along the thalweg, at the beginning of the sloping region. This shallow water column is already vertically mixed in summer by the action of surface cooling. We briefly describe the moorings below and provide more detailed information on the specifications and setup of the instruments in Sect. S2.1. Each mooring included an array of thermistors (Fig. 2.2b). The evolution of the background

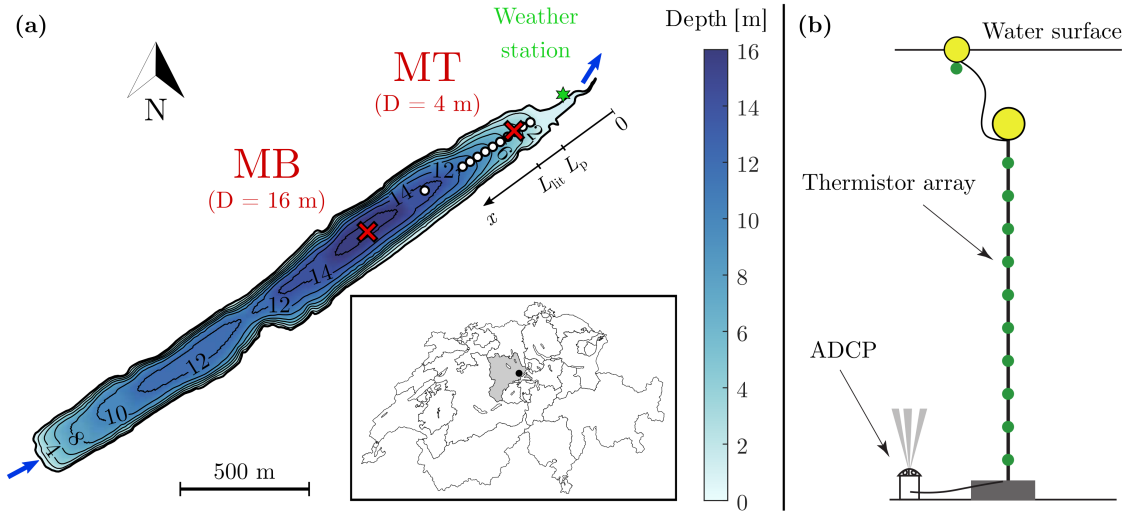


Figure 2.2 – Study site. (a) Bathymetry of Rotsee indicating the location of the two moorings MB and MT (red crosses), the cross-shore transect of CTD profiles (white dots), the weather station (green star), and the length of the plateau and littoral regions (L_p and L_{lit} , respectively). Blue arrows correspond to the main inflow and outflow. The location of Rotsee is shown on the map of Switzerland using a black dot (source: Federal Office of Topography). (b) Schematic of the mooring MT. A similar setup is used for the thermistor array at MB. The detailed setup is provided in Sect. S2.1.

temperature was monitored at MB with Vemco Minilog II-T loggers (accuracy: 0.1°C). High-resolution thermistors RBR TR-1050 and RBRduet T.D (accuracy: 0.002°C) were used at MT to track finer-scale temperature fluctuations near the sloping boundaries. The thermistors were installed from 1 to 13 m above the bottom with a 1 m vertical resolution at MB and from 0.25 to 2 m above the bottom with a 0.25 m resolution at MT. The evolution of the near-surface temperature (0.2 to 0.3 m below the surface) was monitored with Vemco loggers attached to surface buoys at both locations. An upward-looking acoustic Doppler current profiler (ADCP, Nortek Aquadopp profiler 1 MHz) was deployed at MT for fine-scale measurements of the bottom currents (Fig. 2.2b). It collected velocity profiles with a vertical bin resolution of 0.05 m from 0.25 to 3 m above the bottom. Velocity was obtained by averaging 512 burst measurements every 15 min. A week-long maintenance of the moorings was conducted every 40 d on average. The measurement periods of the ADCP were shorter in December and January due to low battery (Sect. S2.1). The monitoring was stopped in May 2019 to avoid any hazard during the European Rowing Championships.

A WxPRO Campbell weather station was installed at the lake shore, near the plateau region, in September 2019 (Fig. 2.2a). It measured atmospheric pressure, air temperature, wind speed, incoming shortwave radiation, and relative humidity every 10 min. In addition, incoming long-wave radiation was obtained from the Lucerne weather station ($47^\circ2'12''\text{ N}$, $8^\circ18'4''\text{ E}$; source

MeteoSwiss), ~ 4 km from Rotsee. The Lucerne station also provided meteorological forcing when the reference Rotsee weather station was not measuring (data gaps and period before September 2019). In these cases, the Lucerne dataset was adjusted based on the Rotsee observations from September 2019 to June 2020. Pressure, air temperature, and shortwave radiation were linearly corrected ($R^2 > 0.9$). This simple method did not allow reliable correction to the relative humidity and wind speed. Instead, we applied a neural network fitting approach to correct these two variables. The shallow neural network consisted of one hidden layer with 50 neurons and was trained by a Levenberg–Marquardt algorithm. A total of 70 % of the reference period from September 2019 to June 2020 was used to train the neural network, and the remaining percentage was equally distributed for validation and testing. All of the meteorological variables measured in Lucerne were used as inputs to the network, and the procedure was repeated for each of the two target variables. The network performance was satisfactory, with a coefficient of determination R^2 and a root-mean-square error E_{RMS} between observations and estimates of $R^2 \approx 0.72$ and $E_{\text{RMS}} \approx 0.67 \text{ m s}^{-1}$ for wind speed and of $R^2 \approx 0.94$ and $E_{\text{RMS}} \approx 4.7\%$ for relative humidity. The uncertainty in wind speed and relative humidity estimates leads to an average uncertainty of 5 % and 3 % of the surface heat fluxes (Sect. 2.2.2), respectively.

We captured the spatial variability in TSs on the morning of 22 August 2019 (Fig. 2.1) by collecting 11 conductivity–temperature–depth (CTD) profiles (CTD60M, Sea&Sun Technology) along the x axis, between 2 and 14 m depth (Fig. 2.2a).

2.2.2 Heat and buoyancy fluxes

Heat fluxes were estimated from meteorological data and lake surface temperature at MB. We assumed that the meteorological conditions and the heat fluxes were spatially uniform over the lake surface (0.5 km^2). Heat fluxes were defined positive in the upward direction (lake cooling) and negative in the downward direction (lake heating). The non-penetrative surface heat flux H_{Q_0} is defined as

$$H_{Q_0} = H_C + H_E + H_{\text{LW},\text{in}} + H_{\text{LW},\text{out}} \quad [\text{W m}^{-2}], \quad (2.1)$$

where H_C and H_E are the respective sensible and latent heat fluxes, and $H_{\text{LW},\text{in}}$ and $H_{\text{LW},\text{out}}$ are the respective incoming and outgoing longwave radiation. The net surface heat flux $H_{0,\text{net}}$ includes the shortwave radiative flux at the surface $H_{\text{SW},0}$:

$$H_{0,\text{net}} = H_{Q_0} + H_{\text{SW},0} \quad [\text{W m}^{-2}]. \quad (2.2)$$

The different terms of the heat budget were calculated similarly to Fink et al. (2014). Cloudiness modulates the proportion of direct and diffuse shortwave radiation and was derived from daily clear-sky irradiance as in Meyers and Dale (1983). We modified the empirical wind and air temperature-based calibration function, f , in the sensible and latent heat flux estimates of Fink et al. (2014) to take the lake fetch into account, as proposed in McJannet et al. (2012).

The non-penetrative surface buoyancy flux B_0 was inferred from H_{Q_0} under the assumption that only heat fluxes modify the potential energy near the surface (Bouffard & Wüest, 2019):

$$B_0 = \frac{\alpha g H_{Q_0}}{\rho C_{p,w}} \quad [\text{W kg}^{-1}]. \quad (2.3)$$

In Eq. (2.3), $\alpha = -(1/\rho)\partial\rho/\partial T$ is the thermal expansivity of water [$^{\circ}\text{C}^{-1}$], g is the gravitational acceleration [m s^{-2}], ρ is the water density [kg m^{-3}], and $C_{p,w}$ is the specific heat of water [$\text{J }^{\circ}\text{C}^{-1} \text{kg}^{-1}$]. The thermal expansivity was estimated from the surface temperature using the relationship reported in Bouffard and Wüest (2019). To calculate water density, we used the equation of state from C.-T. A. Chen and Millero (1986), with a measured average salinity of $S = 0.2 \text{ g kg}^{-1}$ for Rotsee. Our analysis assumed a constant salinity over the year, as the seasonal changes in surface density are controlled by temperature fluctuations rather than variations in salinity.

Similarly, a radiative surface buoyancy flux $B_{\text{SW},0}$ was obtained as follows:

$$B_{\text{SW},0} = \frac{\alpha g H_{\text{SW},0}}{\rho C_{p,w}} \quad [\text{W kg}^{-1}]. \quad (2.4)$$

The net buoyancy flux at the surface is $B_{0,\text{net}} = B_0 + B_{\text{SW},0}$. $B_{0,\text{net}} > 0$ indicates a destabilizing buoyancy flux (net cooling), whereas $B_{0,\text{net}} < 0$ indicates a stabilizing buoyancy flux (net heating). We used $B_{0,\text{net}}$ to identify the daily cooling and heating phases (Sect. 2.3.1), and we averaged B_0 over the daily cooling phase to quantify the intensity of convection (Sect. 2.2.6).

2.2.3 Mixed-layer depth

We used hourly averaged temperature data from MB to calculate the thermocline depth (h_t) and the mixed-layer depth (h_{ML}). Based on the review of Gray et al. (2020), we estimated h_{ML} using the temperature-gradient method with a threshold of $dT/dz = 0.05 \text{ }^{\circ}\text{C m}^{-1}$. The water column was defined as fully mixed when $dT/dz < 0.05 \text{ }^{\circ}\text{C m}^{-1}$ at all depths. In this case, h_{ML} was set to the depth of the bottom temperature sensor. For stratified conditions, the thermocline depth was defined as the depth of maximum gradient in dT/dz . Starting from h_t and moving upward,

the lower end of the mixed layer was reached when the local temperature gradient dropped to $dT/dz < 0.05 \text{ }^{\circ}\text{C m}^{-1}$. When $dT/dz > 0.05 \text{ }^{\circ}\text{C m}^{-1}$ at all depths, the entire column was stratified and h_{ML} was zero.

2.2.4 Occurrence of thermal siphons

We used the velocity data from the Aquadopp profiler at MT to estimate the cross-shore transport over the bottom 3 m of the sloping region. Quality control of the velocity was performed by discarding values with beam correlation below 50 % or signal amplitude weaker than 6 dB above noise floor. The horizontal velocity was projected onto the x axis (angle of 56° from north), which crosses the isobath at MT perpendicularly (Fig. 2.2a). Following the 2D framework of Fig. 2.1, we will now call U_x the “cross-shore velocity”.

The time series of U_x was then divided into 24 h subsets, starting and ending at 17:00 UTC. Each 24 h subset was analyzed separately to identify TS events. We decided to focus on periods when MT was located in the sloping mixed region, with TSs flowing at the bottom of the water column (Fig. 2.1). This condition allowed us to relate our current measurements to scaling formulae of downslope density currents (Sect. 2.3.4). A downslope TS event was detected on a specific day if the three following conditions were met:

1. There was *significant cross-shore flow*, where the depth-averaged velocity of the current $U_x > 0.5 \text{ cm s}^{-1}$ for at least 2 h;
2. There was *weak wind during the selected event*, where $|L_{\text{MO,avg}}|/h_{\text{ML,avg}} < 0.5$ ($|L_{\text{MO,avg}}|$ and $h_{\text{ML,avg}}$ are the averaged Monin–Obukhov length scale (Wüest & Lorke, 2003) and mixed-layer depth during the cross-shore flow event, respectively);
3. There was a *mixed water column at MT before the onset of the flow*, where $dT/dz < 0.05 \text{ }^{\circ}\text{C m}^{-1}$ at all depths.

Cross-shore flows that did not meet conditions no. 2 and no. 3 were noted as “wind-driven circulation” and “stratified flows”, respectively. The term “stratified flows” refers here to any cross-shore flow that occurred when the mixed-layer depth was shallower than the lake depth at MT. This includes basin-scale internal waves and intruding TSs. Further justifications of the above criteria are provided in Sect. S2.4.

2.2.5 Cross-shore transport by thermal siphons

The cross-shore transport was calculated for each identified TS event (Sect. 2.2.4). For each event, we defined subperiods with continuous positive U_x (further details in Sect. S2.4). We calculated the unit-width volume of water transported over each of these subperiods:

$$V_{x,i} = \int_{t_{0,i}}^{t_{f,i}} q_x(t) dt \quad [\text{m}^2], \quad (2.5)$$

where $t_{0,i}$ and $t_{f,i}$ are the initial and final times of subperiod i , respectively, and q_x is the unit-width discharge defined as

$$q_x(t) = \int_{z_{\text{bot}}(t)}^{z_{\text{top}}(t)} U_x(z, t) dz \quad [\text{m}^2 \text{ s}^{-1}]. \quad (2.6)$$

In Eq. (2.6), z_{bot} and z_{top} are the respective bottom and top interfaces of the region over which $U_x > 0$ at time t . For each day, we then defined the TS flushing period as the subperiod with the largest volume transported $V_{x,i}$.

Four daily quantities characterizing the cross-shore transport were calculated over the flushing period of each day ($t_0 < t < t_f$): the average cross-shore velocity U_{avg} and unit-width discharge q_{avg} , the maximum cross-shore velocity U_{max} (both in time and depth), and the flushing timescale $\tau_F = V_{\text{lit}}/q_{\text{avg}}$, with $V_{\text{lit}} \approx 500 \text{ m}^2$ representing the unit-width volume of the littoral region upslope of MT (Fig. 2.1). U_{avg} and q_{avg} were obtained as follows:

$$U_{\text{avg}} = \frac{1}{t_f - t_0} \int_{t_0}^{t_f} \overline{U_x(t)} dt \quad [\text{m s}^{-1}], \quad (2.7)$$

$$q_{\text{avg}} = \frac{1}{t_f - t_0} \int_{t_0}^{t_f} \overline{q_x(t)} dt \quad [\text{m}^2 \text{ s}^{-1}]. \quad (2.8)$$

2.2.6 Scaling formulae

We relate the transport quantities introduced in Sect. 2.2.5 to the forcing parameters using scaling formulae from theoretical and laboratory studies.

The horizontal velocity scale of TSs is $U \sim (B_0 L)^{1/3}$, where B_0 is the destabilizing surface buoyancy flux, and L is a horizontal length scale (Phillips, 1966). Following Wells and Sherman (2001), we

used the horizontal length scale L_{ML} based on the mixed-layer depth:

$$U = c_U (B_0 L_{\text{ML}})^{1/3} \quad [\text{m s}^{-1}], \quad (2.9)$$

where c_U is a proportionality coefficient. For each value of h_{ML} , we calculated L_{ML} as the distance between the northeastern edge of the lake and the location where the mixed layer intersects the lake sloping bottom (Fig. 2.1).

The unit-width discharge is scaled by $q \sim (B_0 L)^{1/3} h$, where h is a vertical length scale. We used the average depth of the littoral region upslope of MT ($h_{\text{lit}} = V_{\text{lit}}/L_{\text{lit}}$, Fig. 2.1) as h :

$$q = c_q (B_0 L_{\text{ML}})^{1/3} h_{\text{lit}} \quad [\text{m}^2 \text{s}^{-1}], \quad (2.10)$$

where c_q is a proportionality coefficient. We defined the flushing timescale from Eq. (2.10) as

$$\tau_F = \frac{V_{\text{lit}}}{q} = c_F \frac{L_{\text{lit}}}{(B_0 L)^{1/3}} \quad [\text{s}], \quad (2.11)$$

where $c_F = 1/c_q$. The flushing timescale represents the time that a TS needs to flush the littoral region of volume V_{lit} .

The daily cooling phase of duration τ_c is defined by $B_{0,\text{net}} > 0$. After the onset of surface cooling, a TS does not form immediately. Vertical convective mixing takes place before the horizontal density gradient starts to drive a TS (Ulloa et al., 2022; Wells & Sherman, 2001). The period between the start of the cooling phase and the TS formation is quantified by an initiation timescale (τ_{ini}). If the littoral region is initially mixed vertically, τ_{ini} equals the transition timescale τ_t derived by Ulloa et al. (2022) under constant surface cooling:

$$\tau_t = \frac{2 (L_{\text{ML}} - L_p)^{2/3}}{B_0^{1/3} (1 - h_p/h_{\text{ML}})^{1/3}} \quad [\text{s}], \quad (2.12)$$

where $L_p \approx 170$ m and $h_p \approx 1$ m, representing the length and depth of the plateau region of Rotsee, respectively (Fig. 2.1). This timescale is based on a three-way momentum balance between the lateral pressure gradient due to differential cooling and the inertial terms (Finnigan & Ivey, 1999).

In Eqs. (2.9)-(2.12), B_0 and L_{ML} are averaged over τ_c every day. We discuss the choice of the length scales L_{ML} and h_{lit} in more detail in Sect. 2.4.3. The key parameters used for the scaling formulae and TS dynamics are listed in Tab. 2.1.

Table 2.1 – Key parameters related to the forcing parameters, bathymetry, and TS dynamics. For seasonally varying parameters, the given ranges of values are daily averages.

Symbol	Units	Ranges of values in Rotsee	Definition and equation
τ_c	h	0-24	Duration of the cooling phase
τ_F	h	5-20	Flushing timescale: $\tau_F = V_{\text{lit}}/q_{\text{avg}}$
τ_{ini}	h	2-170	Initiation timescale: $\tau_{\text{ini}} = \tau_{\text{mix}} + \tau_t$
τ_{mix}	h	0-250	Mixing timescale: $\tau_{\text{mix}} = 0.5 \left(h_{\text{MT}}^2 - h_{\text{ML,ini}}^2 \right) N^2 / [B_0(1 + 2A)]$
τ_t	h	2-45	Transition timescale $\tau_t = 2 (L_{\text{ML}} - L_p)^{2/3} / \left[(1 - h_p/h_{\text{ML}})^{1/3} B_0^{1/3} \right]$
B_0	W kg ⁻¹	0 – 1.4 × 10 ⁻⁷	Surface buoyancy flux: $B_0 = \alpha g H_{Q_0} / (\rho C_{p,w})$
$B_{0,\text{net}}$	W kg ⁻¹	(-1.3 × 10 ⁻⁷) – 1.1 × 10 ⁻⁷	Net surface buoyancy flux: $B_{0,\text{net}} = B_0 + B_{\text{SW},0}$
$B_{\text{SW},0}$	W kg ⁻¹	(-1.8 × 10 ⁻⁷) – 0	Radiative buoyancy flux: $B_{\text{SW},0} = \alpha g H_{\text{SW},0} / (\rho C_{p,w})$
h_p	m	1	Depth of the plateau region
h_{MT}	m	4.2	Depth at MT
FG	-	5-18	Flow geometry parameter: $FG = \sqrt{\langle U_x^2 \rangle} / \sqrt{\langle U_z^2 \rangle}$
$h_{\text{TS,avg}}$	m	1.2-2.4	Daily averaged TS thickness: $h_{\text{TS,avg}} = q_{\text{avg}}/U_{\text{avg}}$
h_{lit}	m	1.7	Average depth of the littoral region: $h_{\text{lit}} = V_{\text{lit}}/L_{\text{lit}}$
h_{ML}	m	0-15.3	Mixed-layer depth
$H_{0,\text{net}}$	W m ⁻²	(-200)–180	Net surface heat flux $H_{0,\text{net}} = H_{Q_0} + H_{\text{SW},0}$
H_{Q_0}	W m ⁻²	(-10)–250	Non-penetrative surface heat flux
$H_{\text{SW},0}$	W m ⁻²	(-300)–0	Surface shortwave heat flux
L_p	m	173	Length of the plateau region
L_{lit}	m	295	Length of the littoral region
L_{ML}	m	200–800	Length of the mixed region
N^2	s ⁻²	10 ⁻⁵ -10 ⁻³	Squared buoyancy frequency below the mixed layer
q_{avg}	m ² s ⁻¹	0.005–0.030	Daily averaged unit-width TS discharge
q_x	m ² s ⁻¹	0–0.07	Unit-width TS discharge
U_{avg}	m s ⁻¹	0.005–0.015	Daily averaged TS cross-shore velocity
U_{max}	m s ⁻¹	0.01–0.04	Daily maximum TS cross-shore velocity
U_x	m s ⁻¹	(-0.05)–0.07	Cross-shore velocity
U_z	m s ⁻¹	(-0.01)–0.01	Vertical velocity
V_{lit}	m ²	499	Unit-width volume of the littoral region
w_*	m s ⁻¹	0.001–0.009	Convective velocity scale: $w_* = (B_0 L_{\text{ML}})^{1/3}$

2.3 Results

2.3.1 Diurnal cycle

The magnitude of the net surface buoyancy flux $B_{0,\text{net}}$ oscillates daily, and the intensity of the diel fluctuation is modulated at a seasonal timescale (Fig. 2.3a). We illustrate the diurnal cycle with an example on 9–10 September 2019 (Fig. 2.3b, c, d). This summertime period is characterized by a strong day–night variability, which is ideal to elucidate how changes in forcing conditions affect the formation and destruction of TSs. The net surface buoyancy flux $B_{0,\text{net}}$ varies from $-2 \times 10^{-7} \text{ W kg}^{-1}$ during daytime to $1 \times 10^{-7} \text{ W kg}^{-1}$ during nighttime (Fig. 2.3b). In contrast to $B_{0,\text{net}}$, B_0 remains positive over 24 h, indicating a continuous cooling at the air–water interface. In late summer, B_0 is $\sim 10^{-7} \text{ W kg}^{-1}$ with a limited variability of $\pm 5 \times 10^{-8} \text{ W kg}^{-1}$ between day and night. The radiative forcing $B_{\text{SW},0}$ is the main driver of the diurnal variability, with diel variations that are 1 order of magnitude larger than B_0 during cloud-free summer days like 9–10 September 2019. We observe differential cooling at night, with lateral temperature gradients of $\sim 5 \times 10^{-4} \text{ }^\circ\text{C m}^{-1}$ in late summer (Fig. 2.1).

We divide the diurnal cycle into a net cooling phase during the night ($B_0 > |B_{\text{SW},0}|$) and a net heating phase during the day ($B_0 < |B_{\text{SW},0}|$). Starting the period at 17:00 UTC, the water column is initially thermally stratified by the radiative heating of the daytime period (Fig. 2.3d). During the first part of the night, convective cooling mixes and deepens the surface layer (period no. 1 in Fig. 2.3d). The water column becomes entirely mixed at MT around 00:00 UTC (see the vertical isotherms starting around 00:00 UTC in Fig. 2.3d). The convective plumes intensify in the second part of the night to reach vertical velocities of $\sim 5 \text{ mm s}^{-1}$ (Fig. 2.3c). A total of 3 h after complete vertical mixing at MT, a cross-shore circulation is initiated (period no. 3 in Fig. 2.3d), with a downslope flow near the bottom (positive U_x) and an opposite flow above (negative U_x). The velocity magnitude of $\sim 1 \text{ cm s}^{-1}$ is typical for TSs. We will hereafter refer to the period during which a TS flows as the flushing period. The interface between the two flows oscillates vertically by 1–2 m ($\sim 100\%$ of the TS thickness), suggesting that the transport is limited by the vertical mixing of convective plumes. At the end of the cooling phase, the water column is distinctly stratified near the bottom, indicating the presence of persistent colder water flowing downslope. A striking observation is the intensification of the TS in phase with the weakening of vertical convection at the onset of radiative heating. The cross-shore velocity increases above 2 cm s^{-1} , and the induced bottom stratification reaches $\sim 0.1 \text{ }^\circ\text{C m}^{-1}$ at the beginning of the heating phase. This strong flushing lasts for several hours, while radiative heating increases and re-stratifies the water

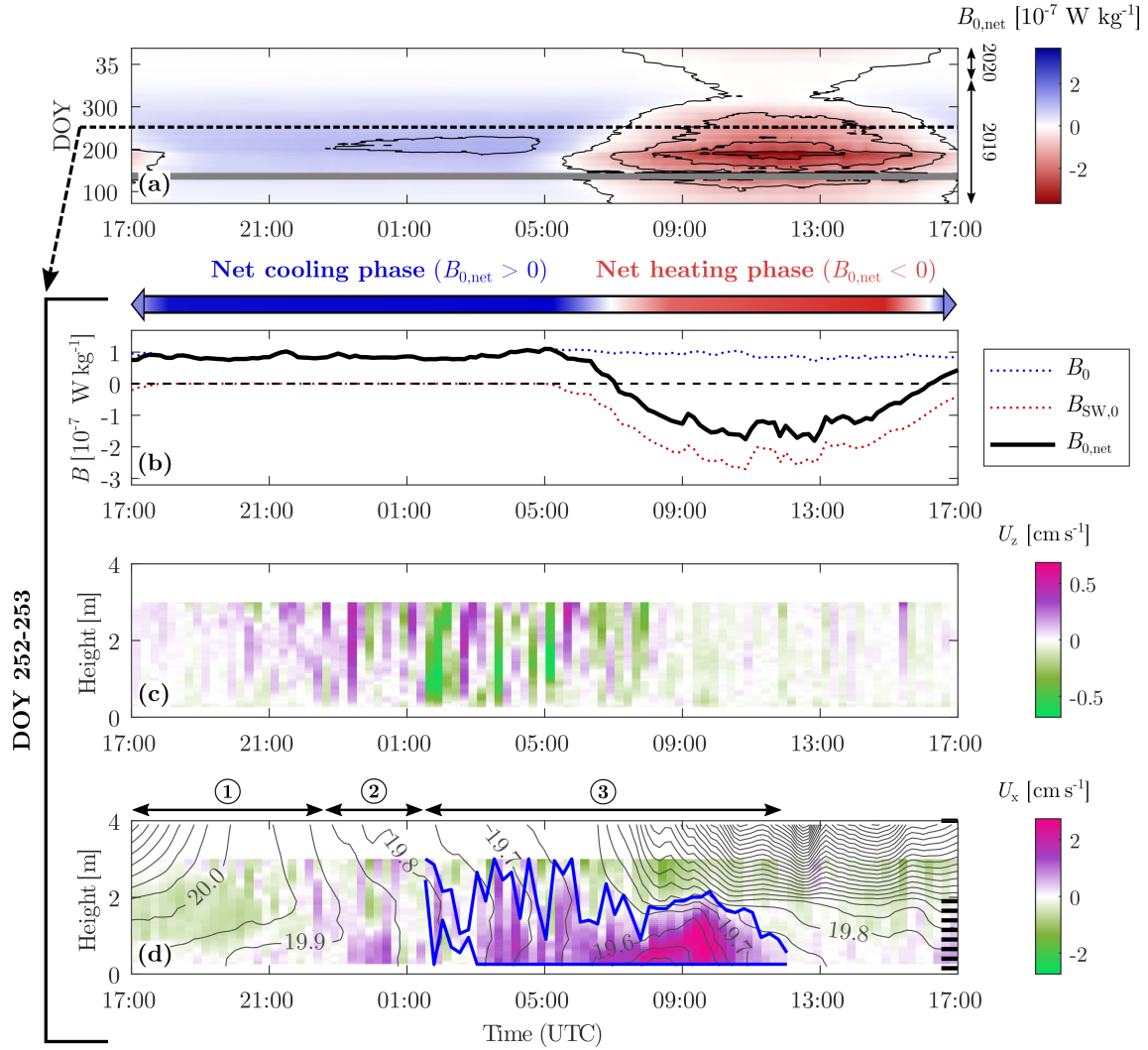


Figure 2.3 – Diurnal cycle of a TS. (a) Net surface buoyancy flux as a function of time during the day, represented over 1 year (from 13 March 2019 to 13 March 2020). DOY stands for “day of the year”. A 30 d moving average has been applied to smooth the time series. The 45 d long period without measurement in May 2019 is shown in gray. The contour lines have a spacing of 1×10^{-7} W kg $^{-1}$. The dashed line corresponds to the diurnal cycle shown in panels (b), (c), and (d) (9–10 September 2019; DOY 252–253). (b) Time series of surface buoyancy fluxes defining the cooling and heating phases on 9–10 September 2019. (c) Vertical velocity measured every 15 min at MT (depth of ~ 4 m) as a function of time and height above the sediment. Positive (purple) values correspond to a flow moving upward. Strong vertical movements are the signature of convective plumes. (d) Cross-shore velocity measured every 15 min at MT as a function of time and height above the sediment. Positive (purple) values correspond to a flow moving offshore (southwestward flow). Black lines are 0.05 °C spaced isotherms that are linearly interpolated between each thermistor. The TS detected by the algorithm and used for the transport calculation is depicted in blue. The vertical resolution of the thermistors is shown by the horizontal black ticks on the right axis. Horizontal arrows identify three periods: (1) deepening of the mixed layer, (2) transition period before the initiation of the TS, and (3) flushing period.

above the density current. The cross-shore flow weakens in the late morning but continues until noon.

The example detailed above presents all of the characteristics of a typical TS, with different phases and inertia between the cooling phase and the flushing period. Other examples, provided in Sect. S2.2 (Fig. S2.2), show that the timing and magnitude of the flow change with the forcing conditions.

2.3.2 Seasonal variability in the forcing parameters

Two key parameters for TS formation are B_0 and h_{ML} (Sect. 2.2.6), which are indirectly related to $B_{0,net}$. Hereafter, we refer to these parameters as “forcing parameters” of TSs. The daily intensity of convective cooling is estimated based on the convective velocity scale $w_* = (B_0 h_{ML})^{1/3}$ (Deardorff, 1970), where B_0 and h_{ML} are daily averages during the cooling phase at MB. These two parameters are both seasonally dependent, and their relationship is characterized by an annual hysteresis cycle (Fig. 2.4a). Although the surface heat flux H_{Q_0} increases from winter to summer, the strong seasonal variability in B_0 (1 order of magnitude larger in summer than in winter) is mostly due to seasonal changes in the thermal expansivity α .

From spring to summer, h_{ML} remains shallow (< 2 m) and B_0 increases from $\sim 10^{-9} \text{ W kg}^{-1}$ in March to $\sim 10^{-7} \text{ W kg}^{-1}$ in August. The latter results in an increase in the convective velocity scale from $w_* \approx 3.8 \pm 0.7$ to $w_* \approx 6.7 \pm 0.9 \text{ mm s}^{-1}$ over the same period (Figs. 2.4a and 2.4b). The lake undergoes net daily heating over this period ($B_{0,net} < 0$), with a cooling phase that remains shorter than 15 h (Fig. 2.4b). In August, $B_{0,net} \approx 0$ and daily heating is balanced by daily cooling. At this period, the intensity of convective mixing reaches its maximum, and the diurnal heating–cooling cycle is pronounced (Fig. 2.3a).

From September to January, the lake undergoes a daily net cooling ($B_{0,net} > 0$) and the mixed layer deepens by convection at an average rate of $\sim 0.1 \text{ m d}^{-1}$, leading to a complete mixing in mid-December. Over the same period, B_0 continuously decreases due to the drop in α with colder temperatures. This decrease in B_0 balances the deepening of h_{ML} , and w_* remains constant around $w_* \approx 7 \pm 1 \text{ mm s}^{-1}$ from August to November. The duration of the cooling phase increases in autumn to reach its maximum in November ($\tau_c \approx 21 \pm 2$ h). Convective cooling is occurring almost continuously at that time. In winter, the convective velocity w_* drops to $w_* \approx 3.5 \pm 1 \text{ mm s}^{-1}$, and the effect of the cooling phase is again balanced by the heating phase ($B_{0,net} \approx 0$, $\tau_c \approx 15 \pm 3$ h in February). The differences between the cooling and heating phases of the diurnal cycle are reduced in winter, with $B_{0,net} \approx 0$ over the entire day (Fig. 2.3a). Note that winter 2019–2020 was warm, and

Rotsee remained mixed from December to February (no inverse stratification, surface temperature $T > 4^\circ\text{C}$).

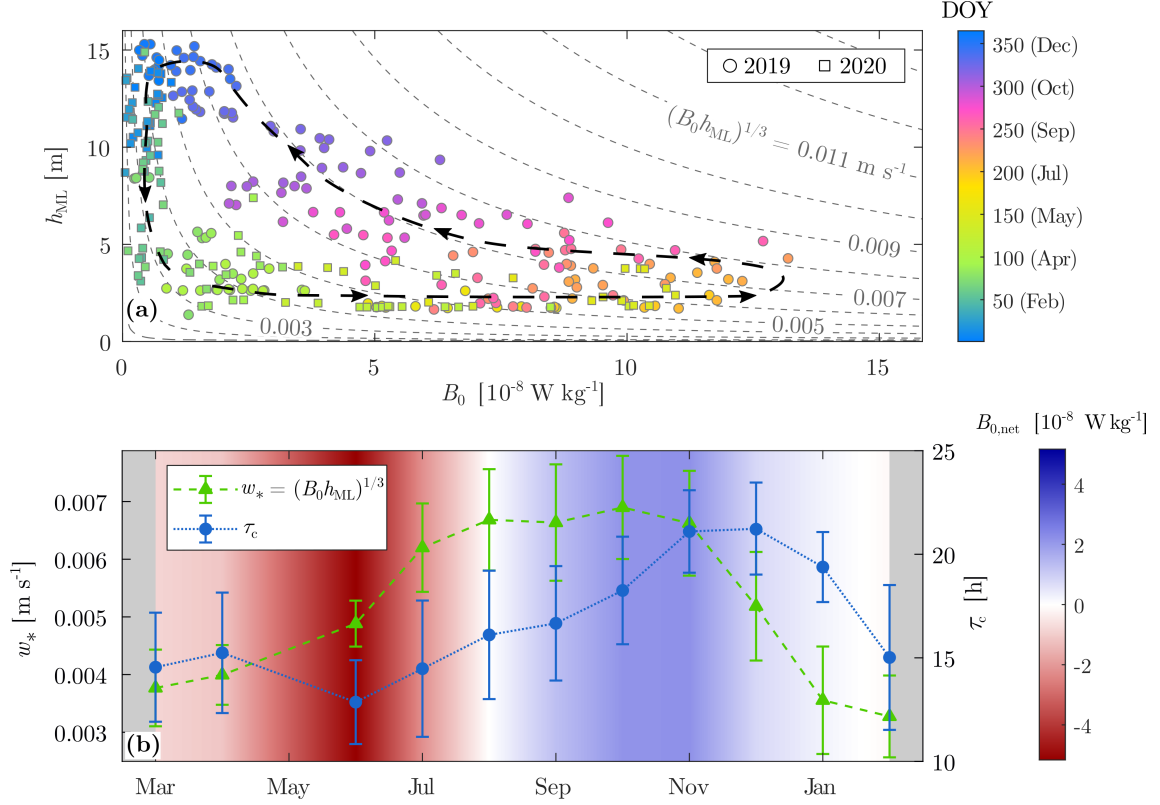


Figure 2.4 – Seasonal variability in the forcing parameters over 1 year (from March 2019 to March 2020). (a) Daily averages of mixed-layer depth as a function of surface buoyancy flux during cooling periods. Gray dashed lines indicate the corresponding convective velocity scale. The black dashed line with arrows is a qualitative representation of the annual cycle. (b) Monthly averages of convective velocity scale w_* during the cooling phase (green line), duration of the cooling phase τ_c (blue line), and net surface buoyancy flux $B_{0,\text{net}}$ (linearly interpolated color map). Error bars represent the standard deviation of w_* and τ_c .

2.3.3 Seasonal occurrence of thermal siphons

We apply our detection algorithm for cross-shore flows (Sect. 2.2.4) on 227 d with continuous measurements at MT from March 2019 to February 2020. We identify 156 d with a significant cross-shore flow (69% of the days with observations), over which 85 d (37%) were reported as TS events. The remaining days with identified cross-shore flow were either associated with wind-driven circulation for 13 d (6%) or stratified flows for 58 d (26%). We estimate the percentage of occurrence of TSs relative to the number of days with measurements (p_{TS}) for each month (Fig. 2.5). Before late July, the mixed layer is usually shallower than 4 m (Fig. 2.4a) and stratified flows prevail at MT (Fig. 2.5). The first events identified as TSs occur on 28 July and 31 July ($p_{\text{TS}} = 12.5\%$

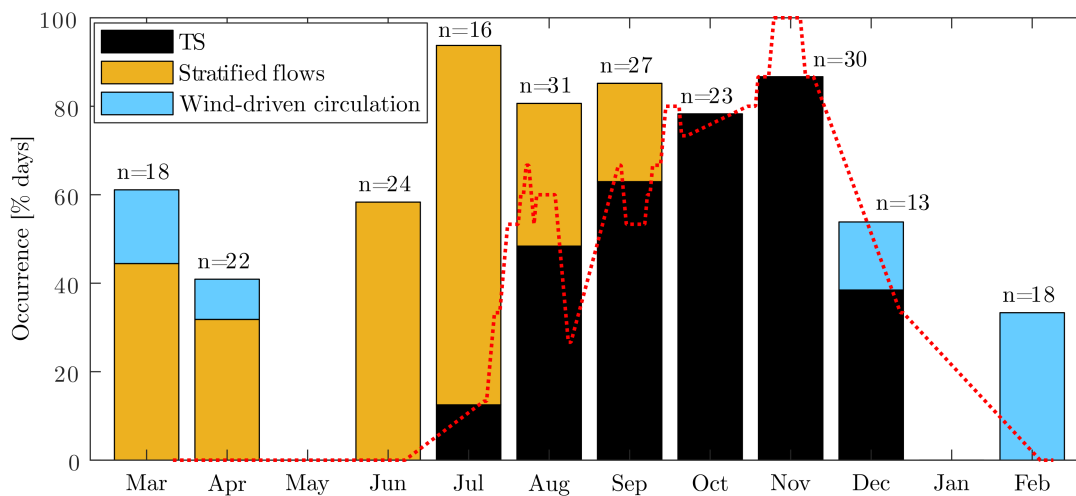


Figure 2.5 – Monthly occurrence of TSs and other cross-shore (southwestward) flows at MT, expressed as a percentage of the days with measurements. The other cross-shore flows are divided between wind-driven circulation ($|L_{MO}|/h_{ML} > 0.5$) and stratified flows at MT ($dT/dz > 0.05 \text{ }^{\circ}\text{C m}^{-1}$). The red dashed line indicates the 15 d moving average of the percentage of occurrence of TSs. The number of days with measurements (n) is shown for each month. Months with less than 10 d of measurements have been removed (May 2019 and January 2020).

in July). However, TSs do not reach a significant percentage of occurrence ($\sim 50\%$) until August. The occurrence increases in autumn to reach 87% in November. In winter, TSs are less common: they only occur on 38% of the days in December, 2 d in early January (not shown in Fig. 2.5 due to the few days measured during this month), and are not observed later in winter.

The 15 d moving average in Fig. 2.5 reveals the short-term variability due to synoptic changes in the meteorological conditions that naturally modulate the seasonal pattern. Although the monthly averaged occurrence increases from August to November, the biweekly percentage of occurrence drops over shorter periods. These periods are associated with strong heating that re-stratifies the water column at MT, reduces surface cooling at night, and prevents TS formation (Sect. S2.2, Fig. S2.1). The 15 d averaged occurrence reaches 100% in November, when a TS is present over 25 consecutive days.

Although TSs become more frequent in autumn, the percentage of occurrence of cross-shore flows (p_{CS}) remains constant at around 80%–90% from July to November. Lateral flows observed at MT in spring and summer primarily result from direct wind forcing or subsequent stratified mixing. These flows may also include TSs intruding before reaching MT and, therefore, not counted as downslope TSs (further details in Sect. S2.4). These different processes become less frequent in autumn due to the deeper mixed layer and are replaced by downslope TSs. Overall, there seems

to be an effect of TSs on the number of cross-shore flows if we compare the period from July to December ($p_{CS} \approx 80 \pm 14 \%$) with the rest of the year ($p_{CS} \approx 47 \pm 12 \%$), suggesting that TSs are the main mechanism connecting the littoral and pelagic regions in Rotsee.

2.3.4 Scaling the cross-shore transport

We compare our field-based transport estimates for the TS events identified in Fig. 2.5 with the laboratory-based scaling formulae introduced in Sect. 2.2.6 (Fig. 2.6). The daily average and maximum cross-shore velocities are linearly correlated with the horizontal velocity scale from Eq. (2.9) ($R^2 > 0.5, p_{\text{val},F} < 0.01$; Figs. 2.6a and 2.6b). The daily average velocity $U_{\text{avg}} \approx 0.9 \pm 0.2 \text{ cm s}^{-1}$ is 3 times lower than the daily maximum velocity $U_{\text{max}} \approx 2.6 \pm 0.7 \text{ cm s}^{-1}$ that occurs in the morning (Fig. 2.3). The best linear fits (with 0 intercept) are given by $U_{\text{avg}} = 0.33(B_0 L_{\text{ML}})^{1/3}$ and $U_{\text{max}} = 0.99(B_0 L_{\text{ML}})^{1/3}$. The 95 % confidence interval of the proportionality coefficient is $0.32 \leq c_U \leq 0.34$ for U_{avg} and $0.95 \leq c_U \leq 1.02$ for U_{max} . Despite the natural variability, a seasonal trend is distinguishable, with a decrease in U_{avg} and U_{max} by a factor of 2 from July to December. This is consistent with the weakening of convective cooling observed in Fig. 2.4.

The unit-width discharge q_{avg} and flushing timescale τ_F are also well predicted by the scaling formulae (Eqs. 2.10 and 2.11, respectively), despite a larger scatter than for the cross-shore velocity ($R^2 \approx 0.2 - 0.3, p_{\text{val},F} < 0.01$; Figs. 2.6c and 2.6d). The unit-width discharge $q_{\text{avg}} \approx 0.015 \pm 0.004 \text{ m}^2 \text{ s}^{-1}$ corresponds to an average thickness of $h_{\text{TS,avg}} = q_{\text{avg}}/U_{\text{avg}} \approx 1.8 \pm 0.2 \text{ m}$ and a flushing timescale of $\tau_F \approx 9.7 \pm 2.7 \text{ h}$. The best relationships (with 0 intercept) are given by $q_{\text{avg}} = 0.34(B_0 L_{\text{ML}})^{1/3} h_{\text{lit}}$ ($R^2 = 0.27$) and $\tau_F = 2.99 L_{\text{lit}} / (B_0 L_{\text{ML}})^{1/3}$ ($R^2 = 0.18$). The 95 % confidence interval of the proportionality coefficient is $0.33 \leq c_q \leq 0.36$ for q_{avg} and $2.83 \leq c_F \leq 3.15$ for τ_F . The strong daily variability is explained by the fluctuating TS thickness during the convective period (Figs. 2.3c and 2.3d), which affects the calculation of the discharge (further details in Sect. S2.4). As observed for the cross-shore velocity, the cross-shore transport weakens from summer to winter: q_{avg} decreases and τ_F increases by a factor of 2. The flushing timescale is $\tau_F \approx 7 \text{ h}$ in summer but reaches $\tau_F \approx 20 \text{ h}$ in winter. However, due to longer TS events in winter than in summer, the volume flushed by a single TS event is independent of the season and remains larger than the volume of the littoral region (Sect. S2.3).

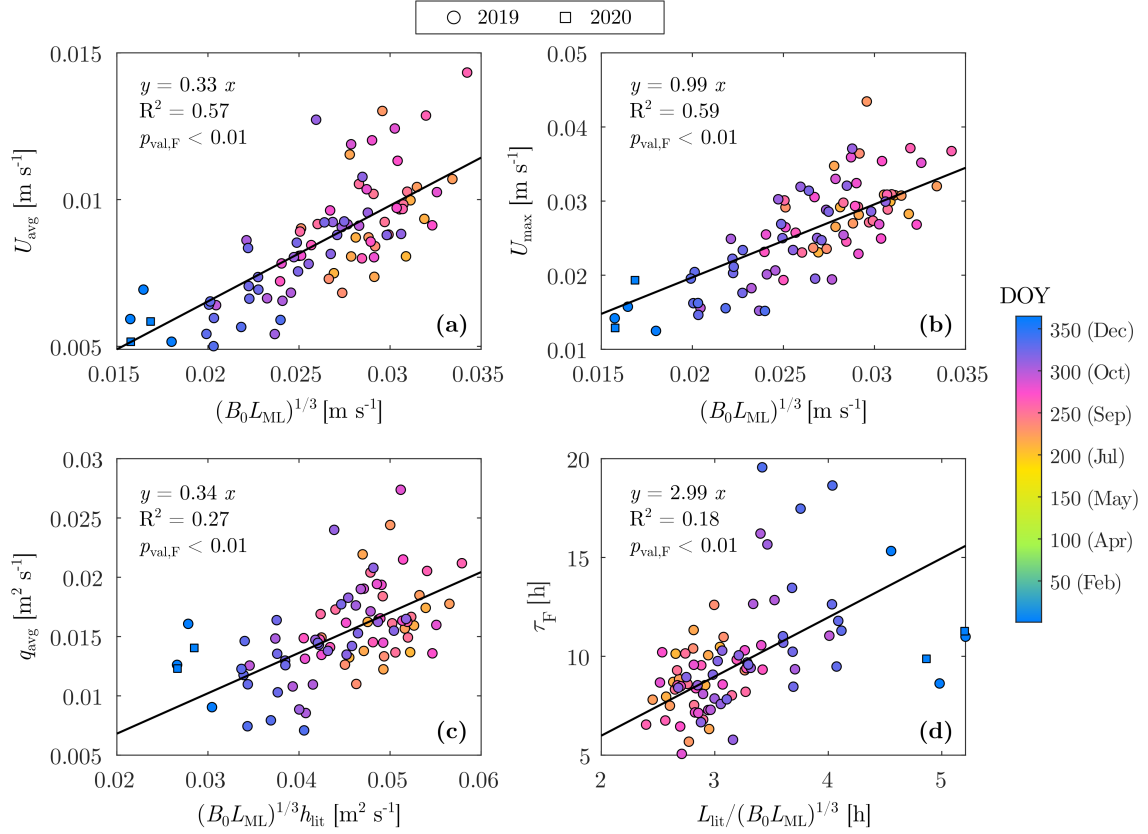


Figure 2.6 – Comparison between transport estimates and scaling formulae. (a) Daily averaged cross-shore velocity, (b) daily maximum cross-shore velocity, (c) daily averaged unit-width discharge, and (d) flushing timescale as a function of scaling formulae (Sect. 2.2.6). The equation of the linear regressions with 0 intercept, the coefficient of determination (R^2), and the p value of an F test ($p_{\text{val},F}$) are indicated

2.3.5 Flushing period

The diurnal cycle described in Sect. 2.3.1 varies at the seasonal scale, as the forcing parameters change. To assess the effects on the flushing period (period no. 3 in Fig. 2.3d), we average the diurnal cycle monthly between August and December (Fig. 2.7). The cooling and heating phases are illustrated with the diurnal cycle of $B_{0,\text{net}}$. The duration of the cooling phase (blue shading in Fig. 2.7) markedly increases from August to December, as already observed in Figs. 2.3a and 2.4b. The histograms of $|B_{0,\text{net}}^{\text{max}}|$ show that the magnitude of and variability in $B_{0,\text{net}}$ decrease over the same period (Figs. 2.7b, d, f, h, j).

These changes in the forcing parameters have a direct effect on the cross-shore transport. The unit-width discharge in Fig. 2.7 (white dotted line) is obtained by monthly averaging the 24 h time series $q_x(t)$. The discharge $q_x(t)$ is calculated from Eq. (2.6) during the flushing period $t_0 < t < t_f$

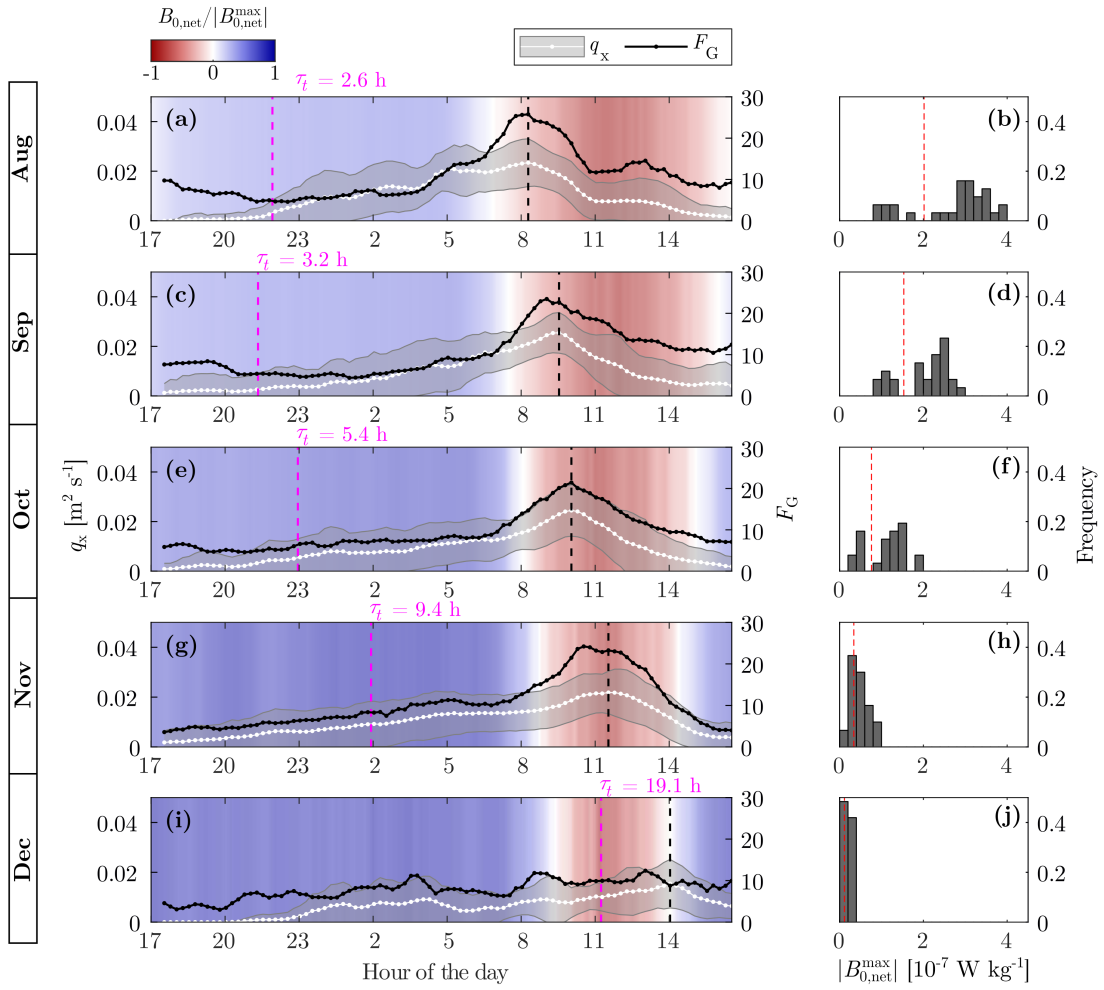


Figure 2.7 – Seasonal variability in the diurnal cycle. (a, c, e, g, i) Monthly average of the diurnal cycle of the unit-width discharge q_x and F_G parameter. Only days with observed TSs between August and December have been averaged. The shaded white area corresponds to average discharge \pm standard deviation. The monthly averaged net buoyancy flux represented as a color map is normalized by the maximum absolute value of each month. The vertical black dashed line indicates the time of maximal q_x . The transition timescale τ_t defines the starting time of the flushing, represented by a pink vertical dashed line. (b, d, f, h, j) Histograms of the maximum absolute value of the net buoyancy flux $|B_{0,net}^{max}|$ for each month. The red vertical line corresponds to $|B_{0,net}^{max}|$ of the monthly averaged diurnal cycles.

and $q_x(t) = 0$ for $t < t_0$ or $t > t_f$. In August and September (Figs. 2.7a and 2.7b), q_x increases at night to reach its maximum at the beginning of the heating phase. The flow generally stops in the late morning, depicted by a drop in q_x at around 10:00 UTC. This cycle corresponds to the example in Fig. 2.3. The daily peak in flushing is also observed in October and November, but it is more spread with a continuous increase in cross-shore transport at night, which can already be seen in the evening (Figs. 2.7e and 2.7g). Thus, the average flushing duration of TSs is longer in late autumn (see, for example, the 24 h long TS event in Sect. S2.2, Fig. S2.2). In December, the peak in

discharge is reduced and the cross-shore transport is nearly continuous over 24 h (Fig. 2.7i). The time of maximal q_x (vertical black dashed line in Fig. 2.7) is delayed from August to December. We associate this maximal q_x with the heating phase, as it always occurs $\sim 1 - 2$ h after $B_{0,\text{net}}$ becomes negative (except in December, during which time the peak is less pronounced).

The diurnal cycle of the cross-shore transport is also described by the flow geometry parameter introduced by Ulloa et al. (2022) as the ratio between the root-mean-square (RMS) of the cross-shore velocity and the RMS of the vertical velocity:

$$F_G(t) = \frac{\sqrt{\langle U_x(t)^2 \rangle}}{\sqrt{\langle U_z(t)^2 \rangle}}, \quad (2.13)$$

where $\langle \dots \rangle$ denotes a depth average. F_G provides information on the relative magnitude of TSs with respect to the surface convection. We expect F_G to be close to unity when surface convection is the only process acting on the water column. A deviation from unity towards larger values of F_G (i.e., $F_G \gg 1$) implies that the flow is anisotropic, with a stronger cross-shore component, as a TS develops. A sharp peak in the monthly averaged F_G is visible at the beginning of the heating phase, from August to November (Fig. 2.7). It matches the time of maximal q_x and results from the combined effect of TS-induced flushing (increase in U_x) and convection weakening (decrease in U_z).

To give a theoretical estimation of the starting time of the flushing, we estimate the initiation timescale of TSs from the monthly averaged transition timescale $\tau_{\text{ini}} \approx \tau_t$ (Eq. (2.12)). The assumption of constant surface cooling is reasonable for nighttime cooling in Rotsee (Fig. 2.3b). The starting time, depicted by a vertical pink dashed line in Fig. 2.7, corresponds to $(t_{\text{sunset}} + \tau_t)$, where t_{sunset} is the time of sunset when $B_{\text{SW},0}$ drops to zero. The increase in τ_t from $\tau_t \approx 3$ h in late summer to $\tau_t \approx 20$ h in winter leads to a later theoretical onset of TSs in winter, despite the earlier time of sunset. Based on this seasonal variability in τ_t , TSs are expected to start in the evening in summer but in the morning in winter. This theoretical starting time, however, can be improved by considering the initial stratification at the beginning of the cooling phase, as further discussed in Sects. 2.4.2 and 2.4.4.

2.4 Discussion

2.4.1 Seasonality of thermal siphons

Our 1-year-long measurements show that both the occurrence and intensity of TSs vary seasonally in lakes with shallow littoral zones comparable to Rotsee. TSs occur regularly from late summer to early winter, with a maximum frequency in November, and are absent the rest of the year (Sect. 2.3.3). While the frequency of TSs increases in autumn, the intensity of the net cross-shore transport decreases compared with the summer period (Sect. 2.3.4). However, the daily averaged volume flushed from the littoral region increases from summer to autumn (Sect. S2.3). The diurnal cycle is well defined in summer and divided into a cooling phase at night and a heating phase during daytime (Sect. 2.3.1). TSs form during the second part of the night and last until late morning, reaching a maximal flushing at the beginning of the heating phase. In autumn, the flushing duration increases, and the time of maximal flushing is shifted later in the day (Sect. 2.3.5).

To explain the TS seasonality, we need to relate it to the seasonal variability in the forcing parameters. The duration of the cooling phase (τ_c) is a key parameter to understand the TS occurrence and the diurnal dynamics, while the intensity of surface cooling (B_0) and the stratification (h_{ML}) parametrize the cross-shore transport. We discuss the effects of the forcing parameters on the TS seasonality in the following sections.

2.4.2 Effects of the forcing parameters on the occurrence of thermal siphons

TS occurrence can be predicted by estimating the initiation timescale τ_{ini} and comparing it with the duration of the cooling phase (τ_c). A TS will occur if the cooling phase is long enough, i.e., $\tau_c > \tau_{ini}$. In initially stratified surface waters, the initiation period is divided into (1) a stratified period, during which the mixed layer deepens, and (2) a transition period, during which the littoral region is vertically mixed (Figs. 2.3d and 2.8a). We express the initiation timescale as $\tau_{ini} = \tau_{mix} + \tau_t$, where τ_{mix} is the time needed to vertically mix the littoral region, and τ_t is the transition timescale given by Eq. (2.12). To estimate τ_{mix} , we use the deepening rate of the mixed layer (Zilitinkevĭc, 1991) as follows:

$$\frac{dh_{ML}}{dt} = (1 + 2A) \frac{B_0}{h_{ML} N^2} \quad [\text{m s}^{-1}], \quad (2.14)$$

where $N^2 = -(g/\bar{\rho})(d\rho/dz)$ [s^{-2}] is the squared buoyancy frequency below the mixed layer, $\bar{\rho}$ is the depth-averaged water density, and $A \approx 0.2$ is an empirical coefficient. The model of Eq. (2.14) assumes that the mixed layer deepens by convection only, without any wind contribution. This assumption is valid for calm conditions, which prevail in Rotsee due to wind sheltering (Zimmermann et al., 2021). The average duration required for mixing the water column at MT, assuming a constant surface cooling B_0 and an initial mixed-layer depth $h_{\text{ML},\text{ini}}$, can be derived from Eq. (2.14) as follows:

$$\tau_{\text{mix}} = (h_{\text{MT}}^2 - h_{\text{ML},\text{ini}}^2) \frac{N^2}{2 B_0 (1 + 2A)} \quad [\text{s}]. \quad (2.15)$$

In Eq. (2.15), the buoyancy frequency squared is approximated as

$N^2 = -(g/\bar{\rho}) [\rho(z = -h_{\text{ML},\text{ini}}) - \rho(z = -h_{\text{MT}})] / [h_{\text{MT}} - h_{\text{ML},\text{ini}}]$. The depth h_{MT} corresponds to the maximum depth of the littoral region upslope of MT (Fig. 2.1), which has to be mixed to observe downslope TSs at MT.

From the seasonality of the forcing parameters (Fig. 2.4), we predict the optimal period for the TS occurrence based on τ_{ini} (Fig. 2.8b). In summer, the shallow mixed layer ($h_{\text{ML}} \approx 2 \text{ m}$) and strong nighttime surface cooling ($B_0 \approx 10^{-7} \text{ W kg}^{-1}$) lead to a short transition timescale of $\tau_t \approx 2 \pm 0.5 \text{ h}$. However, the strong stratification near the surface limits the deepening of the mixed layer and causes τ_{mix} to be too large for the water column to mix at MT (orange period in Fig. 2.8b). The littoral region remains stratified for most of the nights ($h_{\text{ML}} < h_{\text{MT}}$), and the occurrence of downslope TSs at MT is low ($\tau_{\text{ini}} > \tau_c$ on average). Downslope TSs start to be observed in late summer when the mixed layer reaches h_{MT} before the end of the night. Starting in October, the monthly averaged mixed layer is deeper than h_{MT} , and $\tau_{\text{mix}} \approx 0$. At the same time, τ_t increases because of the deepening of the mixed layer and the decrease in B_0 . The transition timescale becomes longer than τ_c in winter (purple period in Fig. 2.8b), reaching its maximum of $\tau_t \approx 23 \pm 7 \text{ h}$ in January. This prevents TSs from forming in winter, except for days with continuous surface cooling (i.e., $\tau_c > 24 \text{ h}$). The transition timescale decreases in spring, but τ_{mix} increases simultaneously due to the re-stratification of the littoral region, which prevents TSs from occurring. Thus, the conditions to observe downslope TSs at MT are optimal between September and December, when $\tau_{\text{ini}} \ll \tau_c$ (gray shaded period in Fig. 2.8b). This period coincides well with our frequent observations of TSs in autumn. The limiting factor for the formation of TSs in spring and summer is τ_{mix} , whereas it is τ_t in winter.

During the optimal period of occurrence, the variability in forcing conditions ($B_{0,\text{net}}$) between days can modify the occurrence condition $\tau_{\text{ini}} < \tau_c$ at a shorter timescale than the seasonal scale. Days with TSs are characterized by higher $B_{0,\text{net}}$ than days without TSs (Sect. S2.2, Fig. S2.1). This results

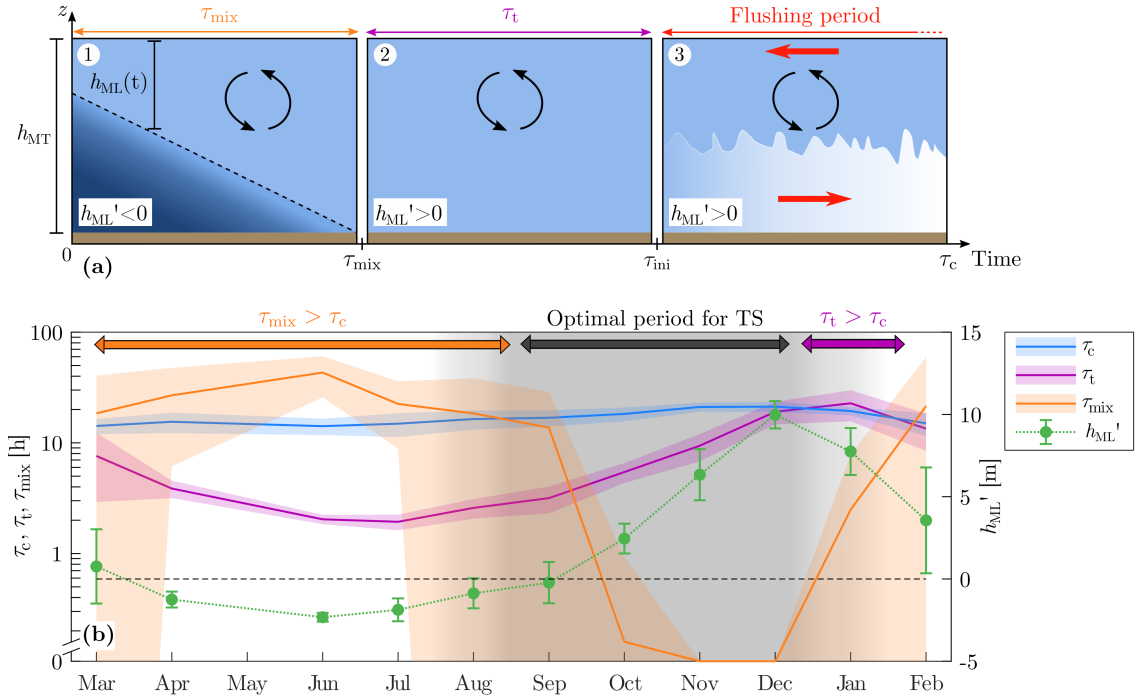


Figure 2.8 – Timescales determining the occurrence of TSs. (a) Schematic of the three periods of the cooling phase at MT (Fig. 2.3d) parameterized by the mixing timescale τ_{mix} , transition timescale τ_t , and cooling duration τ_c . The mixed-layer depth is expressed as the relative depth $h_{ML}' = h_{ML} - h_{MT}$ with respect to $h_{MT} = 4$ m. The mixed layer deepens during the first period ($0 < t < \tau_{mix}$), until the complete mixing of the water column. The transition period ($\tau_{mix} < t < \tau_{ini}$) is dominated by convection. TSs occur during the flushing period ($\tau_{ini} < t < \tau_c$). (b) Effects of the seasonality of τ_{mix} , τ_t , τ_c , and h_{ML}' on the TS occurrence. Monthly averages are represented, with shaded areas (τ_c , τ_t , and τ_{mix}) and error bars (h_{ML}') indicating the monthly standard deviation. Note the log scale for the axis of timescales. The gray shaded period corresponds to optimal conditions for the TS occurrence.

in the short-term variability in the biweekly averaged occurrence in Fig. 2.5. Other mechanisms affect the TS occurrence on a daily basis, such as wind events. Direct wind forcing either enhances or suppresses TSs. We identified several wind events from September to December that prevented any flow in the offshore direction (i.e., no significant flow detected by the algorithm) or, conversely, generated a strong cross-shore circulation (wind-driven circulation in Fig. 2.5).

Although the TS occurrence over short periods may vary from one year to another, we expect the seasonal trend previously described to be repeated every year in Rotsee. We also suggest that a similar trend should be common in other temperate lakes. Most of the TS events reported for other systems were observed in late summer or autumn, corresponding to the occurrence period for Rotsee (James & Barko, 1991a; 1991b; James et al., 1994; Monismith et al., 1990; Rogowski et al., 2019). James and Barko (1991b) showed that the percentage of days with differential cooling in Eau

Galle Reservoir (WI, USA) increased from 31 % in May to 95 % in August. However, these high values do not correspond to the percentage of occurrence of TSs, as differential cooling can happen without necessarily forming a cross-shore circulation. Pálmarsson and Schladow (2008) also found that differential cooling was rare in May and June in Clear Lake (CA, USA). Only 2 nights were cold enough to result in cooling-driven TSs. In winter, TS events are not frequent in Rotsee, but they have been reported for larger systems such as Lake Geneva in January (Fer et al., 2002a; Fer et al., 2002b; Thorpe et al., 1999). A different bathymetry modifies τ_t (Eq. (2.12)), which becomes shorter if h_p/h_{ML} is small or the slope is high, leading to a more frequent TS occurrence in winter. In addition, convective cooling stops earlier in small lakes like Rotsee that reach the temperature of maximum density before larger and deeper lakes.

2.4.3 Effects of the forcing parameters on cross-shore transport

The seasonality of the cross-shore transport induced by TSs can be examined using the scaling for the cross-shore velocity U_x (Eq. (2.9)) and the unit-width discharge q_x (Eq. (2.10)). The timescale τ_F is also a key parameter to assess the seasonality of the littoral region flushing (Eq. (2.11)). We showed that these scaling formulae reproduce the observed seasonality in Rotsee (Fig. 2.6). The weakening of the transport from summer to winter is explained by the decrease in B_0 by a factor of 10, which overcomes the increase in L_{ML} due to the deepening of the mixed layer (Fig. 2.4). However, τ_F remains shorter than the duration of the cooling phase (Fig. 2.8b), and the littoral region upslope of MT ($V_{lit} \approx 500 \text{ m}^2$) is entirely flushed by a single event (Sect. S2.3). The use of the constant length scale h_{lit} in Eq. (2.10) implies that the daily averaged TS thickness, $h_{TS,avg} = q_{avg}/U_{avg}$, should not show any seasonal variability. We observe the following in Rotsee: $h_{TS,avg}$ remains close to its yearly average of $1.8 \pm 0.2 \text{ m}$, without any seasonal trend.

We further compare our scaling for U_x , q_x , and τ_F with previous studies on buoyancy-driven flows. The velocity scale $U \sim (B_0 L)^{1/3}$ from Phillips (1966) is commonly used, with L defined as the horizontal length scale along which a lateral density gradient is set. This length scale varies with the experimental configuration and basin geometry (Tab. 2.2). In laboratory experiments with a localized buoyancy loss, L is the length along which the destabilizing buoyancy flux applies (Harashima & Watanabe, 1986; Sturman & Ivey, 1998; Sturman et al., 1996). For more realistic systems undergoing uniform surface cooling, L is the length of the littoral region, which can be defined as the plateau zone (Ulloa et al., 2022) or the region vertically mixed by convection (Wells & Sherman, 2001). In the first case, $L = L_p$ is a constant, whereas $L = L_{ML}$ varies with the stratification in the second case. We chose to use L_{ML} because it corresponds to the region affected by differential

Table 2.2 – Comparison of the transport scaling formula $q = c_q h (B_0 L)^{1/3}$ between different studies on sloping basins, where h is a vertical length scale, and L is a horizontal length scale. The different notations can be found in Fig. 2.1 and Tab. 2.1. The littoral region is based on the location of the discharge measurement, as in Fig. 2.1. L_{forc} is the length over which the destabilizing forcing B_0 applies.

Study	Geometry of the basin	Length of the littoral region L_{lit}	Horizontal length scale L	Vertical length scale h	Coefficient c_q
Harashima and Watanabe (1986)	Plateau/ Infinite slope	$L_{\text{lit}} < L_p$	$L = L_{\text{forc}} = L_p$	$h = h_p$	$0.13 \leq c_q \leq 0.33$
Sturman and Ivey (1998)	Plateau/ Slope	$L_{\text{lit}} = L_p$	$L = L_{\text{forc}} = L_p$	$h = h_p$	0.2
Ulloa et al. (2022)	Plateau/ Slope	$L_{\text{lit}} = L_p$	$L = L_p$	$h = h_p$	0.35
This study	Plateau/ Slope	$L_p < L_{\text{lit}} \leq L_{\text{ML}}$	$L = L_{\text{ML}}$	$h = h_{\text{lit}}$	0.34

cooling. We expect that a deeper mixed layer will increase the temperature difference ΔT between the littoral and pelagic regions, resulting in a higher velocity U_x . In Eqs. (2.10) and (2.11), the transport is expressed as a function of the velocity scale and the size of the littoral region of length L_{lit} and depth h_{lit} (Fig. 2.1). We defined the littoral region based on the location of MT because we measured the discharge out of this region. This definition of h_{lit} in Eq. (2.10) is consistent with the fact that q_x varies spatially, increasing with distance from the shore (Fer et al., 2002b). The vertical length scale h can also be chosen as the depth of the plateau (h_p) (Fer et al., 2002b; Sturman & Ivey, 1998; Ulloa et al., 2022; Wells & Sherman, 2001) to predict the discharge from the plateau region only. Despite these different choices of length scales, the coefficient $c_q \approx 0.34$ is close to other estimates from the literature (Tab. 2.2). Harashima and Watanabe (1986) found that c_q increases with the flux Reynolds number defined as $Re_f = B_0^{1/3} h_{\text{lit}}^2 / (L_{\text{ML}}^{2/3} \nu)$, where $\nu \approx 1.5 \times 10^{-6} \text{ m}^2 \text{ s}^{-1}$ is the kinematic viscosity of water. The empirical relationship $c_q \approx 0.43 - 1.67/Re_f^{1/2}$ was obtained for $Re_f > 50$. For the days where TSs are observed in Rotsee, Re_f varies from 250 in summer to 50 in winter, with an average value of ~ 140 which leads to $c_q \approx 0.29$, close to our estimate of $c_q \approx 0.34$.

2.4.4 Effects of the forcing parameters on the flushing period

The seasonality of the forcing parameters does not only affect the occurrence and magnitude of TSs but also the diurnal dynamics of the littoral flushing (Fig. 2.7). The initiation of TSs always occurs several hours after the beginning of the cooling phase. This delay is modulated by τ_{ini} and is consistent with previous studies reporting the formation of a TS at night (Fer et al., 2002b; James et al., 1994; Monismith et al., 1990; Pálmarsson & Schladow, 2008) or in the morning (Rogowski

et al., 2019; Sturman et al., 1999). τ_t is a good estimate of the initiation period when the water column is initially mixed ($\tau_{\text{mix}} = 0$). In summer and on warm autumn days, however, the initiation of TSs occurs later than predicted by τ_t , due to the initial stratification at the beginning of the cooling phase ($\tau_{\text{mix}} \neq 0$). This leads to a delay in the increase in q_x and F_G (Figs. 2.7a and 2.7c). In autumn, TS events lasting for more than 24 h lead to monthly averaged $q_x > 0$ before the starting time predicted by τ_t (Figs. 2.7e and 2.7g). In winter, $\tau_t \rightarrow 24$ h implies that the rare TS events are all characterized by a continuous flow (Fig. 2.7i), without any diurnal cycle of flushing.

When a diurnal cycle is present in summer and autumn, the flushing period ends several hours after the beginning of the heating phase (Figs. 2.3 and 2.7). This inertia has already been reported by Monismith et al. (1990), who observed TSs until the mid-afternoon, despite the opposite pressure gradients due to differential heating. In addition to the delay between the end of the cooling and the end of the flow, we also showed that a peak in flushing occurred a few hours after the beginning of the heating phase (Fig. 2.3). The time of maximal flushing is shifted later in the day from summer to winter, as the heating phase starts later (Fig. 2.7). The maximal flushing seems related to the transition from the cooling phase to the heating phase. This finding suggests that convective plumes eroding the flow control the weak initial transport during the cooling phase. A weakening of convection reduces this vertical mixing and finally enables the flushing to reach its maximum intensity. Further investigations are required to better understand this process.

2.4.5 Practical recommendations to predict and measure thermal siphons in other lakes

Rotsee is an ideal field-scale laboratory to investigate TSs, due to wind sheltering and its elongated shape minimizing complex recirculation. To assess the TS seasonality in other lakes, long-term velocity and temperature measurements in the sloping region are required. The developed algorithm to detect TS events (Sect. 2.2.4) and calculate the cross-shore transport (Sect. 2.2.5) fulfilled our requirements but remained lake-specific. The limitations of the algorithm are discussed in more detail in Sect. S2.4. The general structure of the algorithm (Sect. 2.2.4) can serve as a basis for detecting TSs in lakes, by adapting the lake-specific criteria to other systems. The 2D framework of TSs requires specific validation in more complex nearshore systems and large lakes, where the topography, large-scale circulation, and Coriolis may also affect the TS dynamics (Fer et al., 2002b). In these systems, the alongshore velocity component of TSs must be considered in the cross-shore transport analysis. Further development is needed to build a more robust algorithm with lake-independent physically based criteria.

The effects of a different bathymetry can be predicted from the scaling discussed in the previous sections. A shallower nearshore plateau region or a steeper sloping region would decrease the transition timescale τ_t (Eq. (2.12)), causing the initiation of TSs to happen earlier and more often. Higher slopes would also decrease the length of the mixed region L_{ML} and reduce the horizontal velocity of TSs (Eq. (2.9)). Past observations of TSs have reported horizontal velocities ranging from $\sim 0.1 \text{ cm s}^{-1}$ (James & Barko, 1991a; 1991b) to $\sim 10 \text{ cm s}^{-1}$ (Fer et al., 2002b; Roget et al., 1993), with $U_x \sim 1 \text{ cm s}^{-1}$ in most cases (Monismith et al., 1990; Pálmarsson & Schladow, 2008; Rogowski et al., 2019; Sturman et al., 1999). The cross-shore transport q_x and flushing timescale τ_F are strongly dependent on the size and depth of the littoral region considered (Eqs. 2.10, 2.11). A deeper littoral region (larger h_{lit}) would lead to a stronger discharge, and a longer littoral region (larger L_{lit}) would take more time to flush. Values of TS thickness and discharge can be 1 order of magnitude larger in lakes deeper than Rotsee (Fer et al., 2002a; Rogowski et al., 2019; Thorpe et al., 1999). The effects of more complex bathymetries, departing from our 2D framework, could be further investigated with 3D numerical simulations.

Information on lake bathymetry and thermal structure are needed to predict the occurrence ($\tau_{ini} < \tau_c$) and intensity of TSs (U_x, q_x, τ_F) under specific forcing. This approach does not consider wind effects, which deserve further investigation. Windier conditions would hinder TSs by locally enhancing and reducing the cross-shore transport. In this case, the scaling formulae (Eqs. 2.9–2.11) should be modified to take wind shear into account. The littoral region would also be mixed faster under windy conditions, and the effects of wind mixing on τ_{mix} should be included in Eq. (2.15). These questions could be addressed by performing numerical simulations with varying wind speed.

The TS seasonality may evolve in a changing climate, which also needs to be investigated. Changes in heat fluxes, summer stratification, and surface temperature would affect both the intensity (B_0) and occurrence (τ_{ini}) of TSs.

2.5 Conclusions

The flushing of the littoral region by cross-shore flows increases the exchange between nearshore and pelagic waters. In this study, we investigated one of the processes that enhance the renewal of littoral waters, the so-called thermal siphon (TS) driven by differential cooling. From a 1-year-long monitoring of TSs in a small, temperate, wind-sheltered lake, we quantified the seasonality of the cross-shore transport induced by TSs. This seasonality is related to the intensity of surface cooling

(surface buoyancy flux B_0) and the lake stratification (mixed-layer depth h_{ML}). Three aspects of the TS seasonality are highlighted. First, TSs are a recurring process from late summer to winter (when $\tau_c > \tau_{ini}$), occurring on $\sim 80\%$ of autumn days. Second, the seasonal changes in the TS-induced transport are well reproduced by the scaling $U_{avg} \sim 0.33(B_0 L_{ML})^{1/3}$, $q_{avg} \sim 0.34(B_0 L_{ML})^{1/3} h_{lit}$ and $\tau_F = V_{lit}/q_{avg} \sim 2.99 L_{lit}/(B_0 L_{ML})^{1/3}$, where L_{ML} is the length of the region mixed by convection, and $V_{lit} = L_{lit} h_{lit}$ is the unit-width volume of the littoral region. This study provides a field validation of this laboratory and theoretically based scaling. Third, the diurnal dynamics of the flushing follow the seasonal changes in the cooling and heating phases, by evolving from a well-defined diurnal cycle in summer to a more continuous flow in winter.

Our results demonstrate that TSs significantly contribute to the flushing of the nearshore waters. This process occurs frequently during the cooling season ($> 50\%$ of the time), each time flushing the entire littoral region. We stress that this buoyancy-driven transport is, perhaps counter-intuitively, stronger in summer and in the morning. Such a timing has implications for the transport of dissolved compounds, with, for instance, maximal exchange between littoral and pelagic waters at a time of high primary production (summer and daytime). Overall, this study provides a solid framework to integrate the role of TSs in the lake ecosystem dynamics.

Code and data availability

The data (raw and processed data as well as figures) and the scripts used for all the analyses are available for download from the Eawag Research Data Institutional Collection (<https://doi.org/10.25678/00057K>, Doda et al., 2021).

Acknowledgements

We would like to sincerely thank our technician, Michael Plüss, for organizing the field campaigns and helping to set up and maintain the different instruments. We are grateful to the Canton of Luzern, the municipalities of Luzern (Lucerne) and Ebikon, the Rowing Centre Lucerne-Rotsee, the Quartierverein Maihof and Pro Natura associations, and the Rotsee- Badi for their support of our measurements. We are also indebted to Bieito Fernández-Castro for his help with estimating the heat fluxes. Moreover, we acknowledge Love Råman Vinnå, Edgar Hédouin, Josquin Dami, and Alois Zwyssig for their assistance in the field. Discussions with Mathew Wells, Martin Schmid, Oscar Sepúlveda Steiner, and Love Råman Vinnå helped to improve the data analysis and the

quality of the paper. The meteorological data from the Lucerne weather station were provided by MeteoSwiss, the Swiss Federal Office of Meteorology and Climatology. We gratefully acknowledge the three anonymous reviewers for their helpful comments and suggestions.

Financial support

This study was financed by the Swiss National Science Foundation (“Buoyancy driven nearshore transport in lakes” project; HYPolimnetic THERmal SiphonS, HYPOTHESIS, grant no. 175919).

There is no competing interest for any author.

References

- Adams, E., & Wells, S. A. (1984). Field measurements on side arms of Lake Anna, Va. *Journal of Hydraulic Engineering*, 110(6), 773–793. [https://doi.org/10.1061/\(ASCE\)0733-9429\(1984\)110:6\(773\)](https://doi.org/10.1061/(ASCE)0733-9429(1984)110:6(773))
- Ambrosetti, W., Barbanti, L., & Carrara, E. A. (2010). Mechanisms of hypolimnion erosion in a deep lake (Lago Maggiore, N. Italy). *Journal of Limnology*, 69(1), 3–14. <https://doi.org/10.4081/jlimnol.2010.3>
- Bouffard, D., & Wüest, A. (2019). Convection in lakes. *Annual Review of Fluid Mechanics*, 51(1), 189–215. <https://doi.org/10.1146/annurev-fluid-010518-040506>
- Brink, K. (2016). Cross-shelf exchange. *Annual Review of Marine Science*, 8(1), 59–78. <https://doi.org/10.1146/annurev-marine-010814-015717>
- Chen, C.-T. A., & Millero, F. J. (1986). Precise thermodynamic properties for natural waters covering only the limnological range. *Limnology and Oceanography*, 31(3), 657–662. <https://doi.org/10.4319/lo.1986.31.3.0657>
- Cyr, H. (2017). Winds and the distribution of nearshore phytoplankton in a stratified lake. *Water Research*, 122, 114–127. <https://doi.org/10.1016/j.watres.2017.05.066>
- Doda, T., Ramón, C. L., Ulloa, H. N., Wüest, A., & Bouffard, D. (2021). Data for: Seasonality of density currents induced by differential cooling. <https://doi.org/10.25678/00057K>
- Doda, T., Ramón, C. L., Ulloa, H. N., Wüest, A., & Bouffard, D. (2022). Seasonality of density currents induced by differential cooling. *Hydrology and Earth System Sciences*, 26(2), 331–353. <https://doi.org/10.5194/hess-26-331-2022>

- Eccles, D. H. (1974). An outline of the physical limnology of Lake Malawi (Lake Nyasa). *Limnology and Oceanography*, 19(5), 730–742. <https://doi.org/10.4319/lo.1974.19.5.0730>
- Effler, S. W., Prestigiacomo, A. R., Matthews, D. A., Gelda, R. K., Peng, F., Cowen, E. A., & Schweitzer, S. A. (2010). Tripton, trophic state metrics, and near-shore versus pelagic zone responses to external loads in Cayuga Lake, New York, U.S.A. *Fundamental and Applied Limnology*, 178(1), 1–15. <https://doi.org/10.1127/1863-9135/2010/0178-0001>
- Fer, I., Lemmin, U., & Thorpe, S. A. (2002a). Contribution of entrainment and vertical plumes to the winter cascading of cold shelf waters in a deep lake. *Limnology and Oceanography*, 47(2), 576–580. <https://doi.org/10.4319/lo.2002.47.2.0576>
- Fer, I., Lemmin, U., & Thorpe, S. A. (2002b). Winter cascading of cold water in Lake Geneva. *Journal of Geophysical Research*, 107(C6), 3060. <https://doi.org/10.1029/2001JC000828>
- Fink, G., Schmid, M., Wahl, B., Wolf, T., & Wüest, A. (2014). Heat flux modifications related to climate-induced warming of large European lakes. *Water Resources Research*, 50(3), 2072–2085. <https://doi.org/10.1002/2013WR014448>
- Finnigan, T. D., & Ivey, G. N. (1999). Submaximal exchange between a convectively forced basin and a large reservoir. *Journal of Fluid Mechanics*, 378, 357–378. <https://doi.org/10.1017/S0022112098003437>
- Forel, F. A. (1895). *Le Léman - Monographie Limnologique. Tome II*. Editions Rouge. <https://doi.org/10.5962/bhl.title.124608>
- Forrest, A. L., Laval, B. E., Pieters, R., & Lim, D. S. S. (2008). Convectively driven transport in temperate lakes. *Limnology and Oceanography*, 53, 2321–2332. https://doi.org/10.4319/lo.2008.53.5_part_2.2321
- Gray, E., Mackay, E. B., Elliott, J. A., Folkard, A. M., & Jones, I. D. (2020). Wide-spread inconsistency in estimation of lake mixed depth impacts interpretation of limnological processes. *Water Research*, 168, 115136. <https://doi.org/10.1016/j.watres.2019.115136>
- Harashima, A., & Watanabe, M. (1986). Laboratory experiments on the steady gravitational circulation excited by cooling of the water surface. *Journal of Geophysical Research*, 91(C11), 13056–13064. <https://doi.org/10.1029/JC091iC11p13056>
- Hofmann, H. (2013). Spatiotemporal distribution patterns of dissolved methane in lakes: how accurate are the current estimations of the diffusive flux path? *Geophysical Research Letters*, 40(11), 2779–2784. <https://doi.org/10.1002/grl.50453>
- Horsch, G. M., & Stefan, H. G. (1988). Convective circulation in littoral water due to surface cooling. *Limnology and Oceanography*, 33(5), 1068–1083. <https://doi.org/10.4319/lo.1988.33.5.1068>
- Imberger, J., & Patterson, J. C. (1989). Physical Limnology (J. W. Hutchinson & T. Y. Wu, Eds.). *Advances in Applied Mechanics*, 27, 303–475. [https://doi.org/10.1016/S0065-2156\(08\)70199-](https://doi.org/10.1016/S0065-2156(08)70199-)

- James, W. F., & Barko, J. W. (1991a). Estimation of phosphorus exchange between littoral and pelagic zones during nighttime convective circulation. *Limnology and Oceanography*, 36(1), 179–187. <https://doi.org/10.4319/lo.1991.36.1.0179>
- James, W. F., & Barko, J. W. (1991b). Littoral-pelagic phosphorus dynamics during nighttime convective circulation. *Limnology and Oceanography*, 36(5), 949–960. <https://doi.org/10.4319/lo.1991.36.5.0949>
- James, W. F., Barko, J. W., & Eakin, H. L. (1994). Convective water exchanges during differential cooling and heating: implications for dissolved constituent transport. *Hydrobiologia*, 294(2), 167–176. <https://doi.org/10.1007/BF00016857>
- Lövstedt, C. B., & Bengtsson, L. (2008). Density-driven current between reed belts and open water in a shallow lake. *Water Resources Research*, 44(10), W10413. <https://doi.org/10.1029/2008WR006949>
- MacIntyre, S., & Melack, J. M. (1995). Vertical and horizontal transport in lakes: linking littoral, benthic, and pelagic habitats. *Journal of the North American Benthological Society*, 14(4), 599–615. <https://doi.org/10.2307/1467544>
- MacIntyre, S., Romero, J. R., & Kling, G. W. (2002). Spatial-temporal variability in surface layer deepening and lateral advection in an embayment of Lake Victoria, East Africa. *Limnology and Oceanography*, 47(3), 656–671. <https://doi.org/10.4319/lo.2002.47.3.0656>
- McJannet, D., Webster, I., & Cook, F. (2012). An area-dependent wind function for estimating open water evaporation using land-based meteorological data. *Environmental Modelling & Software*, 31, 76–83. <https://doi.org/10.1016/j.envsoft.2011.11.017>
- Meyers, T., & Dale, R. (1983). Predicting daily insolation with hourly cloud height and coverage. *Journal of Climate and Applied Meteorology*, 22(4), 537–545. [https://doi.org/10.1175/1520-0450\(1983\)022<0537:PDIWHC>2.0.CO;2](https://doi.org/10.1175/1520-0450(1983)022<0537:PDIWHC>2.0.CO;2)
- Monismith, S. G., Imberger, J., & Morison, M. L. (1990). Convective motions in the sidearm of a small reservoir. *Limnology and Oceanography*, 35(8), 1676–1702. <https://doi.org/10.4319/lo.1990.35.8.1676>
- Mortimer, C. H. (1952). Water movements in lakes during summer stratification; evidence from the distribution of temperature in Windermere. *Philosophical Transactions of the Royal Society of London. Series B, Biological Sciences*, 236(635), 355–398. <https://doi.org/10.1098/rstb.1952.0005>
- Pálmarrsson, S. Ó., & Schladow, S. G. (2008). Exchange flow in a shallow lake embayment. *Ecological Applications*, 18(8), A89–A106. <https://doi.org/10.1890/06-1618.1>
- Peeters, F., Finger, D., Hofer, M., Brennwald, M., Livingstone, D. M., & Kipfer, R. (2003). Deep-water renewal in Lake Issyk-Kul driven by differential cooling. *Limnology and Oceanography*, 48(4), 1419–1431. <https://doi.org/10.4319/lo.2003.48.4.1419>

- Phillips, O. (1966). On turbulent convection currents and the circulation of the Red Sea. *Deep Sea Research and Oceanographic Abstracts*, 13(6), 1149–1160. [https://doi.org/10.1016/0011-7471\(66\)90706-6](https://doi.org/10.1016/0011-7471(66)90706-6)
- Rao, Y. R., & Schwab, D. J. (2007). Transport and mixing between the coastal and offshore waters in the Great Lakes: a review. *Journal of Great Lakes Research*, 33(1), 202–218. [https://doi.org/10.3394/0380-1330\(2007\)33\[202:TAMBTC\]2.0.CO;2](https://doi.org/10.3394/0380-1330(2007)33[202:TAMBTC]2.0.CO;2)
- Roget, E., Colomer, J., Casamitjana, X., & Llebot, J. E. (1993). Bottom currents induced by baroclinic forcing in Lake Banyoles (Spain). *Aquatic Sciences*, 55(3), 206–227. <https://doi.org/10.1007/BF00877450>
- Rogowski, P., Merrifield, S., Ding, L., Terrill, E., & Gesiriech, G. (2019). Robotic mapping of mixing and dispersion of augmented surface water in a drought frequent reservoir. *Limnology and Oceanography: Methods*, 17(9), 475–489. <https://doi.org/10.1002/lom3.10326>
- Rueda, F., Moreno-Ostos, E., & Cruz-Pizarro, L. (2007). Spatial and temporal scales of transport during the cooling phase of the ice-free period in a small high-mountain lake. *Aquatic Sciences*, 69(1), 115–128. <https://doi.org/10.1007/s00027-006-0823-8>
- Schlatter, J. W., Wüest, A., & Imboden, D. M. (1997). Hypolimnetic density currents traced by sulphur hexafluoride (SF₆). *Aquatic Sciences*, 59(3), 225–242. <https://doi.org/10.1007/BF02523275>
- Sturman, J. J., & Ivey, G. N. (1998). Unsteady convective exchange flows in cavities. *Journal of Fluid Mechanics*, 368, 127–153. <https://doi.org/10.1017/S002211209800175X>
- Sturman, J. J., Ivey, G. N., & Taylor, J. R. (1996). Convection in a long box driven by heating and cooling on the horizontal boundaries. *Journal of Fluid Mechanics*, 310, 61–87. <https://doi.org/10.1017/S0022112096001735>
- Sturman, J. J., Oldham, C. E., & Ivey, G. N. (1999). Steady convective exchange flows down slopes. *Aquatic Sciences*, 61(3), 260–278. <https://doi.org/10.1007/s000270050065>
- Talling, J. F. (1963). Origin of stratification in an African Rift lake. *Limnology and Oceanography*, 8(1), 68–78. <https://doi.org/10.4319/lo.1963.8.1.0068>
- Thorpe, S. A., Lemmin, U., Perrinjaquet, C., & Fer, I. (1999). Observations of the thermal structure of a lake using a submarine. *Limnology and Oceanography*, 44(6), 1575–1582. <https://doi.org/10.4319/lo.1999.44.6.1575>
- Ulloa, H. N., Ramón, C. L., Doda, T., Wüest, A., & Bouffard, D. (2022). Development of overturning circulation in sloping waterbodies due to surface cooling. *Journal of Fluid Mechanics*, 930, A18. <https://doi.org/10.1017/jfm.2021.883>
- Verburg, P., Antenucci, J. P., & Hecky, R. E. (2011). Differential cooling drives large-scale convective circulation in Lake Tanganyika. *Limnology and Oceanography*, 56(3), 910–926. <https://doi.org/10.4319/lo.2011.56.3.0910>

- Wedderburn, E. M. (1907). The temperature of the fresh-water Lochs of Scotland, with special reference to Loch Ness. *Transactions of the Royal Society of Edinburgh*, 45(2), 407–489. <https://doi.org/10.1017/S0080456800022791>
- Wells, M. G., & Sherman, B. (2001). Stratification produced by surface cooling in lakes with significant shallow regions. *Limnology and Oceanography*, 46(7), 1747–1759. <https://doi.org/10.4319/lo.2001.46.7.1747>
- Wetzel, R. G. (2001). *Limnology: Lake and River Ecosystems* (3rd ed.). Academic Press.
- Woodward, B. L., Marti, C. L., Imberger, J., Hipsey, M. R., & Oldham, C. E. (2017). Wind and buoyancy driven horizontal exchange in shallow embayments of a tropical reservoir: Lake Argyle, Western Australia. *Limnology and Oceanography*, 62(4), 1636–1657. <https://doi.org/10.1002/lno.10522>
- Wüest, A., & Lorke, A. (2003). Small-scale hydrodynamics in lakes. *Annual Review of Fluid Mechanics*, 35(1), 373–412. <https://doi.org/10.1146/annurev.fluid.35.101101.161220>
- Zilitinkevič, S. S. (1991). *Turbulent Penetrative Convection* (B. Henderson-Sellers, Ed.). Avebury.
- Zimmermann, M., Mayr, M. J., Bürgmann, H., Eugster, W., Steinsberger, T., Wehrli, B., Brand, A., & Bouffard, D. (2021). Microbial methane oxidation efficiency and robustness during lake overturn. *Limnology and Oceanography Letters*, 6(6), 320–328. <https://doi.org/10.1002/lol2.10209>



Supplementary Information for Chapter 2

S2.1 Instrumentation

Supplementary Information for Chapter 2

Table S2.1 – Specifications and setup of the sensors from the two moorings and the meteorological station. For the ADCP, only the complete days of measurements used for the transport estimates are taken into account in the measurement periods.

Sensors	Accuracy	Resolution	Number	Setup	Periods of measurements
Thermistor array at MB					
Vemco Minilog II-T (temperature)	0.1 °C	0.01 °C	14	Sampling interval [s]: 120;	13.03.19–24.04.19
				Approximate depths [m]:	07.06.19–02.07.19
				0.2, 3, 4, 5, 6, 7, 8, 9, 10, 11,	16.07.29–03.09.19
				12, 13, 14, 15	05.09.19–18.10.19
RBR Duet TD (temperature, pressure)	T: 0.002 °C; P: 0.05 %	T: 5×10 ⁻⁵ °C; P: 0.001 %	1	Sampling interval [s]: 1;	24.10.19–16.12.19
				Approximate depth [m]:	20.12.19–29.01.20
				15	12.02.20–05.06.20
Thermistor array at MT					
Vemco Minilog II-T (temperature)	0.1 °C	0.01 °C	1	Sampling interval [s]: 120;	Same periods than above
				Approximate depth [m]: 0.2	
RBR TR-1050 (temperature)	0.002 °C	5×10 ⁻⁵ °C	8	Sampling interval [s]: 10;	
				Approximate depths [m]:	
				2.4, 2.7, 2.9, 3.2, 3.4, 3.7, 3.9, 4.2	
RBR Duet TD (temperature, pressure)	T: 0.002 °C; P: 0.05 %	T: 5×10 ⁻⁵ °C; P: 0.001 %	1	Sampling interval [s]: 1;	
				Approximate depth [m]: 3.4	
ADCP at MT					
Nortek Aquadopp Profiler 1 MHz (velocity)	1 %	0.1 mm s ⁻¹	1		13.03.19–23.04.19
				Cell size [m]: 0.05;	07.06.19–01.07.19
				Burst interval [s]: 900;	16.07.29–02.09.19
				Sampling interval [s]: 0.5;	05.09.19–16.10.19
				Number of samples per burst: 512	24.10.19–03.12.19
					21.12.19–07.01.20
Campbell meteorostation WxPRO					
Young Wind Sentry (wind speed and direction)	Speed: 0.5 m s ⁻¹ ;	Speed: 0.001 m s ⁻¹ ;	1	Sampling interval [s]: 600;	14.09.19–05.06.20
	Direction: 5°	Direction: 0.1°		Height [m]: 3	
Sensirion SHT75 (air temperature and relative humidity)	T: 0.4 °C;	T: 0.01 °C;	1	Sampling interval [s]: 600;	
	RH: 4 %	RH: 0.03 %		Height [m]: 2	
Setraceram 278 (barometric pressure)	1 hPa	0.01 hPa	1	Sampling interval [s]: 600;	
				Height [m]: 2	
Apogee Instruments SP- 110-SS pyranometer (solar radiation)	5 %	1 W m ⁻²	1	Sampling interval [s]: 600;	
				Height [m]: 3	

S2.2 Diurnal variability in the occurrence and duration of thermal siphons

In addition to the seasonality, TSs also vary between days. A change in forcing conditions ($B_{0,\text{net}}$) between days may enhance or prevent TS formation, by modifying the occurrence condition $\tau_{\text{ini}} < \tau_c$ at a short timescale. We average the net buoyancy flux over 48 h ($B_{0,\text{net}}^{2d}$), for each 24 h subset starting at 17:00 UTC. $B_{0,\text{net}}^{2d}$ is the average of $B_{0,\text{net}}$ between 00:00 UTC on the first day of the 24 h subset and 23:59 UTC on the following day. This quantity includes the effects of the forcing on (1) the initial stratification, which affects τ_{ini} (day preceding the TS event), and (2) the duration of the cooling phase τ_c (following day). We compare the values of $B_{0,\text{net}}^{2d}$ between days with and without TSs (Fig. S2.1). Days with TSs are characterized by higher $B_{0,\text{net}}^{2d}$ than days without TSs, which is confirmed by a t test at a 5 % significance level, from August to December. The variability in the forcing conditions between days also affects the flushing duration of TSs (Fig. S2.2).

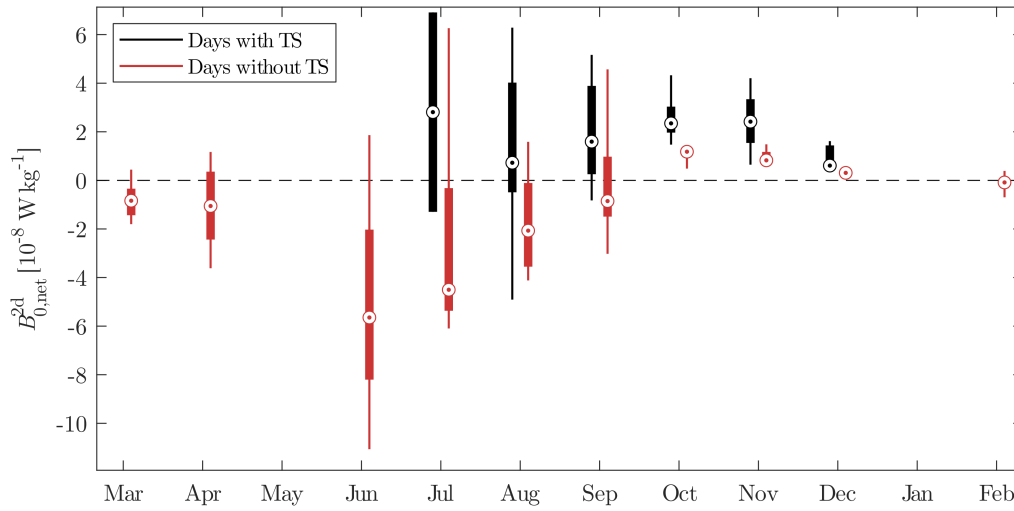


Figure S2.1 – Box plots of the 2 d averaged net surface buoyancy flux for each month, depending on the occurrence of TS events.

S2.3 Seasonality of the flushing of the littoral region

The unit-width volume flushed by each TS event is calculated by integrating the discharge q_x over the flushing period (Eq. (2.5)). We estimate the daily averaged flushed volume $V_{\text{flush},\text{day}}$ and the averaged flushed volume of TS events $V_{\text{flush},\text{TS}}$ by dividing the total volume of water flushed every month by the number of days with measurements and by the number of days with TSs,

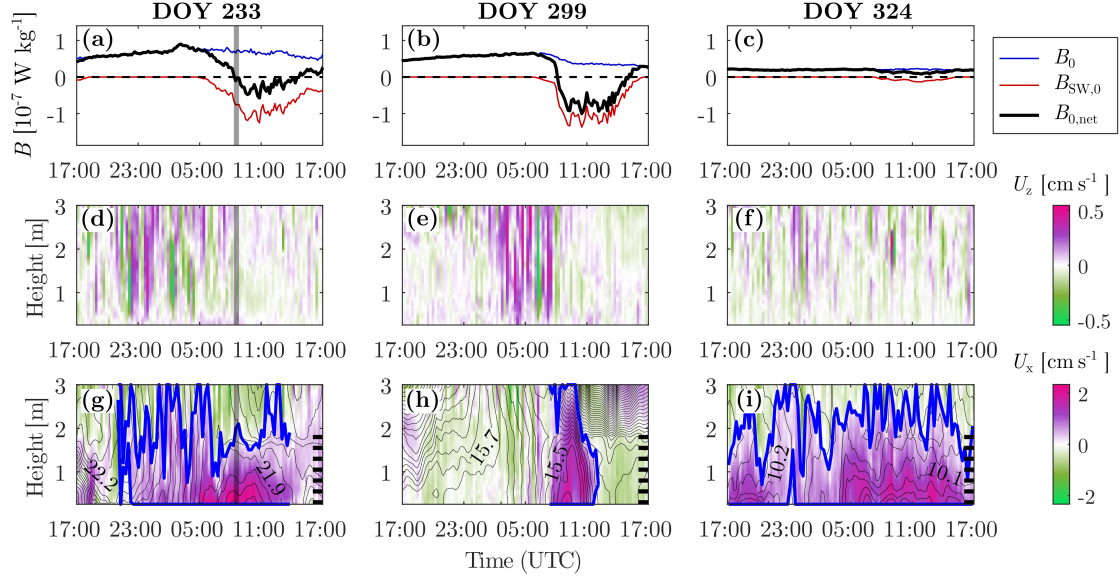


Figure S2.2 – Three examples of TS events, with (a–c) buoyancy fluxes, (d–f) vertical velocity, and (g–i) cross-shore velocity, as in Fig. 2.3. (a, d, g) A long TS event on 21–22 August 2019 due to short heating phases on both days. (b, e, h) A short TS event on 26–27 October 2019 due to strong heating on both days (re-stratification). (c, f, i) Continuous flushing on 20–21 November 2019 due to continuous net cooling. See the caption of Fig. 2.3 for more details about each panel. The gray shaded area in panels (a), (d), and (g) indicates the time of the CTD transect shown in Fig. 2.1.

respectively. The volume $V_{\text{flush,day}}$ includes the effect of the occurrence of TS events on the daily flushing, whereas $V_{\text{flush,TS}}$ only depends on the intensity and duration of a TS event. We express both flushed volumes as fractions of the littoral region of volume V_{lit} (Fig. S2.3). The seasonal trend of $V_{\text{flush,day}}$ is similar to the TS occurrence (Fig. 2.5), with an increase in flushing from July to November (Fig. S2.3a). This indicates that the increase in the TS occurrence from summer to autumn overcomes the weakening of the transport over the same period. The flushed volume of TS events does not vary significantly with season (Fig. S2.3b). A single TS event flushes the littoral region more than once on average. Overall, the TS occurrence is the primary factor controlling the seasonality of the littoral flushing in Rotsee.

S2.4 Identification of thermal siphons by the algorithm

The developed algorithm used to detect TS events (Sect. 2.2.4) and calculate the cross-shore transport (Sect. 2.2.5) aimed at automatizing the identification of TSs and, thus, at limiting subjective bias in the characterization of the process. We manually assessed the performance of the algorithm over different days. We further tested the validity of the identified TS events with the

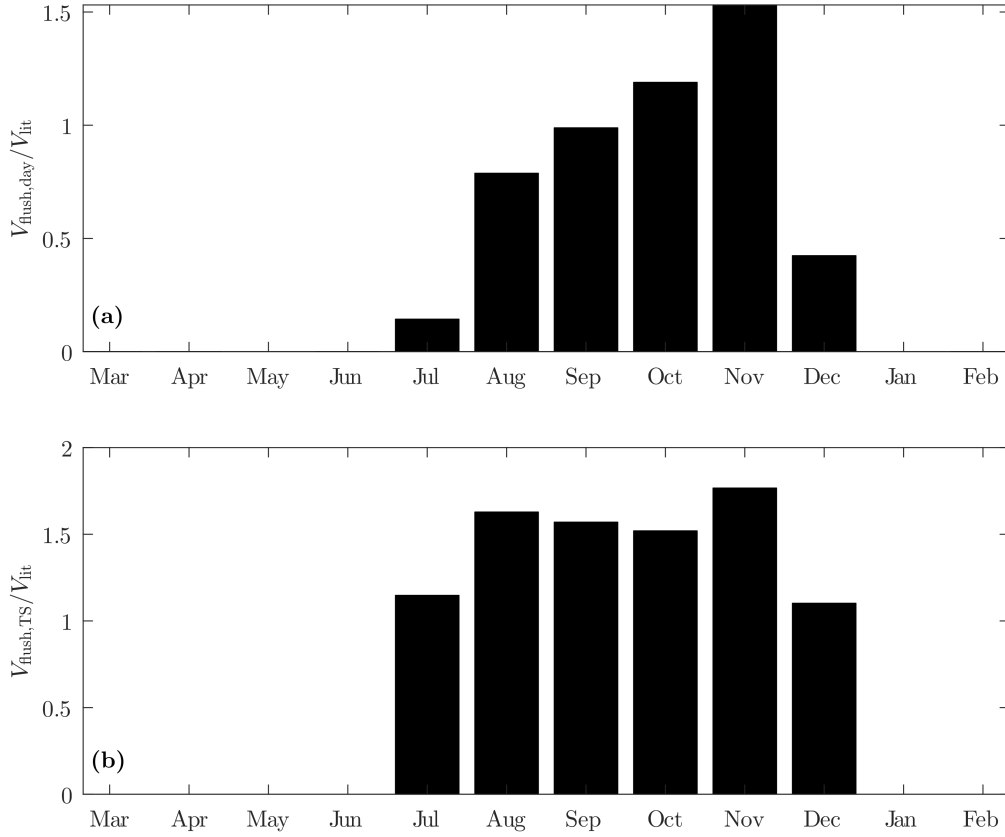


Figure S2.3 – Fraction of the littoral region flushed by TSs in 1 d for each month. Months with less than 10 d of measurements have been removed as in Fig. 2.5 (May 2019 and January 2020). **(a)** The daily averaged flushed fraction including all days with measurements. **(b)** The daily averaged flushed fraction for days with TSs only.

fact that a cross-shore transport resulting from a TS should be associated with a decrease in water temperature (Fig. 2.1). We calculated the correlation $r(U_x, T)$ between the cross-shore velocity U_x and the temperature T from the thermistor array at MT, at each depth and during the cross-shore flow events. The negative correlation during 93 % of the identified TS events ($r(U_x, T) < -0.48$ according to the 95 % confidence interval from a t test) and the lack of clear negative correlation (at a 5 % significance level) during the other days justified the skills of the detection algorithm. The general structure of the algorithm can be used in other systems. However, several criteria are lake-specific and must be adapted to the system of interest. We discuss the limitations of the algorithm below and provide suggestions for improvement.

The definition of a significant cross-shore flow by the algorithm (i.e., $\overline{U_x} > 0.5 \text{ cm s}^{-1}$ or at least 2 h) is lake-specific. This criterion is based on typical examples of TSs in Rotsee, where $\overline{U_x}$ is above

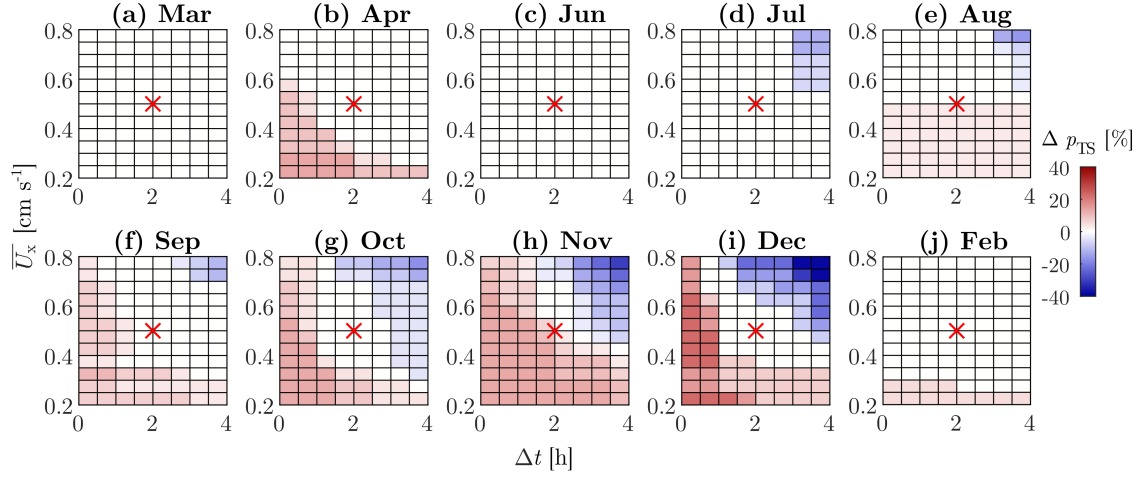


Figure S2.4 – Sensitivity analysis for the criteria used to define cross-shore flows. The effects of modifying the depth-averaged cross-shore velocity $\overline{U_x}$ and the averaging duration Δt are shown as changes in the percentage of occurrence of TSs (p_{TS}) for each month. Δp_{TS} is the percentage difference with respect to the occurrence shown in Fig. 2.5, obtained with $\overline{U_x} = 0.5 \text{ cm s}^{-1}$ and $\Delta t = 2 \text{ h}$ (reference point shown by the red cross).

0.5 cm s^{-1} over most of the flushing period. Theoretical estimates of the period between the onset time and the end of the cooling phase (e.g., $\tau_c - \tau_{ini} \approx 10 \text{ h}$ in autumn) show that most TS events last more than 2 h and justify the chosen threshold for the duration. From a sensitivity analysis (Fig. S2.4), we notice that the TS occurrence does not change significantly if the duration threshold is increased by a few hours. Shorter cross-shore flow events must be discarded because they are not consistent with the gravitational adjustment triggered by differential cooling; they could be wind-driven or result from free surface convection. In Rotsee, cross-shore flows driven by internal waves are expected to be short and to be discarded by the algorithm ($T_{V1H1}/2 \approx 2.5 \text{ h}$ in summer, where T_{V1H1} is the period of V1H1 internal waves). Other types of data could be included to detect TSs, such as lateral temperature gradients, near-surface velocity (return flow), or vertical velocity (convective plumes). Using other techniques, like machine learning algorithms, could also be a useful approach to better identify TS events.

The filter used to discard days with wind-driven circulation is based on the criterion $|L_{MO}|/h_{ML} = \kappa^{-1}|u_*/w_*|^3 > 0.5$, where $\kappa = 0.41$ is the von Kármán constant, and u_* the friction velocity. The ratio u_*/w_* expresses the relative importance of wind shear compared with convection. The threshold value of 0.5 was successfully tested on wind-driven circulation events observed in Rotsee in winter. This filter discards the strongest wind events, but cross-shore flows with $|L_{MO}|/h_{ML} < 0.5$ can still be affected by a wind peak during the flushing period (e.g., interaction between wind and a TS). Being more conservative and decreasing the threshold value from 0.5 to 0.1 would discard TS

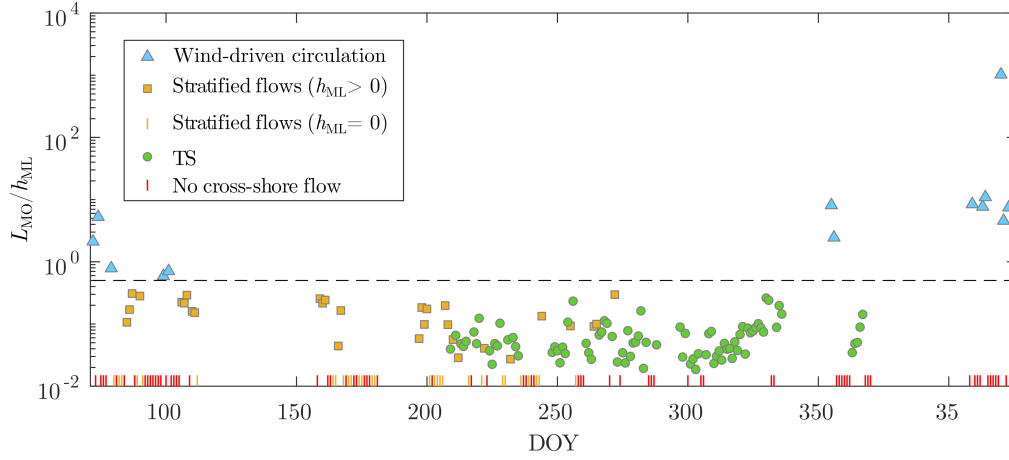


Figure S2.5 – Filtering of the 227 d analyzed, shown as a time series of L_{MO}/h_{ML} from March 2019 to March 2020. Days without a significant cross-shore flow or without a mixed layer are depicted as bottom ticks. Stratified flows are cross-shore flows without complete mixing at MT. The wind-driven circulation threshold $L_{MO}/h_{ML} = 0.5$ is shown by the horizontal dashed line.

events mainly in December (when w_* is low) but would not significantly modify the TS occurrence during the other periods (Fig. S2.5). Additional filters could be implemented to distinguish between TSs and wind-driven cross-shore flows, based, for example, on high-resolution vertical velocity measurements, observed oscillations of the thermocline (e.g., wavelet analysis), estimates of the period of internal waves, and identification of upwelling events (e.g., Wedderburn and Lake numbers) (Imberger & Patterson, 1989).

By discarding days with stratified conditions at MT, the second filter does not consider TSs that intrude before reaching MT and appear as interflows. Thus, TS occurrence in summer is underestimated. In Fig. 2.5, the higher percentage of occurrence of stratified flows in July (81 %) compared with spring (around 40 %–50 %) suggests a possible contribution of intruding TSs. From visual inspection of each event, we estimated that intruding TSs could represent almost half of the stratified flows in July. Including downslope TSs only was relevant, as the transport properties of interflows can be different from downslope gravity currents, for which the scaling formulae were derived. In addition, intruding TS events could be confounded with other baroclinic flows, and further filtering steps would have been required to detect them correctly.

The transport quantities of TSs are averaged over the flushing period (Sect. 2.2.5). The onset of the flushing is challenging to define because of the interaction between TSs and convective plumes (Fig. 2.3c). The cross-shore velocity field can be very variable over time, with vertical fluctuations of the region with positive U_x (Fig. 2.3d). We decided to include only the period over which

the region with positive U_x remained at the same depths (i.e., the limits of the flushing period correspond either to vertical displacements of the region of positive U_x or to $U_x < 0$ at all depths). This approach might sometimes include only a part of the TS event in the transport calculations. Daily averaged velocities should not be affected. The average thickness and discharge, however, vary between days depending whether the vertical oscillations of the TS interface are included or not. The latter is a possible reason for the larger variability observed for q_{avg} and τ_F (Fig. 2.6).

References

- Imberger, J., & Patterson, J. C. (1989). Physical Limnology (J. W. Hutchinson & T. Y. Wu, Eds.). *Advances in Applied Mechanics*, 27, 303–475. [https://doi.org/10.1016/S0065-2156\(08\)70199-](https://doi.org/10.1016/S0065-2156(08)70199-6)

Chapter 3

Penetrative convection modifies the dynamics of downslope gravity currents

Tomy Doda^{1,2}, Hugo N. Ulloa³, Cintia L. Ramón⁴, Alfred Wüest^{1,2}, Damien Bouffard¹

¹Eawag, Swiss Federal Institute of Aquatic Science and Technology, Department of Surface Waters – Research and Management, Kastanienbaum, Switzerland

²Limnology Center, École Polytechnique Fédérale de Lausanne, Lausanne, Switzerland

³Department of Earth and Environmental Science, University of Pennsylvania, Philadelphia, USA

⁴Department of Civil Engineering, University of Granada, Granada, Spain

Submitted to *Geophysical Research Letters*

Author contributions: TD led the data collection and analysis with the help from HU, CR and DB. TD wrote the initial draft of the manuscript, and all coauthors commented on and edited the text.

Abstract

Gravity currents contribute to the transport of heat and mass in atmospheric and aquatic environments. In aquatic systems subject to daily surface cooling, gravity currents propagate through turbulent convective surroundings. Yet, the effects of convection on gravity currents remain unknown. This paper demonstrates how the interaction between penetrative convection and downslope gravity currents impacts the fluid dynamics and transport across littoral aquatic systems. We performed field experiments in an elongated, wind-sheltered lake experiencing differential cooling to resolve the dynamics of gravity currents in convective environments. Our in situ observations reveal that convective plumes penetrate gravity currents, generating large vertical fluctuations that foster the erosion of the stratified layer. Penetrative convection modifies the small-scale dynamics responsible for the stratified flow stability and enhances the vertical mixing between gravity currents and the turbulent surroundings. The intense vertical mixing destroys the stratified downslope flow and limits the basin-scale transport. Our results demonstrate that the interaction between penetrative convection and downslope gravity currents controls the littoral-pelagic connectivity in aquatic ecosystems.

Plain Language Summary

Horizontal differences in fluid density generate flows called gravity currents. These currents transport heat and mass across environmental systems. Such transport depends on the flow dynamics, which are well understood when the surroundings are quiescent. Yet, background turbulent processes such as cooling-induced convection energizes the ambient water in aquatic environments. This study uses a lake experiencing differential cooling as an ideal field-scale laboratory to investigate the effects of convection on the dynamics of gravity currents. Our in situ observations reveal that convective plumes distort the upper interface of gravity currents and limit the flow intensity. These results demonstrate that convection constrains the horizontal transport induced by gravity currents in natural systems.

3.1 Introduction

Gravity currents are ubiquitous flows driven by horizontal density gradients across natural fluid environments (Benjamin, 1968; Huppert, 2006; Simpson, 1982). The dynamics of gravity currents

have been traditionally investigated via laboratory experiments assuming a quiescent ambient fluid (Britter & Linden, 1980; Ellison & Turner, 1959; Lofquist, 1960; Middleton, 1966). The effects of ambient flows (Bühler et al., 1991; C. Chen, 1995; A. J. Hogg et al., 2005; Simpson & Britter, 1980) and boundary mixing (La Rocca et al., 2008; Negretti et al., 2008; Noh & Fernando, 1991; 1992) on the dynamics of gravity currents have been later examined via laboratory and numerical experiments. In nature, gravity currents often propagate through turbulent environments, energized, for example, by wind and thermal convection in the atmosphere (Dailey & Fovell, 1999; Ogawa et al., 2003; Serafin & Zardi, 2010), or by wind, tides, ambient currents and waves in coastal oceans (Hetzl et al., 2015; Mahjabin et al., 2019; Wright et al., 2001). Yet, only a few studies have investigated the erosion and destruction of gravity currents by turbulence in the ambient fluid (Harleman & Ippen, 1960; Linden & Simpson, 1986; Simpson, 1986).

Thermal convection is a pervasive process responsible for amplifying turbulence in fluid environments. It is driven by surface heating in the lower atmosphere (Hall et al., 1975; Stull, 1976) and by surface cooling in aquatic systems (Cushman-Roisin, 1982; Imberger, 1985), and it erodes stratified layers (Deardorff et al., 1969; Veronis, 1963) via plume penetration (Baines, 1975; Ching et al., 1993; Cotel & Kudo, 2008; Folkard, 2000; Noh et al., 1992). Although interactions between gravity currents and atmospheric convection have been examined (Dailey & Fovell, 1999; Ogawa et al., 2003; Serafin & Zardi, 2010), similar observations in aquatic systems are scarce. An example of gravity currents flowing in the presence of penetrative convection in nearshore aquatic systems is the cross-shore overturning circulation driven by differential cooling between shallow and deep waters, aka thermal siphon (Horsch & Stefan, 1988; Monismith et al., 1990). By flowing downslope through the convective mixed layer, thermal siphons interact directly with convective plumes (Bednarz et al., 2008; Fer et al., 2002a; Horsch & Stefan, 1988). Yet, the effects of the surrounding convective environment on gravity current dynamics have not been characterized. Here, we fill this gap by conducting fine spatiotemporal measurements of thermal siphons in a wind-sheltered lake. By analyzing global and local parameters under different thermal forcing scenarios, we show that the intensity of penetrative convection controls the vertical mixing and the hydrodynamic stability of the thermally stratified downslope flow. Thus, in contrast to classical gravity currents in quiescent environments, downslope gravity currents propagating through vigorous convective turbulence experience an abrasive degeneration as they reach deep pelagic waters. Such a degeneration diminishes the large-scale horizontal exchange across nearshore waters.

3.2 Methods

3.2.1 Field experiments and measurements

In situ observations of thermal siphons were conducted in Rotsee (Switzerland), an elongated wind-sheltered lake (Fig. S3.1). The northeastern end of the lake is characterized by a shallow plateau region that forms daily thermal siphons from summer to winter (Doda et al., 2022). Here, we investigate the dynamics of gravity currents on the plane (x, z) , where x is the cross-shore direction along the thalweg, and z is the vertical direction (Fig. 3.1a).

We measured thermal siphons propagating from the northeastern end towards the lake interior from July to December 2019. Measurements are briefly described below, and we refer to Doda et al. (2022) and Fig. S3.1 for further details. Local meteorological forcing was resolved by a weather station installed near the plateau region. A mooring composed of a vertical thermistor array and an up-looking acoustic Doppler current profiler (ADCP) provided high-frequency water temperature and velocity data in the sloping zone off the plateau region (MT, depth of ~ 4 m, slope of 1.5°). The ADCP profiled the water column from 0.25 to 3 m above the bottom, with a vertical bin resolution of 0.05 m. Every 15 min, it collected 4.3 min-long bursts of 512 velocity samples at 2 Hz. A second thermistor array near the deepest point (MB, depth of ~ 16 m) provided background information on the lake thermal structure.

In addition to these seasonal-scale measurements, we deployed two additional vertical thermistor arrays along the lake thalweg, at depths of 2.2 m (ML) and 13.0 m (MS) during short-term campaigns in autumn 2019. We collected conductivity-temperature-depth (CTD) profiles at 13 points along the same cross-shore transect, from P01 (1.3 m deep, 190 m from the shore) to P13 (MB, 800 m offshore from P01). We also profiled the water column at MT every 15 min on 6-7 November.

3.2.2 Data analysis

Surface heat and buoyancy fluxes were estimated from the meteorological data and surface temperature at MB (Doda et al., 2022). The net surface buoyancy flux was computed as $B_{0,\text{net}} = B_{\text{SW},0} + B_0$, where $B_{\text{SW},0}$ and B_0 are shortwave and non-penetrative surface buoyancy fluxes, respectively.

We computed the vertical density structure over time at each mooring by applying the equation of state from Chen and Millero (C.-T. A. Chen & Millero, 1986) to convert temperature into density by assuming constant salinity of $S = 0.2 \text{ g kg}^{-1}$ (Doda et al., 2022). The average surface densities ρ_{ML} and ρ_{MS} were estimated over the upper 1.5 m at ML and over the upper 2.0 m at MS, respectively. We calculated the cross-shore density gradient as $\partial_x \rho = (\rho_{\text{MS}} - \rho_{\text{ML}})/\Delta x$, where $\Delta x = x_{\text{MS}} - x_{\text{ML}} = 400 \text{ m}$ is the cross-shore distance between the two moorings.

We used the algorithm presented in Doda et al. (2022) to detect thermal siphons. The cross-shore velocity u was computed as the horizontal velocity along the x axis. We calculated the thickness of the gravity current over time $h_d(t)$ at MT as the length between the sediment-water interface and the stagnation point $u(h = h_d, t) = 0$.

Cross-shore transects of temperature profiles allowed us to track the bottom stratification induced by the gravity current along x . From each temperature profile $T(z)$, we estimated the current thickness $h_{d,T}$ as the height above the bottom where $dT/dz < 0.03 \text{ }^\circ\text{C m}^{-1}$. The latter gradient threshold was chosen such that $h_{d,T} \approx h_d$ when h_d was steady at MT.

3.2.3 Scaling and dimensionless numbers

We considered a two-layer exchange flow, with a ‘downslope’ stratified current of thickness h_d , density ρ_d and cross-shore velocity $U_d > 0$ and an upper ‘ambient’ layer of thickness h_a , density $\rho_a < \rho_d$ and cross-shore velocity $U_a < 0$ (Fig. 3.1a). The density and velocity of each layer were depth-averaged over h_d and h_a at MT. The depth of the interface between the two layers is $z_d = -h_a = h_d - h_{\text{max}}$, where $h_{\text{max}} \approx 4 \text{ m}$ is the maximum depth at MT.

The downslope flow regime is characterized by the densimetric Froude number Fr_D , expressing the ratio of kinetic to potential energy as (Ellison & Turner, 1959)

$$\text{Fr}_D^2 = \frac{1}{\text{Ri}_b} = \frac{(U_d - U_a)^2}{g' h_d \cos \theta}, \quad (3.1)$$

where Ri_b is the bulk Richardson number, $g' = g(\rho_d - \rho_a)/\rho_0$ is the reduced gravity of the density current, $\rho_0 = 1000 \text{ kg m}^{-3}$ is the reference density and $\theta = 1.5^\circ$ is the slope angle. We neglect the slope effects in the following analysis since $\cos \theta \approx 1$. If the downslope flow is subcritical ($\text{Fr}_D < \text{Fr}_D^{(\text{crit})} = 1$), the upper interface is stable and disturbances can propagate upstream. In contrast, supercritical flows ($\text{Fr}_D > \text{Fr}_D^{(\text{crit})} = 1$) catalyze turbulent mixing across their upper interface (Salinas et al., 2020). The interface stability to shear disturbances can be investigated with

the gradient Richardson number

$$\text{Ri}_g = -\frac{g}{\rho_0} \frac{\partial \rho / \partial z}{(\partial u / \partial z)^2}, \quad (3.2)$$

where shear instabilities grow when $\text{Ri}_g < \text{Ri}_g^{(\text{crit})} = 0.25$ (Miles, 1961). We focused on the interfacial gradient Richardson number at MT $\text{Ri}_{g,\text{int}} = \text{Ri}_g(z = z_d)$. We thus used both Fr_D and $\text{Ri}_{g,\text{int}}$ to characterize shear effects on the interface dynamics.

Based on previous studies on plume impingement at stratified interfaces (Baines, 1975; Cotel & Kudo, 2008; Noh et al., 1992), we quantified the relative intensity of penetrative convection with respect to the stratified downslope flow with the convective Richardson number

$$\text{Ri}_c = \frac{g' h_a}{W_a^2}, \quad (3.3)$$

with $W_a = 1/h_a \int_{-h_a}^0 w(z) dz$ the depth-averaged vertical velocity in the ambient layer. A change of convective regime has been reported at a critical value of $\text{Ri}_c^{(\text{crit})} \approx 10$, below which plumes penetrate across the stratified interface (Cotel & Kudo, 2008; Noh et al., 1992). We further defined the penetration depth of convective plumes as

$$\delta_c = \frac{|W_a|}{N_d}, \quad (3.4)$$

where $N_d = \sqrt{\langle -g/\rho_0 (\partial \rho / \partial z) \rangle_{z < z_d}}$ is the depth-averaged buoyancy frequency in the gravity current. To examine whether convection dominates over shear-driven disturbance across the current interface, we compared δ_c with the thickness of the shear (δ_S) and density (δ_ρ) interfaces (Zhu & Lawrence, 2001):

$$\delta_S = \frac{(U_d - U_a)}{(\partial u / \partial z)_{\text{max}}}, \quad (3.5)$$

and

$$\delta_\rho = \frac{(\rho_d - \rho_a)}{(\partial \rho / \partial z)_{\text{max}}}. \quad (3.6)$$

If $\delta_c > \delta_S, \delta_\rho$, convective plumes penetrate beyond the current interface defined from shear and density and erode the stratified layer.

3.3 Results

3.3.1 Diurnal cycle

We investigate the effect of penetrative convection on gravity currents by examining two distinctive thermal siphon events (Fig. 3.1). The first event (10-11 October 2019) is a canonical scenario expected in the early autumn when the diurnal cycle has well-defined cooling and heating phases that constrain the development of the thermal siphon. In contrast, the second event (6-7 November 2019) represents a persistently cold late-autumn day, with a continuously flowing thermal siphon. We hereafter refer to these scenarios as the cooling-heating and continuous-cooling cases, respectively. Despite the differences in the thermal forcing, both scenarios show two remarkable dynamic regimes: (i) a nighttime convective (C) phase, during which convective plumes interact with the gravity current; (ii) a daytime relaxation (R) phase, during which penetrative convection weakens and the gravity current intensifies.

We found that during the C-phase, surface cooling (net surface buoyancy flux $B_{0,\text{net}} \approx 10^{-7} \text{ W kg}^{-1}$) caused convective mixing with depth-averaged vertical velocities of $\langle w \rangle \approx 10^{-1} \text{ cm s}^{-1}$ (Figs. 3.1b and 3.1c). At the same time, a negative lateral density gradient developed by differential cooling, which increased in time until reaching a quasi-steady magnitude of about $\partial_x \rho \approx -1.5 \times 10^{-4} \text{ kg m}^{-4}$ (Figs. 3.1d and 3.1e). The thermally-driven gravity current was weakly stratified (squared buoyancy frequency $N_d^2 < 1 \times 10^{-4} \text{ s}^{-2}$) and unsteady, with up to $\sim 2 \text{ m}$ vertical fluctuations at its upper interface (Figs. 3.1f and 3.1g). The transition from the C-phase to the R-phase occurred at sunrise when the net cooling heat flux diminished and the intensity of convection weakened. This caused a sudden drop of $|\partial_x \rho|$ and a baroclinic adjustment with an intensification of the downslope gravity current (Figs. 3.1f and 3.1g). In early autumn, strong radiative heating stratified the surface layer (Fig. 3.1f), which was not observed in late autumn (Fig. 3.1g). Despite having different forcing conditions, the current dynamics during the C- and R-phases were similar between the two scenarios. We remark that vertical fluctuations at the interface stopped during the R-phase when penetrative convection weakened, suggesting that convective plumes modified the current dynamics.

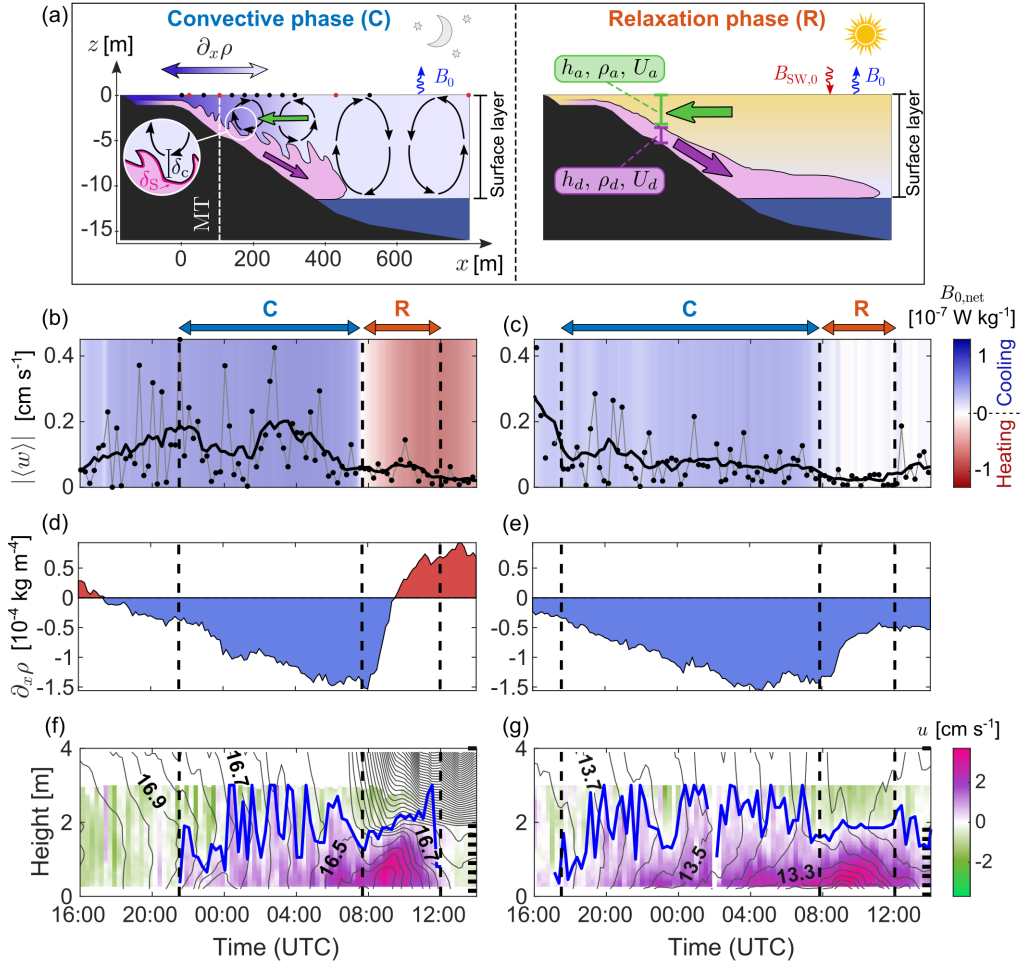


Figure 3.1 – Diurnal phases for two different thermal siphon events in 2019. (a) Schematic of the night-time convective (C) phase and daytime relaxation (R) phase along the lake thalweg. Black arrows represent convective plumes. Dots at the lake surface depict the location of CTD profiles on 6-7 November with moorings in red. (b-g) Time series of (b-c) surface net buoyancy flux (shading) and depth-averaged vertical velocity at MT (black dots are burst-averaged values and the black line is the 2-hour moving average), (d-e) lateral surface density gradient between ML and MS, and (f-g) burst-averaged cross-shore velocity at MT as a function of height above the sediment. Blue lines in (f, g) show the upper interface of the gravity current h_d . Gray lines are 0.05 °C-spaced isotherms, linearly interpolated between thermistors (black ticks on the right vertical axis). Offshore (onshore) velocities are defined positive (negative). (b, d, f) correspond to 10-11 October (cooling-heating case) and (c, e, g) to 6-7 November (continuous-cooling case).

3.3.2 Interface dynamics of the gravity current

We further examined the dynamical regime shift from the C-phase to the R-phase using high-frequency velocity bursts. We compared two 4 h-long sub-periods from each phase of the continuous-cooling scenario (Fig. 3.2). Although the average thickness of the gravity current

was $\overline{h_d} \approx 2$ m for both phases, the variability of h_d was more than four times larger during the C-phase with a standard deviation of 0.70 m, compared to 0.15 m during the R-phase. Fluctuations of $|h'_d| = |h_d - \overline{h_d}| \approx 1$ m indicated vigorous vertical mixing during the C-phase (Fig. 3.2c) and patches of positive u observed above the main interface suggested detrainment of the downslope flow into the upper layer (Fig. 3.2a). During this turbulent phase, vigorous convective downdrafts and updrafts ($|w| \approx 0.5 \text{ cm s}^{-1}$) penetrated across the current interface (Fig. 3.2b). The penetration depth was $\delta_c \approx 0.1 - 1 \text{ m} > \delta_S, \delta_\rho$ (Eqs. 3.4–3.6, Fig. 3.2d) during the C-phase. In contrast, the combined effect of low vertical velocity fluctuations and strong near-bottom stratification prevented the erosion of the downslope gravity current during the R-phase, with $\delta_c \approx 10^{-2} \text{ m} < \delta_S, \delta_\rho$. These observations indicate that the convective regime shift between C- and R-phases modified the intensity of (i) the vertical mixing between the downslope current and the ambient fluid and (ii) the cross-shore flow.

To identify distinctive dynamic properties of the C- and R-phases for the cooling-heating and continuous-cooling scenarios, we computed the probability density function (PDF) of six parameters associated with the strength of the bottom layer stratification, and the destabilising effects of penetrative convection and shear (Fig. 3.3). For both scenarios, the gravity current changed its dynamics between the C- and R-phases, with one-order of magnitude smaller vertical fluctuations $|h'_d|/\overline{h_d}$ and a stronger and less variable stratification $N_d^2 \overline{h_d}/g'_{\max}$ during the R-phase (Figs. 3.3a and 3.3b). The magnitudes of $|h'_d|/\overline{h_d}$ and N_d^2 in the C- and R-phases were the same between the two forcing scenarios. The two scenarios also showed a similar change in the convective regime (Figs. 3.3c and 3.3d). From the C-phase to the R-phase, the mean convective Richardson number Ri_c increased by two orders of magnitude and the mean ratio δ_c/δ_S dropped by one order of magnitude from $\sim 10^{0.5}$ to $\sim 10^{-0.5}$. Such striking changes in Ri_c and δ_c/δ_S confirm that the shift in current dynamics resulted from a weakening of penetrative convection. On average, the flow was supercritical (normalized densimetric Froude number $\text{Fr}_D/\text{Fr}_D^{(\text{crit})} > 1$) and prone to shear instabilities (normalized interfacial gradient Richardson number $\text{Ri}_{g,\text{int}}/\text{Ri}_g^{(\text{crit})} < 1$) during the C-phase for both scenarios (Figs. 3.3e and 3.3f). The surface stratification led to subcritical ($\text{Fr}_D/\text{Fr}_D^{(\text{crit})} < 1$) and stable conditions ($\text{Ri}_{g,\text{int}}/\text{Ri}_g^{(\text{crit})} > 1$) during the R-phase of the cooling-heating case. On the other hand, the flow regime did not change significantly for the continuous-cooling case. The absence of a consistent shift in the flow regime between the C- and R-phases implies that shear was not responsible for the substantial change in the gravity current dynamics.

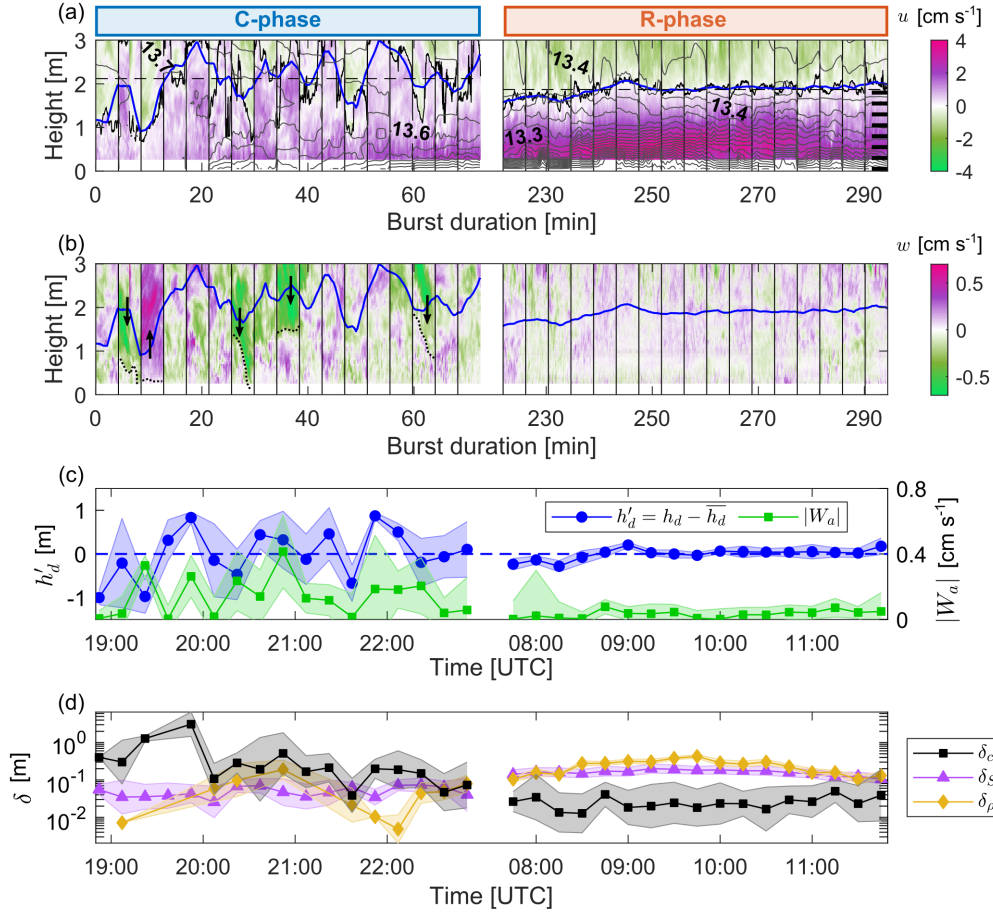


Figure 3.2 – Subsets of the convective and relaxation phases captured in the sloping region (MT) on 6-7 November. (a) High frequency cross-shore velocity over the three first meters above the sediment as a function of time. The bursts are combined together and delimited by vertical black lines. The time is expressed as the burst duration since the first sample. Solid black and blue lines depict the high-frequency and smoothed upper interface of the gravity current, respectively. The dashed horizontal line indicates the average thickness $\overline{h_d}$ during each subset. Grey lines are 0.02 °C-spaced isotherms, linearly interpolated between the thermistors (black ticks on the right vertical axis). (b) Same as (a) for the vertical velocity. Arrows highlight strong convective downdrafts and updrafts that penetrate across the interface. Their penetration depth is qualitatively shown with dotted lines. The blue line is identical to (a). (c) Burst-averaged time series of interface fluctuations h'_d and depth-averaged vertical velocity in the ambient layer $|W_a|$. (d) Burst-averaged time series of penetrative length scale δ_c , shear interface thickness δ_s and density interface thickness δ_ρ . Shaded areas in (c) and (d) show the standard deviation for each burst-average.

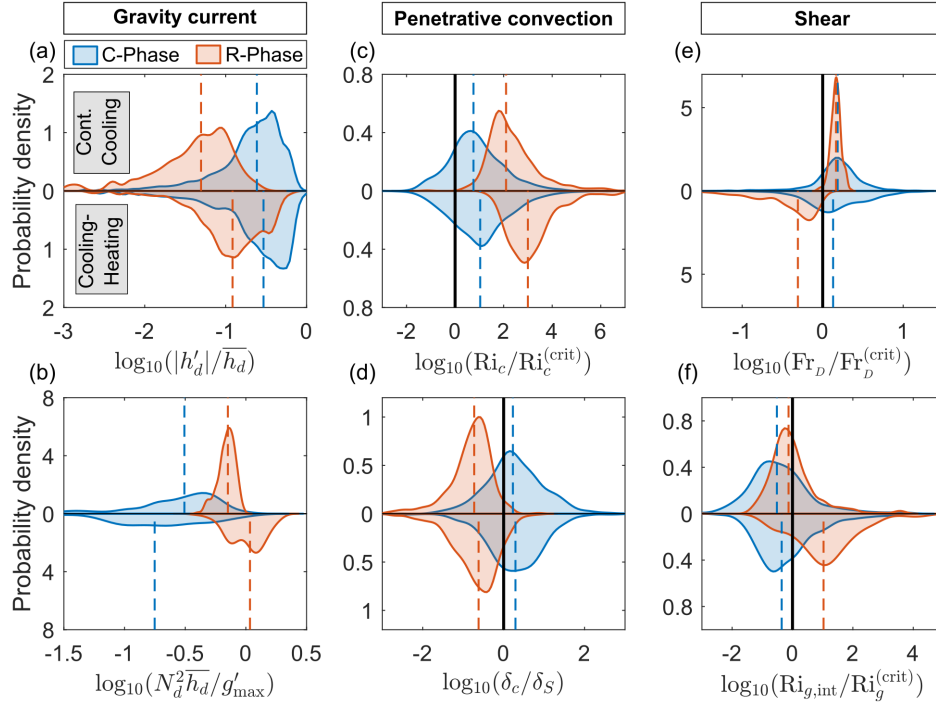


Figure 3.3 – Probability density plots comparing the convective (blue) and relaxation (orange) phases, for the cooling-heating and continuous-cooling scenarios (lower and upper part of each panel, respectively). (a) Vertical fluctuations of the interface h'_d normalized by the mean current thickness $\overline{h_d}$. Large fluctuations, with h_d thicker than the ADCP profiling range (3 m), are not included. (b) Dimensionless squared buoyancy frequency of the gravity current, where $g'_{\max} = g |\partial_x \rho|_{\max} \Delta x / \rho_0 = 5.9 \times 10^{-4} \text{ m s}^{-2}$ is the reduced gravity from the maximum absolute lateral gradient $|\partial_x \rho|_{\max} = 1.5 \times 10^{-4} \text{ kg m}^{-4}$ (Fig. 3.1). (c) Convective Richardson number normalized by $\text{Ri}_c^{(\text{crit})} = 10$. (d) Ratio of penetrative length scale to the shear interface thickness. (e) Densimetric Froude number normalized by $\text{Fr}_D^{(\text{crit})} = 1$. (f) Interfacial gradient Richardson number normalized by $\text{Ri}_g^{(\text{crit})} = 0.25$. In (c, e, f) only positive values are included, corresponding to a stable stratification. The vertical black solid line in (c-f) indicates a ratio of one. Vertical dashed lines show the median values over each phase.

3.3.3 Structure and propagation of the gravity current

The vertical thermal structure and the propagation of the stratified downslope flow during the continuous-cooling scenario were analyzed from temperature profiles (Fig. 3.4). Active convection fostering vertical mixing during the C-phase led to in a weakly stratified downslope flow (vertical temperature gradient $\partial T/\partial z \approx 0.1 \text{ }^\circ\text{C m}^{-1}$, Fig. 3.4a). The near-bottom stratification was spatially variable and dropped to $\partial T/\partial z \approx 0.01 \text{ }^\circ\text{C m}^{-1}$ for $x > 200 \text{ m}$. On average, only the lower 1.5 m at the sloping region (MT) (Fig. 3.1a) were stratified, which represented $h_{d,T}/h_d \approx 60\%$ of the gravity current thickness (Fig. 3.4b). The velocity maximum was located close to the bottom boundary, at $h_{U_{d,\max}} < 0.15 h_d$, and not captured by the ADCP. During the R-phase, $h_{d,T}$ increased at all locations, and the intrusion of cold water was observed at the base of the mixed layer for $x > 400 \text{ m}$ (Fig. 3.4c). The gravity current became entirely stratified, from its base to its upper interface ($h_d \approx h_{d,T}$), and the height of maximal velocity increased to $h_{U_{d,\max}} \approx 0.25 h_d$ (Fig. 3.4d). These results suggest that the vertical mixing during the C-phase eroded the stratified downslope flow and reduced the lateral transport.

3.4 Discussion

By comparing the dynamics of thermal siphons in the presence and absence of convective plumes, this study pinpoints the effects of penetrative convection on the structure and propagation of a thermally-driven gravity current. When convective plumes penetrated across the interface of the downslope flow during the C-phase, we found that (i) the interface of the gravity current experienced large vertical fluctuations and (ii) the dynamic bottom layer of positive cross-shore velocity was only partially stratified. This partial stratification differed, for instance, from the density structure resulting from lock-exchange gravity currents, for which the maximum shear and maximum density gradient coincide and $h_{U_{d,\max}}/h_d \approx 0.2$ (Ellison & Turner, 1959; Thorpe & Ozen, 2007; Wells & Dorrell, 2021). Conversely, in the absence of penetrative convection and vigorous vertical mixing during the R-phase, the downslope flow showed a more stable interface, and it recovered the canonical structure of gravity currents.

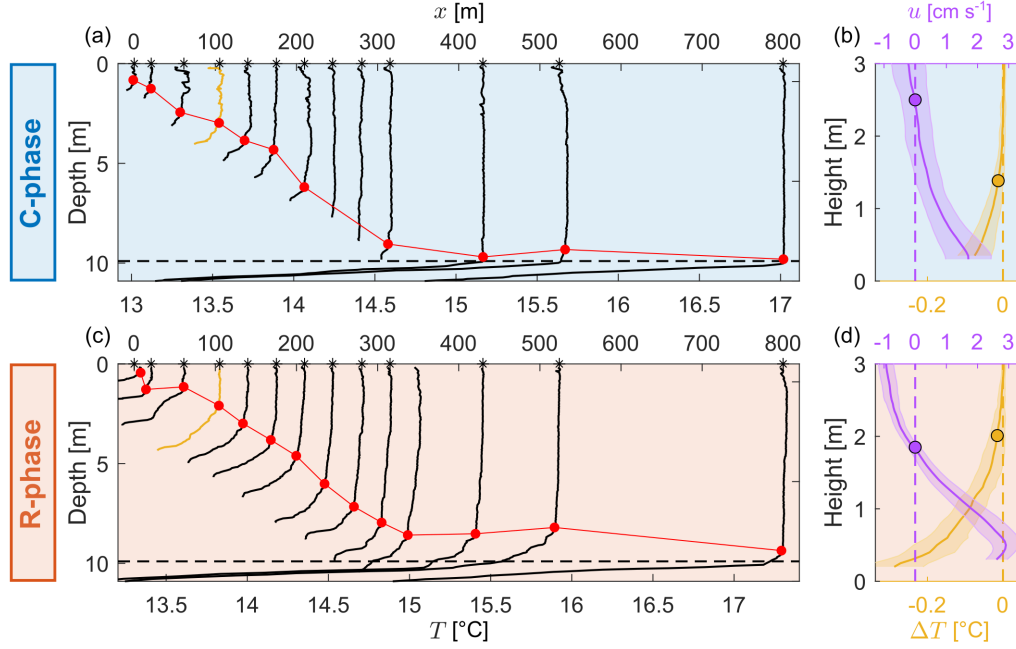


Figure 3.4 – Cross-shore propagation of the gravity current during the convective and relaxation phases on 6-7 November. (a, c) Cross-shore transect of temperature profiles from P01 to P13, as a function of distance x from P01, for (a) the convective phase (period 03:33-04:51 UTC), and (c) the relaxation phase (period 09:43-10:39 UTC). Each temperature profile P_i is shifted proportionally to the distance x_{P_i} from P01 (black stars on the x axis), as $\widetilde{T}_{P_i} = T_{P_i} + x_{P_i} \times 0.005 \text{ } ^\circ\text{C m}^{-1}$, where T_{P_i} and \widetilde{T}_{P_i} are the measured and shifted temperatures, respectively. The temperature profile at MT is shown in yellow. The horizontal dashed line depicts the base of the mixed layer at MB. Red dots indicate the upper interface of the gravity current $h_{d,T}$. (b, d) Average profiles of cross-shore velocity (purple) and temperature anomaly (yellow) at MT, for (b) the convective phase (17:30-07:50 UTC) and (d) the relaxation phase (07:50-12:00 UTC). The temperature anomaly is $\Delta T(z) = T(z) - T_0$, where T_0 is the median temperature above $h_{d,T}$. Shaded area on each profile represents the standard deviation. Dots depict the upper interface of the gravity current, from the stagnation point (h_d , purple dot) and temperature gradient ($h_{d,T}$, yellow dot).

3.4.1 Role of convection in the small-scale interface dynamics

At low Ri_c , the impingement of plumes and thermals deflects stratified interfaces (Baines, 1975; Ching et al., 1993; Cotel & Kudo, 2008; Noh et al., 1992), as observed in convective boundary layers (Deardorff et al., 1969; Stull, 1976). During the C-phase, Ri_c varied over six orders of magnitude due to the temporal fluctuations of W_a and was statistically larger than $Ri_c^{(\text{crit})} = 10$ (Fig. 3.3c). Yet, if we focus on intense convective episodes by including negative Ri_c (Fig. S3.1) and discarding weak convective periods (depth-averaged vertical velocity in the ambient layer $W_a < 1 \times 10^{-3} \text{ m s}^{-1}$), we found that $Ri_c \lesssim Ri_c^{(\text{crit})}$ (interquartile intervals of $-8 < Ri_c < 25$ and $-5 < Ri_c < 25$ for the cooling-heating and continuous-cooling scenarios, respectively). Sullivan

et al. (1998) showed that convective updrafts (downdrafts) push the boundary layer interface locally upward (downward). Such interface fluctuations are linked to the penetration depth δ_c and the convective Richardson number as $\sigma_{h_a}/\overline{h_a} \sim \delta_c/\overline{h_a} \sim \text{Ri}_c^{-\gamma}$, where σ_{h_a} and $\overline{h_a}$ are the standard deviation (similar to $|h'_d|$) and mean of the convective layer thickness, with $\gamma \approx 1$ (Ching et al., 1993; Cotel & Kudo, 2008; Noh et al., 1992). For $\text{Ri}_c \approx 10$ and $\overline{h_a} \approx 1$ m, the standard deviation σ_{h_a} scales with the penetration depth, i.e. $\sigma_{h_a} \approx \delta_c \approx 0.1$ m, which is the same order of magnitude than the fluctuations $|h'_d|$ (Fig. 3.2). Yet, this Ri_c - σ_{h_a} relationship was derived for a horizontally ‘stationary’ stratified interface interacting with vertical plumes, which differs from our case where both the stratified and ambient layers are actively streaming in the horizontal direction. The horizontal flow modifies the plume trajectory and penetration, which could explain the weak relationship between the current dynamics at MT and the local Ri_c ($\gamma \approx 0.1$, Fig. 3.5). The observed small-scale dynamics may also integrate fluctuations generated by convectively forced internal waves (Ansong & Sutherland, 2010; Fritts & Alexander, 2003), shear instabilities (Pawlak & Armi, 2000; Zhu & Lawrence, 2001), pulses and roll waves (Alavian, 1986; Dressler, 1949; Fer et al., 2001; Needham & Merkin, 1984). However, the absence of a consistent shift in the flow regime (Ri_g and Fr_D) between the C- and R-phases (Figs. 3.3e and 3.3f) suggests that shear instabilities and roll waves play a secondary role in the current dynamics. The dominant period of the fluctuations $T_{h'_d} \approx 1$ h (Fig. 3.1) does not match the characteristic periodicity of internal waves and pulses (SI Appendix, Table S1), but agrees with the duration of a convective overturn $\tau_c = 2 \cdot h_a/|W_a| \approx 1$ h, where $h_a \approx 2$ m and $|W_a| \approx 1 \times 10^{-3} \text{ m s}^{-1}$. Therefore, penetrative convection arises to be the primary cause of the fluctuating dynamics observed during the C-phase.

3.4.2 Role of convection in the basin-scale lateral transport

The erosion of the stratified downslope flow by convective plumes (Fig. 3.4) was comparable to the effects of turbulence on fronts propagation (Linden & Simpson, 1986; Simpson, 1986) and exchange flows (A. M. Hogg et al., 2001). Linden and Simpson (Linden & Simpson, 1986) found that turbulent mixing decreased the front velocity U_f of a lock-exchange gravity current, such that $U_f < U_s$, where U_s is the velocity scale based on horizontal density gradients in a quiescent environment. In our case, $U_s = 0.5\sqrt{-g \partial_x \rho \Delta x h_{\text{lit}}/\rho_0} \approx 1.7 \text{ cm s}^{-1}$, where $\Delta x = 400$ m is the cross-shore distance along which $\partial_x \rho \approx -1 \times 10^{-4} \text{ kg m}^{-4}$ was computed (Fig. 3.1) and $h_{\text{lit}} \approx 3$ m is the mean depth of the mixed region experiencing $\partial_x \rho$.

The averaged downslope velocity during the R-phase $U_d \approx 1.5 \pm 0.4 \text{ cm s}^{-1} \approx 0.9 U_s$ matched the scale U_s . In the presence of convection during the C-phase, however, it was only $U_d \approx$

$0.8 \pm 0.3 \text{ cm s}^{-1} \approx 0.5 U_s$ – consistent with Linden and Simpson (Linden & Simpson, 1986). The authors found that the flow became vertically mixed after a distance L_x and ran out of energy to propagate further. In the case of penetrative convection, we posit that the propagation distance scales as $L_x \sim U_s h_d / w_e$, where $w_e = A W_a / \text{Ri}_c = A B_0 h_a / (g' h_d)$ is the convective entrainment velocity, with A an empirical coefficient (Deardorff et al., 1980). This distance represents how far the gravity current propagates before being entirely eroded by penetrative plumes. Considering $g' \sim g \partial_x \rho \Delta x / \rho_0 \approx 4 \times 10^{-4} \text{ m s}^{-2}$, $h_d \approx h_a \approx 2 \text{ m}$, $B_0 \approx 1 \times 10^{-7} \text{ W kg}^{-1}$ and $A \approx 0.2$ (Sullivan et al., 1998), we obtain $L_x \approx 0.5 g'^{3/2} h_{\text{lit}}^{1/2} h_d^2 / (A B_0 h_a) \approx 700 \text{ m}$. The order of magnitude $L_x \approx 10^2 - 10^3 \text{ m}$ is consistent with our observations of complete mixing at around $x \approx 250 \text{ m}$ from P01 (Fig. 3.4a), equivalent to $L_x \approx 200 + x = 450 \text{ m}$ from the shore. The degeneration of the downslope stratified layer before reaching the lake interior confirms the numerical results by Ulloa et al. (2022).

Convective mixing may also modify the growth of the gravity current by entrainment. The net shear entrainment of ambient water into a gravity current is expressed by $E_{\text{net}} = \partial_x (U_d h_d) / (U_d - U_a)$, which has been parametrized as a function of the bulk Richardson number Ri_B in quiescent environments (Cenedese & Adduce, 2010; Ellison & Turner, 1959). Fer et al. (2002a) suggested that convective plumes increase E_{net} in thermal siphons, but their estimate of E_{net} did not include the effects of the large Reynolds number $\text{Re} = U_d h_d / \nu \approx 10^5$. Although we observed a thinner stratified layer in the presence of penetrative convection (Fig. 3.4), we cannot infer the effects of convective plumes on the downstream evolution of the discharge ($U_d h_d$) from a single-point measurements. The contribution of convective plumes to E_{net} could be examined from simultaneous velocity measurements along a cross-shore transect. We stress that the effects of the return flow must be included since $h_d / h_a \approx 1$ as in counterflows (Christodoulou, 1986; Moore & Long, 1971).

During the C-phase, vertical fluxes between the downslope flow and the ambient layer were enhanced by convective mixing, which diluted transported tracers and diminished the cross-shore exchange. A similar reduction in the lateral transport of tracers due to turbulent diffusion has been reported for exchange flows (Helfrich, 1995; A. M. Hogg et al., 2001; Winters & Seim, 2000). The maximal transport was observed during the R-phase or heating phase in Rotsee (Doda et al., 2022), in agreement with numerical simulations of thermal siphons (Chubarenko et al., 2013; Safaie et al., 2022). This relaxation is comparable to the frontogenesis observed by Linden and Simpson (Linden & Simpson, 1986) once turbulence was turned off. The intensification of gravity currents with weaker turbulent mixing has also been observed in the atmosphere (Parker et al., 2005; Sha et al., 1991; Simpson et al., 1977) and estuaries (Hetzl et al., 2015). Although thermal siphons are traditionally perceived as a nocturnal transport process of dissolved gases (Brothers et al., 2017), our results show that penetrative convection delays the time of maximal transport to daylight

conditions. Accounting for this delay is essential to quantify the ecological implications of thermal siphons in aquatic systems.

3.5 Conclusion

The dynamics of downslope flows induced by differential cooling result from the intimate interaction between penetrative convection and gravity currents. Our high-resolution observations demonstrate that convective plumes modify the small-scale dynamics and the basin-scale propagation of gravity currents. Due to the rich fluid dynamics driven by differential cooling, in which shear and convective flows coexist, further investigations of thermal siphons would expand our understanding of geophysical flows interacting with convective surroundings. Future numerical and laboratory experiments would allow examining the shear–convection interplay over a broader range of forcing and boundary conditions. Our study highlights the need for a holistic investigation of geophysical flows that integrates the various interactions between physical processes.

Code and data availability

The scripts used to process, analyzed and plot the data are available for download at: <https://drive.switch.ch/index.php/s/TEFHQyv0PC0Pm0X>.

They will be moved to the Eawag Research Data Institutional Collection and associated with a DOI number once this chapter will be accepted for publication.

Acknowledgements

We sincerely thank our technician, Michael Plüss, for helping us in organizing the field campaigns and maintaining the instruments. We acknowledge Kathrin Baumann, Bieito Fernández-Castro, Sébastien Lavanchy and Love Råman Vinnå for their help in the field. We are grateful to the Canton of Luzern, the municipalities of Luzern and Ebikon, the Rowing Centre Lucerne-Rotsee, the Quartierverein Maihof and Pro Natura associations, and the Rotsee- Badi for supporting us in our measurements. We thank Kraig Winters, Oscar Sepúlveda Steiner and Marco Toffolon for their comments on the figures and the data interpretation.

Financial support

This study was financed by the Swiss National Science Foundation (“Buoyancy driven nearshore transport in lakes” project; HYPOlimnetic THERmal SIphonS, HYPOTHESIS, grant no. 175919).

There is no competing interest for any author.

References

- Alavian, V. (1986). Behavior of density currents on an incline. *Journal of Hydraulic Engineering*, 112(1), 27–42. [https://doi.org/10.1061/\(ASCE\)0733-9429\(1986\)112:1\(27\)](https://doi.org/10.1061/(ASCE)0733-9429(1986)112:1(27))
- Ansong, J. K., & Sutherland, B. R. (2010). Internal gravity waves generated by convective plumes. *Journal of Fluid Mechanics*, 648, 405–434. <https://doi.org/10.1017/S0022112009993193>
- Baines, W. D. (1975). Entrainment by a plume or jet at a density interface. *Journal of Fluid Mechanics*, 68(02), 309–320. <https://doi.org/10.1017/S0022112075000821>
- Bednarz, T. P., Lei, C., & Patterson, J. C. (2008). An experimental study of unsteady natural convection in a reservoir model cooled from the water surface. *Experimental Thermal and Fluid Science*, 32(3), 844–856. <https://doi.org/10.1016/j.expthermflusci.2007.10.007>
- Benjamin, T. B. (1968). Gravity currents and related phenomena. *Journal of Fluid Mechanics*, 31(2), 209–248. <https://doi.org/10.1017/S0022112068000133>
- Britter, R. E., & Linden, P. F. (1980). The motion of the front of a gravity current travelling down an incline. *Journal of Fluid Mechanics*, 99(3), 531–543. <https://doi.org/10.1017/S0022112080000754>
- Brothers, S., Kazanjian, G., Köhler, J., Scharfenberger, U., & Hilt, S. (2017). Convective mixing and high littoral production established systematic errors in the diel oxygen curves of a shallow, eutrophic lake. *Limnology and Oceanography: Methods*, 15(5), 429–435. <https://doi.org/10.1002/lom3.10169>
- Bühler, J., Wright, S. J., & Kim, Y. (1991). Gravity currents advancing into a coflowing fluid. *Journal of Hydraulic Research*, 29(2), 343–357. <https://doi.org/10.1080/00221689109499007>
- Cenedese, C., & Adduce, C. (2010). A new parameterization for entrainment in overflows. *Journal of Physical Oceanography*, 40(8), 1835–1850. <https://doi.org/10.1175/2010JPO4374.1>
- Chen, C. (1995). Numerical simulations of gravity currents in uniform shear flows. *Monthly Weather Review*, 123(11), 3240–3253. [https://doi.org/10.1175/1520-0493\(1995\)123<3240:NSOGCI>2.0.CO;2](https://doi.org/10.1175/1520-0493(1995)123<3240:NSOGCI>2.0.CO;2)

- Chen, C.-T. A., & Millero, F. J. (1986). Precise thermodynamic properties for natural waters covering only the limnological range. *Limnology and Oceanography*, 31(3), 657–662. <https://doi.org/10.4319/lo.1986.31.3.0657>
- Ching, C., Fernando, H., & Noh, Y. (1993). Interaction of a negatively buoyant line plume with a density interface. *Dynamics of Atmospheres and Oceans*, 19(1-4), 367–388. [https://doi.org/10.1016/0377-0265\(93\)90042-6](https://doi.org/10.1016/0377-0265(93)90042-6)
- Christodoulou, G. C. (1986). Interfacial mixing in stratified flows. *Journal of Hydraulic Research*, 24(2), 77–92. <https://doi.org/10.1080/00221688609499323>
- Chubarenko, I. P., Esiukova, E., Stepanova, N., Chubarenko, B., & Baudler, H. (2013). Down-slope cascading modulated by day/night variations of solar heating. *Journal of Limnology*, 72(2), e19. <https://doi.org/10.4081/jlimnol.2013.e19>
- Cotel, A. J., & Kudo, Y. (2008). Impingement of buoyancy-driven flows at a stratified interface. *Experiments in Fluids*, 45(1), 131–139. <https://doi.org/10.1007/s00348-008-0469-5>
- Cushman-Roisin, B. (1982). Penetrative convection in the upper ocean due to surface cooling. *Geophysical & Astrophysical Fluid Dynamics*, 19(1-2), 61–91. <https://doi.org/10.1080/03091928208208947>
- Dailey, P. S., & Fovell, R. G. (1999). Numerical simulation of the interaction between the sea-breeze front and horizontal convective rolls. Part I: offshore ambient flow. *Monthly Weather Review*, 127(5), 858–878. [https://doi.org/10.1175/1520-0493\(1999\)127<0858:NSOTIB>2.0.CO;2](https://doi.org/10.1175/1520-0493(1999)127<0858:NSOTIB>2.0.CO;2)
- Deardorff, J. W., Willis, G. E., & Lilly, D. K. (1969). Laboratory investigation of non-steady penetrative convection. *Journal of Fluid Mechanics*, 35(1), 7–31. <https://doi.org/10.1017/S0022112069000942>
- Deardorff, J. W., Willis, G. E., & Stockton, B. H. (1980). Laboratory studies of the entrainment zone of a convectively mixed layer. *Journal of Fluid Mechanics*, 100(01), 41–64. <https://doi.org/10.1017/S0022112080001000>
- Doda, T., Ramón, C. L., Ulloa, H. N., Wüest, A., & Bouffard, D. (2022). Seasonality of density currents induced by differential cooling. *Hydrology and Earth System Sciences*, 26(2), 331–353. <https://doi.org/10.5194/hess-26-331-2022>
- Dressler, R. F. (1949). Mathematical solution of the problem of roll-waves in inclined open channels. *Communications on Pure and Applied Mathematics*, 2(2-3), 149–194. <https://doi.org/10.1002/cpa.3160020203>
- Ellison, T. H., & Turner, J. S. (1959). Turbulent entrainment in stratified flows. *Journal of Fluid Mechanics*, 6(03), 423–448. <https://doi.org/10.1017/S0022112059000738>
- Fer, I., Lemmin, U., & Thorpe, S. A. (2002a). Contribution of entrainment and vertical plumes to the winter cascading of cold shelf waters in a deep lake. *Limnology and Oceanography*, 47(2), 576–580. <https://doi.org/10.4319/lo.2002.47.2.0576>

- Fer, I., Lemmin, U., & Thorpe, S. A. (2001). Cascading of water down the sloping sides of a deep lake in winter. *Geophysical Research Letters*, 28(10), 2093–2096. <https://doi.org/10.1029/2000GL012599>
- Folkard, A. M. (2000). Laboratory observations of interactions of forced plumes with stratified shear layers. *Fluid Dynamics Research*, 26(6), 355–375. [https://doi.org/10.1016/S0169-5983\(99\)00038-6](https://doi.org/10.1016/S0169-5983(99)00038-6)
- Fritts, D. C., & Alexander, M. J. (2003). Gravity wave dynamics and effects in the middle atmosphere. *Reviews of Geophysics*, 41(1), 1003. <https://doi.org/10.1029/2001RG000106>
- Hall, F. F., Edinger, J. G., & Neff, W. D. (1975). Convective plumes in the planetary boundary layer, investigated with an acoustic echo sounder. *Journal of Applied Meteorology*, 14(4), 513–523. [https://doi.org/10.1175/1520-0450\(1975\)014<0513:CPITPB>2.0.CO;2](https://doi.org/10.1175/1520-0450(1975)014<0513:CPITPB>2.0.CO;2)
- Harleman, D. R. F., & Ippen, A. T. (1960). The turbulent diffusion and convection of saline water in an idealised estuary. *Publ. No. 51* (International Association for Science of Hydrology, Commission of Surface Waters., pp. 362–378).
- Helfrich, K. R. (1995). Time-dependent two-layer hydraulic exchange flows. *Journal of Physical Oceanography*, 25(3), 359–373. [https://doi.org/10.1175/1520-0485\(1995\)025<0359:TDTLHE>2.0.CO;2](https://doi.org/10.1175/1520-0485(1995)025<0359:TDTLHE>2.0.CO;2)
- Hetzel, Y., Pattiaratchi, C., Lowe, R., & Hofmeister, R. (2015). Wind and tidal mixing controls on stratification and dense water outflows in a large hypersaline bay. *Journal of Geophysical Research: Oceans*, 120(9), 6034–6056. <https://doi.org/10.1002/2015JC010733>
- Hogg, A. J., Hallworth, M. A., & Huppert, H. E. (2005). On gravity currents driven by constant fluxes of saline and particle-laden fluid in the presence of a uniform flow. *Journal of Fluid Mechanics*, 539, 349–385. <https://doi.org/10.1017/S002211200500546X>
- Hogg, A. M., Ivey, G. N., & Winters, K. B. (2001). Hydraulics and mixing in controlled exchange flows. *Journal of Geophysical Research: Oceans*, 106(C1), 959–972. <https://doi.org/10.1029/2000JC000266>
- Horsch, G. M., & Stefan, H. G. (1988). Convective circulation in littoral water due to surface cooling. *Limnology and Oceanography*, 33(5), 1068–1083. <https://doi.org/10.4319/lo.1988.33.5.1068>
- Huppert, H. E. (2006). Gravity currents: a personal perspective. *Journal of Fluid Mechanics*, 554, 299–322. <https://doi.org/10.1017/S002211200600930X>
- Imberger, J. (1985). The diurnal mixed layer. *Limnology and Oceanography*, 30(4), 737–770. <https://doi.org/10.4319/lo.1985.30.4.0737>
- La Rocca, M., Adduce, C., Sciortino, G., & Pinzon, A. B. (2008). Experimental and numerical simulation of three-dimensional gravity currents on smooth and rough bottom. *Physics of Fluids*, 20(10), 106603. <https://doi.org/10.1063/1.3002381>

- Linden, P. F., & Simpson, J. E. (1986). Gravity-driven flows in a turbulent fluid. *Journal of Fluid Mechanics*, 172, 481–497. <https://doi.org/10.1017/S0022112086001829>
- Lofquist, K. (1960). Flow and stress near an interface between stratified liquids. *Physics of Fluids*, 3(2), 158–175. <https://doi.org/10.1063/1.1706013>
- Mahjabin, T., Pattiaratchi, C., & Hetzel, Y. (2019). Wind effects on dense shelf water cascades in south-west Australia. *Continental Shelf Research*, 189, 103975. <https://doi.org/10.1016/j.csr.2019.103975>
- Middleton, G. V. (1966). Experiments on density and turbidity currents. II. Uniform flow of density currents. *Canadian Journal of Earth Sciences*, 3(5), 627–637. <https://doi.org/10.1139/e66-044>
- Miles, J. W. (1961). On the stability of heterogeneous shear flows. *Journal of Fluid Mechanics*, 10(04), 496–508. <https://doi.org/10.1017/S0022112061000305>
- Monismith, S. G., Imberger, J., & Morison, M. L. (1990). Convective motions in the sidearm of a small reservoir. *Limnology and Oceanography*, 35(8), 1676–1702. <https://doi.org/10.4319/lo.1990.35.8.1676>
- Moore, M. J., & Long, R. R. (1971). An experimental investigation of turbulent stratified shearing flow. *Journal of Fluid Mechanics*, 49(4), 635–655. <https://doi.org/10.1017/S0022112071002301>
- Needham, D. J., & Merkin, J. H. (1984). On roll waves down an open inclined channel. *Proceedings of the Royal Society of London. A*, 394(1807), 259–278. <https://doi.org/10.1098/rspa.1984.0079>
- Negretti, M., Zhu, D. Z., & Jirka, G. H. (2008). The effect of bottom roughness in two-layer flows down a slope. *Dynamics of Atmospheres and Oceans*, 45(1-2), 46–68. <https://doi.org/10.1016/j.dynatmoce.2008.02.001>
- Noh, Y., & Fernando, H. J. S. (1991). Gravity current propagation along an incline in the presence of boundary mixing. *Journal of Geophysical Research*, 96(C7), 12586–12592. <https://doi.org/10.1029/90JC02488>
- Noh, Y., & Fernando, H. J. S. (1992). The motion of a buoyant cloud along an incline in the presence of boundary mixing. *Journal of Fluid Mechanics*, 235, 557–577. <https://doi.org/10.1017/S0022112092001228>
- Noh, Y., Fernando, H. J. S., & Ching, C. Y. (1992). Flows induced by the impingement of a two-dimensional thermal on a density interface. *Journal of Physical Oceanography*, 22(10), 1207–1220. [https://doi.org/10.1175/1520-0485\(1992\)022<1207:FIBTIO>2.0.CO;2](https://doi.org/10.1175/1520-0485(1992)022<1207:FIBTIO>2.0.CO;2)
- Ogawa, S., Sha, W., Iwasaki, T., & Wang, Z. (2003). A numerical study on the interaction of a sea-breeze front with convective cells in the daytime boundary layer. *Journal of the Meteorological Society of Japan. Ser. II*, 81(4), 635–651. <https://doi.org/10.2151/jmsj.81.635>
- Parker, D. J., Burton, R. R., Diongue-Niang, A., Ellis, R. J., Felton, M., Taylor, C. M., Thorncroft, C. D., Bessemoulin, P., & Tompkins, A. M. (2005). The diurnal cycle of the West African

- monsoon circulation. *Quarterly Journal of the Royal Meteorological Society*, 131(611), 2839–2860. <https://doi.org/10.1256/qj.04.52>
- Pawlak, G., & Armi, L. (2000). Mixing and entrainment in developing stratified currents. *Journal of Fluid Mechanics*, 424, 45–73. <https://doi.org/10.1017/S0022112000001877>
- Safaie, A., Pawlak, G., & Davis, K. A. (2022). Diurnal thermally driven cross-shore exchange in steady alongshore currents. *Journal of Geophysical Research: Oceans*, 127(4), e2021JC017912. <https://doi.org/10.1029/2021JC017912>
- Salinas, J., Balachandar, S., Shringarpure, M., Fedele, J., Hoyal, D., & Cantero, M. (2020). Soft transition between subcritical and supercritical currents through intermittent cascading interfacial instabilities. *Proceedings of the National Academy of Sciences*, 117(31), 18278–18284. <https://doi.org/10.1073/pnas.2008959117>
- Serafin, S., & Zardi, D. (2010). Daytime heat transfer processes related to slope flows and turbulent convection in an idealized mountain valley. *Journal of the Atmospheric Sciences*, 67(11), 3739–3756. <https://doi.org/10.1175/2010JAS3428.1>
- Sha, W., Kawamura, T., & Ueda, H. (1991). A numerical study on sea/land breezes as a gravity current: Kelvin–Helmholtz billows and inland penetration of the sea-breeze front. *Journal of the Atmospheric Sciences*, 48(14), 1649–1665. [https://doi.org/10.1175/1520-0469\(1991\)048<1649:ANSOSB>2.0.CO;2](https://doi.org/10.1175/1520-0469(1991)048<1649:ANSOSB>2.0.CO;2)
- Simpson, J. E. (1982). Gravity currents in the laboratory, atmosphere, and ocean. *Annual Review of Fluid Mechanics*, 14(1), 213–234. <https://doi.org/10.1146/annurev.fl.14.010182.001241>
- Simpson, J. E. (1986). Mixing at the front of a gravity current. *Acta Mechanica*, 63(1-4), 245–253. <https://doi.org/10.1007/BF01182551>
- Simpson, J. E., & Britter, R. E. (1980). A laboratory model of an atmospheric mesofront. *Quarterly Journal of the Royal Meteorological Society*, 106(449), 485–500. <https://doi.org/10.1002/qj.49710644907>
- Simpson, J. E., Mansfield, D. A., & Milford, J. R. (1977). Inland penetration of sea-breeze fronts. *Quarterly Journal of the Royal Meteorological Society*, 103(435), 47–76. <https://doi.org/10.1002/qj.49710343504>
- Stull, R. B. (1976). Internal gravity waves generated by penetrative convection. *Journal of the Atmospheric Sciences*, 33(7), 1279–1286. [https://doi.org/10.1175/1520-0469\(1976\)033<1279:IGWGBP>2.0.CO;2](https://doi.org/10.1175/1520-0469(1976)033<1279:IGWGBP>2.0.CO;2)
- Sullivan, P. P., Moeng, C.-H., Stevens, B., Lenschow, D. H., & Mayor, S. D. (1998). Structure of the entrainment zone capping the convective atmospheric boundary layer. *Journal of the Atmospheric Sciences*, 55(19), 3042–3064. [https://doi.org/10.1175/1520-0469\(1998\)055<3042:SOTEZC>2.0.CO;2](https://doi.org/10.1175/1520-0469(1998)055<3042:SOTEZC>2.0.CO;2)

- Thorpe, S. A., & Ozen, B. (2007). Are cascading flows stable? *Journal of Fluid Mechanics*, 589, 411–432. <https://doi.org/10.1017/S0022112007007902>
- Ulloa, H. N., Ramón, C. L., Doda, T., Wüest, A., & Bouffard, D. (2022). Development of overturning circulation in sloping waterbodies due to surface cooling. *Journal of Fluid Mechanics*, 930, A18. <https://doi.org/10.1017/jfm.2021.883>
- Veronis, G. (1963). Penetrative convection. *The Astrophysical Journal*, 137, 641–663. <https://doi.org/10.1086/147538>
- Wells, M. G., & Dorrell, R. M. (2021). Turbulence processes within turbidity currents. *Annual Review of Fluid Mechanics*, 53(1), 59–83. <https://doi.org/10.1146/annurev-fluid-010719-060309>
- Winters, K. B., & Seim, H. E. (2000). The role of dissipation and mixing in exchange flow through a contracting channel. *Journal of Fluid Mechanics*, 407, 265–290. <https://doi.org/10.1017/S0022112099007727>
- Wright, L. D., Friedrichs, C. T., Kim, S. C., & Scully, M. E. (2001). Effects of ambient currents and waves on gravity-driven sediment transport on continental shelves. *Marine Geology*, 175(1-4), 25–45. [https://doi.org/10.1016/S0025-3227\(01\)00140-2](https://doi.org/10.1016/S0025-3227(01)00140-2)
- Zhu, D. Z., & Lawrence, G. A. (2001). Holmboe’s instability in exchange flows. *Journal of Fluid Mechanics*, 429, 391–409. <https://doi.org/10.1017/S002211200000286X>

Supplementary Information for Chapter 3

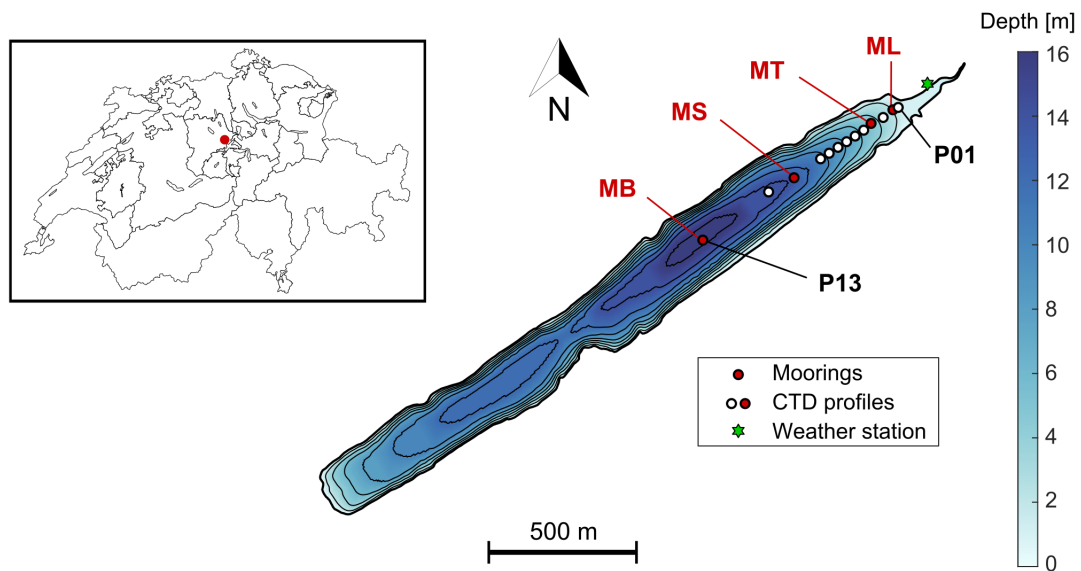


Figure S3.1 – Bathymetric map of Rotsee including the weather station (green star), moorings (red dots) and CTD profiles (white and red dots). Black lines are 2 m spaced isobaths. The location of Rotsee is shown on the map of Switzerland by a red dot. Source: Federal Office of Topography.

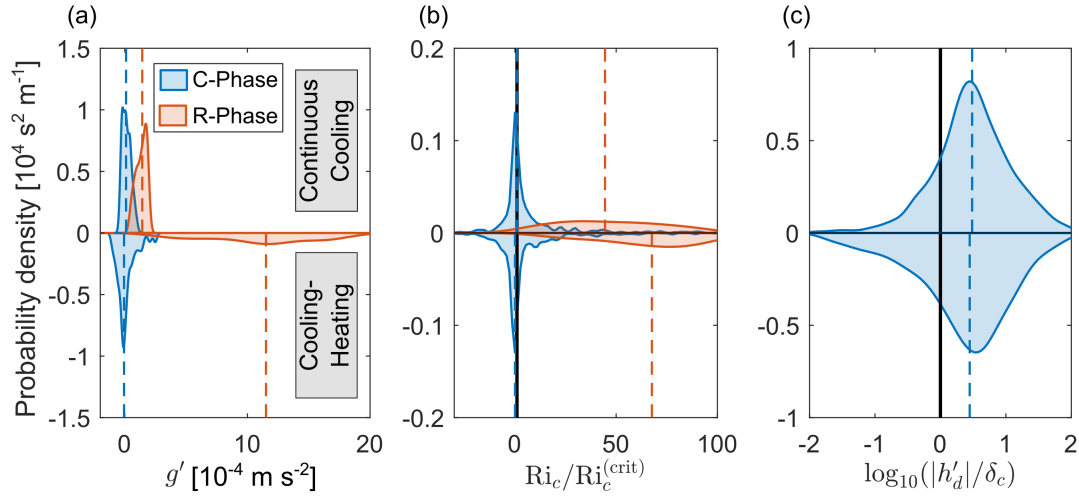


Figure S3.2 – Probability density plots comparing the convective (blue) and relaxation (orange) phases, for the cooling-heating and continuous-cooling scenarios (lower and upper part of each panel, respectively), for (a) the reduced gravity of the gravity current, (b) the convective Richardson number normalized by $Ri_c^{(crit)} = 10$, and (c) the vertical fluctuations of the interface $|h'_d|$ normalized by the penetration depth δ_c (during the C-phase only). Both negative and positive values are included in (a) and (b). The intervals shown are a subset of the dataset (without extreme values). The vertical dashed lines show the median values over each phase. The vertical black solid line in (b) and (c) indicates a ratio of one, which overlaps with the median values of the C-phase in (b).

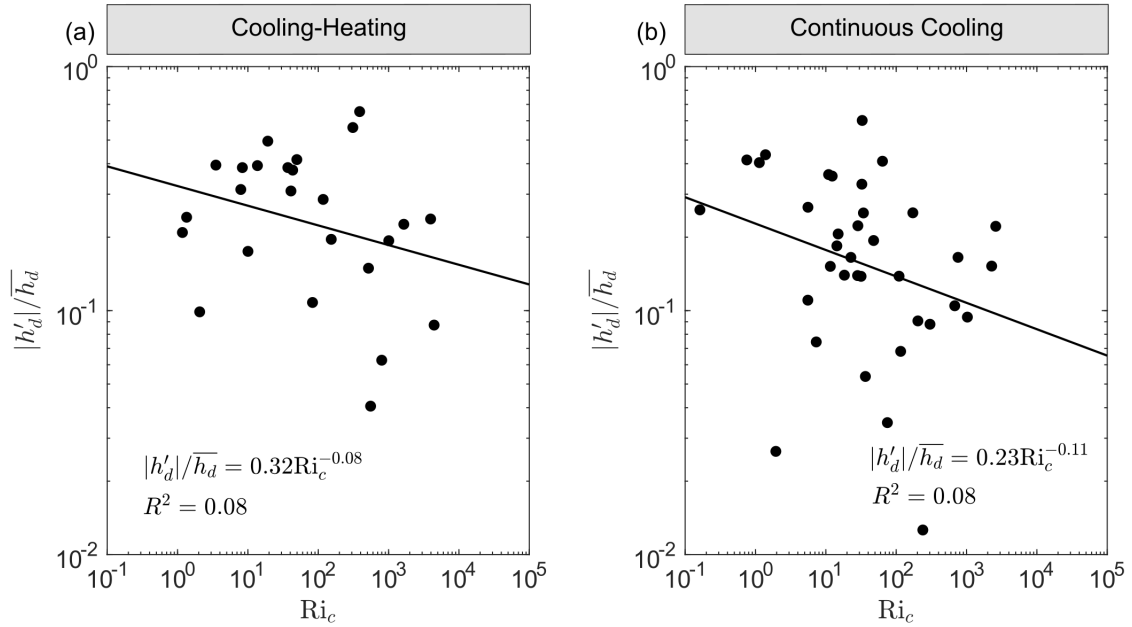


Figure S3.3 – Burst-averaged vertical fluctuations of the interface normalized by the mean current thickness $|h'_d|/\overline{h_d}$ as a function of the convective Richardson number Ri_c during the C-phase for (a) the cooling-heating case (10-11 October) and (b) the continuous-cooling case (6-7 November). The black line indicates the best fit $|h'_d|/\overline{h_d} = \beta Ri_c^{-\gamma}$ with β and γ two fitting coefficients. The equation of the fit and coefficient of determination R^2 are shown.

Table S3.1 – Potential mechanisms generating interface fluctuations. The periodicity of these fluctuations are estimated using the buoyancy frequency $N_d^2 \approx 1 \times 10^{-4} \text{ s}^{-2}$, the length and average depth of the plateau region $L_p \approx 200 \text{ m}$ and $h_p \approx 1 \text{ m}$, and the maximal reduced gravity $g'_{\max} = 5.9 \times 10^{-4} \text{ m s}^{-2}$. The estimated periodicities can be compared with the observed $T_{h'_d} \approx 1 \text{ h}$. Convectively driven internal waves (oscillator effect) and shear instabilities in marginally unstable flows both lead to high frequency fluctuations ($T_{\text{IW, mech}} \ll T_{\text{shear}} \ll T_{h'_d}$) whereas periodic pluses lead to low frequency fluctuations ($T_{\text{pulses}} \gg T_{h'_d}$). Shear instabilities and roll waves depend on the flow regime, which did not consistently change between the C- and R-phases, suggesting that these processes do not explain the observed fluctuations.

Process	Formation	Expected period	Reference(s)
Internal waves	<ul style="list-style-type: none"> – Updrafts-downdrafts (mechanical oscillator effect) – Penetration into the shear flow (obstacle effect) – Heat fluxes within the stratified layer (thermal forcing effect) 	$T_{\text{IW, mech}} = 1/N_d = 2 \text{ min}$	Fritts and Alexander, 2003 Ansong and Sutherland, 2010
Shear instabilities	Marginal instability: $\text{Fr}_D \gtrsim \text{Fr}_D^{(\text{crit})}$, $\text{Ri}_{g, \text{int}} \lesssim \text{Ri}_g^{(\text{crit})}$ (no difference between the C- and R-phases for the continuous-cooling scenario)	$T_{\text{shear}} \approx 1/N_d = 2 \text{ min}$	Pawlak and Armi, 2000 Thorpe and Ozen, 2007
Pulses	Periodic replacement of flushed littoral waters by the surface return flow	$T_{\text{pulses}} = \left(1 + \frac{1}{\sqrt{2}}\right) \frac{L_p}{\sqrt{0.5 g'_{\max} h_p}} \approx 5.5 \text{ h}$	Fer et al., 2001
Roll waves	Condition of formation: $\text{Fr}_D > 2$ (no difference between the C- and R-phases for the continuous-cooling scenario)	–	Dressler, 1949 Needham and Merkin, 1984

Chapter 4

Lake surface cooling drives littoral-pelagic exchanges of dissolved gases

Tomy Doda^{1,2}, Cintia L. Ramón⁴, Hugo N. Ulloa³, Matthias S. Brennwald⁵, Rolf Kipfer⁵, Marie-Elodie Perga⁶, Alfred Wüest², Carsten J. Schubert¹, Damien Bouffard¹

¹Eawag, Swiss Federal Institute of Aquatic Science and Technology, Department of Surface Waters – Research and Management, Kastanienbaum, Switzerland

²Limnology Center, École Polytechnique Fédérale de Lausanne, Lausanne, Switzerland

³Department of Earth and Environmental Science, University of Pennsylvania, Philadelphia, USA

⁴Department of Civil Engineering, University of Granada, Granada, Spain

⁵Eawag, Swiss Federal Institute of Aquatic Science and Technology, Department of Water Resources and Drinking Water, Dübendorf, Switzerland

⁶Faculty of Geoscience and Environment, Institute of Earth Surface Dynamics, University of Lausanne, Lausanne, Switzerland

In preparation.

Author contributions: TD, MB and DB designed the field experiments. TD led the data collection and analysis. TD wrote the initial draft of the manuscript, and all coauthors commented on and edited the text.

Abstract

Lakes produce, consume and exchange gases with the atmosphere. Estimates of reaction rates and vertical fluxes of dissolved gases are traditionally derived from a one-dimensional vertical representation of lakes that assumes negligible lateral fluxes. A growing concern about errors and anomalies resulting from this assumption motivates the need for a better comprehension of lateral transport mechanisms. Recent studies have suggested that the daily convective circulation driven by differential cooling was responsible for frequent littoral-pelagic exchanges of dissolved gases that potentially affected the offshore gases distribution. This lateral transport, however, remains to be observed and quantified. Here, we provide the direct evidence that the convective circulation exchanges dissolved gases laterally. Based on a gas tracer experiment and high frequency measurements of dissolved oxygen and methane in a wind-sheltered eutrophic lake, we found that the convective circulation transports littoral gases offshore and pelagic gases onshore. Lateral advective fluxes exceeded reaction rates and caused similar concentration anomalies as the ones reported in other lakes. Our results reveal that convective circulation is a key lateral exchange mechanism in lakes with shallow littoral regions. The traditional, one-dimensional, framework must be revisited to include such lateral fluxes in lake ecosystem studies.

4.1 Introduction

Lake ecosystems have traditionally been studied by representing their pelagic zone as a vertical water column disconnected from the watershed. This one-dimensional framework has led limnologists to quantify vertical fluxes of dissolved substances and to minimize the contribution of lateral fluxes (Reynolds, 2008; Vander Zanden & Vadeboncoeur, 2020). In particular, lateral fluxes of dissolved gases are assumed diffusive or even negligible in greenhouse gases budget and ecosystem metabolism estimates (Antenucci et al., 2013; Bogard et al., 2014; Brothers et al., 2017; Brothers & Vadeboncoeur, 2021; Czikowsky et al., 2018; Donis et al., 2017; Encinas Fernández et al., 2014). Unexplained anomalies in the pelagic region have recently challenged this assumption. Such anomalies include oxic methane peaks (Donis et al., 2017; Grossart et al., 2011; Günthel et al., 2019; Murase et al., 2003; Tsunogai et al., 2020; van Grinsven et al., 2021; Wang et al., 2017; Xiao et al., 2020), noisy and erroneous metabolic estimates (Brothers et al., 2017; Coloso et al., 2008; Hanson et al., 2008; Idrizaj et al., 2016; Lauster et al., 2006; Staehr et al., 2010), vertical differences in carbon isotopic ratios (Murase et al., 2003; Schubert et al., 2010; Tsunogai et al., 2020) and missing sources of gases in mass balances (Czikowsky et al., 2018). While biological processes partly explain some

of these anomalies (Bogard et al., 2014; Grossart et al., 2011; Yao et al., 2016), numerous studies have pointed to a contribution of lateral transport from the littoral region, motivated by the recurrent littoral-pelagic differences in dissolved gases concentrations (Brothers et al., 2017; DelSontro et al., 2018; Encinas Fernández et al., 2016; Hanson et al., 2008; Hofmann et al., 2010; Idrizaj et al., 2016; Murase et al., 2003; Sadro et al., 2011; Tsunogai et al., 2020). Yet, these studies have lacked a direct quantification of the lateral exchange.

One of the lateral transport mechanisms mentioned for dissolved gases is the two-layer convective circulation driven by differential cooling (Brothers et al., 2017; Czikowsky et al., 2018; Hanson et al., 2008; Sadro et al., 2011), also known as thermal siphons (Monismith et al., 1990). When the sloping region of lakes experiences surface cooling, a lateral density gradient forms, driving a downslope gravity current (lower branch of the circulation) and a surface return flow (upper branch) (Horsch & Stefan, 1988; Monismith et al., 1990) (Fig. 4.1). In presence of a negative (positive) lateral gradient of concentration, the offshore transport of littoral waters by the lower branch would increase (decrease) pelagic concentrations in the surface mixed layer (compounds A and B in Fig. 4.1a). We hypothesize that the upper branch would cause an additional lateral transport in the opposite direction and modify concentrations in the sloping region. A specificity of the convective circulation is its daily occurrence in wind-sheltered lakes with shallow nearshore regions (Doda et al., 2022), potentially generating frequent littoral-pelagic exchanges of dissolved gases (Brothers et al., 2017). This advective transport would be stronger than diffusion or horizontal dispersion used to model lateral exchange in mass balances (Antenucci et al., 2013; DelSontro et al., 2018; Donis et al., 2017; Peeters et al., 2019). Although the convective circulation has been reported in numerous lakes (e.g., Doda et al., 2022; Fer et al., 2002b; James & Barko, 1991a; Monismith et al., 1990; Pålmarsson & Schladow, 2008), its role for the lateral exchange of dissolved gases remains to be proven.

In this study, we investigate the transport of dissolved gases by convective circulation in a wind-sheltered eutrophic lake (Rotsee, Switzerland), during autumn turnover. We demonstrate the downslope transport of a littoral gas tracer by the lower branch of the circulation and its intrusion into the pelagic zone. Based on opposite lateral gradients of oxygen and methane, we further show that the two branches transport reactive gases in both directions, fast enough to overcome consumption rates. By causing concentration anomalies in the sloping and pelagic regions, the convective circulation highlights the necessity of considering lateral fluxes in lake ecosystem studies.

4.2 Methods

4.2.1 Study site

Rotsee is a small eutrophic peri-alpine lake in Central Switzerland (47°4'29" N, 8°19'29" E; elevation of 419 m above sea level; surface area of 0.5 km², mean and maximum depths of 9 m and 16 m, respectively). It is an elongated lake (2.5 km long, 0.2 km wide), wind-sheltered and characterized by a 200 m long and 1 m deep plateau region at its northeastern end (Fig. S4.1). This shallow littoral region generates thermal siphons at a daily frequency in autumn (Doda et al., 2022). The anoxic hypolimnion of Rotsee accumulates methane during the summer stratified season, which is brought to the epilimnion during autumn lake turnover to be oxidized or emitted to the atmosphere (Mayr et al., 2020; Schubert et al., 2010; Schubert et al., 2012; Zimmermann et al., 2021).

4.2.2 Physical measurements

We defined the x axis as the preferential flow direction along the lake thalweg and we set its origin at the end of the plateau region (point M0, Fig. 4.1a). To monitor the cross-shore circulation originating from the northeastern plateau region, we deployed four vertical thermistor arrays (M1, MT, M2, MI) along the x axis, from 21 to 27 November 2020 (Fig. 4.1a, Fig. S4.1). The thermistors (RBR TR-1050, RBR TR-1060, RBR Solo-T) collected high-frequency water temperature (1-10 s sampling interval), with a vertical resolution of 0.25-0.5 m. Water velocity was measured over time and depth by bottom-moored upward-looking acoustic Doppler current profilers (ADCPs), at M1 (Nortek Aquadopp Profiler 2MHz, profiling 0.23-1.76 m above the sediment with 0.03 m vertical resolution), MT (Teledyne RD Instruments WorkHorse 1200 kHz, profiling 0.75-3.80 m above the sediment with 0.05 m vertical resolution) and MI (Teledyne RD Instruments WorkHorse 600 kHz, profiling 0.8-6.4 m above the sediment with 0.1 m vertical resolution). The three ADCPs provided burst-averaged three-dimensional velocity every 15 min. An additional thermistor array (MB, Vemco Minilog II-T loggers, 1 m vertical resolution, 2 min sampling interval) monitored the background thermal structure near the deepest point. A WxPRO Campbell weather station installed on the lake shore near the plateau region (47°4'34" N, 8°19'38" E) provided local meteorological forcing during the entire measurement period. Further details on the long-term physical measurements are given in Doda et al. (2022).

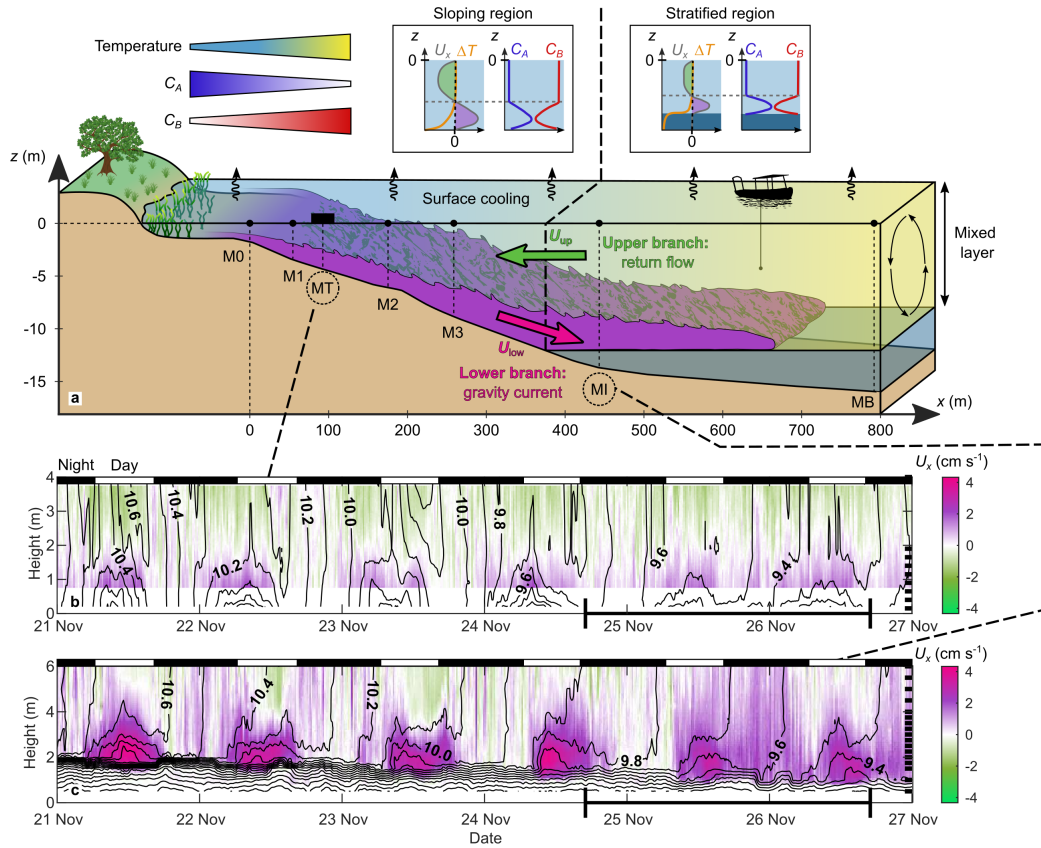


Figure 4.1 – Differential cooling drives a diurnal cross-shore convective circulation. (a) Schematic of the two-layer circulation along a cross-shore transect. The lower branch (purple) is a downslope gravity current of velocity U_{low} that intrudes at the base of the mixed layer. The upper branch (green) is an opposite surface flow of velocity U_{up} directed towards the shore. The lateral transport induced by this circulation is depicted for two hypothetical dissolved compounds A and B. Compound A (blue) is more concentrated nearshore whereas compound B (red) is more concentrated offshore. Theoretical profiles of cross-shore velocity (U_x), temperature anomaly with respect to the surface (ΔT) and concentration of compounds A (C_A) and B (C_B) are shown for the sloping and stratified regions, defined respectively as the regions shallower and deeper than the mixed layer depth. Epilimnion (mixed layer) and hypolimnion are represented in the profiles with light and dark blue areas, respectively. Vertical dashed lines indicate the location of the seven measurement stations in Rotsee, where dissolved gases concentrations were measured by two mass spectrometers, installed at MT (platform) and on a boat. (b,c) Six days-long time series of cross-shore velocity as a function of height above the sediment, measured in the (b) sloping region (MT, 4.2 m deep) and (c) stratified region (MI, 13.3 m deep). Note that the scale of the y-axis is different between (b) and (c). Black lines are 0.1 °C spaced isotherms, from linearly interpolated temperature between each thermistor. Horizontal black ticks on the right axis indicate the vertical resolution of the thermistors. Day and night periods are shown by black and white rectangles, respectively. The experiment period on 24-26 November is highlighted on the x axis.

4.2.3 Dissolved gases measurements during the two-days-long campaign

We performed a two-days-long campaign from 24 to 26 November 2020 to quantify the lateral transport of dissolved gases by thermal siphons. Two portable mass spectrometers “miniRuedi” measured the concentration of seven gases, including methane and krypton (Brennwald et al., 2016). Each miniRuedi received lake water pumped from specific depths. The inflowing water was filtered before entering a gas-equilibrium membrane contactor, where dissolved gases were transferred to the air phase and brought to the mass spectrometer through a capillary. One miniRuedi was installed on a moored rowing platform at MT. It continuously sampled the littoral region (M0, $x = 0$ m, 1.6 m deep) at 0.9 m and 1.3 m depth and the sloping region (MT, $x = 90$ m, 4.3 m deep), in the upper (0.6 m deep) and lower (3.8 m deep) branches of the circulation (Fig. 4.1a and Tab. S4.1). Lake water was collected at each of these four locations by a submersible pump and carried to the miniRuedi via a PVC tube. The outflowing water of the miniRuedi was pumped to the southeastern shore, to prevent any contamination of the measurements at MT. The second miniRuedi sampled the five other stations (M1, M2, M3, MI, MB) from a boat (Fig. 4.1a and Tab. S4.1). The samples were continuously collected at each mooring for several hours before moving to another location. Two submersible pumps, both combined with a RBR duet-TD logger for pressure measurements, were lowered at two different depths for each station. One pump was kept at around 0.5 m below the surface (upper branch of the circulation), the other was used to profile different depths (M3, MI) or the base of the mixed layer only (M1, M2, MB; lower branch of the circulation). The outflowing water of the miniRuedi was pumped back to the sampling depth. Both miniRuedis sampled the different inlets (depths) one after the other. The same inlet was sampled every 14 min on the boat and every 28 min on the platform. These sampling intervals were longer than the water residence time in the tube (approximately 7 min between M0 and the moored miniRuedi). For each inlet, average gas concentrations were computed from 5 repeated samples, spaced 17 s apart. The measurements were calibrated by sampling a standard gas (air enriched with 1 % CH₄ and 1 % CO₂) every hour. In addition, cross-calibration between the two miniRuedis was performed from measurements at nearby locations. At each location, the average methane concentration in the mixed layer was computed by averaging the surface and bottom concentrations.

We collected Conductivity-Temperature-Depth-Oxygen (CTDO) profiles (Sea & Sun Technology CTD60M) every ≈ 15 min, from the boat at M1, M2, MI and MB (same periods than for the miniRuedi, Tab. S4.1) and from the platform at MT (24 November 17:00-26 November 11:00, with an interruption between 17:00 and 21:00 on 25 November). Both profilers were equipped with an optical oxygen sensor that measured the percentage of saturation of dissolved oxygen. For each

profile, we calculated the average oxygen saturation in the mixed layer interior, between 1.5 and 2.5 m depth, to remove the oxygen peaks at the surface (atmospheric input) and at the bottom (lateral transport).

4.2.4 Gas tracer experiment

We performed a gas tracer experiment on 25 November by injecting krypton (inert gas) in the littoral region at M0, and tracking its offshore transport with both miniRuedis. A 10 L krypton bottle (approximately 60 moles of Kr at 142 bar) was installed at the shore and connected to an impermeable pipe that reached M0. A diffuser, made of a 20 m-long porous pipe, was placed on the sediment, perpendicularly to the x-axis, with M0 in its middle. The diffuser produced bubbles, which mixed the gas vertically across the water column. On 25 November, we started the injection at 3:50 UTC by opening the krypton bottle. All the gas was injected after approximately 4 h.

4.2.5 Velocity data analysis

The velocity data collected by the ADCPs was projected onto the x-axis (56° angle from north) to obtain the cross-shore velocity U_x . The depth of the interface z_d between the two branches of the circulation was found from the stagnation point $U_x = 0$. Depth-averaged velocities of the lower and upper branches were calculated as $U_{\text{low}}(t) = \frac{1}{z_d - z_{\text{sed}}} \int_{z_{\text{sed}}}^{z_d} U_x(z, t) dz$ and $U_{\text{up}}(t) = -\frac{1}{z_d} \int_{z_d}^0 U_x(z, t) dz$, respectively.

4.3 Cross-shore convective circulation driven by differential cooling

To quantify the convective circulation driven by differential cooling, we collected 6 days-long time series of velocity and temperature in late November 2020, in the sloping region (MT, shallower than the mixed layer depth) and stratified region (MI), off the northeastern plateau of Rotsee (Figs. 4.1b and 4.1c). Differential cooling occurred continuously during this period and led to lateral surface temperature gradients of $\partial T / \partial x \approx 5 \times 10^{-4} \text{ } ^\circ\text{C m}^{-1}$ (Fig. S4.2b). We detected thermal siphons at a daily frequency, generating cold downslope pulses in the sloping region with cross-shore velocities of $U_x \sim 1 \text{ cm s}^{-1}$, thickness of $h_{\text{low}} \sim 1 \text{ m}$ and bottom stratification of $\partial T / \partial z \sim 0.1 \text{ } ^\circ\text{C m}^{-1}$. Thermal siphons formed at night, intensified in the morning and weakened in the early afternoon (Fig.

4.1b), as reported by Doda et al. (2022). In the stratified region, the gravity current flowed for the entire day at the base of the surface mixed layer around 12 m depth (Fig. 4.1c). It reached the lake deepest point (MB), 800 m offshore from the plateau region (Fig. S4.2d). The unit-width discharge of the upper and lower branches of the circulation was $q_x \sim 0.01 \text{ m}^2 \text{ s}^{-1}$, which led to a complete flushing of the 200 m-long plateau region in approximately 6 h. These time series demonstrate that thermal siphons regularly exchanged water between the littoral and pelagic regions of Rotsee and had the potential to transport dissolved gases laterally.

The two-days-long campaign (24-26 November) was divided into two different hydrodynamic periods. During the first night, the convective circulation was weak in the sloping region (vertically mixed water column, $U_x < 1 \text{ cm s}^{-1}$) and absent in the stratified region. After sunrise on 25 November, the circulation intensified in both regions and persisted until the end of the campaign, despite being weaker during the second night. This flow intensification suggests a stronger lateral exchange on 25 November.

4.4 Lateral transport of a littoral gas tracer

Our primary objective was to determine whether thermal siphons were capable of transporting littoral gases offshore. To address this question, we performed a tracer experiment by injecting an inert gas (krypton) in the littoral region at M0 and we measured its concentration at different locations along a cross-shore transect, with two portable mass spectrometers (Fig. 4.2). After the injection on 25 November (03:50 UTC), the krypton concentration at M0 reached $\sim 1 \mu\text{mol L}^{-1}$ which was three orders of magnitude larger than the background concentration offshore (Figs. 4.2b and 4.2c). A sharp increase of krypton concentration was captured at M1 and MT, 1.1 h and 1.9 h after the injection, respectively (Fig. 4.2b). This increase was confined to the downslope flow (0.5 m above the sediment), and absent from the surface layer (Fig. 4.2c), which indicates that the lower branch of the circulation transported the krypton plume offshore. The slow increase of surface krypton concentration at MT 3 h after the injection was likely due to vertical mixing between the two branches of the circulation. The approximate plume velocity of 1.4 cm s^{-1} , estimated from the time of krypton arrival at each station, is close to the peak velocity of the downslope flow (Fig. 4.2a), which confirms the downslope krypton transport by the thermal siphon.

Krypton was further transported into the stratified region, more than 400 m offshore from M0, where the krypton plume intruded at the base of the mixed layer (Fig. 4.2d). The krypton concentrations in the intrusive plume at MI were more than one order of magnitude lower than

in the downslope flow, which could be an indicator of dilution with the upper layer. Yet, we cannot provide robust dilution estimates, as the location of MI was not necessarily aligned with the trajectory of the most concentrated part of the plume. The increase in average plume velocity between MT and MI was consistent with the flow intensification in the morning (Figs. 4.2a and 4.2b). This tracer experiment demonstrates that the lower branch of the convective circulation is capable of bringing littoral gases to the stratified region.

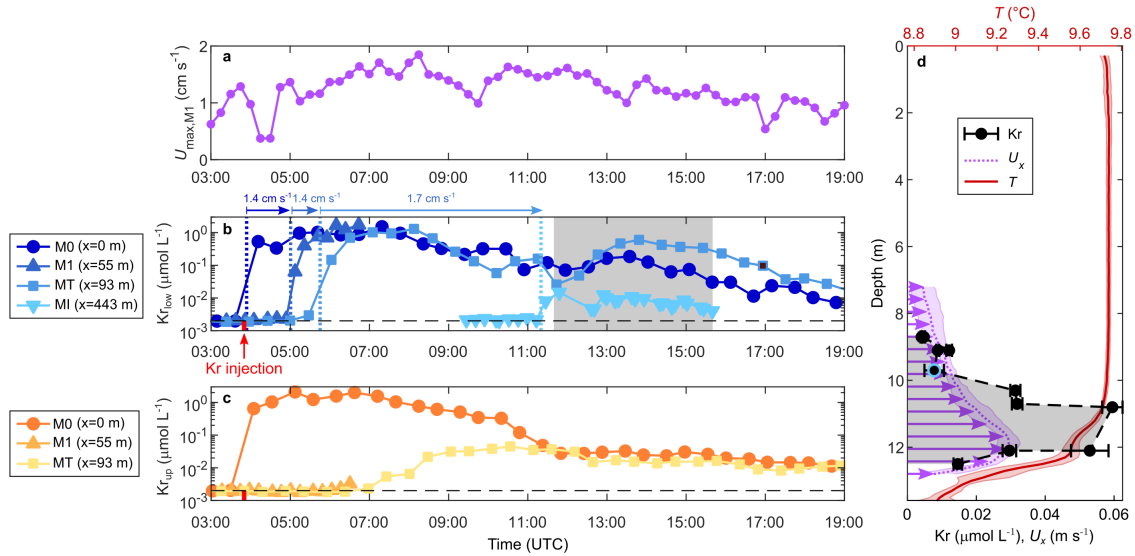


Figure 4.2 – The lower branch of the circulation transports injected krypton offshore. (a) Time series of the maximal cross-shore velocity of the gravity current at M1 on 25 November. (b,c) Time series of krypton concentrations at several locations along the cross-shore transect on 25 November, in (b) the lower branch and (c) the upper branch of the circulation. The time of krypton injection at M0 is indicated by a red tick on the x axis. The horizontal black dashed line shows the background krypton concentration of $\approx 10^{-3} \mu\text{mol L}^{-1}$. Note the logarithmic scale on the y axis. Vertical dotted lines in (b) correspond to the arrival time of the krypton plume at each location, which is used to estimate the plume velocity indicated on the upper x axis. (d) Time-averaged vertical profiles of temperature (red), cross-shore velocity (purple) and krypton concentration (black dots) in the stratified region at MI (11:40-15:40, gray area in (b)). The standard deviation is depicted with a shaded area on the velocity and temperature profiles and with horizontal error bars on the krypton profile. The blue circle indicates the location of the MI time series in (b).

4.5 Littoral-pelagic downslope transport of oxygen

After having demonstrated the downslope transport of a littoral gas tracer, we investigated the transport of naturally present dissolved gases. We collected Conductivity-Temperature-Depth-Oxygen (CTDO) profiles along a cross-shore transect on 25 November and expressed the dissolved oxygen concentration in percent saturation, independent of temperature. The oxygen saturation

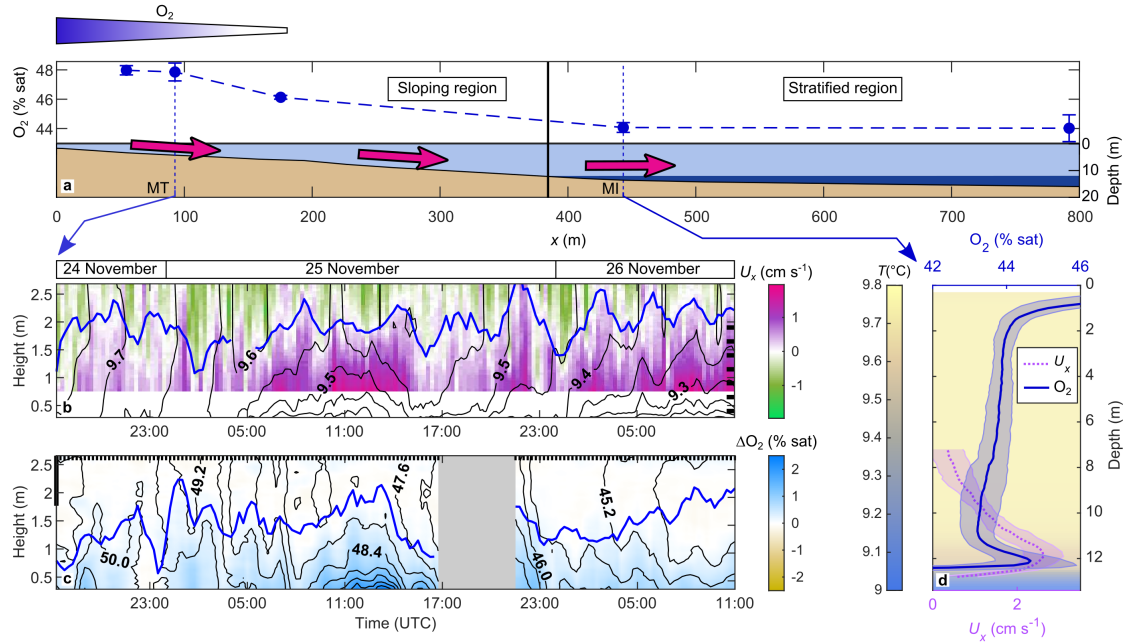


Figure 4.3 – The lower branch of the circulation transports oxygen offshore. (a) Cross-shore gradient of oxygen saturation in the mixed layer from CTDO profiles (25 November, 03:00-20:00). Percent saturation is averaged between 1.5 and 2.5 m depth and between different profiles. Vertical error bars indicate the standard deviation. The cross-shore topography is represented in the lower part of the panel, with light and dark blue areas corresponding to the epilimnion and the hypolimnion, respectively. The vertical black line delimits the sloping and stratified regions. Oxygen saturation is higher nearshore, as compound A in Fig. 4.1, which leads to a net offshore transport by the downslope gravity current (purple arrows). (b,c) Time series of (b) cross-shore velocity and (c) oxygen concentration in the sloping region at MT, as a function of height above the sediment, from 24 to 26 November. The velocity time series in b are a subset of Fig. 4.1b, where black lines are 0.05 °C spaced isotherms and the blue line is the upper interface of the gravity current. The oxygen saturation in c is linearly interpolated from oxygen profiles collected every 15 min (vertical ticks on the upper x axis). The measurements were stopped between 17:00 and 21:00 on 25 November (gray area). The color map shows the oxygen saturation anomaly with respect to the mixed layer interior (1.5-2.5 m depth, thick line on the left y-axis). Black lines are 0.4 % spaced isolines and the blue line is the upper boundary of the bottom stratification (defined as $\partial T / \partial z > 0.01$ °C m⁻¹ from temperature profiles). (d) Time-averaged vertical profiles of oxygen (blue) and cross-shore velocity (purple) in the stratified region at MI (09:00-15:45). The shaded area around each profile indicates the standard deviation. The background color map represents the time-averaged temperature profile.

averaged in the mixed layer was less than 50 % (under saturation) and was 4 % higher in the littoral region than in the pelagic region, leading to a cross-shore gradient of $\partial O_2 / \partial x = -0.01$ % m⁻¹ (equivalent to -0.03 μmol L⁻¹ m⁻¹) (Fig. 4.3a, Fig. S4.3). The lower oxygen saturation in the pelagic region could result from the strong methane oxidation observed in Rotsee during fall turnover (Mayr et al., 2020; Schubert et al., 2010; Schubert et al., 2012; Zimmermann et al., 2021). Oxygen

was thereby similar to compound A in Fig. 4.1, indicating a possible offshore transport by the lower branch of the circulation, as observed in the tracer experiment.

Continuous measurements in the sloping region (MT) revealed the presence of a persistent oxic bottom layer, with oxygen saturation anomalies of $\Delta O_2 \sim 1\%$ with respect to the surface layer (equivalent to a concentration difference of $3 \mu\text{mol L}^{-1}$) (Fig. 4.3c). This oxic layer was 1-2 m thick and coincided with the stratified downslope flow (Fig. 4.3b). The bottom oxygen saturation increased in response to the current intensification on 25 November. While we cannot neglect benthic primary production during the day, the persistence of the oxic layer at night is a signature of downslope oxygen transport by the lower branch of the circulation. The net advective oxygen flux into the pelagic region was $F_{O_2,adv} \approx U_x \Delta O_2 \approx 3 \text{ mol m}^{-2} \text{ d}^{-1}$ with $U_x \approx 1 \text{ cm s}^{-1}$ and $\Delta O_2 \approx 3 \mu\text{mol L}^{-1}$, which is one order of magnitude larger than the lateral flux due to horizontal dispersion $F_{O_2,disp} = -K_x \partial O_2 / \partial x \sim 0.1 \text{ mol m}^{-2} \text{ d}^{-1}$ with $K_x \sim 0.1 \text{ m}^2 \text{ s}^{-1}$ (Antenucci et al., 2013; Peeters & Hofmann, 2015).

The gravity current intrusion transported oxygen across the stratified region, forming an oxic peak of 1.5 % saturation (equivalent to $5 \mu\text{mol L}^{-1}$) at the base of the mixed layer (Fig. 4.3d), similar to the intrusion of krypton (Fig. 4.2d). To observe such a peak in the pelagic region, the lateral transport must overcome oxygen consumption rates. Based on a typical oxidation rates of $R_{ox} = 10 \mu\text{mol O}_2 \text{ L}^{-1} \text{ d}^{-1}$ in Rotsee (Mayr et al., 2020; Schubert et al., 2010), $3 \mu\text{mol L}^{-1}$ of oxygen would be consumed during the 6 h long transport from the littoral to the stratified region (Fig. 4.2b). This represents only 20 % of the lateral oxygen concentration difference of $14 \mu\text{mol L}^{-1}$ between M1 and MI, which suggests an oxic peak of $\sim 10 \mu\text{mol L}^{-1}$ if only advection and oxidation rates are considered. Although the observed peak of $5 \mu\text{mol L}^{-1}$ was lower than predicted, its presence confirms a net oxygen transport to the pelagic region by the gravity current.

4.6 Pelagic-littoral surface transport of methane

Besides the offshore transport of littoral gases, we hypothesized that thermal siphons could also transport pelagic gases towards the shore (Fig. 4.1a). To verify this hypothesis, we measured methane concentrations with two portable mass spectrometers, spatially along a cross-shore transect and continuously in the sloping region (MT). The mixed layer was strongly oversaturated in methane, with concentrations of $\sim 10 \mu\text{mol L}^{-1}$ (Fig. 4.4a), consistent with previous measurements during mixing events in Rotsee (Schubert et al., 2012). Methane concentrations were higher in the pelagic region, leading to a lateral gradient of $\partial \text{CH}_4 / \partial x = 0.015 \mu\text{mol L}^{-1} \text{ m}^{-1}$. This positive

gradient differed from the common observations of higher littoral methane concentrations (e.g., Encinas Fernández et al., 2016; Hofmann, 2013; Murase et al., 2003; Schmidt & Conrad, 1993; Xiao et al., 2020), but agrees with reversed gradients during fall turnover in eutrophic lakes (Loken et al., 2019). Vertical convective mixing bringing accumulated methane from the hypolimnion to the epilimnion was likely responsible for the positive methane gradient in Rotsee. The relationship with the oxygen gradient $\partial\text{CH}_4/\partial x \approx -0.5\partial\text{O}_2/\partial x$ was consistent with methane oxidation stoichiometry. This positive methane gradient implies a potential onshore transport by the upper branch of the circulation, as for compound B in Fig. 4.1.

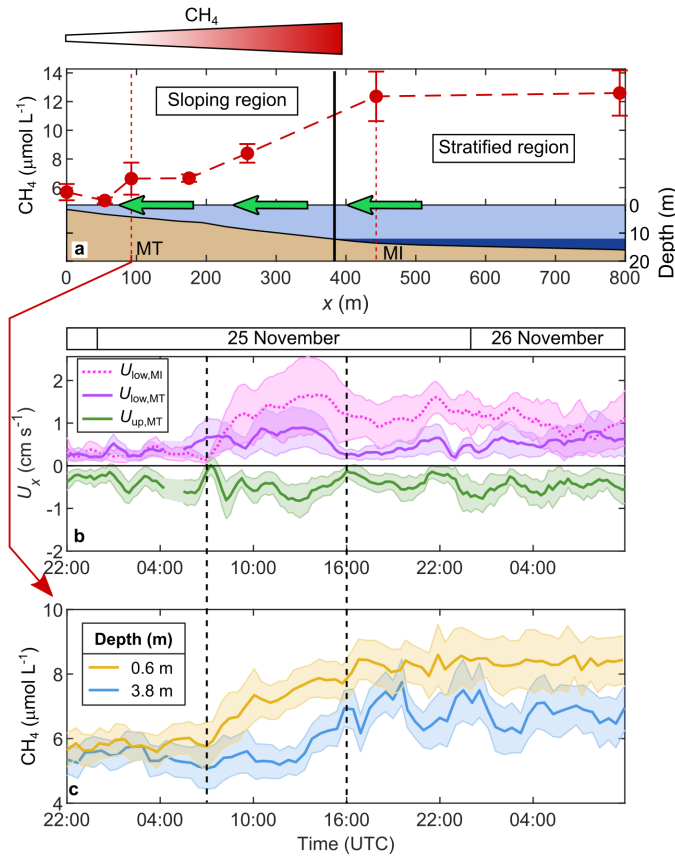


Figure 4.4 – The upper branch of the circulation transports methane onshore. (a) Cross-shore gradient of methane concentrations in the mixed layer (24 November 16:15 – 26 November 11:00). Concentrations are averaged over time and depth, between the surface and the base of the mixed layer. Vertical error bars indicate the standard deviation. The cross-shore topography is represented as in Fig. 4.3a. Methane concentrations are higher offshore, as compound B in Fig. 4.1, which leads to a net onshore transport by the surface return flow (green arrows). (b) Time series of depth-averaged cross-shore velocity in the lower branch (purple, $U_{\text{low}} > 0$) and in the upper branch (green, $U_{\text{up}} < 0$) of the circulation at MT, and in the intrusion at MI (dotted line, $U_{\text{low}} > 0$), from 24 to 26 November. Shaded areas depict the standard deviation. (c) Time series of methane concentration in the upper branch (yellow) and lower branch (blue) of the circulation at MT. Shaded areas depict the standard deviation. The vertical dashed lines in (b) and (c) delimit the period of stronger circulation on 25 November, around 07:00-16:00.

We verified this surface lateral transport by comparing the time series of methane concentration in the sloping region (MT), before and after the flow intensification on 25 November (Figs. 4.4b and 4.4c). The convective circulation was weak during the night ($U_{\text{low}} \approx -U_{\text{up}} \approx 0.3 \text{ cm s}^{-1}$) and methane concentrations at MT were vertically homogeneous in the mixed layer around $5\text{--}6 \mu\text{mol L}^{-1}$. When the convective circulation intensified in both the sloping and stratified region (07:00-16:00), reaching velocities of $U_{\text{low}} \approx -U_{\text{up}} \approx 1 \text{ cm s}^{-1}$, the surface methane concentration at MT increased by $\Delta\text{CH}_4 \approx 2 \mu\text{mol L}^{-1}$. This temporal increase confirms the surface methane transport from MI to MT by the upper branch of the circulation, leading to a net onshore flux of $F_{\text{CH}_4, \text{adv}} \approx U_x \Delta\text{CH}_4 \approx 2 \text{ mol m}^{-2} \text{ d}^{-1}$, with $U_x \approx 1 \text{ cm s}^{-1}$. The increase of bottom methane concentration 6 h after the flow intensification might be due to vertical mixing between the two branches of the circulation. Once the flow became steady, the surface methane concentration at MT remained around $8 \mu\text{mol L}^{-1}$ which was $4 \mu\text{mol L}^{-1}$ lower than at MI. This concentration difference resulted from methane losses by oxidation and atmospheric exchange during the $\tau = 8 \text{ h}$ long travel time from the stratified region to MT (300 m distance travelled at 1 cm s^{-1} velocity). The amount of methane oxidized during this period was $\tau \cdot R_{\text{ox}} = 2 \mu\text{mol L}^{-1}$ according to typical oxidation rates of $R_{\text{ox}} = 5 \mu\text{mol CH}_4 \text{ L}^{-1} \text{ d}^{-1}$ in autumn in Rotsee (Mayr et al., 2020; Schubert et al., 2010). Atmospheric exchange decreased the methane concentration by $\tau \cdot F_{\text{atm}}/h = 2 \mu\text{mol L}^{-1}$, with $F_{\text{atm}} = 0.5 \mu\text{mol CH}_4 \text{ m}^{-2} \text{ s}^{-1}$ the atmospheric methane flux measured in Rotsee during fall turnover events (Schubert et al., 2012) and $h = 7 \text{ m}$ the average depth between MT and the stratified region. Based on the initial concentration difference of $6 \mu\text{mol L}^{-1}$ between MT and MI (Fig. 4.4a), the total methane loss of $4 \mu\text{mol L}^{-1}$ suggests an increase of surface methane concentration of $2 \mu\text{mol L}^{-1}$ at MT, which agrees well with the observed ΔCH_4 . Methane was transported across the entire sloping region and reached M0 a few hours after MT (Fig. S4.4).

4.7 Implications for lateral transport in lakes

Our data demonstrate that convective circulation transports dissolved gases between the littoral and pelagic regions, in both directions. These lateral fluxes were one order of magnitude larger than horizontal dispersion fluxes used to model lateral transport of gases (DelSontro et al., 2018; Peeters et al., 2019). Lateral advection exceeded consumption rates and modified vertical concentration profiles in the sloping and stratified regions. Although these observations are specific to our study site, they provide a comprehensive understanding of a lateral transport mechanism ubiquitous to lakes with shallow littoral areas (Doda et al., 2022; Fer et al., 2002b; Horsch & Stefan, 1988; James & Barko, 1991a; Monismith et al., 1990; Pálmarsson & Schladow, 2008). These types of lakes are often characterized by lateral gradients of dissolved oxygen, carbon dioxide and methane (Cardinale

et al., 1997; Encinas Fernández et al., 2016; Hofmann, 2013; Loken et al., 2019; Mohseni et al., 2001; Murase et al., 2003; Xiao et al., 2020), making the convective circulation capable of modifying the vertical gases distribution offshore.

In Rotsee, we illustrated the lower branch downslope transport with oxygen and the upper branch onshore transport with methane, because lateral concentration gradients were negative for oxygen and positive for methane. The exchange mechanism is not gas-specific and only depends on the gradient direction. Thus, we would observe similar transport effects between different gases that have comparable lateral gradients. Negative methane gradients of $|\partial\text{CH}_4/\partial x| \sim 10^{-4} - 10^{-2} \mu\text{mol L}^{-1} \text{m}^{-1}$ have been reported in lakes (Encinas Fernández et al., 2016; Hofmann, 2013; Hofmann et al., 2010; Loken et al., 2019; Murase et al., 2003; Xiao et al., 2020) and observed in Rotsee in summer (Fig. S4.5), implying a downslope methane transport (compound A in Fig. 4.1). This transport would generate a methane peak at the base of the mixed layer, as observed for krypton and oxygen in our case, if advection would overcome methane losses. From methane oxidation rates of $R_{\text{ox}} = 0.01 - 1 \mu\text{mol L}^{-1} \text{d}^{-1}$ (Donis et al., 2017; Günthel et al., 2019; Mayr et al., 2020; Schubert et al., 2010) and cross-shore velocities of $U_x \sim 0.01 \text{m s}^{-1}$, minimum lateral gradients required to overcome oxidations rates are $|\partial\text{CH}_4/\partial x| \approx R_{\text{ox}}/U_x \sim 10^{-5} - 10^{-3} \mu\text{mol L}^{-1} \text{m}^{-1}$ which are of the same order of magnitude than typical methane gradients. Convective circulation can thereby contribute to the observed methane peaks in the pelagic region of lakes with lateral methane gradients. In Lake Hallwil and Lake Stechlin, where oxic methane peaks of $\Delta\text{CH}_4 \sim 0.1 - 1 \mu\text{mol L}^{-1}$ have been reported at a distance of $L_x \sim 1 \text{km}$ from the shore, methane oxidation rates and littoral-pelagic concentration differences were $R_{\text{ox}} \sim 0.01 \mu\text{mol L}^{-1} \text{d}^{-1}$ and $\Delta_x\text{CH}_4 \sim 0.1 - 1 \mu\text{mol L}^{-1}$ (gradient of $|\Delta_x\text{CH}_4/L_x| \sim 10^{-4} - 10^{-3} \mu\text{mol L}^{-1} \text{m}^{-1}$), respectively (Donis et al., 2017; Günthel et al., 2019; Xiao et al., 2020). Convective circulation would generate a peak of $\Delta\text{CH}_4 = \Delta_x\text{CH}_4 - R_{\text{ox}}L_x/U_x \sim 0.1 - 1 \mu\text{mol L}^{-1}$, if we neglect vertical mixing between the two branches. This estimate is of the same order of magnitude than observed ΔCH_4 , which indicates that convective circulation can be equally important as other biological and physical processes generating methane peaks.

Positive and negative oxygen and carbon dioxide lateral gradients are both possible, depending on the differences in metabolic rates between littoral and pelagic regions (Brothers et al., 2017; Brothers & Vadeboncoeur, 2021; Cardinale et al., 1997; Idrizaj et al., 2016; Lauster et al., 2006; Mohseni et al., 2001; Sadro et al., 2011). By assuming nighttime positive and daytime negative oxygen gradients (Brothers et al., 2017), the lower branch of the convective circulation would transport oxygen-depleted water in the morning and oxygen-enriched water in the afternoon, thereby modifying the pelagic oxygen concentration. This daily exchange would cause errors in

the estimation of metabolic rates from the diel oxygen method, as suggested by Hanson et al. (2008) and Brothers et al. (2017). However, our data shows that the circulation is weak in the pelagic zone at night (Fig. 4.1c), and should not modify estimates of nighttime respiration. The main effect of the convective circulation would be an underestimation of gross primary production during daylight conditions due to the intrusion of oxygen-depleted littoral waters. Because of the daily periodicity of thermal siphons, such a bias would not be removed by the standard multiple days averaged procedure (Staehr et al., 2010).

By demonstrating the role of the convective circulation for littoral-pelagic gas exchanges, our results reveal that the presence of shallow littoral regions modifies the offshore vertical gas distribution at a daily frequency. We stress that a one-dimensional vertical framework is insufficient to estimate production and consumption rates of dissolved gases, particularly in small wind-sheltered lakes where convective circulation occurs at a daily frequency. Quantifying lateral fluxes should become systematic in greenhouse gases budgets and ecosystem metabolism studies.

Code and data availability

The scripts used to process, analyzed and plot the data are available for download at: <https://drive.switch.ch/index.php/s/E3gVaO7VglhS98h>. They will be moved to the Eawag Research Data Institutional Collection and associated with a DOI number once this chapter will be accepted for publication.

Acknowledgements

We sincerely thank our technician, Michael Plüss, for helping us in organizing the field campaigns, and all the other people who participated to the fieldwork: Fabian Bärenbold, Hannah Chmiel, Guillaume Cunillera, Benedikt Ehrenfels, Alex Lightfoot, Sebastiano Piccolroaz, Love Råman Vinnå, Cas Retel, Serge Robert, James Runnalls and Oscar Sepúlveda Steiner. We are grateful to the Canton of Luzern, the municipalities of Luzern and Ebikon, the Rowing Centre Lucerne-Rotsee, the Quartierverein Maihof and Pro Natura associations, and the Rotsee- Badi for supporting us in our measurements.

Financial support

This study was financed by the Swiss National Science Foundation (“Buoyancy driven nearshore transport in lakes” project; HYPOlimnetic THERmal SIphonS, HYPOTHESIS, grant no. 175919).

There is no competing interest for any author.

References

- Antenucci, J. P., Tan, K. M., Eikaas, H. S., & Imberger, J. (2013). The importance of transport processes and spatial gradients on in situ estimates of lake metabolism. *Hydrobiologia*, 700(1), 9–21. <https://doi.org/10.1007/s10750-012-1212-z>
- Bogard, M. J., del Giorgio, P. A., Boutet, L., Chaves, M. C. G., Prairie, Y. T., Merante, A., & Derry, A. M. (2014). Oxic water column methanogenesis as a major component of aquatic CH₄ fluxes. *Nature Communications*, 5(1), 5350. <https://doi.org/10.1038/ncomms6350>
- Brennwald, M. S., Schmidt, M., Oser, J., & Kipfer, R. (2016). A portable and autonomous mass spectrometric system for on-site environmental gas analysis. *Environmental Science & Technology*, 50(24), 13455–13463. <https://doi.org/10.1021/acs.est.6b03669>
- Brothers, S., Kazanjian, G., Köhler, J., Scharfenberger, U., & Hilt, S. (2017). Convective mixing and high littoral production established systematic errors in the diel oxygen curves of a shallow, eutrophic lake. *Limnology and Oceanography: Methods*, 15(5), 429–435. <https://doi.org/10.1002/lom3.10169>
- Brothers, S., & Vadeboncoeur, Y. (2021). Shoring up the foundations of production to respiration ratios in lakes. *Limnology and Oceanography*, 66(7), 2762–2778. <https://doi.org/10.1002/lno.11787>
- Cardinale, B. J., Burton, T. M., & Brady, V. J. (1997). The community dynamics of epiphytic midge larvae across the pelagic–littoral interface: do animals respond to changes in the abiotic environment? *Canadian Journal of Fisheries and Aquatic Sciences*, 54(10), 2314–2322. <https://doi.org/10.1139/f97-138>
- Coloso, J. J., Cole, J. J., Hanson, P. C., & Pace, M. L. (2008). Depth-integrated, continuous estimates of metabolism in a clear-water lake. *Canadian Journal of Fisheries and Aquatic Sciences*, 65(4), 712–722. <https://doi.org/10.1139/f08-006>
- Czikowsky, M. J., MacIntyre, S., Tedford, E. W., Vidal, J., & Miller, S. D. (2018). Effects of wind and buoyancy on carbon dioxide distribution and air–water flux of a stratified temperate lake.

- Journal of Geophysical Research: Biogeosciences*, 123(8), 2305–2322. <https://doi.org/10.1029/2017JG004209>
- DelSontro, T., del Giorgio, P. A., & Prairie, Y. T. (2018). No longer a paradox: the interaction between physical transport and biological processes explains the spatial distribution of surface water methane within and across lakes. *Ecosystems*, 21(6), 1073–1087. <https://doi.org/10.1007/s10021-017-0205-1>
- Doda, T., Ramón, C. L., Ulloa, H. N., Wüest, A., & Bouffard, D. (2022). Seasonality of density currents induced by differential cooling. *Hydrology and Earth System Sciences*, 26(2), 331–353. <https://doi.org/10.5194/hess-26-331-2022>
- Donis, D., Flury, S., Stöckli, A., Spangenberg, J. E., Vachon, D., & McGinnis, D. F. (2017). Full-scale evaluation of methane production under oxic conditions in a mesotrophic lake. *Nature Communications*, 8(1), 1661. <https://doi.org/10.1038/s41467-017-01648-4>
- Encinas Fernández, J., Peeters, F., & Hofmann, H. (2014). Importance of the autumn overturn and anoxic conditions in the hypolimnion for the annual methane emissions from a temperate lake. *Environmental Science & Technology*, 48(13), 7297–7304. <https://doi.org/10.1021/es4056164>
- Encinas Fernández, J., Peeters, F., & Hofmann, H. (2016). On the methane paradox: Transport from shallow water zones rather than in situ methanogenesis is the major source of CH₄ in the open surface water of lakes. *Journal of Geophysical Research: Biogeosciences*, 121(10), 2717–2726. <https://doi.org/10.1002/2016JG003586>
- Fer, I., Lemmin, U., & Thorpe, S. A. (2002b). Winter cascading of cold water in Lake Geneva. *Journal of Geophysical Research*, 107(C6), 3060. <https://doi.org/10.1029/2001JC000828>
- Grossart, H.-P., Frindte, K., Dziallas, C., Eckert, W., & Tang, K. W. (2011). Microbial methane production in oxygenated water column of an oligotrophic lake. *Proceedings of the National Academy of Sciences*, 108(49), 19657–19661. <https://doi.org/10.1073/pnas.1110716108>
- Günthel, M., Donis, D., Kirillin, G., Ionescu, D., Bizic, M., McGinnis, D. F., Grossart, H.-P., & Tang, K. W. (2019). Contribution of oxic methane production to surface methane emission in lakes and its global importance. *Nature Communications*, 10(1), 5497. <https://doi.org/10.1038/s41467-019-13320-0>
- Hanson, P. C., Carpenter, S. R., Kimura, N., Wu, C., Cornelius, S. P., & Kratz, T. K. (2008). Evaluation of metabolism models for free-water dissolved oxygen methods in lakes. *Limnology and Oceanography: Methods*, 6(9), 454–465. <https://doi.org/10.4319/lom.2008.6.454>
- Hofmann, H. (2013). Spatiotemporal distribution patterns of dissolved methane in lakes: how accurate are the current estimations of the diffusive flux path? *Geophysical Research Letters*, 40(11), 2779–2784. <https://doi.org/10.1002/grl.50453>

- Hofmann, H., Federwisch, L., & Peeters, F. (2010). Wave-induced release of methane: littoral zones as source of methane in lakes. *Limnology and Oceanography*, 55(5), 1990–2000. <https://doi.org/10.4319/lo.2010.55.5.1990>
- Horsch, G. M., & Stefan, H. G. (1988). Convective circulation in littoral water due to surface cooling. *Limnology and Oceanography*, 33(5), 1068–1083. <https://doi.org/10.4319/lo.1988.33.5.1068>
- Idrizaj, A., Laas, A., Anijalg, U., & Nöges, P. (2016). Horizontal differences in ecosystem metabolism of a large shallow lake. *Journal of Hydrology*, 535, 93–100. <https://doi.org/10.1016/j.jhydrol.2016.01.037>
- James, W. F., & Barko, J. W. (1991a). Estimation of phosphorus exchange between littoral and pelagic zones during nighttime convective circulation. *Limnology and Oceanography*, 36(1), 179–187. <https://doi.org/10.4319/lo.1991.36.1.0179>
- Lauster, G. H., Hanson, P. C., & Kratz, T. K. (2006). Gross primary production and respiration differences among littoral and pelagic habitats in northern Wisconsin lakes [Publisher: NRC Research Press Ottawa, Canada]. *Canadian Journal of Fisheries and Aquatic Sciences*, 63(5), 1130–1141. <https://doi.org/10.1139/f06-018>
- Loken, L. C., Crawford, J. T., Schramm, P. J., Stadler, P., Desai, A. R., & Stanley, E. H. (2019). Large spatial and temporal variability of carbon dioxide and methane in a eutrophic lake. *Journal of Geophysical Research: Biogeosciences*, 124(7), 2248–2266. <https://doi.org/10.1029/2019JG005186>
- Mayr, M. J., Zimmermann, M., Dey, J., Brand, A., Wehrli, B., & Bürgmann, H. (2020). Growth and rapid succession of methanotrophs effectively limit methane release during lake overturn. *Communications Biology*, 3(1), 108. <https://doi.org/10.1038/s42003-020-0838-z>
- Mohseni, O., Stefan, H. G., Wright, D., & Johnson, G. J. (2001). Dissolved oxygen depletion in a small deep lake with a large littoral zone. *Lake and Reservoir Management*, 17(4), 288–298. <https://doi.org/10.1080/07438140109354136>
- Monismith, S. G., Imberger, J., & Morison, M. L. (1990). Convective motions in the sidearm of a small reservoir. *Limnology and Oceanography*, 35(8), 1676–1702. <https://doi.org/10.4319/lo.1990.35.8.1676>
- Murase, J., Sakai, Y., Sugimoto, A., Okubo, K., & Sakamoto, M. (2003). Sources of dissolved methane in Lake Biwa. *Limnology*, 4(2), 91–99. <https://doi.org/10.1007/s10201-003-0095-0>
- Pálmarrsson, S. Ó., & Schladow, S. G. (2008). Exchange flow in a shallow lake embayment. *Ecological Applications*, 18(8), A89–A106. <https://doi.org/10.1890/06-1618.1>
- Peeters, F., Encinas Fernandez, J., & Hofmann, H. (2019). Sediment fluxes rather than oxic methanogenesis explain diffusive CH₄ emissions from lakes and reservoirs. *Scientific Reports*, 9(1), 243. <https://doi.org/10.1038/s41598-018-36530-w>

- Peeters, F., & Hofmann, H. (2015). Length-scale dependence of horizontal dispersion in the surface water of lakes: Horizontal dispersion in lakes. *Limnology and Oceanography*, 60(6), 1917–1934. <https://doi.org/10.1002/lno.10141>
- Reynolds, C. S. (2008). A changing paradigm of pelagic food webs. *International Review of Hydrobiology*, 93(4-5), 517–531. <https://doi.org/10.1002/iroh.200711026>
- Sadro, S., Melack, J. M., & MacIntyre, S. (2011). Spatial and temporal variability in the ecosystem metabolism of a high-elevation lake: integrating benthic and pelagic habitats. *Ecosystems*, 14(7), 1123–1140. <https://doi.org/10.1007/s10021-011-9471-5>
- Schmidt, U., & Conrad, R. (1993). Hydrogen, carbon monoxide, and methane dynamics in Lake Constance. *Limnology and Oceanography*, 38(6), 1214–1226. <https://doi.org/10.4319/lo.1993.38.6.1214>
- Schubert, C. J., Lucas, F. S., Durisch-Kaiser, E., Stierli, R., Diem, T., Scheidegger, O., Vazquez, F., & Müller, B. (2010). Oxidation and emission of methane in a monomictic lake (Rotsee, Switzerland). *Aquatic Sciences*, 72(4), 455–466. <https://doi.org/10.1007/s00027-010-0148-5>
- Schubert, C. J., Diem, T., & Eugster, W. (2012). Methane emissions from a small wind shielded lake determined by eddy covariance, flux chambers, anchored funnels, and boundary model calculations: a comparison. *Environmental Science & Technology*, 46(8), 4515–4522. <https://doi.org/10.1021/es203465x>
- Staehr, P. A., Bade, D., Van de Bogert, M. C., Koch, G. R., Williamson, C., Hanson, P., Cole, J. J., & Kratz, T. (2010). Lake metabolism and the diel oxygen technique: state of the science. *Limnology and Oceanography: Methods*, 8(11), 628–644. <https://doi.org/10.4319/lom.2010.8.0628>
- Tsunogai, U., Miyoshi, Y., Matsushita, T., Komatsu, D. D., Ito, M., Sukigara, C., Nakagawa, F., & Maruo, M. (2020). Dual stable isotope characterization of excess methane in oxic waters of a mesotrophic lake. *Limnology and Oceanography*, 65(12), 2937–2952. <https://doi.org/10.1002/lno.11566>
- Vander Zanden, M. J., & Vadeboncoeur, Y. (2020). Putting the lake back together 20 years later: what in the benthos have we learned about habitat linkages in lakes? *Inland Waters*, 10(3), 305–321. <https://doi.org/10.1080/20442041.2020.1712953>
- van Grinsven, S., Oswald, K., Wehrli, B., Jegge, C., Zopfi, J., Lehmann, M. F., & Schubert, C. J. (2021). Methane oxidation in the waters of a humic-rich boreal lake stimulated by photosynthesis, nitrite, Fe(III) and humics. *Biogeosciences*, 18(10), 3087–3101. <https://doi.org/10.5194/bg-18-3087-2021>
- Wang, Q., Dore, J. E., & McDermott, T. R. (2017). Methylphosphonate metabolism by *Pseudomonas* sp. populations contributes to the methane oversaturation paradox in an oxic freshwater

- lake. *Environmental Microbiology*, 19(6), 2366–2378. <https://doi.org/10.1111/1462-2920.13747>
- Xiao, S., Liu, L., Wang, W., Lorke, A., Woodhouse, J., & Grossart, H.-P. (2020). A Fast-Response Automated Gas Equilibrator (FaRAGE) for continuous in situ measurement of CH₄ and CO₂ dissolved in water. *Hydrology and Earth System Sciences*, 24(7), 3871–3880. <https://doi.org/10.5194/hess-24-3871-2020>
- Yao, M., Henny, C., & Maresca, J. A. (2016). Freshwater bacteria release methane as a by-product of phosphorus acquisition (J. E. Kostka, Ed.). *Applied and Environmental Microbiology*, 82(23), 6994–7003. <https://doi.org/10.1128/AEM.02399-16>
- Zimmermann, M., Mayr, M. J., Bürgmann, H., Eugster, W., Steinsberger, T., Wehrli, B., Brand, A., & Bouffard, D. (2021). Microbial methane oxidation efficiency and robustness during lake overturn. *Limnology and Oceanography Letters*, 6(6), 320–328. <https://doi.org/10.1002/lol2.10209>

Supplementary Information for Chapter 4

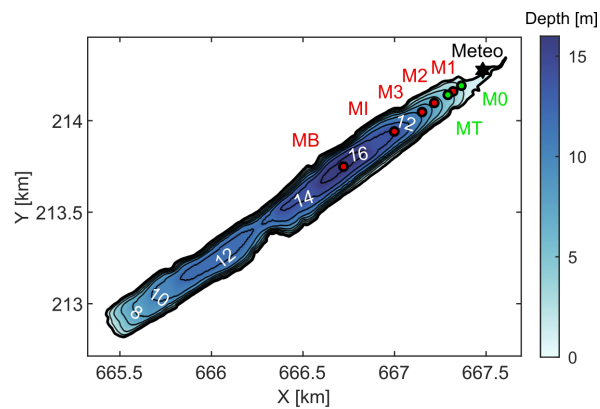


Figure S4.1 – Bathymetric map of Rotsee. Red and green dots indicate the location of the seven measurement stations. Continuous measurements of dissolved gases were collected at M0 and MT (green dots). The black star depicts the weather station. Black lines are 2 m spaced isobaths.

Table S4.1 – Characteristics of the measurement stations

Station	x (m)	Lake depth (m)	miniRuedi	Measurement period (UTC)	Pump	Depth from the surface (m)	Height above the sediment (m)	Sampling interval (min)
M0	0	1.6	Platform	24 Nov (16:15) – 26 Nov (11:00)	A B	0.9 1.3	0.7 0.3	28 28
M1	55	3.3	Boat	25 Nov (03:00-06:40)	E F	0.4 2.8	2.9 0.5	14 14
MT	93	4.2	Platform	24 Nov (16:15) – 26 Nov (11:00)	C D	0.6 3.8	3.6 0.4	28 28
M2	175	6.2	Boat	25 Nov (07:15-09:10)	E F	0.4 5.4	5.8 0.8	14 14
M3	259	8.7	Boat	25 Nov (22:15) – 26 Nov (11:00)	E F	0.5 7.6-8.3	8.2 0.4-1.1	14 14
MI	443	13.6	Boat	25 Nov (09:15-15:40)	E F	9.7 8.7-12.5	3.9 1.1-4.9	14 14
MB	792	15.9	Boat	25 Nov (16:45-21:20)	E F	9.7 0.5	6.2 15.4	14 14

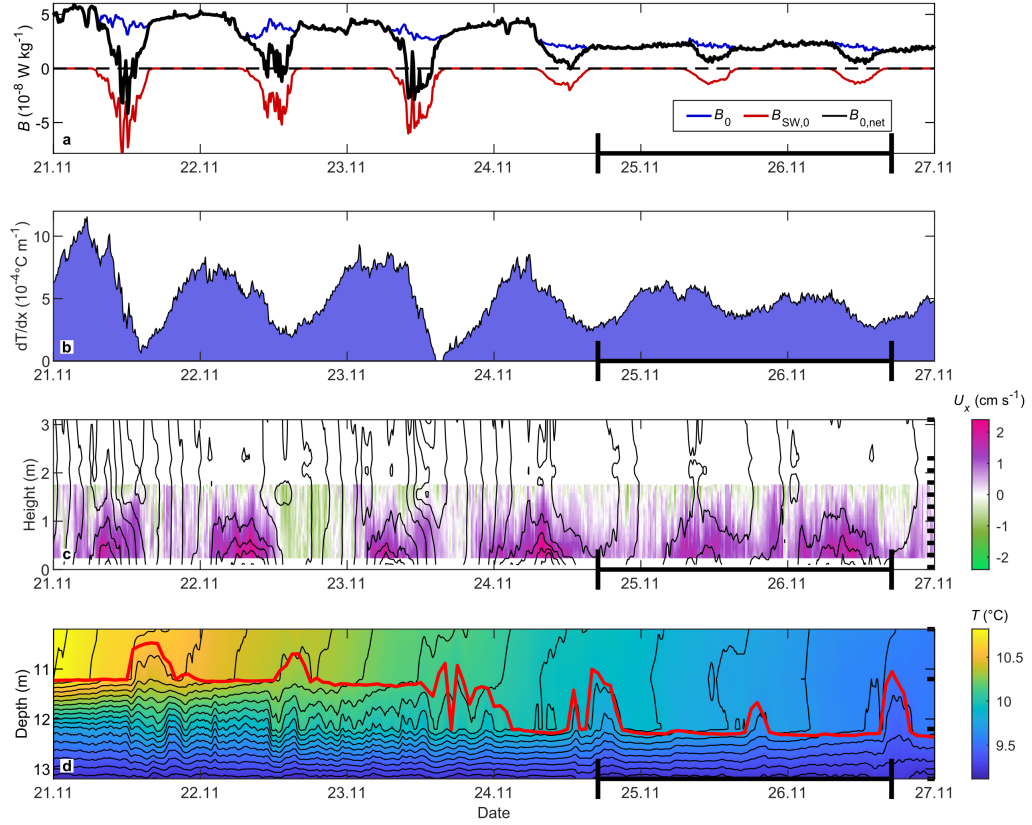


Figure S4.2 – Forcing conditions and convective circulation. Six days long time series of (a) surface buoyancy fluxes, (b) lateral temperature gradients between M1 and MI, (c) cross-shore velocity at M1 and (d) water temperature at MB, on 21-27 November 2020 (same period as in Figs. 4.1b and 4.1c). The experiment period on 24-26 November is highlighted on the x axis. (a) The non-penetrative surface buoyancy flux (B_0), the shortwave surface buoyancy flux ($B_{SW,0}$) and the net surface buoyancy flux ($B_{0,net} = B_0 + B_{SW,0}$) were computed as in Doda et al. (2022). Destabilizing fluxes are positive (cooling), whereas stabilizing fluxes are negative (heating). Net surface cooling ($B_{0,net} > 0$) occurred over the entire experiment period (24-26 November). (b) The lateral temperature gradients were calculated from mixed layer averaged temperature at M1 and MI (390 m apart). Positive temperature gradients correspond to differential cooling. (c) The cross-shore velocity is represented as in Figs. 4.1b and 4.1c. Black lines are 0.1°C spaced isotherms, from linearly interpolated temperature between each thermistor (black ticks on the right y-axis). (d) Black lines are 0.1°C spaced isotherms, from linearly interpolated temperature between each thermistor (black ticks on the right y-axis). The red line depicts the mixed layer depth, defined as in Doda et al. (2022). The daily thickening of the bottom stratified layer in the afternoon (rise of the red interface) indicates intrusions of cold water from the convective circulation.

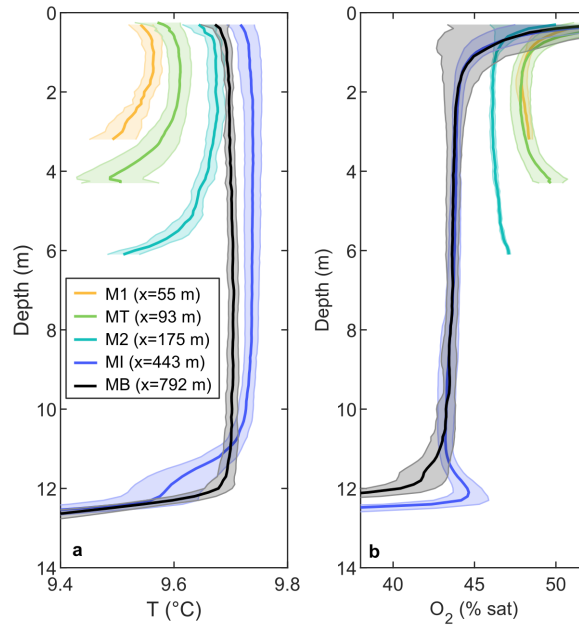


Figure S4.3 – Cross-shore variability of temperature and oxygen saturation. Temporally averaged profiles of **(a)** temperature and **(b)** oxygen saturation at five locations along the cross-shore transect (25 November, 03:00-20:00). Shaded areas depict the standard deviation. **(a)** The lateral mixed layer temperature gradient due to differential cooling between M1 and MI (sloping region) is $\partial T / \partial x \approx 4 \times 10^{-4} \text{ } ^\circ\text{C m}^{-1}$. The bottom stratification induced by the downslope gravity current is visible at M1, MT and M2. The intrusion at MI creates a cold layer at the base of the mixed layer, that is not observed at MB. **(b)** The lateral mixed layer oxygen gradient between M1 and MI (sloping region) of $\partial O_2 / \partial x \approx -1 \text{ } \%\text{m}^{-1}$ is the same as in Fig. 4.3a. The bottom oxic layer induced by the downslope oxygen transport is visible at M1, MT and M2. The intrusion at MI creates an oxic peak at the base of the mixed layer, that is not observed at MB.

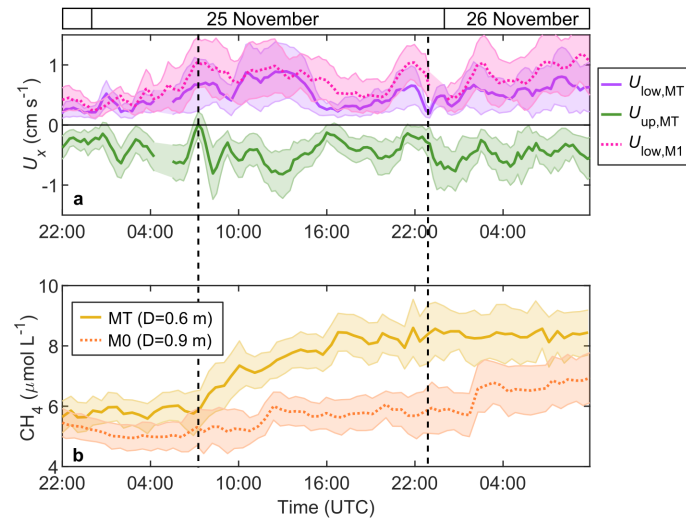


Figure S4.4 – Surface transport of methane across the sloping region. (a) Time series of depth-averaged cross-shore velocity in the lower branch (purple, $U_{low} > 0$) and in the upper branch (green, $U_{up} < 0$) of the circulation at MT, and in the lower branch at M1 (dotted line, $U_{low} > 0$), from 24 to 26 November. Shaded areas depict the standard deviation. (b) Time series of methane concentration in the upper branch of the circulation at MT (solid line) and M0 (dotted line). Shaded areas depict the standard deviation. The vertical dashed lines show two flow intensification events in the sloping region on 25 November, after 07:00 and after 23:00. Both events enhanced the surface methane transport from MT to M0, as shown by the sharp concentration increase at M0 4-5 h after each flow intensification.

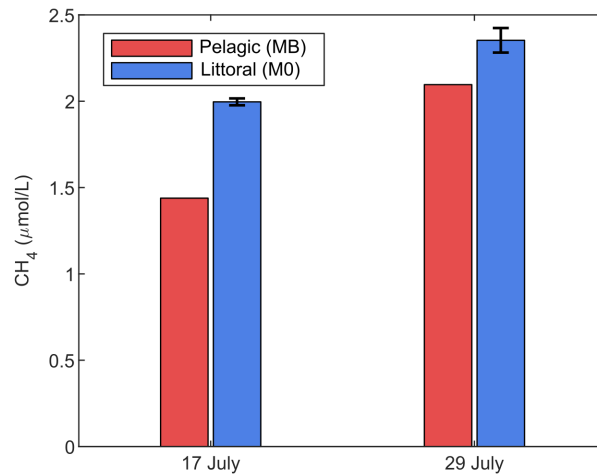


Figure S4.5 – Littoral-pelagic surface methane concentrations in summer (July 2019). Surface (1-2 m depth) methane concentrations were measured from water samples with the headspace method (Schubert et al., 2010). The error bars indicate the standard deviation between replicates. Littoral methane concentrations were constantly higher than pelagic concentrations, leading to a negative lateral methane gradient of $\partial CH_4 / \partial x \approx -10^{-4} \mu\text{mol L}^{-1} \text{m}^{-1}$ between M0 and MB.

Chapter 5

Towards a parametrization of cooling-driven lateral transport in lakes

Tomy Doda^{1,2}, Hugo Cruz¹, James Runnalls¹, Cintia L. Ramón⁴, Hugo N. Ulloa³, Edgar Hédouin¹, Michael Plüss¹, Damien Bouffard¹

¹Eawag, Swiss Federal Institute of Aquatic Science and Technology, Department of Surface Waters – Research and Management, Kastanienbaum, Switzerland

²Limnology Center, École Polytechnique Fédérale de Lausanne, Lausanne, Switzerland

³Department of Earth and Environmental Science, University of Pennsylvania, Philadelphia, USA

⁴Department of Civil Engineering, University of Granada, Granada, Spain

*In preparation.*¹

Author contributions: TD, DB, MP and HC designed the field experiments. HC, JR, TD and EH created the databases. TD and HC analyzed the data. TD wrote the initial draft of the manuscript, with comments from CL, HU and DB.

¹This chapter is not at the submission stage yet. The structure, text and figures will be modified to make the chapter suitable for publication.

Abstract

In lakes, differential cooling generates a cross-shore convective circulation, known as the thermal siphon, that exchanges water laterally between the littoral and pelagic regions at a daily frequency. By bringing littoral compounds offshore, this lateral transport process modifies the biogeochemical properties of the pelagic zone, which can have ecological implications for the lake ecosystem. Yet, thermal siphons are not included in mass balances and one-dimensional models. The parameters controlling their occurrence in lakes are not well established and a simple method predicting the resulting lateral transport is lacking. In this study, we collected high-resolution measurements of thermal siphons in six Swiss lakes. We validated theoretical scaling formulae that estimate the formation and intensity of these lateral flows. Based on this scaling relationships, we provided a procedure to predict thermal siphons from the lake bathymetry, meteorological forcing and vertical thermal structure. This predictive procedure can be used to assess the significance of cooling-driven lateral transport in a given lake.

5.1 Introduction

In lakes, cross-shore flows connect the littoral and pelagic regions and transport heat, dissolved compounds and particulate matter laterally (MacIntyre & Melack, 1995; Rao & Schwab, 2007). Such lateral transport have ecological implications for the pelagic ecosystem by bringing pollutants offshore (Bonvin et al., 2011), inducing a horizontal migration of organisms (Razlutskiy et al., 2021) and modifying the distribution of greenhouse gases (Hofmann et al., 2010). Despite its effects on biogeochemical measurements in the pelagic zone, lateral transport is often neglected in lake ecosystem research (Vander Zanden & Vadeboncoeur, 2020).

Recent studies have pushed for a better quantification of cross-shore flows and their induced lateral transport (Brothers et al., 2017; Czikowsky et al., 2018; Sadro et al., 2011). In particular, the convective circulation driven by differential cooling, also known as the thermal siphon (Monismith et al., 1990), is known to be an efficient and regular flushing mechanism for the littoral region (Doda et al., 2022; Fer et al., 2002b; James & Barko, 1991a; Pálmarrsson & Schladow, 2008). Thermal siphons (TSs) occur when the sloping sides of lakes experience surface cooling. The shallower littoral region cools faster than the deeper pelagic region, which generates lateral density gradients. The colder (denser) littoral waters plunge as a downslope gravity current that intrudes at the base of the mixed layer during stratified conditions. An onshore surface flow forms simultaneously by

continuity (Horsch & Stefan, 1988; Monismith et al., 1990). Although TSs have been reported in lakes of diverse shapes (Doda et al., 2022; Fer et al., 2002b; Monismith et al., 1990; Pálmarrsson & Schladow, 2008; Roget et al., 1993; Sturman et al., 1999), there is currently no method to predict the TS contribution to lateral transport in a given lake.

Scaling relationships linking the forcing parameters (surface buoyancy flux B_0 , wind shear stress τ_w) to the TS intensity (velocity and discharge) have been derived from dimensional analysis and verified in laboratory and numerical experiments (Harashima & Watanabe, 1986; Phillips, 1966; Ramón et al., 2022; Sturman & Ivey, 1998; Ulloa et al., 2022; Wells & Sherman, 2001). The time required for TS to form has also been related to the forcing conditions via a transition timescale (Ulloa et al., 2022). In the field, transport scaling formulae have been applied to estimate the TS intensity in absence of velocity measurements (Rueda et al., 2007; Sadro et al., 2011; Sharip et al., 2012), and Sturman et al. (1999) and Chubarenko (2010) showed that the discharge scaling formulae comport with field observations. Yet, most of available field velocity measurements lack a vertical resolution, as they were derived from either tracer experiments (James & Barko, 1991a), drogue movements (Monismith et al., 1990) or velocity time series at specific depths (Fer et al., 2002b; Pálmarrsson & Schladow, 2008; Roget et al., 1993).

We recently tested the transport scaling formulae on high-resolution TS velocity data collected over one year in Rotsee, an elongated wind-sheltered Swiss lake (Doda et al., 2022). We showed that the transport seasonality was well predicted by the scaling relationships. We also explained the TS occurrence by comparing the transition timescale with the duration of the cooling phase for different seasons. Because of its elongated shape and the prevalence of low wind conditions, Rotsee is an ideal field-scale laboratory for TSs but is not necessarily representative of other systems. We need TS observations from other lakes to generalize our findings and determine whether the scaling formulae can reproduce the variability in TS occurrence and intensity. To address this question, we collected high-resolution velocity and temperature measurements in nine lakes that differed by their bathymetry and forcing conditions. We reported TS events in six of the lakes, for which we successfully tested the scaling relationships of the TS velocity, discharge and transition period. Based on these relationships, we proposed a procedure to predict the occurrence and intensity of TSs in lakes.

5.2 Methods

5.2.1 Study sites and field measurements

We investigated cooling-driven TSs in nine Swiss lakes, in winter and autumn 2021 (Fig. 5.1a). The main lake characteristics are provided in Supplementary Information (Tab. S5.1). The lakes' shape varied from elongated cases (e.g., Hongrin, Joux, Hallwil) to rounded-like cases (e.g., Lioson, Oeschinen, Soppen). The lakes were located at 400–1800 m above sea level, had a surface area of 0.1–100 km² and a maximum depth of 27–214 m. For each lake, we determined a cross-shore transect of interest, originating from a shallow littoral zone that potentially produced TSs. The mean slope along the transect ranged from 0.01 to 0.1 (Tab. S5.1).

We deployed two moorings in each lake for approximately 1–2 weeks (Fig. 5.1a), in February 2021 (Luzern) and between August and November 2021 (all the other lakes). Mooring “MB” monitored the background thermal stratification offshore with a vertical thermistor array (Vemco Minilog-II loggers with 1 m spacing and 2 min sampling interval, RBR TR-1060 and RBR Solo-T loggers near the mixed layer base with 0.5 m spacing and 1–5 s sampling interval). Mooring “MT” sampled the sloping region shallower than the mixed layer depth. Its location was aligned with the selected cross-shore transect, where TSs were expected. MT consisted of a high-resolution vertical thermistor array (RBR Solo-T loggers with 0.25 m spacing and 1 Hz sampling frequency) to capture the thermal signature of TSs and two upward-looking acoustic Doppler current profilers (ADCPs) to measure the TS velocity. One ADCP (Nortek Aquadopp profiler 1 MHz) sampled the current velocity from 0.2 to 2–3 m above the sediment with a 0.05 m vertical bin size. The other ADCP (Teledyne RD Instruments WorkHorse 600 or 1200 kHz depending on the campaign) profiled the upper part of the water column with a 0.05–0.1 m vertical bin size. Both ADCPs computed the burst-averaged velocity every 15 min. The RDI ADCP did not collect measurements in Oeschinensee, Lake Lungern and Lake Sarnen. In Luzern Bay, only one ADCP was used (Teledyne RD Instruments WorkHorse 1200 kHz) and collected velocity profiles over the first 18 m above the sediment, with a 1 m vertical bin size. A Campbell ClimaVUE50 weather station installed at the lake shore provided meteorological forcing at a 10 min temporal resolution, except for Lake Sarnen and Luzern Bay where we retrieved data from nearby MeteoSwiss weather stations (Giswil and Luzern, respectively).

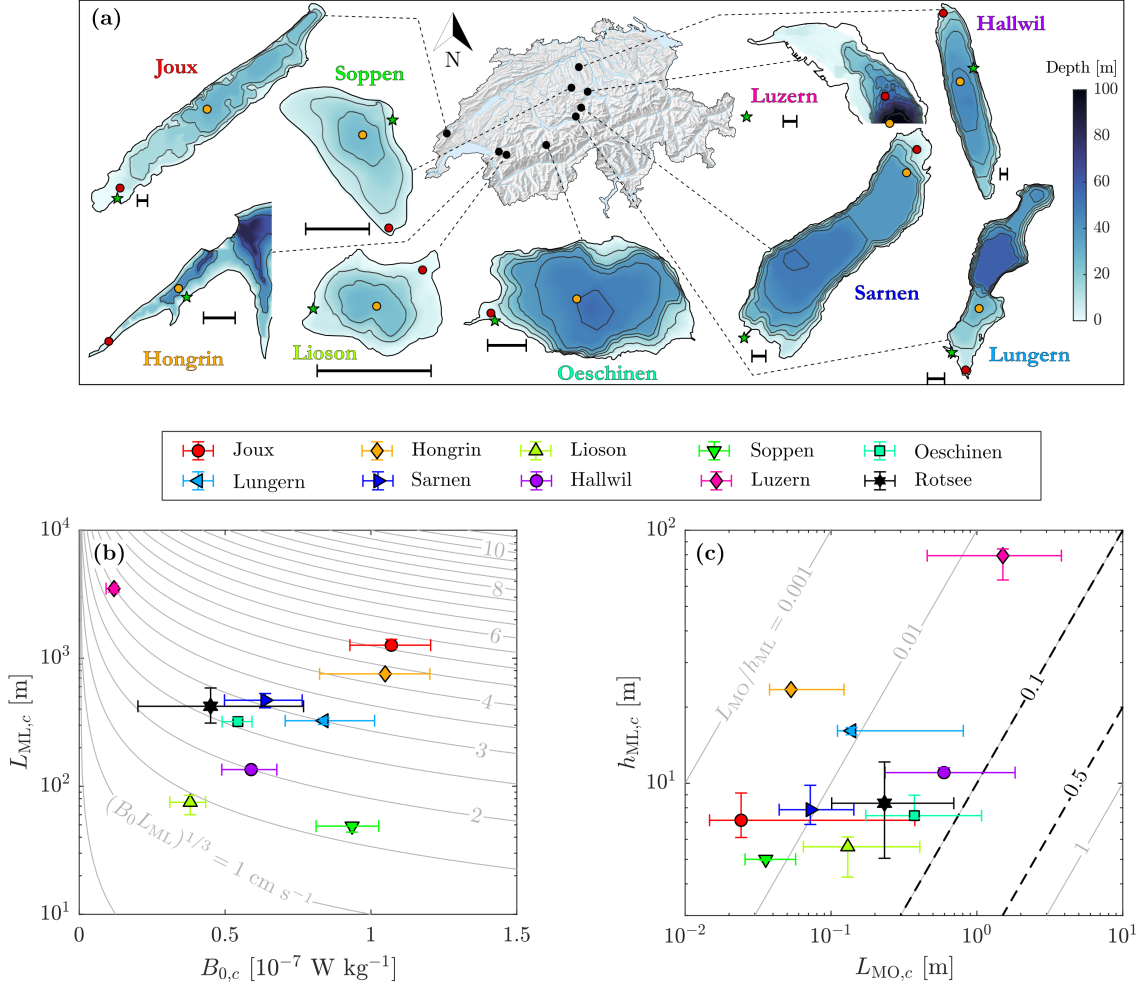


Figure 5.1 – Bathymetric maps and forcing conditions characterizing the nine study sites. (a) Location of the lakes on the map of Switzerland and bathymetric map of each lake (Source: Federal Office of Topography). For Lac de l’Hongrin and Lake Lucerne (Luzern), only the basin where measurements were taken is shown. On the bathymetric maps, the orange dot, red dot and green star depict the offshore mooring (MB), the littoral mooring (MT) and the weather station, respectively. Black lines are 30 m spaced isobaths for Hongrin and 10 m spaced isobaths for the other lakes. The horizontal scale bar is 300 m-long for each lake. (b) Length of the mixed region $L_{ML,c}$ as a function of the surface buoyancy flux $B_{0,c}$, both averaged over the cooling phases during the deployment period. Note the logarithmic scale on the y axis. The gray lines indicate the TS velocity scale $U \sim (B_0 L_{ML})^{1/3}$ (spacing of 1 cm s⁻¹). (c) Mixed layer depth $h_{ML,c}$ as a function of the Monin-Obukhov length scale $L_{MO,c}$, both averaged over the cooling phases during the deployment period. Note the logarithmic scales for both axes. The gray lines indicate the non-dimensional Monin-Obukhov length scale $\chi_{MO} = L_{MO}/h_{ML}$ (logarithmic spacing). The black dashed lines delimit the wind-convection interaction regime $0.1 \lesssim \chi_{MO} \lesssim 0.5$ from Ramón et al. (2022). In (b) and (c), dots are median values and error bars depict the 25 % and 75 % quantiles. Data from Rotsee (August-December 2019) is shown by a black star in (b) and (c).

5.2.2 Forcing parameters

We used the same 2D framework as in Doda et al. (2022), with a vertical z axis directed upward and a horizontal x axis aligned with the selected cross-shore transect and directed towards the lake center.

We estimated surface heat and buoyancy fluxes from meteorological forcing and surface water temperature at MB, as described in Doda et al. (2022). For Luzern Bay, surface water temperature was not measured and we used instead the temperature of the Reuss river at the outflow, provided by the Swiss Federal Office of the Environment (monitoring station “Luzern, Geismattbrücke”). The net surface buoyancy flux was calculated as

$$B_{0,\text{net}} = B_0 + B_{\text{SW},0} \quad [\text{W kg}^{-1}], \quad (5.1)$$

where B_0 is the non-penetrative surface buoyancy flux and $B_{\text{SW},0}$ is the radiative surface buoyancy flux. Positive surface buoyancy fluxes are directed upward and destabilize the stratification (convection). Negative surface buoyancy fluxes are directed downward and stratify the water column.

We defined the mixed layer depth h_{ML} from hourly averaged temperature at MB, by using a temperature gradient threshold of $\partial T / \partial z < 0.05 \text{ } ^\circ\text{C m}^{-1}$ (see details in Doda et al. (2022)). The length of the mixed region L_{ML} is the distance between the shore and the point where the mixed layer intersects the lake bottom. It was computed from the bathymetry along the cross-shore transect $h_{\text{max}}(x)$ as

$$h_{\text{max}}(x = L_{\text{ML}}) = h_{\text{ML}} \quad [\text{m}], \quad (5.2)$$

where $h_{\text{max}}(x)$ is the lake depth at a distance x from the shore.

The wind contribution to the mixed layer deepening was expressed by the Monin-Obukhov length scale (Wüest & Lorke, 2003):

$$L_{\text{MO}} = \frac{u_*}{k B_0} \quad [\text{m}], \quad (5.3)$$

where $u_* = \sqrt{\tau_w / \rho_0}$ is the friction velocity, $\tau_w = \rho_a C_{10} W_{10}^2$ is the surface wind shear stress, ρ_0 and ρ_a are the water and air densities, respectively, C_{10} is the wind drag coefficient, W_{10} is the wind speed at 10 m height, and $k = 0.41$ is the von Kármán constant. A non-dimensional Monin-Obukhov

length scale was obtained by normalizing L_{MO} by h_{ML} :

$$\chi_{MO} = \frac{L_{MO}}{h_{ML}}. \quad (5.4)$$

This quantity represents the fraction of the mixed layer dominated by wind shear. Wind shear overcomes convection when $\chi_{MO} > 1$ (Ramón et al., 2022).

5.2.3 Thermal siphon events and transport estimates

The velocity data from both ADCPs at MT was quality checked by discarding values with low correlation and was projected onto the x axis to obtain the cross-shore velocity u . We selected diurnal TS events manually from the time series of forcing parameters and cross-shore velocity. The selection criteria were the presence of a two-layer circulation during a cooling period ($B_{0,net} > 0$), with low wind conditions ($\chi_{MO} \ll 1$) and an initially mixed water column at MT. Each TS event, starting at t_0 and ending at t_f , was defined as a period with continuous $u > 0$ near the bottom. When a TS event lasted for several days, we divided it into daily sub-events. We identified a cooling phase associated with each TS event. This cooling phase started at $t_{c,0} < t_0$ when $B_{0,net}$ became positive and ending at $t_{c,f} > t_0$ when $B_{0,net}$ became negative. The duration of the cooling phase was

$$\tau_c = t_{c,f} - t_{c,0} \quad [\text{s}]. \quad (5.5)$$

We averaged the parameters B_0 and L_{ML} during τ_c and called them $B_{0,c}$ and $L_{ML,c}$, respectively. The time of vertical mixing $t_{mix} \geq t_{c,0}$ was reached before each TS event when $\partial T / \partial z < 0.05 \text{ } ^\circ\text{C m}^{-1}$ over the entire water column at MT. If this condition was initially met, $t_{mix} = t_{c,0}$. The mixing period $\tau_{mix} = t_{mix} - t_{c,0}$ represented the time required for penetrative convection to erode the stratification from the previous heating phase at MT (Doda et al., 2022). The observed duration of the transition period required for the TS formation was

$$\tau_{t,obs} = t_0 - t_{mix} \quad [\text{s}]. \quad (5.6)$$

We computed $\tau_{t,obs}$ for all lakes except Luzern Bay, where water temperature at MT was only measured deeper than 30 m below the surface, which prevented to calculate t_{mix} .

Transport quantities were averaged for each TS event as in Doda et al. (2022). We computed the thickness $h_d(t)$ of the downslope gravity current as the height of the stagnation point where $u = 0$

at time t . We calculated the depth and time averaged TS velocity as

$$U_{\text{avg}} = \frac{1}{t_f - t_0} \int_{t_0}^{t_f} \left(\frac{1}{h_d(t)} \int_{-h_{\text{max,MT}}}^{-h_{\text{max}}+h_d(t)} u(z, t) dz \right) dt \quad [\text{m s}^{-1}], \quad (5.7)$$

where $h_{\text{max,MT}}$ is the lake depth at MT. The time averaged unit-width discharged was computed as

$$q_{\text{avg}} = \frac{1}{t_f - t_0} \int_{t_0}^{t_f} \left(\int_{-h_{\text{max,MT}}}^{-h_{\text{max}}+h_d(t)} u(z, t) dz \right) dt \quad [\text{m}^2 \text{s}^{-1}]. \quad (5.8)$$

The flushing timescale represents the time required for a TS event to flush a given littoral region of unit-width volume V_{lit} . It was defined as

$$\tau_{F,\text{avg}} = \frac{V_{\text{lit}}}{q_{\text{avg}}} \quad [\text{s}]. \quad (5.9)$$

In our case, the littoral region was the region upslope of MT, of length $L_{\text{lit}} = x(h = h_{\text{max,MT}})$, unit-width volume $V_{\text{lit}} = \int_0^{L_{\text{lit}}} h(x) dx$ and averaged depth $h_{\text{lit}} = V_{\text{lit}}/L_{\text{lit}}$ (Doda et al., 2022).

5.2.4 Transport scaling

We tested available scaling formulae for the TS velocity U , unit-width discharge q and duration of transition period τ_t by comparing them with the measured U_{avg} , q_{avg} and $\tau_{t,\text{obs}}$. We used the same scaling formulae as in Rotsee (Doda et al., 2022). These included the horizontal velocity scale (Phillips, 1966; Wells & Sherman, 2001)

$$U \sim (B_0 L_{\text{ML}})^{1/3} \quad [\text{m s}^{-1}], \quad (5.10)$$

the unit-width discharge scale

$$q \sim (B_0 L_{\text{ML}})^{1/3} h_{\text{lit}} \quad [\text{m}^2 \text{s}^{-1}], \quad (5.11)$$

and the transition timescale (Ulloa et al., 2022)

$$\tau_t \sim \frac{2 (L_{\text{ML}} - L_p)^{2/3}}{B_0^{1/3} (1 - h_p/h_{\text{ML}})^{1/3}} \quad [\text{s}], \quad (5.12)$$

where L_p and h_p are the length and depth of the littoral plateau region, respectively. If the slope was continuous without a clear plateau, $L_p = h_p = 0$.

In presence of a cross-shore wind stress with $0.1 < \chi_{MO} < 0.5$, the discharge scaling (5.11) must be modified into (Ramón et al., 2022)

$$q_{\text{tot}} \sim q_{\text{conv}} + q_w = (B_0 L_{\text{ML}})^{1/3} h_{\text{lit}} + \frac{\tau_w h_{\text{max,MT}}^2}{27 \rho_0 \nu_z} \quad [\text{m}^2 \text{s}^{-1}], \quad (5.13)$$

where q_{conv} is the convective-induced discharge from Eq. (5.11), q_w is the wind-induced discharge and $\nu_z \approx 10^{-4} \text{m}^2 \text{s}^{-1}$ is the vertical eddy viscosity. In elongated lakes similar to Rotsee, wind has a preferential direction along the lake fetch (main axis) which makes Eq. (5.13) suitable to estimate the total q_{tot} along the same direction. In rounded lakes, the wind effects are more complex and can lead to 3D circulation patterns not reproduced by Eq. (5.13). To be consistent between all the lakes, we discarded TS events occurring during windy conditions (time averaged $\chi_{MO} > 0.1$) and tested the scaling (5.11). A further investigation should focus on testing the validity of Eq. (5.13) in the field.

5.3 Results and discussion

5.3.1 Forcing conditions

The bathymetric parameters and forcing conditions varied between lakes (Figs. 5.1b and 5.1c). The surface buoyancy flux B_0 ranged from 10^{-8} to 10^{-7}W kg^{-1} , which was similar to the seasonality of B_0 in Rotsee (Doda et al., 2022). The mixed layer depth h_{ML} varied from $\approx 5 \text{m}$ to $\approx 100 \text{m}$, leading to a mixed region length L_{ML} spanning 3 orders of magnitude from 10^1 to 10^3m . This variability allowed us to cover a wider range of TS velocity scales than in Rotsee (Fig. 5.1b).

Low wind conditions ($\chi_{MO} < 0.1$) prevailed on average, but with a large temporal variability of L_{MO} (Fig. 5.1c). Short wind events with $\chi_{MO} > 0.1$ occurred for most lakes. They were more regular in Joux, Hongrin, Lake Lungern and Lake Hallwil. Yet, calm periods with $\chi_{MO} < 0.1$ were frequent enough in all lakes to analyze the velocity time times for TS events identification.

5.3.2 Thermal siphon events

We identified cross-shore flows meeting our TS criteria (Sect. 5.2.3) in all lakes but we only kept the lakes where such flows occurred regularly over several days. This was not the case in Joux and Lake Sarnen where local cross-shore flow events were likely wind-driven. We did not include

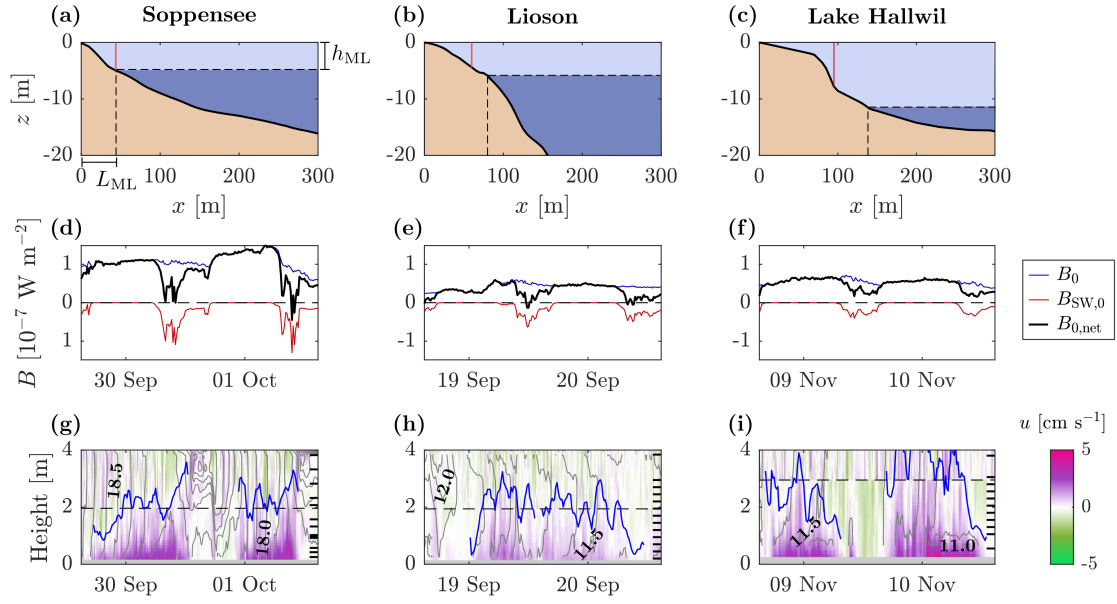


Figure 5.2 – Examples of thermal siphon events in Soppensee, Lioson and Lake Hallwil. (a-c) Bathymetry along the selected cross-shore transect in (a) Soppensee, (b) Lioson and (c) Lake Hallwil. The vertical red line depicts the location of the MT mooring. The light and dark blue areas correspond to the mixed layer and deeper stratified layer, respectively, averaged over the 48 h long time series shown in (d)-(f). The three lakes are ordered according to the length of the mixed region, from (a) $L_{ML} = 44$ m to (c) $L_{ML} = 142$ m. (d-f) 48 h long time series (starting and ending at 15:00 UTC) of surface buoyancy fluxes in (d) Soppensee, (e) Lioson and (f) Lake Hallwil. (g-i) 48 h long time series of cross-shore velocity measured at MT over the first 4 m above the sediment in (g) Soppensee, (h) Lioson and (i) Lake Hallwil. Positive u values (purple) correspond to downslope gravity currents. The horizontal dashed line delimits the Aquadopp (below) and RDI (above) data. The blue line depicts the upper interface ($u = 0$) of the gravity currents identified as TS events. Gray lines are $0.1\text{ }^{\circ}\text{C}$ spaced isotherms, linearly interpolated between the thermistors shown by black ticks on the right vertical axis. The same 48 h time series with additional parameters are provided in Supplementary Informations (Figs. S5.1, S5.2 and S5.5.)

the data from Hongrin neither, where a river inflow generated strong and nearly continuous downslope flows that made the TS identification difficult. Overall, 35 events from the remaining six lakes were identified as TSs occurring during low wind conditions and kept for the rest of the analysis.

To illustrate the effects of varying bathymetry and forcing conditions on the TS dynamics, we present examples of TS events from three lakes (Soppen, Lioson and Hallwil) in Fig. 5.2. The mixed layer was $h_{ML} = 5, 6$ and 11 m for the three lakes, leading to a mixed region length of $L_{ML} = 44, 80$ and 142 m, respectively (Figs. 5.2a, 5.2b and 5.2c). The forcing time series show two diurnal cycles during which net surface cooling dominated ($B_{0,net} > 0$) (Figs. 5.2d, 5.2e and 5.2f). For the three lakes, daytime periods were characterized by weak radiative heating that did not overcome

surface cooling ($B_{0,\text{net}} \approx 0$). Surface cooling was twice as high in Soppensee ($B_0 \approx 1 \times 10^{-7} \text{ W kg}^{-1}$) as at the two other locations ($B_0 \approx 0.5 \times 10^{-7} \text{ W kg}^{-1}$). We observed TSs during both diurnal cycles in each lake, starting at night and persisting until the following morning (Figs. 5.2g, 5.2h and 5.2i). TSs were continuous over the two days in Lioson, but stopped during the day in Soppensee and Lake Hallwil likely because of radiatively-induced restratification (Fig. S5.2) and wind forcing (Fig. S5.5), respectively. The characteristics of these events, including cross-shore velocities of $u \sim 1 \text{ cm s}^{-1}$, weak bottom stratification and inertia with respect to the forcing conditions, agree with other TS observations (e.g., Doda et al., 2022; Monismith et al., 1990; Pálmarsson & Schladow, 2008; Rogowski et al., 2019).

Over the entire measurement period, TSs were consistently weaker in Lioson (averaged velocity of $U_{\text{avg}} \approx 0.5 \text{ cm s}^{-1}$) than in the two other lakes ($U_{\text{avg}} \approx 1 \text{ cm s}^{-1}$). The higher TS velocity in Soppensee than in Lioson is consistent with the stronger surface cooling (for a similar mixed layer depth). The higher TS velocity in Lake Hallwil (for a similar forcing) is explained by the larger mixed region experiencing differential cooling. These observations confirm that both the forcing conditions (B_0) and the bathymetry-dependent effects of stratification (L_{ML}) affect the TS intensity, as expected from scaling relationships (Sect. 5.2.4). The thicker TS in Lake Hallwil ($h_d \approx 3 \text{ m}$) compared to the two other sites ($h_d \approx 2 \text{ m}$) is also consistent with the deeper measurement location $h_{\text{max,MT}} = 7 \text{ m}$ (Tab. S5.1). More detailed time series of these events and similar examples from other lakes are provided in Supplementary Information (Figs. S5.1-S5.6).

5.3.3 Transport scaling

We tested the transport scaling relationships by averaging the measured transport quantities (Sect. 5.2.3) and scaling parameters (Sect. 5.2.3) for each lake (Fig. 5.3). Despite inter-lake variability, the scaling relationships for the cross-shore velocity (Eq. (5.10)), unit-width discharge (Eq. (5.11)) and transition timescale (Eq. (5.12)) reproduced the general trend. The best linear fits (with 0 intercept) for the TS velocity and discharge are $U_{\text{avg}} = 0.33 (B_{0,c} L_{\text{ML},c})^{1/3}$ and $q_{\text{avg}} = 0.32 (B_{0,c} L_{\text{ML},c})^{1/3} h_{\text{lit}}$, respectively. The proportionality coefficients of $c_U = 0.33$ and $c_q = 0.32$ are close to the coefficients $c_U = 0.33$ and $c_q = 0.34$ derived from the transport seasonality in Rotsee (Doda et al., 2022). The coefficient c_q is also consistent with recent numerical studies reporting $c_q \approx 0.3$ (Ramón et al., 2022; Ulloa et al., 2022).

The range of cross-shore velocities covered by the different sites remained limited, from $U_{\text{avg}} = 0.4 \text{ cm s}^{-1}$ to $U_{\text{avg}} = 1.7 \text{ cm s}^{-1}$ (Fig. 5.3a), because of the weak dependence of U on B_0 and L_{ML} ($1/3$ exponent). Conversely, the discharge q is proportional to h_{lit} , which makes it more sensitive to

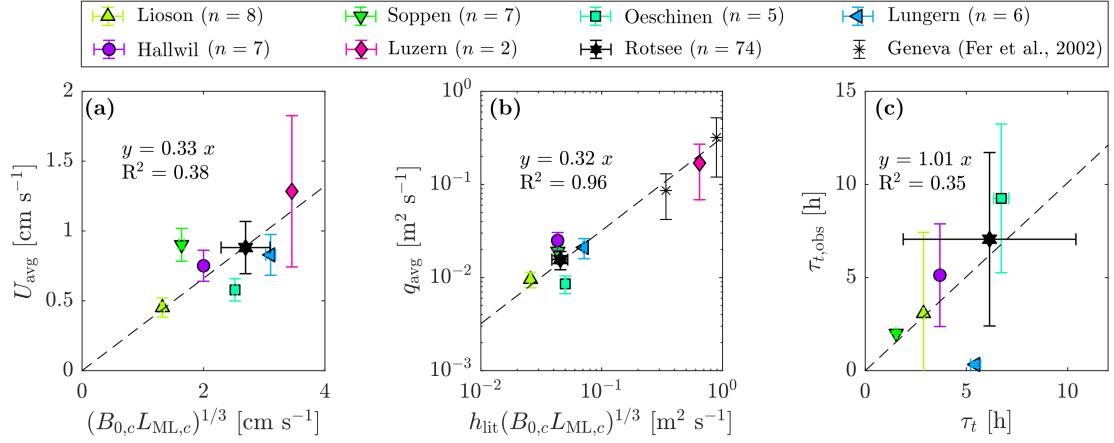


Figure 5.3 – Comparison between transport observations and scaling relationships. Lake averaged (a) cross-shore velocity, (b) unit-width discharge, and (c) duration of the transition period, as a function of the respective scaling relationships (Sect. 5.2.4). The points include the six lakes where TS were observed as well as the data from Rotsee (Doda et al., 2022) and the TS discharge at two locations in Lake Geneva (Fer et al., 2002b) in (b). In (c), the duration of the transition period $\tau_{t,\text{obs}}$ was not computed in Luzern (Sect. 5.2.3). The scaling parameters $B_{0,c}$ and $L_{\text{ML},c}$ are averages over the cooling phase of each TS event. The horizontal and vertical error bars represent the standard deviation. The number of events averaged for each lake (n) is indicated in the legend. The dashed line corresponds to the best linear fit (with 0 intercept), whose equation and coefficient of determination (R^2) are indicated. The p value of an F test was $p < 0.01$ for the three fits. Note the logarithmic scale in (b).

the bathymetry and led to one-order of magnitude differences in q_{avg} between lakes (Fig. 5.3b). Luzern Bay was the only lake of our dataset with a deep mixed region ($h_{\text{ML}} \sim 10^2 \text{ m}$, Fig. 5.1c) and deep littoral region ($h_{\text{lit}} \approx 20 \text{ m}$). We added the transport estimates from Fer et al. (2002b) in Lake Geneva to compare the Luzern estimates with another deep lake (Fig. 5.3b). The results were similar for both lakes, with TS thickness and discharge of $h_d \sim 10^1 \text{ m}$ and $q_{\text{avg}} \sim 10^{-1} \text{ m}^2 \text{s}^{-1}$, respectively (Fig. S5.6). These high values control the linear regression in Fig. 5.3b, which explains the high R^2 . Additional observations at intermediate values of h_{lit} are required to improve the robustness of the fit. The root-mean-square percent errors of 25 % for U and 36 % for q indicate that the simple scaling formulae do not fully resolve the inter-lake variability but reproduce the general trend. The scaling formula for q is particularly sensitive to the accuracy of the bathymetry data and the definition of the littoral region. For example, the depth h_{lit} (and the resulting q) is increased by a factor of ≈ 2 if it is chosen as the depth where discharge is computed ($h_{\text{lit}} = h_{\text{max,MT}}$) instead of the averaged depth of the region upslope of MT. We also noticed similar differences in h_{lit} depending on the bathymetry resolution used (interpolated bathymetry from topographic maps compared to high-resolution bathymetry from in-situ profiles). These scaling formulae are therefore suitable for order of magnitude estimates but cannot capture the transport variability

between lakes of similar size and depth (i.e., $L_{ML} \sim 10^2$ m and $h_{lit} \sim 10^0$ m for most lakes of our dataset).

The transition timescale predicted the TS formation in most lakes, despite the strong variability of $\tau_{t,obs}$ between events (Fig. 5.3c). The regression slope of ≈ 1 indicates that τ_t does not need a proportionality coefficient to estimate the duration of the transition period. The low $\tau_{t,obs}$ for Lake Lungern was due to the presence of a continuous bottom stratification at MT which led to $t_{mix} \approx t_0$ and $\tau_{t,obs} \approx 0$ (example in Fig. S5.4). This bottom stratification may have been an effect of an inflow near MT. If $\tau_{t,obs}$ is computed from the start of the cooling phase instead, $\tau_{t,obs} = t_0 - t_{c,0} \approx 4.1 \pm 2.6$ h for Lake Lungern, which is closer to the predicted $\tau_t = 5.4$ h. The starting time of a TS event is difficult to determine in the field due to the presence of discontinuous flows, which explains the intra-lake variability in $\tau_{t,obs}$. Yet, the root-mean-square error of 2.4 h is low with respect to this variability, which confirms that τ_t is a suitable predictor for TS formation. The scaling formula should be further tested in deep lakes where $\tau_t > 10$ h to cover a wider range of values.

5.3.4 Predictive procedure

To predict the TS occurrence and intensity in a given lake, we propose a simple procedure based on the previous scaling formulae (Fig. 5.4). The objective of this predictive procedure is to provide spatio-temporal estimates of the TS-induced transport to identify regions within a lake where TSs are likely to occur and optimal periods for TS formation. This approach could be used to select a lake based on the presence or absence of TSs, plan specific measurements to minimize or to assess the effects of lateral transport, or re-analyze collected data for a posteriori identification of potential lateral transport effects.

The procedure requires three types of input data: 3D bathymetry, time series of meteorological forcing and time series of the vertical thermal structure. The time series must have at least hourly resolution. The thermal structure can be obtained from in-situ measurements (thermistor array) or numerical simulations (1D model). Time series of forcing quantities are first calculated from the meteorological and temperature data (steps 1-3 in Fig. 5.4). One or several locations of interest are then selected, for which transport estimates will be calculated (step 4). These locations can be based on specific measurement points or be uniformly distributed over the lake surface to create a TS occurrence map. Steps 4-6 are performed for each selected location P of coordinates (x_P, y_P, z_P) . A cross-shore transect of bathymetry $h_{max}(x)$ is determined as the longest path from the shore to the lake center that goes through point P and crosses the isobaths perpendicularly. The length of the littoral region L_{lit} is then defined as the distance along the cross-shore transect from the shore

to point P. The depth h_{lit} is the averaged depth along this distance. If a littoral plateau region is present, its length L_p and depth h_p are computed. Time series of $L_{\text{ML}}(t)$ are calculated with Eq. (5.2) (step 5).

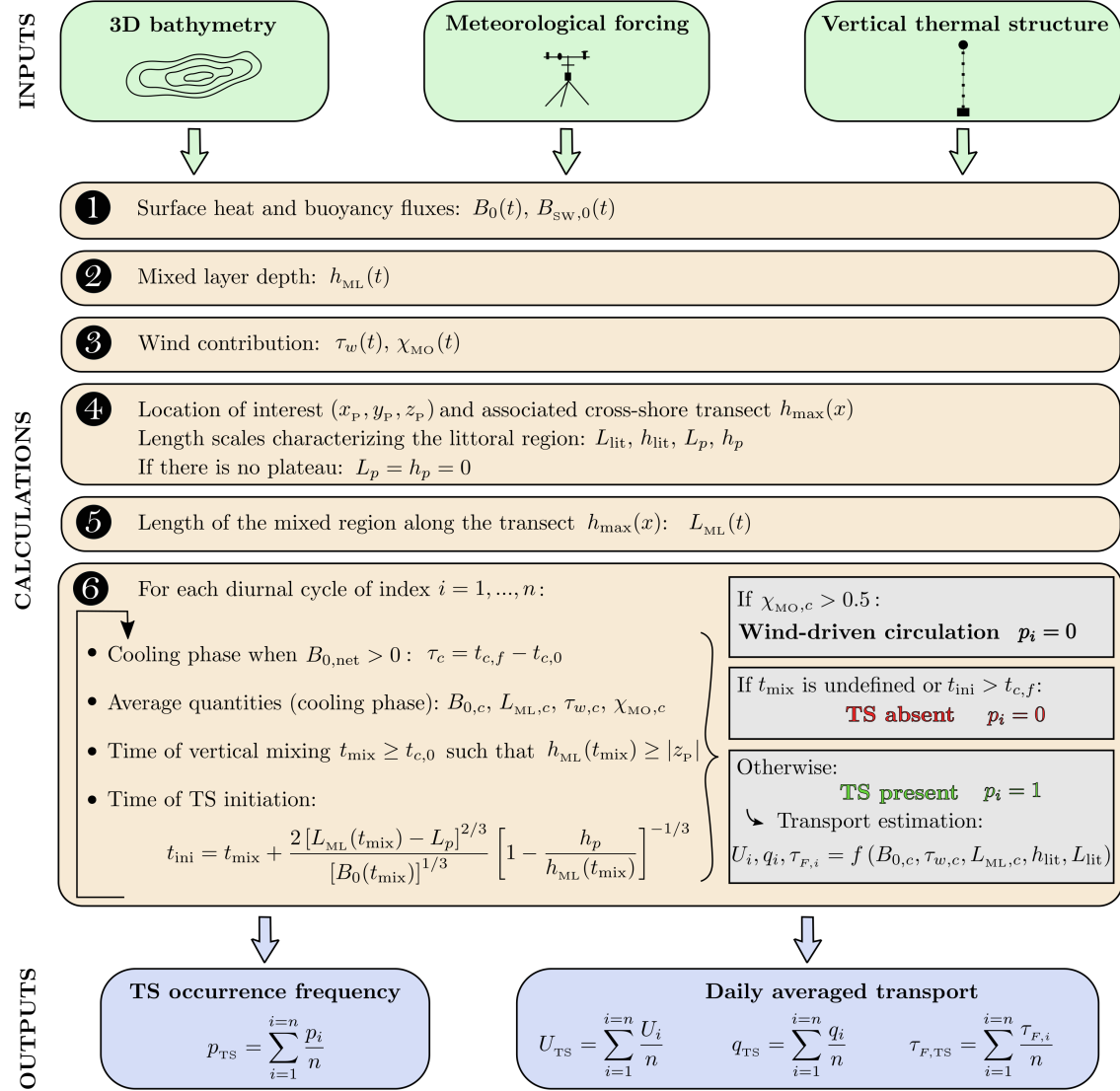


Figure 5.4 – Diagram schematizing the TS predictive procedure. The green boxes represent input data. The orange boxes are the computation steps required to determine the TS occurrence and intensity at a given location. The blue boxes are output quantities summarizing the TS occurrence and transport over the entire time series.

Step 6 is iterative and repeated for each diurnal cycle of the time series. The diurnal cycles are defined such that they include the entire cooling periods (e.g., starting and ending at 15:00 UTC for Switzerland). The starting and ending time of the cooling phase (Eq. (5.5)), the forcing quantities averaged over the cooling phase, the time of vertical mixing t_{mix} , the transition timescale τ_t (Eq. (5.12)) and the time of TS initiation $t_{\text{ini}} = t_{\text{mix}} + \tau_t$ are calculated for each diurnal cycle. A TS event is likely to occur on that day if wind is weak ($\chi_{\text{MO}} < 0.5$) and TS forms before the end of the cooling phase ($t_{\text{ini}} < t_{c,f}$). If it is the case, the transport-related quantities U , q and τ_F are computed with Eqs. (5.10), (5.13) and (5.9), respectively. Step 6 is repeated for all n diurnal cycles to obtain time series of TS occurrence and intensity at location P used to determine TS optimal occurrence periods. The daily TS occurrence and transport quantities are averaged over the time series to provide summary estimates p_{TS} , U_{TS} , q_{TS} and $\tau_{F,\text{TS}}$ for the period considered.

By applying steps 4-6 to different locations, the spatial variability in TS occurrence and intensity can be used to identify lake regions affected by TSs. This procedure focuses on downslope gravity currents occurring in the mixed region $h_{\text{max}} < h_{\text{ML}}$ and does not include the TS intrusions into the stratified region. Estimating the propagation distance of TS intrusions could be the subject of further investigations. Yet, a map of the TS occurrence highlighting littoral regions where TSs originate would provide a first indication of potential effects of lateral transport in the pelagic region.

5.3.5 Sensitivity analysis

To illustrate the effects of varying forcing, stratification and bathymetry on the TS occurrence and intensity, we performed a sensitivity analysis based on the scaling formulae used in the predictive procedure (Fig. 5.5). We varied B_0 and h_{ML} over two orders of magnitude and compared two slopes $S = 0.01, 0.1$ and two cooling period durations $\tau_c = 12, 24$ h, selected from the range of values observed in our dataset (Fig. 5.1, Tab. S5.1). We computed the transport quantities for a littoral region of averaged depth $h_{\text{lit}} = 5$ m. This value is based on the typical depth of the littoral region from our dataset. Choosing another depth would not qualitatively change the results of the sensitivity analysis.

The TS occurrence condition (assuming an initially mixed water column) is $\tau_t < \tau_c$. This condition corresponds to the area below the black line in Figs. 5.5d–i. According to Eq. (5.12), the transition timescale decreases for increasing B_0 or decreasing L_{ML} , as these changes lead to a faster development of lateral density gradients (Ulloa et al., 2022). Lower values of L_{ML} are reached for shallower h_{ML} or steeper slopes. Thus, TSs occur more frequently if (1) B_0 increases (from left to

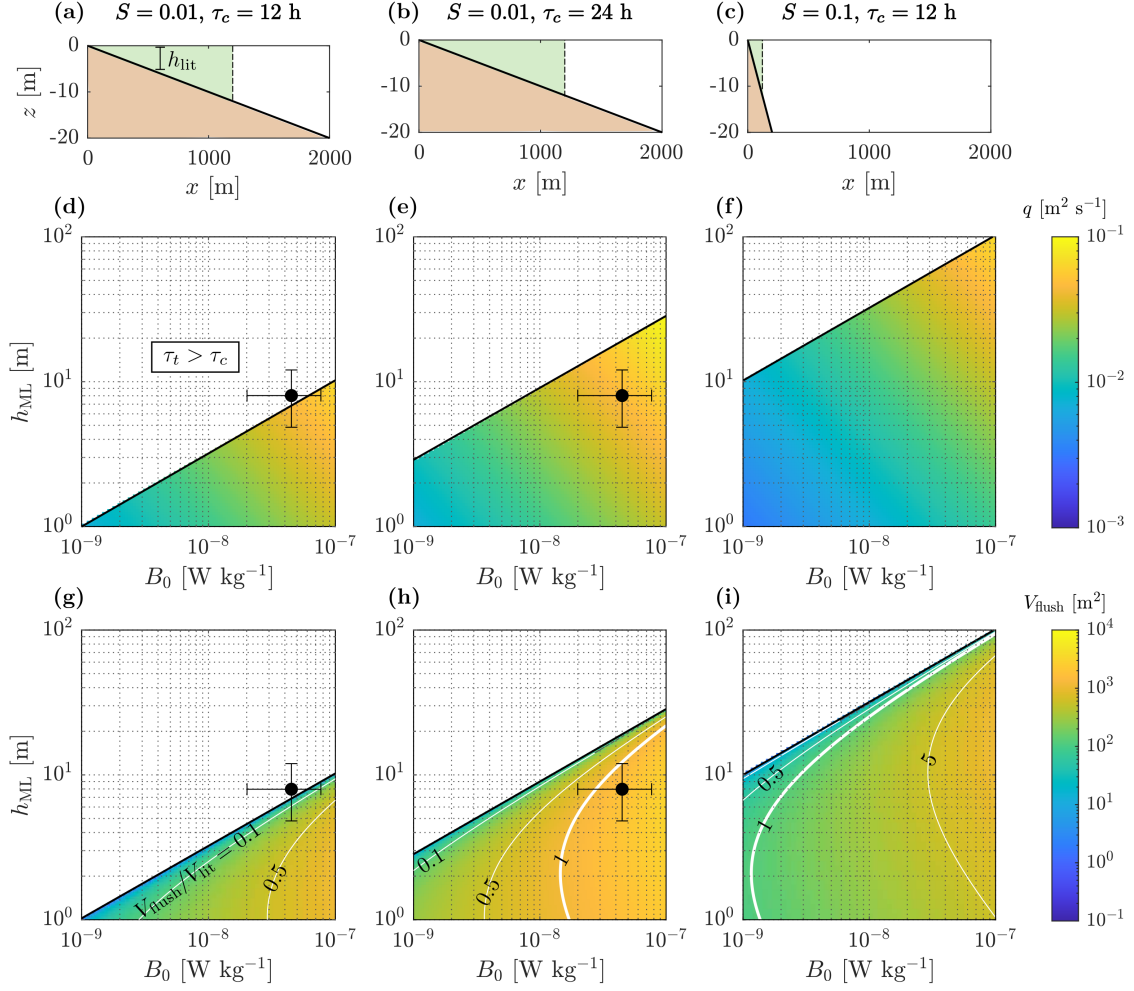


Figure 5.5 – Sensitivity analysis of the parameters controlling the TS occurrence and intensity. Three scenarios are considered, including (a, d, g) low slope and short cooling period, (b, e, h) low slope and long cooling period, and (c, f, i) high slope and short cooling period. (a, b, c) Bathymetry along the cross-shore transect for the three scenarios. The green area depicts the littoral region defined by an average depth of $h_{\text{lit}} = 5$ m. (d, e, f) Unit-width discharge as a function of the surface buoyancy flux B_0 and mixed layer depth h_{ML} for the three scenarios. The discharge values are shown only when the TS occurrence condition $\tau_t < \tau_c$ is met (region below the black solid line). The black dot in (d) and (e) corresponds to the median values of B_0 and h_{ML} in Rotsee and error bars indicate the 25 % and 75 % quantiles as in Figs. 5.1b and 5.1c. (g, h, i) Flushed unit-width volume at the end of the cooling phase, as a function of B_0 and h_{ML} for the three scenarios. The flushed volume is calculated by integrating q over time, between the TS initiation and the end of the cooling phase: $V_{\text{flush}} = q(\tau_c - \tau_t)$. The black dot in (g) and (h) is the same as in (d) and (e). White lines indicate the number of times the littoral region is entirely flushed at the end of the cooling phase.

right in Figs. 5.5d–i), (2) h_{ML} decreases (from top to bottom in Figs. 5.5d–i), (3) the slope increases (from Fig. 5.5d to Fig. 5.5f) or (4) τ_c increases (from Fig. 5.5d to Fig. 5.5e). These four parameters vary between lakes but also temporally. The transition timescale decreases from summer to winter due to the decrease of B_0 and the deepening of h_{ML} , but the longer τ_c can lead to a net increase

in TS occurrence. This is illustrated with the example of Rotsee in Fig. 5.5. When $\tau_c = 12$ h, the typical B_0 and h_{ML} values in Rotsee lead to conditions very close to the occurrence criterion $\tau_t > \tau_c$, indicating a low TS occurrence (Figs. 5.5d and 5.5g). When $\tau_c = 24$ h, the occurrence region on the B_0 - h_{ML} plot expands and the same forcing conditions lead to more frequent TSs (Figs. 5.5e and 5.5h).

The TS discharge increases with B_0 and h_{ML} for a given slope (Figs. 5.5d–f). These two parameters vary in an opposite direction from summer to winter (decrease of B_0 , deepening of h_{ML}). In Rotsee, the seasonality of B_0 overcame the mixed layer deepening and we observed a net transport weakening over the autumn period (Doda et al., 2022). An increase in slope reduces L_{ML} which leads to a lower q for the same forcing conditions (Fig. 5.5f). Although TSs form faster and are more frequent in a steeper lake, the resulting lateral transport is weaker.

To combine the effects of TS occurrence and intensity on the net transport, we computed the integrated unit-width flushed volume V_{flush} during the cooling phase (Figs. 5.5g–i). The increase in slope from Fig. 5.5g to Fig. 5.5i produces a longer but weaker TS event, which does not change V_{flush} . However, doubling τ_c from Fig. 5.5g to Fig. 5.5h leads to longer TSs of the same intensity, which increases V_{flush} by almost one order of magnitude. If V_{flush} is normalized by the volume of the littoral region V_{lit} , the steep scenario corresponds to the highest littoral flushing rate (5 times more flushing than the low slope scenario with long τ_c) because of the smaller littoral region (Fig. 5.5c). Thus, the implications of a different bathymetry depend on the region and transport quantities of interest. For given forcing conditions, a steeper lake forms TSs more frequently that flush the littoral region at a higher rate. Yet, the effects of the lateral transport on the pelagic zone are reduced due to the smaller flushed volume.

5.4 Conclusions

This study presented high-resolution observations of cooling-driven thermal siphons from six lakes of various bathymetries experiencing different forcing conditions. Our results demonstrate that TS is an ubiquitous lateral transport process. This unique dataset allowed us to test theoretically and laboratory based transport scaling formulae on different systems. Despite the natural variability, we found that differences in TS formation (transition timescale τ_t) and intensity (cross-shore velocity U and unit-width discharge q) between lakes are well reproduced by the existing scaling formulae. Such relationships provide order of magnitude estimates of TS-induced lateral transport which can be used to assess the significance of TSs in a given lake. For this purpose, we proposed a

predictive procedure computing the TS occurrence and averaged lateral transport from bathymetry, meteorological forcing and vertical thermal structure. We further discussed the effects of changing forcing and bathymetry on the TS occurrence and intensity. These results demonstrate that TS-induced lateral transport varies seasonally and spatially. Small and steep lakes tend to produce frequent but weak TSs ($q \sim 10^{-2} \text{ m}^2 \text{ s}^{-1}$) whereas large lakes with shallow regions lead to one order of magnitude larger TS discharge ($q \sim 10^{-1} \text{ m}^2 \text{ s}^{-1}$).

The robustness of the scaling relationships and the predictive procedure would benefit from further TS observations, particularly in medium-size lakes where $L_{ML} \sim 10^3 \text{ m}$ and $h_{lit} \sim 10 \text{ m}$. In addition, a next step will consist of testing and potentially improving our proposed predictive procedure on lakes with available TS observations. To encourage further in-situ quantification of TSs and the development of a larger TS database, we make our data publicly available (via the datalakes portal) and our transport analyses easily reproducible. We believe that further in-situ observations of TSs from various systems combined with laboratory and numerical experiments will lead to a robust predictive method that could ultimately include the TS-induced transport into one-dimensional lake models.

Code and data availability

The data collected in the nine lakes of this study is available on the datalakes web portal for visualization and download (preliminary versions):

- ◇ Luzern Bay: <https://www.datalakes-eawag.ch/datadetail/927>
- ◇ Lac de Joux: <https://www.datalakes-eawag.ch/datadetail/922>
- ◇ Lac de l'Hongrin: <https://www.datalakes-eawag.ch/datadetail/924>
- ◇ Lac Lioson: <https://www.datalakes-eawag.ch/datadetail/925>
- ◇ Soppensee: <https://www.datalakes-eawag.ch/datadetail/930>
- ◇ Oeschinensee: <https://www.datalakes-eawag.ch/datadetail/928>
- ◇ Lake Lungern: <https://www.datalakes-eawag.ch/datadetail/926>
- ◇ Lake Sarnen: <https://www.datalakes-eawag.ch/datadetail/929>
- ◇ Lake Hallwil: <https://www.datalakes-eawag.ch/datadetail/923>

The scripts used to process, analyzed and plot the data are available for download at: <https://drive.switch.ch/index.php/s/xZrLuoNjSpFnXHI>. They will be moved to the Eawag Research Data Institutional Collection and associated with a DOI number once this chapter will be accepted for publication.

Acknowledgements

We sincerely thank all the people who participated to the field campaigns (in alphabetical order): Guillaume Cunillera, Christian Dinkel, Nathalie Friese, Abolfazl Irani Rahaghi, David Janssen, Sébastien Lavanchy, Oscar Sepúlveda Steiner, Judith van der Giessen and Sigrid van Grinsven. We are grateful to the Cantons of Vaud, Berne, Obwalden, Luzern and Aarau for their support. We particularly thank Bernhard Pfyffer and Angelo Foletti for giving us access to Soppensee and to their “Bootshaus”, and the hydroelectricity company Alpiq for their help in planning the field campaigns in Hongrin. We are also grateful to Daniel McGinnis and César Ordoñez, who facilitated the field campaigns in Lioson and Soppensee and provided bathymetry data for both lakes. The meteorological data from the Lucerne and Giswil (Lake Sarnen) weather stations were provided by MeteoSwiss, the Swiss Federal Office of Meteorology and Climatology. The temperature data from the Reuss river used to calculate the heat fluxes in Luzern Bay was provided by the Swiss Federal Office of the Environment.

Financial support

This study was financed by the Swiss National Science Foundation (“Buoyancy driven nearshore transport in lakes” project; HYPOlimnetic THERmal SiphonS, HYPOTHESIS, grant no. 175919).

There is no competing interest for any author.

References

- Bonvin, F., Rutler, R., Chèvre, N., Halder, J., & Kohn, T. (2011). Spatial and temporal presence of a wastewater-derived micropollutant plume in Lake Geneva. *Environmental Science & Technology*, 45(11), 4702–4709. <https://doi.org/10.1021/es2003588>

- Brothers, S., Kazanjian, G., Köhler, J., Scharfenberger, U., & Hilt, S. (2017). Convective mixing and high littoral production established systematic errors in the diel oxygen curves of a shallow, eutrophic lake. *Limnology and Oceanography: Methods*, 15(5), 429–435. <https://doi.org/10.1002/lom3.10169>
- Chubarenko, I. P. (2010). Horizontal convective water exchange above a sloping bottom: The mechanism of its formation and an analysis of its development. *Oceanology*, 50(2), 166–174. <https://doi.org/10.1134/S0001437010020025>
- Czikowsky, M. J., MacIntyre, S., Tedford, E. W., Vidal, J., & Miller, S. D. (2018). Effects of wind and buoyancy on carbon dioxide distribution and air-water flux of a stratified temperate lake. *Journal of Geophysical Research: Biogeosciences*, 123(8), 2305–2322. <https://doi.org/10.1029/2017JG004209>
- Doda, T., Ramón, C. L., Ulloa, H. N., Wüest, A., & Bouffard, D. (2022). Seasonality of density currents induced by differential cooling. *Hydrology and Earth System Sciences*, 26(2), 331–353. <https://doi.org/10.5194/hess-26-331-2022>
- Fer, I., Lemmin, U., & Thorpe, S. A. (2002b). Winter cascading of cold water in Lake Geneva. *Journal of Geophysical Research*, 107(C6), 3060. <https://doi.org/10.1029/2001JC000828>
- Harashima, A., & Watanabe, M. (1986). Laboratory experiments on the steady gravitational circulation excited by cooling of the water surface. *Journal of Geophysical Research*, 91(C11), 13056–13064. <https://doi.org/10.1029/JC091iC11p13056>
- Hofmann, H., Federwisch, L., & Peeters, F. (2010). Wave-induced release of methane: littoral zones as source of methane in lakes. *Limnology and Oceanography*, 55(5), 1990–2000. <https://doi.org/10.4319/lo.2010.55.5.1990>
- Horsch, G. M., & Stefan, H. G. (1988). Convective circulation in littoral water due to surface cooling. *Limnology and Oceanography*, 33(5), 1068–1083. <https://doi.org/10.4319/lo.1988.33.5.1068>
- James, W. F., & Barko, J. W. (1991a). Estimation of phosphorus exchange between littoral and pelagic zones during nighttime convective circulation. *Limnology and Oceanography*, 36(1), 179–187. <https://doi.org/10.4319/lo.1991.36.1.0179>
- MacIntyre, S., & Melack, J. M. (1995). Vertical and horizontal transport in lakes: linking littoral, benthic, and pelagic habitats. *Journal of the North American Benthological Society*, 14(4), 599–615. <https://doi.org/10.2307/1467544>
- Monismith, S. G., Imberger, J., & Morison, M. L. (1990). Convective motions in the sidearm of a small reservoir. *Limnology and Oceanography*, 35(8), 1676–1702. <https://doi.org/10.4319/lo.1990.35.8.1676>
- Pálmarrsson, S. Ó., & Schladow, S. G. (2008). Exchange flow in a shallow lake embayment. *Ecological Applications*, 18(8), A89–A106. <https://doi.org/10.1890/06-1618.1>

- Phillips, O. (1966). On turbulent convection currents and the circulation of the Red Sea. *Deep Sea Research and Oceanographic Abstracts*, 13(6), 1149–1160. [https://doi.org/10.1016/0011-7471\(66\)90706-6](https://doi.org/10.1016/0011-7471(66)90706-6)
- Ramón, C. L., Ulloa, H. N., Doda, T., & Bouffard, D. (2022). Flushing the lake littoral region: the interaction of differential cooling and mild winds. *Water Resources Research*, 58(3), e2021WR030943. <https://doi.org/10.1029/2021WR030943>
- Rao, Y. R., & Schwab, D. J. (2007). Transport and mixing between the coastal and offshore waters in the Great Lakes: a review. *Journal of Great Lakes Research*, 33(1), 202–218. [https://doi.org/10.3394/0380-1330\(2007\)33\[202:TAMBTC\]2.0.CO;2](https://doi.org/10.3394/0380-1330(2007)33[202:TAMBTC]2.0.CO;2)
- Razlutskij, V. I., Buseva, Z. F., Yu. Feniova, I., & Semenchenko, V. P. (2021). Convective circulation influences horizontal movement by planktonic crustaceans in the littoral zone of a mesotrophic lake. *Freshwater Biology*, 66(4), 716–729. <https://doi.org/10.1111/fwb.13672>
- Roget, E., Colomer, J., Casamitjana, X., & Llebot, J. E. (1993). Bottom currents induced by baroclinic forcing in Lake Banyoles (Spain). *Aquatic Sciences*, 55(3), 206–227. <https://doi.org/10.1007/BF00877450>
- Rogowski, P., Merrifield, S., Ding, L., Terrill, E., & Gesiriech, G. (2019). Robotic mapping of mixing and dispersion of augmented surface water in a drought frequent reservoir. *Limnology and Oceanography: Methods*, 17(9), 475–489. <https://doi.org/10.1002/lom3.10326>
- Rueda, F., Moreno-Ostos, E., & Cruz-Pizarro, L. (2007). Spatial and temporal scales of transport during the cooling phase of the ice-free period in a small high-mountain lake. *Aquatic Sciences*, 69(1), 115–128. <https://doi.org/10.1007/s00027-006-0823-8>
- Sadro, S., Melack, J. M., & MacIntyre, S. (2011). Spatial and temporal variability in the ecosystem metabolism of a high-elevation lake: integrating benthic and pelagic habitats. *Ecosystems*, 14(7), 1123–1140. <https://doi.org/10.1007/s10021-011-9471-5>
- Sharip, Z., Hipsey, M., Schooler, S., & Hobbs, R. (2012). Physical circulation and spatial exchange dynamics in a shallow floodplain wetland. *International Journal of Design & Nature and Ecodynamics*, 7(3), 274–291. <https://doi.org/10.2495/DNE-V7-N3-274-291>
- Sturman, J. J., & Ivey, G. N. (1998). Unsteady convective exchange flows in cavities. *Journal of Fluid Mechanics*, 368, 127–153. <https://doi.org/10.1017/S002211209800175X>
- Sturman, J. J., Oldham, C. E., & Ivey, G. N. (1999). Steady convective exchange flows down slopes. *Aquatic Sciences*, 61(3), 260–278. <https://doi.org/10.1007/s000270050065>
- Ulloa, H. N., Ramón, C. L., Doda, T., Wüest, A., & Bouffard, D. (2022). Development of overturning circulation in sloping waterbodies due to surface cooling. *Journal of Fluid Mechanics*, 930, A18. <https://doi.org/10.1017/jfm.2021.883>

- Vander Zanden, M. J., & Vadeboncoeur, Y. (2020). Putting the lake back together 20 years later: what in the benthos have we learned about habitat linkages in lakes? *Inland Waters*, 10(3), 305–321. <https://doi.org/10.1080/20442041.2020.1712953>
- Wells, M. G., & Sherman, B. (2001). Stratification produced by surface cooling in lakes with significant shallow regions. *Limnology and Oceanography*, 46(7), 1747–1759. <https://doi.org/10.4319/lo.2001.46.7.1747>
- Wüest, A., & Lorke, A. (2003). Small-scale hydrodynamics in lakes. *Annual Review of Fluid Mechanics*, 35(1), 373–412. <https://doi.org/10.1146/annurev.fluid.35.101101.161220>



Supplementary Information for Chapter 5

Table S5.1 – Geometrical characteristics of the lakes and measurement information

Lake	Elevation [m]	Surface area [km ²]	Average depth [m]	Maximum depth [m]	Slope h_{ML}/L_{ML}	Depth MB [m]	Depth MT [m]	Measurement period
Lake Lucerne (Luzern)	434	113.6	104	214	0.02	104	55	Feb 12-16
Lake Hallwil	449	10.0	28	48	0.08	41	7	Oct 26-Nov 12
Lake Sarnen	469	7.0	33	51	0.02	39	6	Oct 14-28
Soppensee	593	0.2	12	27	0.10	25	5	Sep 29-Oct 7
Lake Lungern	688	1.7	33	68	0.05	24	6	Oct 14-23
Lac de Joux	1004	8.5	22	32	0.01	32	4	Aug 25-Sep 8
Lac de l'Hongrin	1250	1.6	33	105	0.03	47	11	Sep 2-23
Oeschinensee	1578	1.1	34	56	0.02	52	5	Oct 1-8
Lac Lioson	1848	0.1	14	28	0.07	26	4	Sep 10-24
Rotsee (Doda et al., 2022)	419	0.5	9	16	0.02	16	4	Mar 2019-Mar 2020

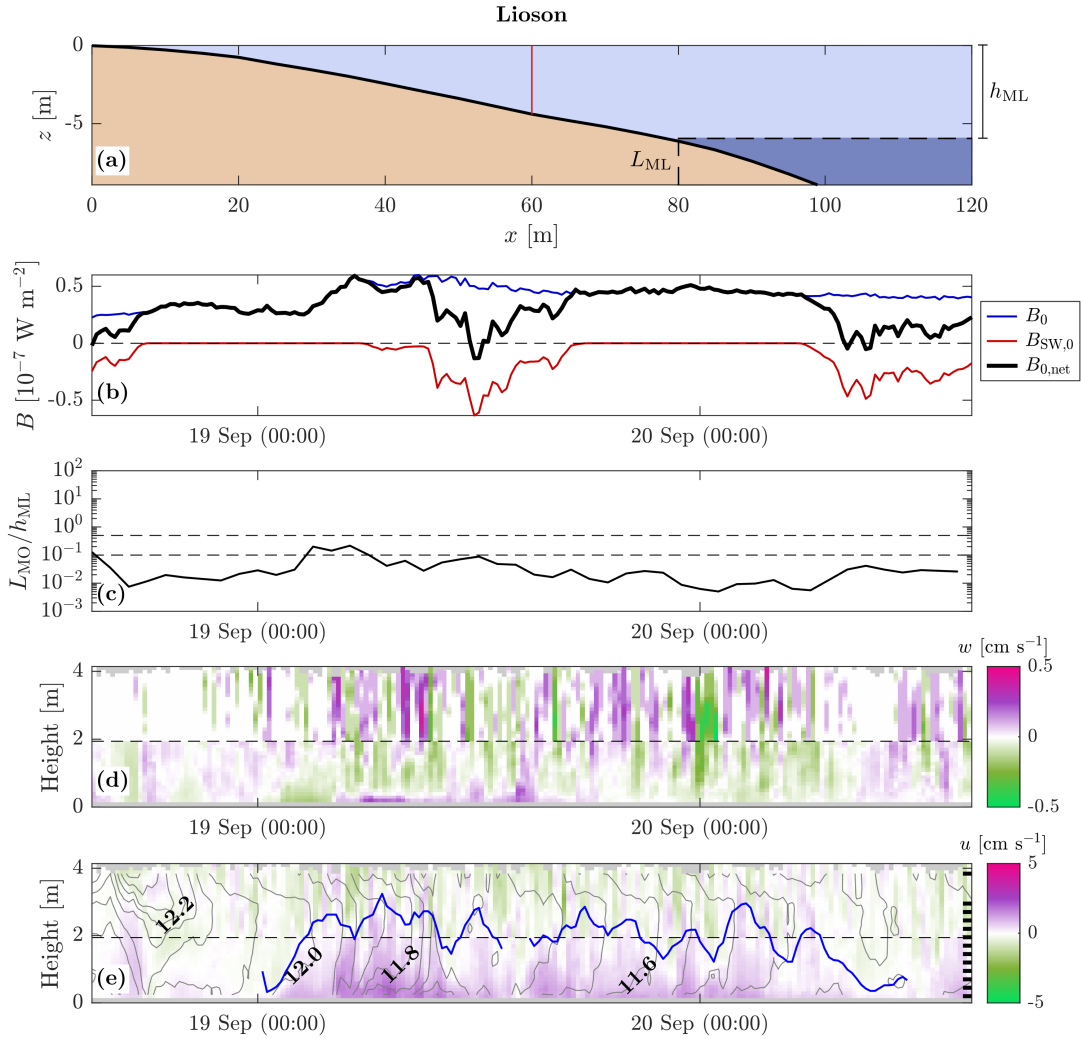


Figure S5.1 – Examples of thermal siphon events in Lioson on 18-20 September. (a) Bathymetry along the selected cross-shore transect. The vertical red line depicts the location of the MT mooring. The light and dark blue areas correspond to the mixed layer and deeper stratified layer, respectively, averaged over the 48 h long time series shown in (b)-(e). (b) 48 h long time series (starting and ending at 15:00 UTC) of surface buoyancy fluxes. (c) 48 h long time series of non-dimensional Monin-Obukhov length χ_{MO} . The two horizontal dashed lines delimit the wind-convection interaction regime $0.1 \lesssim \chi_{MO} \lesssim 0.5$ from Ramón et al. (2022). (d) 48 h long time series of vertical velocity measured at MT as a function of height from the sediment to the surface. Positive w values (purple) correspond to an upward flow. The horizontal dashed line delimits the Aquadopp (below) and RDI (above) data. (e) 48 h long time series of cross-shore velocity measured at MT as a function of height from the sediment to the surface. Positive u values (purple) correspond to downslope gravity currents. The horizontal dashed line is the same as in (d). The blue line depicts the upper interface ($u = 0$) of the gravity currents identified as TS events. Gray lines are 0.05°C spaced isotherms, linearly interpolated between the thermistors shown by black ticks on the right vertical axis.

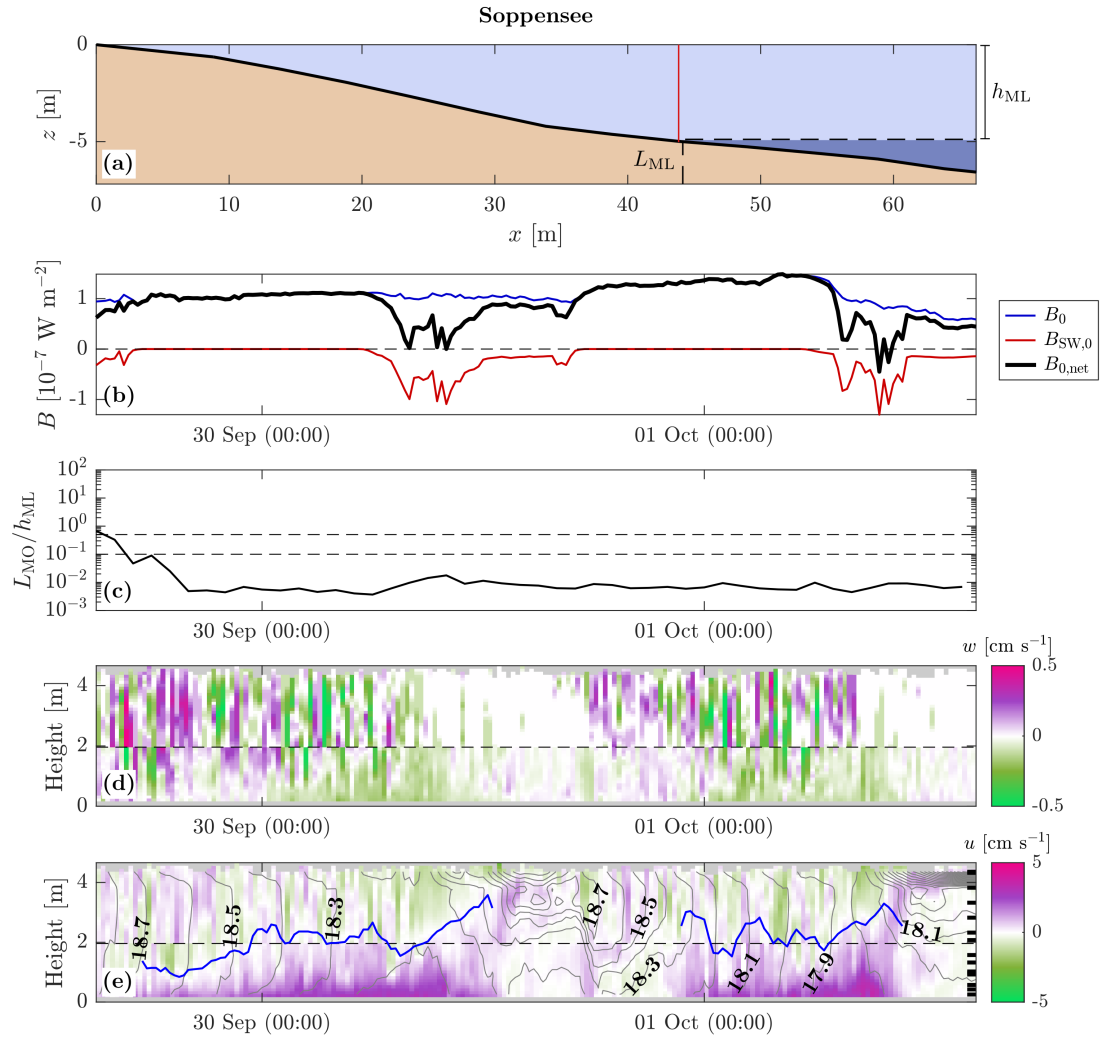


Figure S5.2 – Examples of thermal siphon events in Soppensee on 29 September-01 October. See the caption of Fig. S5.1 for details. In **(e)**, the isotherms are spaced by 0.1 °C.

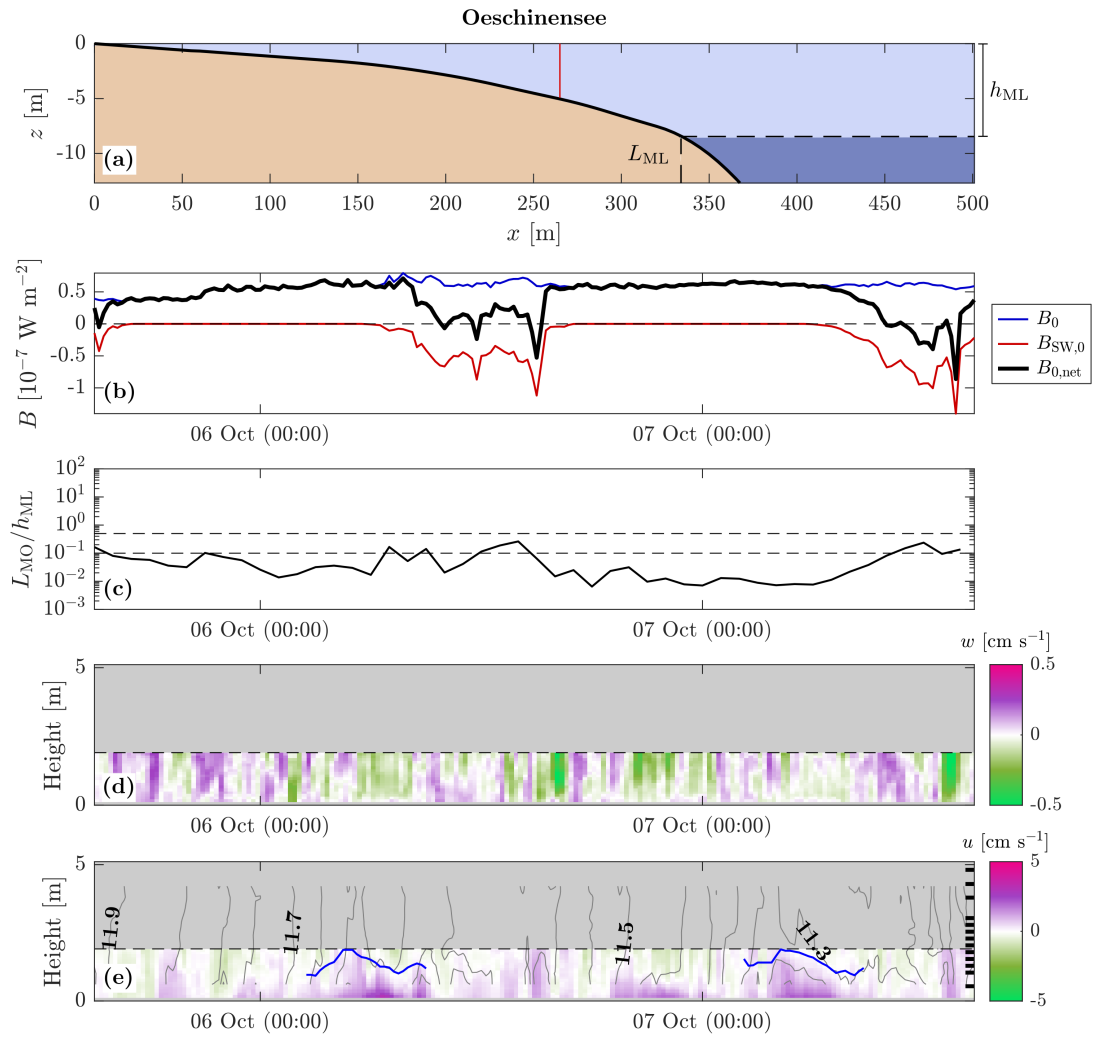


Figure S5.3 – Examples of thermal siphon events in Oeschinensee on 5-7 October. See the caption of Fig. S5.1 for details. The RDI ADCP did not collect velocity data.

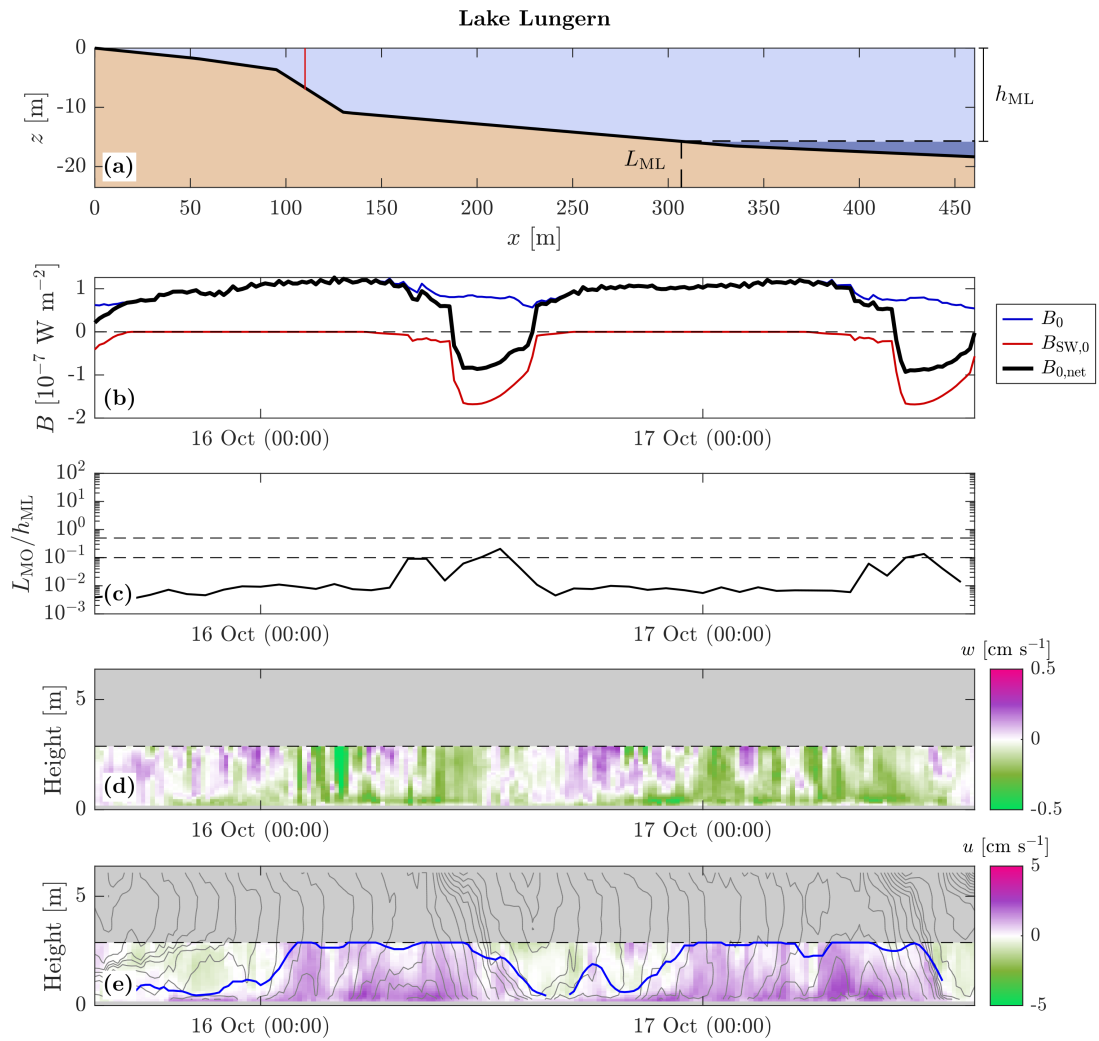


Figure S5.4 – Examples of thermal siphon events in Lake Lungern on 15-17 October. See the caption of Fig. S5.1 for details. The RDI ADCP did not collect velocity data.

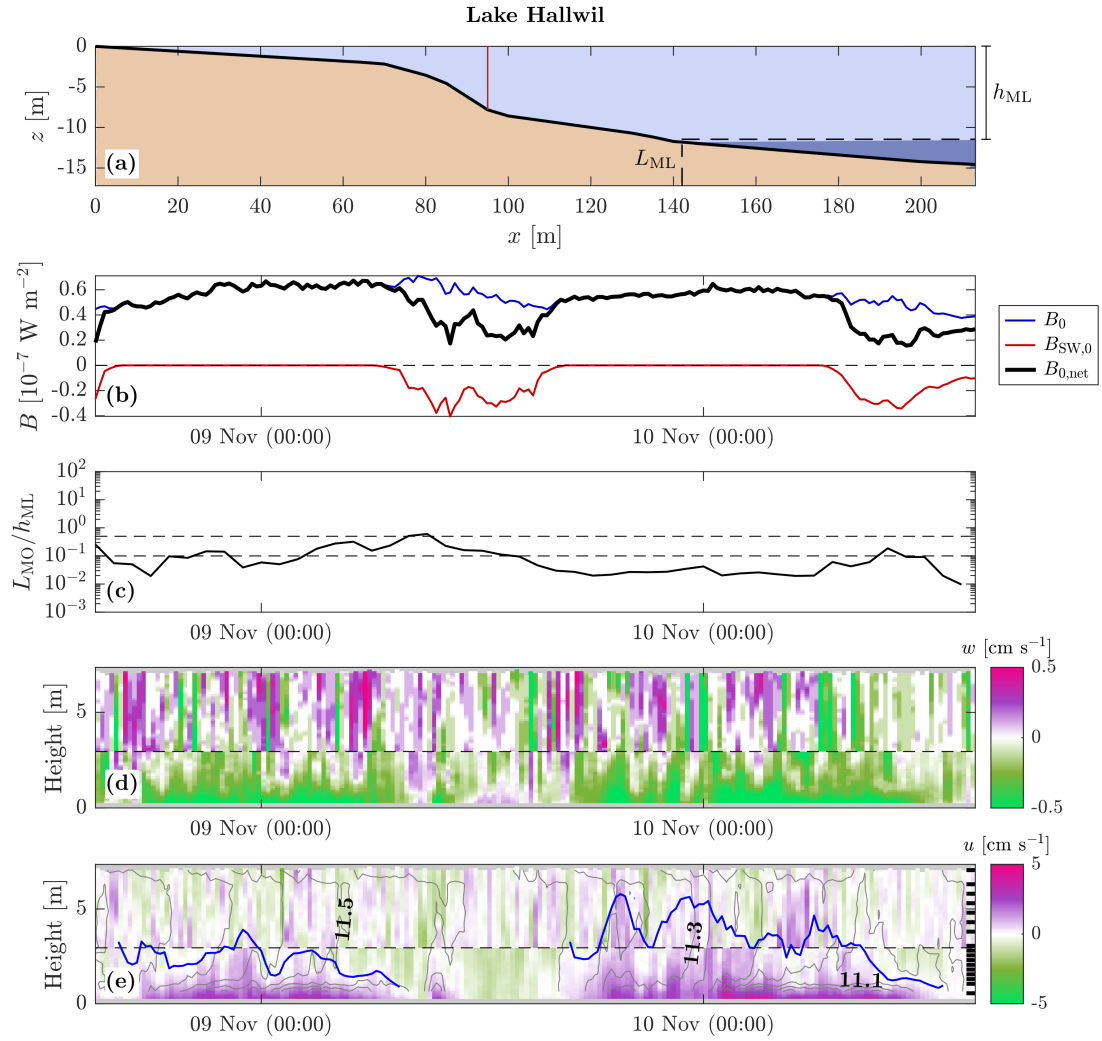


Figure S5.5 – Examples of thermal siphon events in Lake Hallwil on 8-10 November. See the caption of Fig. S5.1 for details.

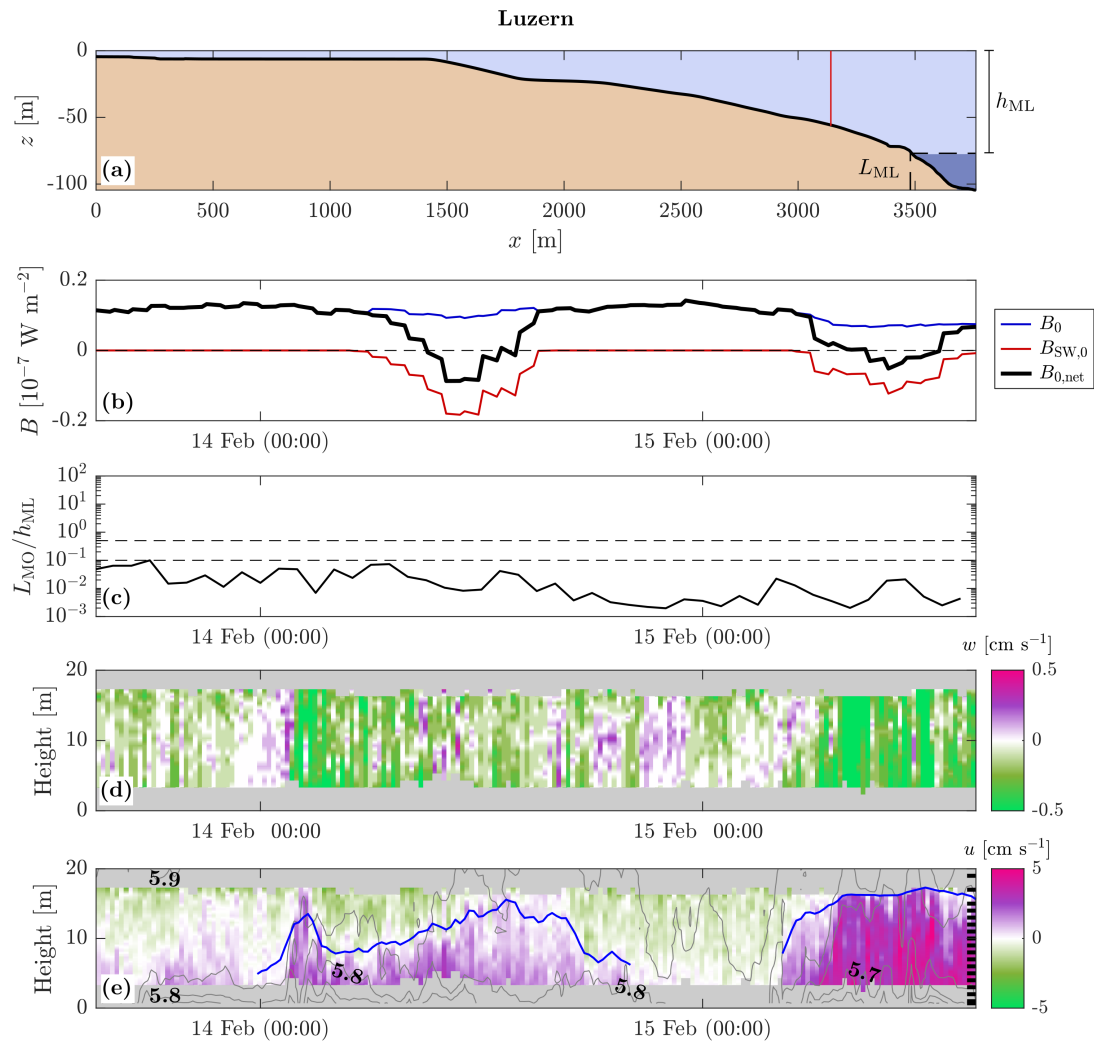


Figure S5.6 – Examples of thermal siphon events in Luzern Bay on 13-15 February. See the caption of Fig. S5.1 for details.

Chapter 6

Conclusions and outlook

6.1 Summary of the thesis

This thesis aimed at quantifying the occurrence and dynamics of TSs to improve the prediction of cooling-driven lateral transport in lakes. We studied the seasonality of TSs (Chapter 2), their interaction with penetrative convection (Chapter 3), their implications for the lateral transport of dissolved gases (Chapter 4) and their variability between different lakes (Chapter 5). It is now time to go back to the initial research questions asked in Fig. 1.3 and to provide answers based on the knowledge acquired through the four chapters. This figure becomes Fig. 6.1, which now includes the main quantities computed in the thesis and the main findings of each chapter. The two other publications of the HYPOTHESIS project, based on numerical simulations, are also shown in Fig. 6.1.

In Ulloa et al. (2022), we focused on the formation of TSs, from the onset of surface cooling to the development of a quasi steady-state convective circulation. The numerical simulations showed that the TS formation is not immediate. We identified three regimes: an initial convective regime characterized by convective cells and no horizontal circulation; a transition regime during which the TS forms in the sloping zone and expands horizontally; and a quasi steady-state regime starting when TS occupies the entire mixed region of length L_{ML} . We determined the transition timescale τ_t corresponding to the duration of regime I. This timescale is a central parameter to estimate the occurrence of TSs.

In Ramón et al. (2022), we investigated the combined effects of convection and cross-shore wind stress on the lateral transport. We observed that wind could either enhance or suppress TSs, if it was directed towards the shore or towards the lake center, respectively. We found that an additive model $q_c + q_w$, with q_c the convectively driven discharge and q_w the wind-driven discharge, was a

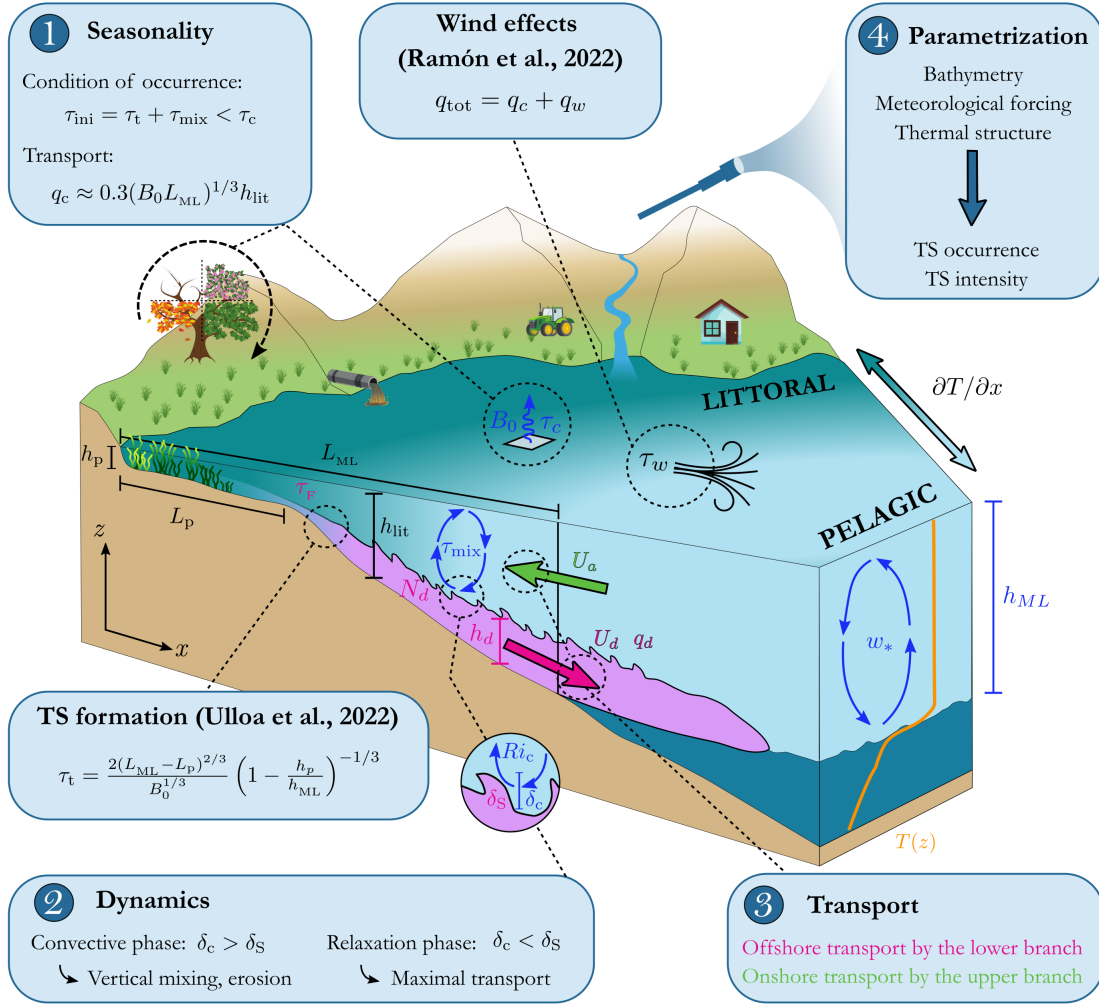


Figure 6.1 – Schematic of the cooling-driven thermal siphon, including the main quantities and findings of each chapter. The four numbered boxes include the main findings of each chapter. Two additional boxes correspond to the other publications of the HYPOTHESIS project. The quantities associated with the downslope gravity current and penetrative convection are shown in pink and blue, respectively.

suitable estimate for the total cross-shore discharge q_{tot} , in the interaction regime $0.1 < \chi_{MO} < 0.5$, with χ_{MO} the non-dimensional Monin-Obukhov length. This scaling provides an estimate of the cross-shore discharge during moderate wind conditions.

In Chapter 2, we monitored TSs in Rotsee over one year to determine their seasonality. We found that TSs were frequent from August to December and we explained this optimal occurrence period by comparing the TS initiation timescale $\tau_{ini} = \tau_t + \tau_{mix}$ with the duration of the cooling phase τ_c , where τ_{mix} is the mixing timescale. TSs occurred when the cooling phase was longer than the initiation period: $\tau_{ini} < \tau_c$. We also tested available transport scaling formulae and showed that they were reproducing the weakening of TS from summer to winter, despite the temporal

variability between TS events. This suggested that scaling relationships are suitable to predict the TS seasonality. A striking observation was the consistent increase of TS discharge during the heating phase, which seemed linked to the weakening of penetrative convection and motivated us to investigate the interaction between TS and convective plumes.

This interaction was addressed in Chapter 3. We identified two dynamical phases from typical examples of diurnal cycles measured in Rotsee: a nighttime convective phase when convective plumes penetrated into the gravity current (penetration depth δ_c larger than shear interface thickness δ_s) and a daytime relaxation phase with weaker convection ($\delta_c < \delta_s$). The dynamics of the gravity current changed from large vertical fluctuations and weak stratification during the convective phase to a more steady and stronger flow during the relaxation phase. We attributed this change of dynamics to the effects of penetrative convection, expressed by the convective Richardson number Ri_c . We suggested that convective plumes eroded the stratified current and delayed the maximal transport to daylight conditions.

In Chapter 4, we examined the role of TS for the lateral transport of dissolved gases. Based on the gas tracer experiment, we demonstrated that the downslope flow was capable of bringing gases from the littoral to the stratified region. From reversed lateral gradients of oxygen and methane, we observed an offshore transport of oxygen by the lower branch and an onshore surface transport of methane by the upper branch of the circulation. These results reveal that TSs modify the distribution of gases and, more generally, create concentration anomalies in the pelagic zone.

We finally generalized our findings to other lakes in Chapter 5, with the objective of better predicting the TS occurrence and intensity. We identified TS events in six lakes and tested the same transport scaling formulae than in Rotsee. We found that these scaling relationships reproduced the spatial variability of TSs between lakes, although additional TS observations are required to improve the transport estimates. We provided a procedure to predict the TS-induced transport from bathymetry, meteorological forcing and vertical thermal structure.

6.2 Perspectives for future studies

We present here several open research questions that could motivate further investigations on TSs.

6.2.1 Duration of the flushing period

The formation of TSs has been well described by laboratory and numerical studies (Bednarz et al., 2008; Horsch & Stefan, 1988; Ulloa et al., 2022) and has led to the definition of the transition timescale τ_t (Finnigan & Ivey, 1999; Ulloa et al., 2022; Wells & Sherman, 2001). We showed in Chapter 2 and Chapter 5 that τ_t is suitable to estimate the starting time of a TS event (or flushing period). Conversely, the end of the event is not well established which prevents to estimate the total volume of water transported by a single event in our predictive procedure (Chapter 5). In Fig. 5.5, we estimated V_{flush} at the end of the cooling phase but our observations showed that TSs persist several hours during the heating phase. This inertia has been investigated in laboratory and numerical experiments by reproducing periodic cycles of surface cooling and surface heating (Bednarz et al., 2009a; Bednarz et al., 2009b; Farrow, 2004; Mao et al., 2019). In temperate lakes, the heating phase is controlled by radiative heating rather than surface heating ($B_0 > 0$ during the heating phase), which differs from the previous investigations. In Rotsee and in the lakes of Chapter 5, we observed longer TSs on cloudy days and shorter TSs on sunny days, indicating that the duration of the flushing period was directly related to the intensity of solar radiation. We therefore suggest to examine the interaction between TSs and radiative heating in the future. Besides the change of the TS driving force $\partial\rho/\partial x$ (i.e., transition from differential cooling to differential heating), future studies should also focus on the effects of re-stratification on the TS propagation and the effects of decaying penetrative convection on the current dynamics (relaxation phase from Chapter 3).

6.2.2 Entrainment into the downslope gravity current

In the four chapters of the thesis, we quantified the TS-induced transport at a specific location in the sloping region. We know that the discharge q increases with propagation distance x , as reported by Fer et al. (2002b) and observed from the differences in q between the lakes of Chapter 5. This implies a net entrainment of ambient water into the gravity current, characterized by an entrainment coefficient $E = 1/U(\partial q/\partial x)$ (Ellison & Turner, 1959). Quantifying this entrainment is crucial to predict the transport at different locations (Dallimore et al., 2001), determine the

intrusion depth of the gravity current for the case of a linear stratification (Wells & Nadarajah, 2009) and estimate the dilution of transported tracers (Christodoulou, 1986). Although there exist parametrizations that estimate E from the bulk Richardson number Ri_b for gravity currents propagating into a quiescent environment (Cenedese & Adduce, 2010; Ellison & Turner, 1959), it is unclear whether these parametrizations are valid for thermal siphons as they occur in presence of penetrative convection and an opposite ambient flow. Fer et al. (2002a) suggested that convective plumes may increase E . However, from velocity measurements at two locations in Rotsee and from the numerical simulations of Ulloa et al. (2022), we calculated lower E than expected from Ri_b . These preliminary results show that estimating the entrainment in TSs is not straightforward and further work is required to quantify E in the field or via numerical simulations. A bulk net entrainment can be derived from $\partial q / \partial x$, but local entrainment-detrainment velocities between the two layers are also relevant, as they control the dilution of transported tracers (Christodoulou, 1986). The local vertical mixing could be quantified from measurements of vertical turbulent fluxes near the upper interface of the current (Dallimore et al., 2001).

6.2.3 Intrusion of TSs

The predictive procedure of Chapter 5 focuses on TSs in the mixed region, where the lake depth is $h_{\max} < h_{ML}$ and the gravity current flows downslope. It does not predict the occurrence and intensity of the TS intrusion in the stratified region. A question that remains to be answered is: “how far does the current go?”. This is relevant to assess the effects of TSs on biogeochemical measurements performed at the lake deepest point, far away from the shore (Vander Zanden & Vadeboncoeur, 2020). In Rotsee, we detected the thermal signature of the TS intrusion at MB, 800 m away from the shore (Fig. S4.2), and 3D numerical tracer experiments (not shown) have demonstrated that TSs propagate along the entire basin. Yet, high-resolution velocity measurements at the lake deepest point are lacking to quantify the intrusion. Future field or numerical work could reproduce our transport analysis for the intrusion region (timing, discharge q , relationship with the forcing conditions) with the aim of including the stratified region in the predictive procedure. Quantifying the dilution of tracers along the intrusion path would also be important to assess the contribution of TS to the concentration anomalies observed offshore (Brothers et al., 2017; DelSontro et al., 2018). In addition, the effects of the intrusion on the vertical fluxes (vertical diffusivity) and mixed layer deepening could be investigated via turbulence measurements.

6.2.4 Effects of TSs on turbulence

Turbulence in the mixed layer is parametrized as a function of the surface buoyancy flux B_0 and friction velocity u_* . Departures from this scaling relationship have suggested that additional processes such as TS intrusions affect the near-surface turbulence (Tedford et al., 2014). Fer et al. (2002c) attributed the higher turbulence near the sloping sides of Lake Geneva to downslope TSs. Yet, the effects of TSs on the cross-shore variability of turbulence and the turbulent kinetic energy budget are unknown. TS-induced turbulence could be quantified in the field with a combination of continuous microstructure profiles and high-resolution velocity measurements (Fernández Castro et al., 2021).

6.2.5 Contribution of TSs to the methane paradox

The origin of over-saturated methane concentrations in the oxic layer of lakes is debated, although it is acknowledged that both in-situ methane production and lateral transport can be responsible for oxic methane peaks (DelSontro et al., 2018). In Chapter 4, we showed that the lower branch of the convective circulation transports gases from the littoral to the pelagic region and generates concentration peaks at the base of the mixed layer that are comparable in magnitude to the observed methane peaks. Yet, we did not observe an offshore transport of methane since the lateral methane gradient was reversed ($\partial\text{CH}_4/\partial x > 0$). To quantify the contribution of TSs to oxic methane peaks, our measurements must be repeated in a lake where $\partial\text{CH}_4/\partial x < 0$ and oxic methane peaks are observed. Longer time series (\sim weeks) of velocity and gases concentrations would also help to differentiate between the effects of TS and biological processes.

6.2.6 Global prediction of TSs

The predictive procedure proposed in Chapter 5 could be applied to a large database of lakes to assess the role of TSs at a global scale. The vertical thermal structure used as an input can be obtained from one-dimensional models (Gaudard et al., 2019; Hipsey et al., 2019). Lakes should be selected to cover a wide range of bathymetries and forcing conditions. Based on the results, it may be possible to identify relationships between the predicted TS occurrence and intensity and the general lake characteristics (e.g., shape, elevation, mean depth, wind exposure). Such relationships would provide a simple approach for estimating the role of TSs in lakes where no input data is available.

These estimates will remain approximate and will not replace the in situ quantification of lateral transport. Combining physical and biogeochemical measurements should become more systematic to improve our understanding of the lake ecosystem functioning. As this thesis showed with a specific example, *everything is connected* in lakes.

Bibliography

- Adams, E., & Wells, S. A. (1984). Field measurements on side arms of Lake Anna, Va. *Journal of Hydraulic Engineering*, 110(6), 773–793. [https://doi.org/10.1061/\(ASCE\)0733-9429\(1984\)110:6\(773\)](https://doi.org/10.1061/(ASCE)0733-9429(1984)110:6(773))
- Alavian, V. (1986). Behavior of density currents on an incline. *Journal of Hydraulic Engineering*, 112(1), 27–42. [https://doi.org/10.1061/\(ASCE\)0733-9429\(1986\)112:1\(27\)](https://doi.org/10.1061/(ASCE)0733-9429(1986)112:1(27))
- Alavian, V., Jirka, G. H., Denton, R. A., Johnson, M. C., & Stefan, H. G. (1992). Density currents entering lakes and reservoirs. *Journal of Hydraulic Engineering*, 118(11), 1464–1489. [https://doi.org/10.1061/\(ASCE\)0733-9429\(1992\)118:11\(1464\)](https://doi.org/10.1061/(ASCE)0733-9429(1992)118:11(1464))
- Ambrosetti, W., Barbanti, L., & Carrara, E. A. (2010). Mechanisms of hypolimnion erosion in a deep lake (Lago Maggiore, N. Italy). *Journal of Limnology*, 69(1), 3–14. <https://doi.org/10.4081/jlimnol.2010.3>
- Ansong, J. K., & Sutherland, B. R. (2010). Internal gravity waves generated by convective plumes. *Journal of Fluid Mechanics*, 648, 405–434. <https://doi.org/10.1017/S0022112009993193>
- Antenucci, J. P., Tan, K. M., Eikaas, H. S., & Imberger, J. (2013). The importance of transport processes and spatial gradients on in situ estimates of lake metabolism. *Hydrobiologia*, 700(1), 9–21. <https://doi.org/10.1007/s10750-012-1212-z>
- Baines, W. D. (1975). Entrainment by a plume or jet at a density interface. *Journal of Fluid Mechanics*, 68(02), 309–320. <https://doi.org/10.1017/S0022112075000821>
- Bednarz, T. P., Lei, C., & Patterson, J. C. (2008). An experimental study of unsteady natural convection in a reservoir model cooled from the water surface. *Experimental Thermal and Fluid Science*, 32(3), 844–856. <https://doi.org/10.1016/j.expthermflusci.2007.10.007>
- Bednarz, T. P., Lei, C., & Patterson, J. C. (2009a). Unsteady natural convection induced by diurnal temperature changes in a reservoir with slowly varying bottom topography. *International Journal of Thermal Sciences*, 48(10), 1932–1942. <https://doi.org/10.1016/j.ijthermalsci.2009.02.011>

- Bednarz, T. P., Lei, C., & Patterson, J. C. (2009b). An experimental study of unsteady natural convection in a reservoir model subject to periodic thermal forcing using combined PIV and PIT techniques. *Experiments in Fluids*, 47(1), 107–117. <https://doi.org/10.1007/s00348-009-0641-6>
- Benjamin, T. B. (1968). Gravity currents and related phenomena. *Journal of Fluid Mechanics*, 31(2), 209–248. <https://doi.org/10.1017/S0022112068000133>
- Biemond, B., Amadori, M., Toffolon, M., Piccolroaz, S., Van Haren, H., & Dijkstra, H. A. (2021). Deep-mixing and deep-cooling events in Lake Garda: Simulation and mechanisms. *Journal of Limnology*, 80(2). <https://doi.org/10.4081/jlimnol.2021.2010>
- Bogard, M. J., del Giorgio, P. A., Boutet, L., Chaves, M. C. G., Prairie, Y. T., Merante, A., & Derry, A. M. (2014). Oxic water column methanogenesis as a major component of aquatic CH₄ fluxes. *Nature Communications*, 5(1), 5350. <https://doi.org/10.1038/ncomms6350>
- Bonvin, F., Rutler, R., Chèvre, N., Halder, J., & Kohn, T. (2011). Spatial and temporal presence of a wastewater-derived micropollutant plume in Lake Geneva. *Environmental Science & Technology*, 45(11), 4702–4709. <https://doi.org/10.1021/es2003588>
- Bouffard, D., & Wüest, A. (2019). Convection in lakes. *Annual Review of Fluid Mechanics*, 51(1), 189–215. <https://doi.org/10.1146/annurev-fluid-010518-040506>
- Brennwald, M. S., Schmidt, M., Oser, J., & Kipfer, R. (2016). A portable and autonomous mass spectrometric system for on-site environmental gas analysis. *Environmental Science & Technology*, 50(24), 13455–13463. <https://doi.org/10.1021/acs.est.6b03669>
- Brink, K. (2016). Cross-shelf exchange. *Annual Review of Marine Science*, 8(1), 59–78. <https://doi.org/10.1146/annurev-marine-010814-015717>
- Britter, R. E., & Linden, P. F. (1980). The motion of the front of a gravity current travelling down an incline. *Journal of Fluid Mechanics*, 99(3), 531–543. <https://doi.org/10.1017/S0022112080000754>
- Brothers, S., Kazanjian, G., Köhler, J., Scharfenberger, U., & Hilt, S. (2017). Convective mixing and high littoral production established systematic errors in the diel oxygen curves of a shallow, eutrophic lake. *Limnology and Oceanography: Methods*, 15(5), 429–435. <https://doi.org/10.1002/lom3.10169>
- Brothers, S., & Vadeboncoeur, Y. (2021). Shoring up the foundations of production to respiration ratios in lakes. *Limnology and Oceanography*, 66(7), 2762–2778. <https://doi.org/10.1002/lno.11787>
- Bühler, J., Wright, S. J., & Kim, Y. (1991). Gravity currents advancing into a coflowing fluid. *Journal of Hydraulic Research*, 29(2), 343–357. <https://doi.org/10.1080/00221689109499007>
- Canals, M., Puig, P., de Madron, X. D., Heussner, S., Palanques, A., & Fabres, J. (2006). Flushing submarine canyons. *Nature*, 444(7117), 354–357. <https://doi.org/10.1038/nature05271>

Bibliography

- Cannaby, H., White, M., & Bowyer, P. (2007). Dynamical response to differential rates of temperature change over sloping topography: Lough Corrib, Ireland. *Journal of Geophysical Research*, 112(C9), C09009. <https://doi.org/10.1029/2006JC003890>
- Cardinale, B. J., Burton, T. M., & Brady, V. J. (1997). The community dynamics of epiphytic midge larvae across the pelagic–littoral interface: do animals respond to changes in the abiotic environment? *Canadian Journal of Fisheries and Aquatic Sciences*, 54(10), 2314–2322. <https://doi.org/10.1139/f97-138>
- Carpenter, S. R., Caraco, N. F., Correll, D. L., Howarth, R. W., Sharpley, A. N., & Smith, V. H. (1998). Nonpoint pollution of surface waters with phosphorus and nitrogen. *Ecological Applications*, 8(3), 559–568. [https://doi.org/10.1890/1051-0761\(1998\)008\[0559:NPOSWW\]2.0.CO;2](https://doi.org/10.1890/1051-0761(1998)008[0559:NPOSWW]2.0.CO;2)
- Cenedese, C., & Adduce, C. (2010). A new parameterization for entrainment in overflows. *Journal of Physical Oceanography*, 40(8), 1835–1850. <https://doi.org/10.1175/2010JPO4374.1>
- Chen, C. (1995). Numerical simulations of gravity currents in uniform shear flows. *Monthly Weather Review*, 123(11), 3240–3253. [https://doi.org/10.1175/1520-0493\(1995\)123<3240:NSOGCI>2.0.CO;2](https://doi.org/10.1175/1520-0493(1995)123<3240:NSOGCI>2.0.CO;2)
- Chen, C.-T. A., & Millero, F. J. (1986). Precise thermodynamic properties for natural waters covering only the limnological range. *Limnology and Oceanography*, 31(3), 657–662. <https://doi.org/10.4319/lo.1986.31.3.0657>
- Ching, C., Fernando, H., & Noh, Y. (1993). Interaction of a negatively buoyant line plume with a density interface. *Dynamics of Atmospheres and Oceans*, 19(1-4), 367–388. [https://doi.org/10.1016/0377-0265\(93\)90042-6](https://doi.org/10.1016/0377-0265(93)90042-6)
- Christodoulou, G. C. (1986). Interfacial mixing in stratified flows. *Journal of Hydraulic Research*, 24(2), 77–92. <https://doi.org/10.1080/00221688609499323>
- Chubarenko, I. P. (2010). Horizontal convective water exchange above a sloping bottom: The mechanism of its formation and an analysis of its development. *Oceanology*, 50(2), 166–174. <https://doi.org/10.1134/S0001437010020025>
- Chubarenko, I. P., Esiukova, E., Stepanova, N., Chubarenko, B., & Baudler, H. (2013). Down-slope cascading modulated by day/night variations of solar heating. *Journal of Limnology*, 72(2), e19. <https://doi.org/10.4081/jlimnol.2013.e19>
- Coloso, J. J., Cole, J. J., Hanson, P. C., & Pace, M. L. (2008). Depth-integrated, continuous estimates of metabolism in a clear-water lake. *Canadian Journal of Fisheries and Aquatic Sciences*, 65(4), 712–722. <https://doi.org/10.1139/f08-006>
- Cortés, A., Fleenor, W. E., Wells, M. G., de Vicente, I., & Rueda, F. J. (2014). Pathways of river water to the surface layers of stratified reservoirs. *Limnology and Oceanography*, 59(1), 233–250. <https://doi.org/10.4319/lo.2014.59.1.0233>

- Cortés, A., & MacIntyre, S. (2020). Mixing processes in small arctic lakes during spring. *Limnology and Oceanography*, 65(2), 260–288. <https://doi.org/10.1002/lno.11296>
- Cotel, A. J., & Kudo, Y. (2008). Impingement of buoyancy-driven flows at a stratified interface. *Experiments in Fluids*, 45(1), 131–139. <https://doi.org/10.1007/s00348-008-0469-5>
- Cushman-Roisin, B. (1982). Penetrative convection in the upper ocean due to surface cooling. *Geophysical & Astrophysical Fluid Dynamics*, 19(1-2), 61–91. <https://doi.org/10.1080/03091928208208947>
- Cyr, H. (2017). Winds and the distribution of nearshore phytoplankton in a stratified lake. *Water Research*, 122, 114–127. <https://doi.org/10.1016/j.watres.2017.05.066>
- Czikowsky, M. J., MacIntyre, S., Tedford, E. W., Vidal, J., & Miller, S. D. (2018). Effects of wind and buoyancy on carbon dioxide distribution and air-water flux of a stratified temperate lake. *Journal of Geophysical Research: Biogeosciences*, 123(8), 2305–2322. <https://doi.org/10.1029/2017JG004209>
- Dailey, P. S., & Fovell, R. G. (1999). Numerical simulation of the interaction between the sea-breeze front and horizontal convective rolls. Part I: offshore ambient flow. *Monthly Weather Review*, 127(5), 858–878. [https://doi.org/10.1175/1520-0493\(1999\)127<0858:NSOTIB>2.0.CO;2](https://doi.org/10.1175/1520-0493(1999)127<0858:NSOTIB>2.0.CO;2)
- Dallimore, C. J., Imberger, J., & Ishikawa, T. (2001). Entrainment and turbulence in saline underflow in Lake Ogawara. *Journal of Hydraulic Engineering*, 127(11), 937–948. [https://doi.org/10.1061/\(ASCE\)0733-9429\(2001\)127:11\(937\)](https://doi.org/10.1061/(ASCE)0733-9429(2001)127:11(937))
- Deardorff, J. W., Willis, G. E., & Lilly, D. K. (1969). Laboratory investigation of non-steady penetrative convection. *Journal of Fluid Mechanics*, 35(1), 7–31. <https://doi.org/10.1017/S0022112069000942>
- Deardorff, J. W., Willis, G. E., & Stockton, B. H. (1980). Laboratory studies of the entrainment zone of a convectively mixed layer. *Journal of Fluid Mechanics*, 100(01), 41–64. <https://doi.org/10.1017/S0022112080001000>
- Deardorff, J. W. (1970). Convective velocity and temperature scales for the unstable planetary boundary layer and for Rayleigh convection. *Journal of the Atmospheric Sciences*, 27(8), 1211–1213. [https://doi.org/10.1175/1520-0469\(1970\)027<1211:CVATSF>2.0.CO;2](https://doi.org/10.1175/1520-0469(1970)027<1211:CVATSF>2.0.CO;2)
- DelSontro, T., del Giorgio, P. A., & Prairie, Y. T. (2018). No longer a paradox: the interaction between physical transport and biological processes explains the spatial distribution of surface water methane within and across lakes. *Ecosystems*, 21(6), 1073–1087. <https://doi.org/10.1007/s10021-017-0205-1>
- Doda, T., Ramón, C. L., Ulloa, H. N., Wüest, A., & Bouffard, D. (2021). Data for: Seasonality of density currents induced by differential cooling. <https://doi.org/10.25678/00057K>

Bibliography

- Doda, T., Ramón, C. L., Ulloa, H. N., Wüest, A., & Bouffard, D. (2022). Seasonality of density currents induced by differential cooling. *Hydrology and Earth System Sciences*, 26(2), 331–353. <https://doi.org/10.5194/hess-26-331-2022>
- Donis, D., Flury, S., Stöckli, A., Spangenberg, J. E., Vachon, D., & McGinnis, D. F. (2017). Full-scale evaluation of methane production under oxic conditions in a mesotrophic lake. *Nature Communications*, 8(1), 1661. <https://doi.org/10.1038/s41467-017-01648-4>
- Donohue, I., & Garcia Molinos, J. (2009). Impacts of increased sediment loads on the ecology of lakes. *Biological Reviews*, 84(4), 517–531. <https://doi.org/10.1111/j.1469-185X.2009.00081.x>
- Dressler, R. F. (1949). Mathematical solution of the problem of roll-waves in inclined open channels. *Communications on Pure and Applied Mathematics*, 2(2-3), 149–194. <https://doi.org/10.1002/cpa.3160020203>
- Eccles, D. H. (1974). An outline of the physical limnology of Lake Malawi (Lake Nyasa). *Limnology and Oceanography*, 19(5), 730–742. <https://doi.org/10.4319/lo.1974.19.5.0730>
- Effler, S. W., Prestigiacomo, A. R., Matthews, D. A., Gelda, R. K., Peng, F., Cowen, E. A., & Schweitzer, S. A. (2010). Tripton, trophic state metrics, and near-shore versus pelagic zone responses to external loads in Cayuga Lake, New York, U.S.A. *Fundamental and Applied Limnology*, 178(1), 1–15. <https://doi.org/10.1127/1863-9135/2010/0178-0001>
- Ellison, T. H., & Turner, J. S. (1959). Turbulent entrainment in stratified flows. *Journal of Fluid Mechanics*, 6(03), 423–448. <https://doi.org/10.1017/S00222112059000738>
- Encinas Fernández, J., Peeters, F., & Hofmann, H. (2014). Importance of the autumn overturn and anoxic conditions in the hypolimnion for the annual methane emissions from a temperate lake. *Environmental Science & Technology*, 48(13), 7297–7304. <https://doi.org/10.1021/es4056164>
- Encinas Fernández, J., Peeters, F., & Hofmann, H. (2016). On the methane paradox: Transport from shallow water zones rather than in situ methanogenesis is the major source of CH₄ in the open surface water of lakes. *Journal of Geophysical Research: Biogeosciences*, 121(10), 2717–2726. <https://doi.org/10.1002/2016JG003586>
- Farrow, D. E., & Patterson, J. C. (1993). On the response of a reservoir sidearm to diurnal heating and cooling. *Journal of Fluid Mechanics*, 246, 143–161. <https://doi.org/10.1017/S0022112093000072>
- Farrow, D. E. (2004). Periodically forced natural convection over slowly varying topography. *Journal of Fluid Mechanics*, 508, 1–21. <https://doi.org/10.1017/S002211200400847X>
- Farrow, D. E. (2013). Periodically driven circulation near the shore of a lake. *Environmental Fluid Mechanics*, 13(3), 243–255. <https://doi.org/10.1007/s10652-012-9261-4>
- Farrow, D. E. (2016). A numerical model of periodically forced circulation near the shore of a lake. *Environmental Fluid Mechanics*, 16(5), 983–995. <https://doi.org/10.1007/s10652-016-9461-4>

- Fer, I., Lemmin, U., & Thorpe, S. A. (2002a). Contribution of entrainment and vertical plumes to the winter cascading of cold shelf waters in a deep lake. *Limnology and Oceanography*, 47(2), 576–580. <https://doi.org/10.4319/lo.2002.47.2.0576>
- Fer, I., Lemmin, U., & Thorpe, S. A. (2002b). Winter cascading of cold water in Lake Geneva. *Journal of Geophysical Research*, 107(C6), 3060. <https://doi.org/10.1029/2001JC000828>
- Fer, I., Lemmin, U., & Thorpe, S. A. (2001). Cascading of water down the sloping sides of a deep lake in winter. *Geophysical Research Letters*, 28(10), 2093–2096. <https://doi.org/10.1029/2000GL012599>
- Fer, I., Lemmin, U., & Thorpe, S. A. (2002c). Observations of mixing near the sides of a deep lake in winter. *Limnology and Oceanography*, 47(2), 535–544. <https://doi.org/10.4319/lo.2002.47.2.0535>
- Fernández Castro, B., Bouffard, D., Troy, C., Ulloa, H. N., Piccolroaz, S., Sepúlveda Steiner, O., Chmiel, H. E., Serra Moncadas, L., Lavanchy, S., & Wüest, A. (2021). Seasonality modulates wind-driven mixing pathways in a large lake. *Communications Earth & Environment*, 2(1), 215. <https://doi.org/10.1038/s43247-021-00288-3>
- Fink, G., Schmid, M., Wahl, B., Wolf, T., & Wüest, A. (2014). Heat flux modifications related to climate-induced warming of large European lakes. *Water Resources Research*, 50(3), 2072–2085. <https://doi.org/10.1002/2013WR014448>
- Finnigan, T. D., & Ivey, G. N. (1999). Submaximal exchange between a convectively forced basin and a large reservoir. *Journal of Fluid Mechanics*, 378, 357–378. <https://doi.org/10.1017/S0022112098003437>
- Folkard, A. M. (2000). Laboratory observations of interactions of forced plumes with stratified shear layers. *Fluid Dynamics Research*, 26(6), 355–375. [https://doi.org/10.1016/S0169-5983\(99\)00038-6](https://doi.org/10.1016/S0169-5983(99)00038-6)
- Forel, F. A. (1892). *Le Léman - Monographie Limnologique. Tome I*. Editions Rouge. <https://doi.org/10.5962/bhl.title.124608>
- Forel, F. A. (1895). *Le Léman - Monographie Limnologique. Tome II*. Editions Rouge. <https://doi.org/10.5962/bhl.title.124608>
- Forrest, A. L., Laval, B. E., Pieters, R., & Lim, D. S. S. (2008). Convectively driven transport in temperate lakes. *Limnology and Oceanography*, 53, 2321–2332. https://doi.org/10.4319/lo.2008.53.5_part_2.2321
- Fritts, D. C., & Alexander, M. J. (2003). Gravity wave dynamics and effects in the middle atmosphere. *Reviews of Geophysics*, 41(1), 1003. <https://doi.org/10.1029/2001RG000106>
- Gaudard, A., Răman Vinnă, L., Bärenbold, F., Schmid, M., & Bouffard, D. (2019). Toward an open access to high-frequency lake modeling and statistics data for scientists and practitioners –

Bibliography

- the case of Swiss lakes using Simstrat v2.1. *Geoscientific Model Development*, 12(9), 3955–3974. <https://doi.org/10.5194/gmd-12-3955-2019>
- Gray, E., Mackay, E. B., Elliott, J. A., Folkard, A. M., & Jones, I. D. (2020). Wide-spread inconsistency in estimation of lake mixed depth impacts interpretation of limnological processes. *Water Research*, 168, 115136. <https://doi.org/10.1016/j.watres.2019.115136>
- Grossart, H.-P., Frindte, K., Dziallas, C., Eckert, W., & Tang, K. W. (2011). Microbial methane production in oxygenated water column of an oligotrophic lake. *Proceedings of the National Academy of Sciences*, 108(49), 19657–19661. <https://doi.org/10.1073/pnas.1110716108>
- Günthel, M., Donis, D., Kirillin, G., Ionescu, D., Bizic, M., McGinnis, D. F., Grossart, H.-P., & Tang, K. W. (2019). Contribution of oxic methane production to surface methane emission in lakes and its global importance. *Nature Communications*, 10(1), 5497. <https://doi.org/10.1038/s41467-019-13320-0>
- Hall, F. F., Edinger, J. G., & Neff, W. D. (1975). Convective plumes in the planetary boundary layer, investigated with an acoustic echo sounder. *Journal of Applied Meteorology*, 14(4), 513–523. [https://doi.org/10.1175/1520-0450\(1975\)014<0513:CPITPB>2.0.CO;2](https://doi.org/10.1175/1520-0450(1975)014<0513:CPITPB>2.0.CO;2)
- Hanson, P. C., Carpenter, S. R., Kimura, N., Wu, C., Cornelius, S. P., & Kratz, T. K. (2008). Evaluation of metabolism models for free-water dissolved oxygen methods in lakes. *Limnology and Oceanography: Methods*, 6(9), 454–465. <https://doi.org/10.4319/lom.2008.6.454>
- Harashima, A., & Watanabe, M. (1986). Laboratory experiments on the steady gravitational circulation excited by cooling of the water surface. *Journal of Geophysical Research*, 91(C11), 13056–13064. <https://doi.org/10.1029/JC091iC11p13056>
- Harleman, D. R. F., & Ippen, A. T. (1960). The turbulent diffusion and convection of saline water in an idealised estuary. *Publ. No. 51* (International Association for Science of Hydrology, Commission of Surface Waters., pp. 362–378).
- Helfrich, K. R. (1995). Time-dependent two-layer hydraulic exchange flows. *Journal of Physical Oceanography*, 25(3), 359–373. [https://doi.org/10.1175/1520-0485\(1995\)025<0359:TDTLHE>2.0.CO;2](https://doi.org/10.1175/1520-0485(1995)025<0359:TDTLHE>2.0.CO;2)
- Hetzel, Y., Pattiaratchi, C., Lowe, R., & Hofmeister, R. (2015). Wind and tidal mixing controls on stratification and dense water outflows in a large hypersaline bay. *Journal of Geophysical Research: Oceans*, 120(9), 6034–6056. <https://doi.org/10.1002/2015JC010733>
- Hipsey, M. R., Bruce, L. C., Boon, C., Busch, B., Carey, C. C., Hamilton, D. P., Hanson, P. C., Read, J. S., de Sousa, E., Weber, M., & Winslow, L. A. (2019). A General Lake Model (GLM 3.0) for linking with high-frequency sensor data from the Global Lake Ecological Observatory Network (GLEON). *Geoscientific Model Development*, 12(1), 473–523. <https://doi.org/10.5194/gmd-12-473-2019>

- Hofmann, H. (2013). Spatiotemporal distribution patterns of dissolved methane in lakes: how accurate are the current estimations of the diffusive flux path? *Geophysical Research Letters*, 40(11), 2779–2784. <https://doi.org/10.1002/grl.50453>
- Hofmann, H., Federwisch, L., & Peeters, F. (2010). Wave-induced release of methane: littoral zones as source of methane in lakes. *Limnology and Oceanography*, 55(5), 1990–2000. <https://doi.org/10.4319/lo.2010.55.5.1990>
- Hofmann, H., Lorke, A., & Peeters, F. (2011). Wind and ship wave-induced resuspension in the littoral zone of a large lake. *Water Resources Research*, 47(9), W09505. <https://doi.org/10.1029/2010WR010012>
- Hogg, A. J., Hallworth, M. A., & Huppert, H. E. (2005). On gravity currents driven by constant fluxes of saline and particle-laden fluid in the presence of a uniform flow. *Journal of Fluid Mechanics*, 539, 349–385. <https://doi.org/10.1017/S002211200500546X>
- Hogg, A. M., Ivey, G. N., & Winters, K. B. (2001). Hydraulics and mixing in controlled exchange flows. *Journal of Geophysical Research: Oceans*, 106(C1), 959–972. <https://doi.org/10.1029/2000JC000266>
- Horsch, G. M., & Stefan, H. G. (1988). Convective circulation in littoral water due to surface cooling. *Limnology and Oceanography*, 33(5), 1068–1083. <https://doi.org/10.4319/lo.1988.33.5.1068>
- Horsch, G. M., Stefan, H. G., & Gavali, S. (1994). Numerical simulation of cooling-induced convective currents on a littoral slope. *International Journal for Numerical Methods in Fluids*, 19(2), 105–134. <https://doi.org/10.1002/fld.1650190203>
- Huppert, H. E. (2006). Gravity currents: a personal perspective. *Journal of Fluid Mechanics*, 554, 299–322. <https://doi.org/10.1017/S002211200600930X>
- Idrizaj, A., Laas, A., Anijalg, U., & Nõges, P. (2016). Horizontal differences in ecosystem metabolism of a large shallow lake. *Journal of Hydrology*, 535, 93–100. <https://doi.org/10.1016/j.jhydrol.2016.01.037>
- Imberger, J. (1985). The diurnal mixed layer. *Limnology and Oceanography*, 30(4), 737–770. <https://doi.org/10.4319/lo.1985.30.4.0737>
- Imberger, J., & Patterson, J. C. (1989). Physical Limnology (J. W. Hutchinson & T. Y. Wu, Eds.). *Advances in Applied Mechanics*, 27, 303–475. [https://doi.org/10.1016/S0065-2156\(08\)70199-6](https://doi.org/10.1016/S0065-2156(08)70199-6)
- Ivanov, V., Shapiro, G., Huthnance, J., Aleynik, D., & Golovin, P. (2004). Cascades of dense water around the world ocean. *Progress in Oceanography*, 60(1), 47–98. <https://doi.org/10.1016/j.pocan.2003.12.002>
- James, W. F., & Barko, J. W. (1991a). Estimation of phosphorus exchange between littoral and pelagic zones during nighttime convective circulation. *Limnology and Oceanography*, 36(1), 179–187. <https://doi.org/10.4319/lo.1991.36.1.0179>

Bibliography

- James, W. F., & Barko, J. W. (1991b). Littoral-pelagic phosphorus dynamics during nighttime convective circulation. *Limnology and Oceanography*, 36(5), 949–960. <https://doi.org/10.4319/lo.1991.36.5.0949>
- James, W. F., Barko, J. W., & Eakin, H. L. (1994). Convective water exchanges during differential cooling and heating: implications for dissolved constituent transport. *Hydrobiologia*, 294(2), 167–176. <https://doi.org/10.1007/BF00016857>
- Jenny, J.-P., Anneville, O., Arnaud, F., Baulaz, Y., Bouffard, D., Domaizon, I., Bocaniov, S. A., Chèvre, N., Dittrich, M., Dorioz, J.-M., Dunlop, E. S., Dur, G., Guillard, J., Guinaldo, T., Jacquet, S., Jamoneau, A., Jawed, Z., Jeppesen, E., Krantzberg, G., ... Weyhenmeyer, G. A. (2020). Scientists' Warning to Humanity: Rapid degradation of the world's large lakes. *Journal of Great Lakes Research*, 46(4), 686–702. <https://doi.org/10.1016/j.jglr.2020.05.006>
- Juutinen, S., Alm, J., Larmola, T., Huttunen, J. T., Morero, M., Martikainen, P. J., & Silvola, J. (2003). Major implication of the littoral zone for methane release from boreal lakes. *Global Biogeochemical Cycles*, 17(4), 1117. <https://doi.org/10.1029/2003GB002105>
- Kirillin, G. B., Forrest, A. L., Graves, K. E., Fischer, A., Engelhardt, C., & Laval, B. E. (2015). Axisymmetric circulation driven by marginal heating in ice-covered lakes. *Geophysical Research Letters*, 42(8), 2893–2900. <https://doi.org/10.1002/2014GL062180>
- La Rocca, M., Adduce, C., Sciortino, G., & Pinzon, A. B. (2008). Experimental and numerical simulation of three-dimensional gravity currents on smooth and rough bottom. *Physics of Fluids*, 20(10), 106603. <https://doi.org/10.1063/1.3002381>
- Lauster, G. H., Hanson, P. C., & Kratz, T. K. (2006). Gross primary production and respiration differences among littoral and pelagic habitats in northern Wisconsin lakes [Publisher: NRC Research Press Ottawa, Canada]. *Canadian Journal of Fisheries and Aquatic Sciences*, 63(5), 1130–1141. <https://doi.org/10.1139/f06-018>
- Lei, C., & Patterson, J. C. (2005). Unsteady natural convection in a triangular enclosure induced by surface cooling. *International Journal of Heat and Fluid Flow*, 26(2), 307–321. <https://doi.org/10.1016/j.ijheatfluidflow.2004.08.010>
- Lemmin, U. (2020). Insights into the dynamics of the deep hypolimnion of Lake Geneva as revealed by long-term temperature, oxygen, and current measurements. *Limnology and Oceanography*, 65(9), 2092–2107. <https://doi.org/10.1002/lno.11441>
- Linden, P. F., & Simpson, J. E. (1986). Gravity-driven flows in a turbulent fluid. *Journal of Fluid Mechanics*, 172, 481–497. <https://doi.org/10.1017/S0022112086001829>
- Lofquist, K. (1960). Flow and stress near an interface between stratified liquids. *Physics of Fluids*, 3(2), 158–175. <https://doi.org/10.1063/1.1706013>
- Loken, L. C., Crawford, J. T., Schramm, P. J., Stadler, P., Desai, A. R., & Stanley, E. H. (2019). Large spatial and temporal variability of carbon dioxide and methane in a eutrophic lake.

- Journal of Geophysical Research: Biogeosciences*, 124(7), 2248–2266. <https://doi.org/10.1029/2019JG005186>
- Lövstedt, C. B., & Bengtsson, L. (2008). Density-driven current between reed belts and open water in a shallow lake. *Water Resources Research*, 44(10), W10413. <https://doi.org/10.1029/2008WR006949>
- MacIntyre, S., & Melack, J. M. (1995). Vertical and horizontal transport in lakes: linking littoral, benthic, and pelagic habitats. *Journal of the North American Benthological Society*, 14(4), 599–615. <https://doi.org/10.2307/1467544>
- MacIntyre, S., Romero, J. R., & Kling, G. W. (2002). Spatial-temporal variability in surface layer deepening and lateral advection in an embayment of Lake Victoria, East Africa. *Limnology and Oceanography*, 47(3), 656–671. <https://doi.org/10.4319/lo.2002.47.3.0656>
- Mahjabin, T., Pattiaratchi, C., & Hetzel, Y. (2019). Wind effects on dense shelf water cascades in south-west Australia. *Continental Shelf Research*, 189, 103975. <https://doi.org/10.1016/j.csr.2019.103975>
- Mao, Y., Lei, C., & Patterson, J. C. (2010). Unsteady near-shore natural convection induced by surface cooling. *Journal of Fluid Mechanics*, 642, 213–233. <https://doi.org/10.1017/S0022112009991765>
- Mao, Y., Lei, C., & Patterson, J. C. (2019). Natural convection in a reservoir induced by sinusoidally varying temperature at the water surface. *International Journal of Heat and Mass Transfer*, 134, 610–627. <https://doi.org/10.1016/j.ijheatmasstransfer.2019.01.071>
- Mayr, M. J., Zimmermann, M., Dey, J., Brand, A., Wehrli, B., & Bürgmann, H. (2020). Growth and rapid succession of methanotrophs effectively limit methane release during lake overturn. *Communications Biology*, 3(1), 108. <https://doi.org/10.1038/s42003-020-0838-z>
- McJannet, D., Webster, I., & Cook, F. (2012). An area-dependent wind function for estimating open water evaporation using land-based meteorological data. *Environmental Modelling & Software*, 31, 76–83. <https://doi.org/10.1016/j.envsoft.2011.11.017>
- Meyers, T., & Dale, R. (1983). Predicting daily insolation with hourly cloud height and coverage. *Journal of Climate and Applied Meteorology*, 22(4), 537–545. [https://doi.org/10.1175/1520-0450\(1983\)022<0537:PDIWHC>2.0.CO;2](https://doi.org/10.1175/1520-0450(1983)022<0537:PDIWHC>2.0.CO;2)
- Middleton, G. V. (1966). Experiments on density and turbidity currents. II. Uniform flow of density currents. *Canadian Journal of Earth Sciences*, 3(5), 627–637. <https://doi.org/10.1139/e66-044>
- Miles, J. W. (1961). On the stability of heterogeneous shear flows. *Journal of Fluid Mechanics*, 10(04), 496–508. <https://doi.org/10.1017/S0022112061000305>
- Mohseni, O., Stefan, H. G., Wright, D., & Johnson, G. J. (2001). Dissolved oxygen depletion in a small deep lake with a large littoral zone. *Lake and Reservoir Management*, 17(4), 288–298. <https://doi.org/10.1080/07438140109354136>

Bibliography

- Molina, L., Pawlak, G., Wells, J. R., Monismith, S. G., & Merrifield, M. A. (2014). Diurnal cross-shore thermal exchange on a tropical forereef. *Journal of Geophysical Research: Oceans*, 119(9), 6101–6120. <https://doi.org/10.1002/2013JC009621>
- Monismith, S. G., Genin, A., Reidenbach, M. A., Yahel, G., & Koseff, J. R. (2006). Thermally driven exchanges between a coral reef and the adjoining ocean. *Journal of Physical Oceanography*, 36(7), 1332–1347. <https://doi.org/10.1175/JPO2916.1>
- Monismith, S. G., Imberger, J., & Morison, M. L. (1990). Convective motions in the sidearm of a small reservoir. *Limnology and Oceanography*, 35(8), 1676–1702. <https://doi.org/10.4319/lo.1990.35.8.1676>
- Moore, M. J., & Long, R. R. (1971). An experimental investigation of turbulent stratified shearing flow. *Journal of Fluid Mechanics*, 49(4), 635–655. <https://doi.org/10.1017/S0022112071002301>
- Mortimer, C. H. (1952). Water movements in lakes during summer stratification; evidence from the distribution of temperature in Windermere. *Philosophical Transactions of the Royal Society of London. Series B, Biological Sciences*, 236(635), 355–398. <https://doi.org/10.1098/rstb.1952.0005>
- Murase, J., Sakai, Y., Sugimoto, A., Okubo, K., & Sakamoto, M. (2003). Sources of dissolved methane in Lake Biwa. *Limnology*, 4(2), 91–99. <https://doi.org/10.1007/s10201-003-0095-0>
- Needham, D. J., & Merkin, J. H. (1984). On roll waves down an open inclined channel. *Proceedings of the Royal Society of London. A.*, 394(1807), 259–278. <https://doi.org/10.1098/rspa.1984.0079>
- Negretti, M., Zhu, D. Z., & Jirka, G. H. (2008). The effect of bottom roughness in two-layer flows down a slope. *Dynamics of Atmospheres and Oceans*, 45(1-2), 46–68. <https://doi.org/10.1016/j.dynatmoce.2008.02.001>
- Noh, Y., & Fernando, H. J. S. (1991). Gravity current propagation along an incline in the presence of boundary mixing. *Journal of Geophysical Research*, 96(C7), 12586–12592. <https://doi.org/10.1029/90JC02488>
- Noh, Y., & Fernando, H. J. S. (1992). The motion of a buoyant cloud along an incline in the presence of boundary mixing. *Journal of Fluid Mechanics*, 235, 557–577. <https://doi.org/10.1017/S0022112092001228>
- Noh, Y., Fernando, H. J. S., & Ching, C. Y. (1992). Flows induced by the impingement of a two-dimensional thermal on a density interface. *Journal of Physical Oceanography*, 22(10), 1207–1220. [https://doi.org/10.1175/1520-0485\(1992\)022<1207:FIBTIO>2.0.CO;2](https://doi.org/10.1175/1520-0485(1992)022<1207:FIBTIO>2.0.CO;2)
- Ogawa, S., Sha, W., Iwasaki, T., & Wang, Z. (2003). A numerical study on the interaction of a sea-breeze front with convective cells in the daytime boundary layer. *Journal of the Meteorological Society of Japan. Ser. II*, 81(4), 635–651. <https://doi.org/10.2151/jmsj.81.635>

- Pálmarrsson, S. Ó., & Schladow, S. G. (2008). Exchange flow in a shallow lake embayment. *Ecological Applications*, 18(8), A89–A106. <https://doi.org/10.1890/06-1618.1>
- Parker, D. J., Burton, R. R., Diongue-Niang, A., Ellis, R. J., Felton, M., Taylor, C. M., Thorncroft, C. D., Bessemoulin, P., & Tompkins, A. M. (2005). The diurnal cycle of the West African monsoon circulation. *Quarterly Journal of the Royal Meteorological Society*, 131(611), 2839–2860. <https://doi.org/10.1256/qj.04.52>
- Pattiaratchi, C., Hollings, B., Woo, M., & Welhena, T. (2011). Dense shelf water formation along the south-west Australian inner shelf. *Geophysical Research Letters*, 38(10), L10609. <https://doi.org/10.1029/2011GL046816>
- Pawlak, G., & Armi, L. (2000). Mixing and entrainment in developing stratified currents. *Journal of Fluid Mechanics*, 424, 45–73. <https://doi.org/10.1017/S0022112000001877>
- Peeters, F., Encinas Fernandez, J., & Hofmann, H. (2019). Sediment fluxes rather than oxic methanogenesis explain diffusive CH₄ emissions from lakes and reservoirs. *Scientific Reports*, 9(1), 243. <https://doi.org/10.1038/s41598-018-36530-w>
- Peeters, F., Finger, D., Hofer, M., Brennwald, M., Livingstone, D. M., & Kipfer, R. (2003). Deep-water renewal in Lake Issyk-Kul driven by differential cooling. *Limnology and Oceanography*, 48(4), 1419–1431. <https://doi.org/10.4319/lo.2003.48.4.1419>
- Peeters, F., & Hofmann, H. (2015). Length-scale dependence of horizontal dispersion in the surface water of lakes: Horizontal dispersion in lakes. *Limnology and Oceanography*, 60(6), 1917–1934. <https://doi.org/10.1002/lno.10141>
- Phillips, O. (1966). On turbulent convection currents and the circulation of the Red Sea. *Deep Sea Research and Oceanographic Abstracts*, 13(6), 1149–1160. [https://doi.org/10.1016/0011-7471\(66\)90706-6](https://doi.org/10.1016/0011-7471(66)90706-6)
- Ramón, C. L., Ulloa, H. N., Doda, T., & Bouffard, D. (2022). Flushing the lake littoral region: the interaction of differential cooling and mild winds. *Water Resources Research*, 58(3), e2021WR030943. <https://doi.org/10.1029/2021WR030943>
- Ramón, C. L., Ulloa, H. N., Doda, T., Winters, K. B., & Bouffard, D. (2021). Bathymetry and latitude modify lake warming under ice. *Hydrology and Earth System Sciences*, 25(4), 1813–1825. <https://doi.org/10.5194/hess-25-1813-2021>
- Rao, Y. R., & Schwab, D. J. (2007). Transport and mixing between the coastal and offshore waters in the Great Lakes: a review. *Journal of Great Lakes Research*, 33(1), 202–218. [https://doi.org/10.3394/0380-1330\(2007\)33\[202:TAMBTC\]2.0.CO;2](https://doi.org/10.3394/0380-1330(2007)33[202:TAMBTC]2.0.CO;2)
- Razlutskiy, V. I., Buseva, Z. F., Yu. Feniova, I., & Semenchenko, V. P. (2021). Convective circulation influences horizontal movement by planktonic crustaceans in the littoral zone of a mesotrophic lake. *Freshwater Biology*, 66(4), 716–729. <https://doi.org/10.1111/fwb.13672>

Bibliography

- Reynolds, C. S. (2008). A changing paradigm of pelagic food webs. *International Review of Hydrobiology*, 93(4-5), 517–531. <https://doi.org/10.1002/iroh.200711026>
- Roget, E., Colomer, J., Casamitjana, X., & Llebot, J. E. (1993). Bottom currents induced by baroclinic forcing in Lake Banyoles (Spain). *Aquatic Sciences*, 55(3), 206–227. <https://doi.org/10.1007/BF00877450>
- Rogowski, P., Merrifield, S., Ding, L., Terrill, E., & Gesiriech, G. (2019). Robotic mapping of mixing and dispersion of augmented surface water in a drought frequent reservoir. *Limnology and Oceanography: Methods*, 17(9), 475–489. <https://doi.org/10.1002/lom3.10326>
- Rueda, F., Moreno-Ostos, E., & Cruz-Pizarro, L. (2007). Spatial and temporal scales of transport during the cooling phase of the ice-free period in a small high-mountain lake. *Aquatic Sciences*, 69(1), 115–128. <https://doi.org/10.1007/s00027-006-0823-8>
- Sadro, S., Melack, J. M., & MacIntyre, S. (2011). Spatial and temporal variability in the ecosystem metabolism of a high-elevation lake: integrating benthic and pelagic habitats. *Ecosystems*, 14(7), 1123–1140. <https://doi.org/10.1007/s10021-011-9471-5>
- Safaie, A., Pawlak, G., & Davis, K. A. (2022). Diurnal thermally driven cross-shore exchange in steady alongshore currents. *Journal of Geophysical Research: Oceans*, 127(4), e2021JC017912. <https://doi.org/10.1029/2021JC017912>
- Salinas, J., Balachandar, S., Shringarpure, M., Fedele, J., Hoyal, D., & Cantero, M. (2020). Soft transition between subcritical and supercritical currents through intermittent cascading interfacial instabilities. *Proceedings of the National Academy of Sciences*, 117(31), 18278–18284. <https://doi.org/10.1073/pnas.2008959117>
- Schindler, D. E., & Scheuerell, M. D. (2002). Habitat coupling in lake ecosystems. *Oikos*, 98(2), 177–189. <https://doi.org/10.1034/j.1600-0706.2002.980201.x>
- Schlatter, J. W., Wüest, A., & Imboden, D. M. (1997). Hypolimnetic density currents traced by sulphur hexafluoride (SF₆). *Aquatic Sciences*, 59(3), 225–242. <https://doi.org/10.1007/BF02523275>
- Schmid, M., & Read, J. (2021). Heat budget of lakes. *Reference Module in Earth Systems and Environmental Sciences*. Elsevier. <https://doi.org/10.1016/B978-0-12-819166-8.00011-6>
- Schmidt, U., & Conrad, R. (1993). Hydrogen, carbon monoxide, and methane dynamics in Lake Constance. *Limnology and Oceanography*, 38(6), 1214–1226. <https://doi.org/10.4319/lo.1993.38.6.1214>
- Schmieder, K. (2004). European lake shores in danger — concepts for a sustainable development. *Limnologica*, 34(1-2), 3–14. [https://doi.org/10.1016/S0075-9511\(04\)80016-1](https://doi.org/10.1016/S0075-9511(04)80016-1)
- Schubert, C. J., Lucas, F. S., Durisch-Kaiser, E., Stierli, R., Diem, T., Scheidegger, O., Vazquez, F., & Müller, B. (2010). Oxidation and emission of methane in a monomictic lake (Rotsee, Switzerland). *Aquatic Sciences*, 72(4), 455–466. <https://doi.org/10.1007/s00027-010-0148-5>

- Schubert, C. J., Diem, T., & Eugster, W. (2012). Methane emissions from a small wind shielded lake determined by eddy covariance, flux chambers, anchored funnels, and boundary model calculations: a comparison. *Environmental Science & Technology*, 46(8), 4515–4522. <https://doi.org/10.1021/es203465x>
- Serafin, S., & Zardi, D. (2010). Daytime heat transfer processes related to slope flows and turbulent convection in an idealized mountain valley. *Journal of the Atmospheric Sciences*, 67(11), 3739–3756. <https://doi.org/10.1175/2010JAS3428.1>
- Sha, W., Kawamura, T., & Ueda, H. (1991). A numerical study on sea/land breezes as a gravity current: Kelvin–Helmholtz billows and inland penetration of the sea-breeze front. *Journal of the Atmospheric Sciences*, 48(14), 1649–1665. [https://doi.org/10.1175/1520-0469\(1991\)048<1649:ANSOSB>2.0.CO;2](https://doi.org/10.1175/1520-0469(1991)048<1649:ANSOSB>2.0.CO;2)
- Shapiro, G. I. (2003). Dense water cascading off the continental shelf. *Journal of Geophysical Research*, 108(C12), 3390. <https://doi.org/10.1029/2002JC001610>
- Shapiro, G. I., & Hill, A. E. (1997). Dynamics of dense water cascades at the shelf edge. *Journal of Physical Oceanography*, 27(11), 2381–2394. [https://doi.org/10.1175/1520-0485\(1997\)027<2381:DODWCA>2.0.CO;2](https://doi.org/10.1175/1520-0485(1997)027<2381:DODWCA>2.0.CO;2)
- Sharip, Z., Hipsey, M., Schooler, S., & Hobbs, R. (2012). Physical circulation and spatial exchange dynamics in a shallow floodplain wetland. *International Journal of Design & Nature and Ecodynamics*, 7(3), 274–291. <https://doi.org/10.2495/DNE-V7-N3-274-291>
- Simpson, J. E. (1982). Gravity currents in the laboratory, atmosphere, and ocean. *Annual Review of Fluid Mechanics*, 14(1), 213–234. <https://doi.org/10.1146/annurev.fl.14.010182.001241>
- Simpson, J. E. (1986). Mixing at the front of a gravity current. *Acta Mechanica*, 63(1-4), 245–253. <https://doi.org/10.1007/BF01182551>
- Simpson, J. E., & Britter, R. E. (1980). A laboratory model of an atmospheric mesofront. *Quarterly Journal of the Royal Meteorological Society*, 106(449), 485–500. <https://doi.org/10.1002/qj.49710644907>
- Simpson, J. E., Mansfield, D. A., & Milford, J. R. (1977). Inland penetration of sea-breeze fronts. *Quarterly Journal of the Royal Meteorological Society*, 103(435), 47–76. <https://doi.org/10.1002/qj.49710343504>
- Solomon, C. T., Jones, S. E., Weidel, B. C., Buffam, I., Fork, M. L., Karlsson, J., Larsen, S., Lennon, J. T., Read, J. S., Sadro, S., & Saros, J. E. (2015). Ecosystem consequences of changing inputs of terrestrial dissolved organic matter to lakes: current knowledge and future challenges. *Ecosystems*, 18(3), 376–389. <https://doi.org/10.1007/s10021-015-9848-y>
- Soloviev, A., & Lukas, R. (2014). *The near-surface layer of the ocean: structure, dynamics, and applications* (2nd ed.). Springer.

Bibliography

- Staehr, P. A., Bade, D., Van de Bogert, M. C., Koch, G. R., Williamson, C., Hanson, P., Cole, J. J., & Kratz, T. (2010). Lake metabolism and the diel oxygen technique: state of the science. *Limnology and Oceanography: Methods*, 8(11), 628–644. <https://doi.org/10.4319/lom.2010.8.0628>
- Stefan, H. G., Horsch, G. M., & Barko, J. W. (1989). A model for the estimation of convective exchange in the littoral region of a shallow lake during cooling. *Hydrobiologia*, 174(3), 225–234. <https://doi.org/10.1007/BF00008162>
- Stocker, R., & Imberger, J. (2003). Horizontal transport and dispersion in the surface layer of a medium-sized lake. *Limnology and Oceanography*, 48(3), 971–982. <https://doi.org/10.4319/lo.2003.48.3.0971>
- Strayer, D. L., & Dudgeon, D. (2010). Freshwater biodiversity conservation: recent progress and future challenges. *Journal of the North American Benthological Society*, 29(1), 344–358. <https://doi.org/10.1899/08-171.1>
- Stull, R. B. (1976). Internal gravity waves generated by penetrative convection. *Journal of the Atmospheric Sciences*, 33(7), 1279–1286. [https://doi.org/10.1175/1520-0469\(1976\)033<1279:IGWGBP>2.0.CO;2](https://doi.org/10.1175/1520-0469(1976)033<1279:IGWGBP>2.0.CO;2)
- Sturman, J. J., & Ivey, G. N. (1998). Unsteady convective exchange flows in cavities. *Journal of Fluid Mechanics*, 368, 127–153. <https://doi.org/10.1017/S002211209800175X>
- Sturman, J. J., Ivey, G. N., & Taylor, J. R. (1996). Convection in a long box driven by heating and cooling on the horizontal boundaries. *Journal of Fluid Mechanics*, 310, 61–87. <https://doi.org/10.1017/S0022112096001735>
- Sturman, J. J., Oldham, C. E., & Ivey, G. N. (1999). Steady convective exchange flows down slopes. *Aquatic Sciences*, 61(3), 260–278. <https://doi.org/10.1007/s000270050065>
- Sullivan, P. P., Moeng, C.-H., Stevens, B., Lenschow, D. H., & Mayor, S. D. (1998). Structure of the entrainment zone capping the convective atmospheric boundary layer. *Journal of the Atmospheric Sciences*, 55(19), 3042–3064. [https://doi.org/10.1175/1520-0469\(1998\)055<3042:SOTEZC>2.0.CO;2](https://doi.org/10.1175/1520-0469(1998)055<3042:SOTEZC>2.0.CO;2)
- Symonds, G., & Gardiner-Garden, R. (1994). Coastal density currents forced by cooling events. *Continental Shelf Research*, 14(2-3), 143–157. [https://doi.org/10.1016/0278-4343\(94\)90010-8](https://doi.org/10.1016/0278-4343(94)90010-8)
- Talling, J. F. (1963). Origin of stratification in an African Rift lake. *Limnology and Oceanography*, 8(1), 68–78. <https://doi.org/10.4319/lo.1963.8.1.0068>
- Tedford, E. W., MacIntyre, S., Miller, S. D., & Czikowsky, M. J. (2014). Similarity scaling of turbulence in a temperate lake during fall cooling. *Journal of Geophysical Research: Oceans*, 119(8), 4689–4713. <https://doi.org/10.1002/2014JC010135>

- Thorpe, S. A., Lemmin, U., Perrinjaquet, C., & Fer, I. (1999). Observations of the thermal structure of a lake using a submarine. *Limnology and Oceanography*, 44(6), 1575–1582. <https://doi.org/10.4319/lo.1999.44.6.1575>
- Thorpe, S. A., & Ozen, B. (2007). Are cascading flows stable? *Journal of Fluid Mechanics*, 589, 411–432. <https://doi.org/10.1017/S0022112007007902>
- Tsunogai, U., Miyoshi, Y., Matsushita, T., Komatsu, D. D., Ito, M., Sukigara, C., Nakagawa, F., & Maruo, M. (2020). Dual stable isotope characterization of excess methane in oxic waters of a mesotrophic lake. *Limnology and Oceanography*, 65(12), 2937–2952. <https://doi.org/10.1002/lno.11566>
- Ulloa, H. N., Davis, K. A., Monismith, S. G., & Pawlak, G. (2018). Temporal variability in thermally driven cross-shore exchange: The role of semidiurnal tides. *Journal of Physical Oceanography*, 48(7), 1513–1531. <https://doi.org/10.1175/JPO-D-17-0257.1>
- Ulloa, H. N., Ramón, C. L., Doda, T., Wüest, A., & Bouffard, D. (2022). Development of overturning circulation in sloping waterbodies due to surface cooling. *Journal of Fluid Mechanics*, 930, A18. <https://doi.org/10.1017/jfm.2021.883>
- Ulloa, H. N., Winters, K. B., Wüest, A., & Bouffard, D. (2019). Differential heating drives downslope flows that accelerate mixed-layer warming in ice-covered waters. *Geophysical Research Letters*, 46(23), 13872–13882. <https://doi.org/10.1029/2019GL085258>
- Vadeboncoeur, Y., McIntyre, P. B., & Vander Zanden, M. J. (2011). Borders of biodiversity: life at the edge of the world's large lakes. *BioScience*, 61(7), 526–537. <https://doi.org/10.1525/bio.2011.61.7.7>
- Vander Zanden, M. J., & Vadeboncoeur, Y. (2020). Putting the lake back together 20 years later: what in the benthos have we learned about habitat linkages in lakes? *Inland Waters*, 10(3), 305–321. <https://doi.org/10.1080/20442041.2020.1712953>
- van Grinsven, S., Oswald, K., Wehrli, B., Jegge, C., Zopfi, J., Lehmann, M. F., & Schubert, C. J. (2021). Methane oxidation in the waters of a humic-rich boreal lake stimulated by photosynthesis, nitrite, Fe(III) and humics. *Biogeosciences*, 18(10), 3087–3101. <https://doi.org/10.5194/bg-18-3087-2021>
- Verburg, P., Antenucci, J. P., & Hecky, R. E. (2011). Differential cooling drives large-scale convective circulation in Lake Tanganyika. *Limnology and Oceanography*, 56(3), 910–926. <https://doi.org/10.4319/lo.2011.56.3.0910>
- Veronis, G. (1963). Penetrative convection. *The Astrophysical Journal*, 137, 641–663. <https://doi.org/10.1086/147538>
- Vincent, W. F. (2018). *Lakes: a very short introduction* (Vol. 547). Oxford University Press. <https://doi.org/10.1093/actrade/9780198766735.001.0001>

Bibliography

- Wang, Q., Dore, J. E., & McDermott, T. R. (2017). Methylphosphonate metabolism by *Pseudomonas* sp. populations contributes to the methane oversaturation paradox in an oxic freshwater lake. *Environmental Microbiology*, 19(6), 2366–2378. <https://doi.org/10.1111/1462-2920.13747>
- Warren, G. J., Lesht, B. M., & Barbiero, R. P. (2018). Estimation of the width of the nearshore zone in Lake Michigan using eleven years of MODIS satellite imagery. *Journal of Great Lakes Research*, 44(4), 563–572. <https://doi.org/10.1016/j.jglr.2017.11.011>
- Wedderburn, E. M. (1907). The temperature of the fresh-water Lochs of Scotland, with special reference to Loch Ness. *Transactions of the Royal Society of Edinburgh*, 45(2), 407–489. <https://doi.org/10.1017/S0080456800022791>
- Wells, M. G., & Dorrell, R. M. (2021). Turbulence processes within turbidity currents. *Annual Review of Fluid Mechanics*, 53(1), 59–83. <https://doi.org/10.1146/annurev-fluid-010719-060309>
- Wells, M. G., & Nadarajah, P. (2009). The intrusion depth of density currents flowing into stratified water bodies. *Journal of Physical Oceanography*, 39(8), 1935–1947. <https://doi.org/10.1175/2009JPO4022.1>
- Wells, M. G., & Sherman, B. (2001). Stratification produced by surface cooling in lakes with significant shallow regions. *Limnology and Oceanography*, 46(7), 1747–1759. <https://doi.org/10.4319/lo.2001.46.7.1747>
- Wetzel, R. G. (2001). *Limnology: Lake and River Ecosystems* (3rd ed.). Academic Press.
- Weyhenmeyer, G. A., Kosten, S., Wallin, M. B., Tranvik, L. J., Jeppesen, E., & Roland, F. (2015). Significant fraction of CO₂ emissions from boreal lakes derived from hydrologic inorganic carbon inputs. *Nature Geoscience*, 8(12), 933–936. <https://doi.org/10.1038/ngeo2582>
- Winfield, I. J. (2004). Fish in the littoral zone: ecology, threats and management. *Limnologica*, 34(1-2), 124–131. [https://doi.org/10.1016/S0075-9511\(04\)80031-8](https://doi.org/10.1016/S0075-9511(04)80031-8)
- Winters, K. B., & Seim, H. E. (2000). The role of dissipation and mixing in exchange flow through a contracting channel. *Journal of Fluid Mechanics*, 407, 265–290. <https://doi.org/10.1017/S0022112099007727>
- Woodward, B. L., Marti, C. L., Imberger, J., Hipsey, M. R., & Oldham, C. E. (2017). Wind and buoyancy driven horizontal exchange in shallow embayments of a tropical reservoir: Lake Argyle, Western Australia. *Limnology and Oceanography*, 62(4), 1636–1657. <https://doi.org/10.1002/lno.10522>
- Wright, L. D., Friedrichs, C. T., Kim, S. C., & Scully, M. E. (2001). Effects of ambient currents and waves on gravity-driven sediment transport on continental shelves. *Marine Geology*, 175(1-4), 25–45. [https://doi.org/10.1016/S0025-3227\(01\)00140-2](https://doi.org/10.1016/S0025-3227(01)00140-2)

- Wu, X., Cahl, D., & Voulgaris, G. (2018). Effects of wind stress and surface cooling on cross-shore exchange. *Journal of Physical Oceanography*, 48(11), 2627–2647. <https://doi.org/10.1175/JPO-D-17-0216.1>
- Wüest, A., & Lorke, A. (2003). Small-scale hydrodynamics in lakes. *Annual Review of Fluid Mechanics*, 35(1), 373–412. <https://doi.org/10.1146/annurev.fluid.35.101101.161220>
- Xiao, S., Liu, L., Wang, W., Lorke, A., Woodhouse, J., & Grossart, H.-P. (2020). A Fast-Response Automated Gas Equilibrator (FaRAGE) for continuous in situ measurement of CH₄ and CO₂ dissolved in water. *Hydrology and Earth System Sciences*, 24(7), 3871–3880. <https://doi.org/10.5194/hess-24-3871-2020>
- Yao, M., Henny, C., & Maresca, J. A. (2016). Freshwater bacteria release methane as a by-product of phosphorus acquisition (J. E. Kostka, Ed.). *Applied and Environmental Microbiology*, 82(23), 6994–7003. <https://doi.org/10.1128/AEM.02399-16>
- Zhu, D. Z., & Lawrence, G. A. (2001). Holmboe’s instability in exchange flows. *Journal of Fluid Mechanics*, 429, 391–409. <https://doi.org/10.1017/S002211200000286X>
- Zilitinkevič, S. S. (1991). *Turbulent Penetrative Convection* (B. Henderson-Sellers, Ed.). Avebury.
- Zimmermann, M., Mayr, M. J., Bürgmann, H., Eugster, W., Steinsberger, T., Wehrli, B., Brand, A., & Bouffard, D. (2021). Microbial methane oxidation efficiency and robustness during lake overturn. *Limnology and Oceanography Letters*, 6(6), 320–328. <https://doi.org/10.1002/lol2.10209>

Tomy Doda

Curriculum Vitae

Brunnmattstrasse 18

6048 Horw

+41 (0)76 226 8086

+41 (0)58 765 2298

tomy.doda@eawag.ch

PhD Student in Aquatic Physics

Personal information

Nationality French

Birth date 23 February 1995

Marital status Single

Education

2018–2022 **Ph.D. in Civil and Environmental Engineering**, Eawag (Kastanienbaum, Switzerland); Ecole Polytechnique Fédérale de Lausanne (EPFL, Lausanne, Switzerland).
Supervisors: Dr. Damien Bouffard, Prof. Alfred Wüest, Prof. Christophe Ancely

Feb–Aug **Master thesis**, University of British Columbia (UBC, Vancouver, Canada).

2015 Supervisors: Prof. Gregory Lawrence, Dr. Roger Pieters, Dr. Edmund Tedford, Prof. Alfred Wüest

2015–2017 **M.Sc. in Environmental Sciences and Engineering**, Ecole Polytechnique Fédérale de Lausanne (EPFL, Lausanne, Switzerland).

2014–2015 **Exchange program, third year of Bachelor**, University of Waterloo (Waterloo, Canada).

2012–2015 **B.Sc. in Environmental Sciences and Engineering**, Ecole Polytechnique Fédérale de Lausanne (EPFL, Lausanne, Switzerland).

Work Experience

2019–2020 **Doctoral assistant**, Ecole Polytechnique Fédérale de Lausanne (EPFL, Lausanne, Switzerland).

Limnology (×2), Quantitative Methods.

2018–2020 **Doctoral assistant**, Eidgenössische Technische Hochschule (ETHZ, Zürich, Switzerland).

Biogeochemical Modelling of Sediments, Lakes and Oceans (×3).

2015–2017 **Student assistant**, Ecole Polytechnique Fédérale de Lausanne (EPFL, Lausanne, Switzerland).

Probabilities and Statistics, Analysis I, Analysis III (×2), Analysis IV, Environmental Bioprocess Design, Quantitative Methods.

Jul–Aug 2015 **Professional Internship**, Canton de Vaud (Lausanne, Switzerland).

Internship at the Environmental Department (landfill remediation).

Publications

Published

- [4] Ramón, C. L., Ulloa, H. N., Doda, T., & Bouffard, D. (2022). Flushing the lake littoral region: The interaction of differential cooling and mild winds. *Water Resources Research*, 58(3).
- [3] Doda, T., Ramón, C. L., Ulloa, H. N., Wüest, A., & Bouffard, D. (2022). Seasonality of density currents induced by differential cooling. *Hydrology and Earth System Sciences*, 26(2), 331–353.
- [2] Ulloa, H. N., Ramón, C. L., Doda, T., Wüest, A., & Bouffard, D. (2022). Development of overturning circulation in sloping waterbodies due to surface cooling. *Journal of Fluid Mechanics*, 930, A18.
- [1] Ramón, C. L., Ulloa, H. N., Doda, T., Winters, K. B., & Bouffard, D. (2021). Bathymetry and latitude modify lake warming under ice. *Hydrology and Earth System Sciences*, 25(4), 1813–1825.

Submitted & In preparation

- [1] Doda, T., Ramón, C. L., Ulloa, H. N., Wüest, A., & Bouffard, D. Penetrative convection modifies the dynamics of downslope gravity currents. Submitted to *Geophysical Research Letters*.
- [2] Doda, T., Ramón, C. L., Ulloa, H. N., Brennwald, M. S., Kipfer R., Perga M. E., Wüest, A., Schubert C. J. & Bouffard, D. Lake surface cooling drives littoral-pelagic exchanges of dissolved gases. In preparation.
- [3] Doda, T., Cruz, H., Runnalls J., Ramón, C. L., Ulloa, H. N., Hédouin E., Plüss M. & Bouffard, D. Towards a parametrization of cooling-driven lateral transport in lakes. In preparation.
- [4] Perga M. E., Minaudo C., Doda T., Arthaud F., Beria H., Chmiel H.E., Escoffier N., Lambert T., Napolleoni R., Obrador B., Perolo P., Rüegg J., Ulloa H. & Bouffard D. Near-bed stratification controls bottom hypoxia in ice-covered alpine lakes. Submitted to *Limnology and Oceanography*.

Awards

- 2021 Best Poster Award from the Swiss Society for Hydrology and Limnology, at the 2021 Swiss Geoscience Meeting (online)
- 2020 Best Poster Award at the Center for Ecology, Evolution, and Biogeochemistry (CEEB) poster competition (Eawag)
- 2020 Best Poster Award from the Swiss Society for Hydrology and Limnology, at the 2020 Swiss Geoscience Meeting (online)
- 2018 Second Best Poster Award at the Center for Ecology, Evolution, and Biogeochemistry (CEEB) poster competition (Eawag)
- 2018 Second Best Poster Award at the 2018 Physical Processes in Natural Waters workshop (Solothurn, Switzerland)

- 2017 Prix de la Société Suisse de Géomatique et de Gestion du Territoire, rewarded to the student from the Environmental Sciences and Engineering Department (SIE, EPFL) with the best Master average
- 2017 Prix SIA Vaud, rewarded to the engineer from the School of Architecture, Civil and Environmental Engineering (ENAC, EPFL) with the best Master average

Computer skills

Programming and sharing Matlab, Python, Git

Typing L^AT_EX, Microsoft Word

Graphics and Multimedia Inkscape, Microsoft Power Point, VSDC Video Editor

Languages

French Mothertongue

English Advanced

German Basic

Spanish Basic

Interests

Mountain sports, biking, winter swimming, violin, photography.